IPPJ-AM-33

PROCEEDINGS
ON
SYMPOSIUM ON ATOMIC COLLISION DATA FOR DIAGNOSTICS AND MODELLING OF FUSION PLASMAS

EDITED BY
H. TAWARA

INSTITUTE OF PLASMA PHYSICS
NAGOYA UNIVERSITY

NAGOYA, JAPAN

IPPJ-AM-33

PROCEEDINGS
ON
SYMPOSIUM ON ATOMIC COLLISION DATA FOR DIAGNOSTICS AND MODELLING OF FUSION PLASMAS
AUGUST 29 – 30, 1983

Edited by
Hiroyuki TAWARA

Institute of Plasma Physics, Nagoya University
Chikusa-ku, Nagoya 464, Japan

December 1983

Foreword

"Symposium on Atomic Collision Data for Diagnostics and Modelling of Fusion Plasmas" was held at the Institute of Plasma Physics, Nagoya University, on August 29-30, 1982, on the occasion of the second meeting of the Coordinated Research Program (CRP) of the International Atomic Energy Agency which was also held in the Institute on the following days, August 31 through September 2. About seventy scientists including twelve from abroad attended the Symposium.

This Symposium was organized in order to exchange information and to promote discussions, among atomic and plasma physicist, on atomic collision processes which are believed to play an important role in fusion plasmas themselves and their diagnostics and modelling.

The topics of the Symposium were as follows:

1. Atomic processes and their data for modelling and diagnosing plasmas in Tokamaks and inertial confinements
2. Atomic collision data for laboratory plasma and evaluation of atomic data from plasma experiments
3. Related basic atomic collision processes
4. Reports on activities of atomic data evaluation in CRP.

This Proceedings includes 18 papers which were presented at the Symposium. The editor would like to express his sincere thanks to the contributors to the Proceedings who wrote summaries of their interesting talks and also to those who joined in discussions at the Symposium. He is also indebted to Prof. H. Momota, Prof. J. Fujita and Dr. T. Kato for their help in organizing the Symposium.

The financial support from the Grant-in-Aid for Fusion Research, the Ministry of Education, Science and Culture, is highly acknowledged.

H. Tawara
Editor

CONTENTS

Atomic Processes for Plasma Diagnostics in Tokamaks

Satoshi KASAI

Division of Thermonuclear Fusion Research,

Tokai Research Establishment, JAERI

Tokai, 319-11, Japan

Abstract

Transport phenomena of metal impurities in neutral beam heated plasmas (JFT-2) and in ohmically heated plasmas (ISX-B) are analyzed. It is shown that the ion temperature in the plasma center can be estimated from spectroscopic measurements by observing the forbidden-lines of highly ionized ions. Spectroscopic observations of charge transfer processes in ISX-B plasmas during neutral beam heating and their application to determination of the density of fully ionized oxygen are discussed.

All these results indicate requirements of accurate calculations and measurements of rate coefficients for ionization, recombination (radiative, dielectronic and charge transfer), and excitation in order to understand plasma properties in high temperature tokamaks.

I. Introduction

In the past few years, much effort in tokamak plasma research is devoted to supplementary heating experiments, mainly neutral beam (NB) and ion cyclotron range of frequencies (ICRF) as well as to development of plasma diagnostics. In plasmas with the increased electron and ion temperature, most of light and metal impurities are in highly ionized stages and fully ionized hydrogen-like and helium-like ions are expected to be present . In these plasmas, the spectral emission from these impurities is increasingly extended to soft X-ray region, and then a number of new requirements for diagnostics, particularly for spectroscopic diagnostics, are proposed. It is also expected from neo-classical plasma theory that impurity transport phenomena during supplementary heating are different from those in ohmically heated plasmas in tokamaks.

In the present paper, the following experimental results in the JFT-2 tokamak in JAERI and in the ISX-B tokamak in ORNL, where I had joined the study of impurity behavior in 1980, are described.

(1) Metal impurity transport in ohmically heated plasmas in ISX-B[1] and in neutral beam heated plasmas in JFT-2.[2]

(2) Measurements of Doppler ion temperature and toroidal plasma rotation velocity in JRT-2.[3]

(3) Measurements of charge transfer process during neutral beam injection in ISX-B and application of this measurement for estimate of contents of fully ionized

ions.[4]

A summary of atomic data requirements is presented in the last section.

II. Experimental Results in JFT-2 and ISX-B Tokamaks

(1) Metal impurity transport in ohmically heated plasmas (ISX-B) and in neutral beam heated plasmas (JFT-2)

One of the main purposes of spectroscopic diagnostics is the determination of contents of low-z and high-z impurities and radiation losses from tokamak plasmas. Another purpose is to make clear the impurity transport across the confining magnetic field and to find a method of efficient impurity control. Such studies become much important in relatively high-power supplementary heating plasmas.

Figures 1 and 2 show time-behaviors of the averaged electron density, soft X-ray and emission rate of iron spectral lines in deuterium and hydrogen plasmas heated ohmically in ISX-B. The electron density and temperature are nearly the same in both discharges. The significant difference between the results in hydrogen and deuterium is the temporal behavior of the interior ions and the soft X-ray. They are nearly constant during hydrogen sequence, but they continuously increase at a rate much faster than the increase of the electron density after about 70 ms during deuterium sequence. In contrast to the Fe XVI and Fe XIII radiations, the Fe IX line remains nearly constant in both

sequences. This indicates that the influx of iron is nearly constant. Therefore, the temporal increase of the soft X-ray signal and of the iron lines indicates impurity accumulation in deuterium plasmas but that is not the case in hydrogen plasmas.

The present results emphasize the need for a deeper understanding of particle transport mechanisms in order to assess the impurity problems in future, long-pulse machines.

Some plasma theorists predict that metal impurity ions are driven out from a central region of plasma during neutral beam injection in the direction of a plasma current (co-injection), meanwhile they are accumulated near the center of plasma during injection in the opposite direction of a plasma current (counter-injection). Neutral beam is injected tangentially to a plasma current in both cases.

Figure 3 shows time-behaviors of the line-integrated intensity of the Fe XIX, Fe XVIII, Fe XV and Fe X lines measured along the central chord in deuterium plasmas with 1 MW hydrogen beam injection at 100 ms in JFT-2. The solid and dashed lines indicate time-behaviors in co-injection and counter-injection, respectively. When the neutral beam is injected, the emission from ions in low-charge states such as Fe XV and Fe X decreases due to the rise of the electron temperature in both cases. Behaviors of the Fe X line indicate that the iron influx into the plasma does not increase significantly during injection. During co-injection the emission from Fe XVIII is constant or slightly decreases and Fe XIX increases gradually due to heating of the central plasma. On the other hand, during counter-injection,

intensities of the Fe XIX and Fe XVIII lines increase by about one order of magnitude, compared with those before injection. After 120 ms, they diminish quickly, meanwhile Fe XV and Fe X radiate strongly. This is due to the excess radiation cooling near the central region of the plasma.

In another experimental sequence, the temporal behaviors of spatial profiles of the Fe XVIII line radiation were investigated during co- and counter-injection. During co-injection, the profiles become slightly hollow, meanwhile, in counter-injection, they become peaked with time. Such experimentally observed spatial- and time-behaviors strongly suggest the enhanced outward-diffusion of impurity ions in co-injection, in addition to neo-classical and anomalous diffusions, as found in numerical simulation, whereas the enhanced inward-diffusion in counter-injection.

From these results, I can conclude that iron impurity is driven out from the central region of the plasma by co-injection, and accumulated into the central region by counter-injection, though there are some unknown factors in counter-injected discharges.

(2) Doppler ion temperature and rotation velocity of plasmas (JFT-2)

The ion temperature and its spatial profile can be obtained from energy-spectrum measurements of charge-changed neutrals and Doppler broadening measurements of impurity spectral lines.

In plasmas with electron temperature less than several hundreds of eV, for example in JFT-2, some allowed spectral lines emitted from light impurity ions such as O VII(=1623Å), C IV(λ =1548Å), C III(λ=2297Å), C II(λ=2837Å) and N V(λ=1239Å) are used to determine the spatial profiles of ion temperature from their Doppler broadened profiles, because the emission from these ions is distributed from the plasmas center to its periphery.

When electron temperature increases by supplementary heating, these ions tend to be distributed only in peripheral region. Then, we need other spectral lines produced in the hot core region in order to determine the central ion temperature. Figure 4 shows the temporal plasma-temperature during supplementary heating (NBI : 2 MW and ICRF : 0.5 MW). The dash-dot line shows the central electron temperature. The solid line shows the ion temperature obtained by Doppler broadened profile of the Ti XVIII line. Uncertainties are due to shot-to-shot reproducibility and relatively weak intensity of the line. The central ion temperature is also determined by the energy-spectrum analysis of charge-changed neutral particles. The ion temperatures determined with two methods agree well each other within experimental uncertainties.

Another application of the forbidden lines is measurements of toroidal rotation-velocity of a plasma during imbalanced tangential injection of neutral beam. In JFT-2, time- and spatial-variations of rotation velocity were determined through measurement of the Doppler shift of the Ti XIV, O VII and C V lines. In co-injection, the plasma rotates in the direction of

the current. The velocity in the central region gradually increases. Maximum rotation velocity is found to be about 1.5 x 10^6 cm/s during injection. These measurements are very important in understanding the effects of plasma rotation on the particle transport.

It is concluded that Doppler broadening technique in observation of the forbidden lines of impurity ions is very useful in determining the ion temperature and plasma rotation velocity in tokamak plasmas.

(3) Charge transfer process during neutral beam injection (ISX-B)[4)]

Spectral-line excitation from charge transfer process has been observed during neutral beam heating in ORMAK, ISX-B, PLT, PDX and DITE.

Figure 5 shows the time-behavior of spectral signals of the 3→2 transition of O^{7+} ions in ISX-B. The grazing incidence spectrometer used for line-integrated spectral observation is located so that its field of view includes high energy hydrogen atoms from the west-beam, but not from the east-beam. When the west beam is operated alone, the spectral signals observed result from the sum of charge exchange and electron excitation (Fig. 5(a)). On the other hand, because the lifetime of the excited states is less than 2 x 10^{-10}s, the excited ions produced by charge capture in collision with the east-beam particles decay before they move along the toroidal magnetic field into the field

of view of the spectrometer. Therefore, when only the east-beam is operated, the spectral signal as shown in Fig. 5(b) arises solely from electron excitation. The direct charge-transfer signal as shown in Fig. 5(c) is obtained by subtracting signals in east-beam shot from those in west-beam shot.

The concentration of O^{8+} in the center of the plasma, n_8, is determined from signals due to charge-change through the following relationship:

$$S_c = \int_{-a}^{a} j(r) n_8(r) \sigma dr.$$

Here S_c is the measured emission rate of a spectral line, $j(r)$ is the current density of the neutral beam, and is the cross-section for charge change. The integral is evaluated along the optic axis of the spectrometer. In the present case, the well-localized concentration of O^{8+} can not be obtained because the heating neutral beam is so wide-spread at the point of observation. While using this equation, the profile of O^{8+} is assumed to be both flat and peaked and two different profiles of the electron density are assumed. From this result, the concentration of O^{8+} near the plasma center is estimated to be approximately 2×10^{11} cm^{-3} in this plasma with the central electron density of about 3×10^{13} cm^{-3}.

Therefore, we can use spectral lines from charge transfer to estimate contents of fully ionized or partially ionized impurity ions such as C, O, Ti, Fe and Ni.

III. Conclusion

In order to get better understanding of the hot plasma properties in tokamaks, we have to measure a number of quantities such as contents of low-Z and high-Z impurities, the effective ionic charge (Z_{eff}), plasma temperature and its density. Also we have to know impurity transport process to find efficient impurity control methods.

Until now, uncertainties of the rate coefficients for ionization, excitation and recombination (radiative and dielectronic) are estimated to be a factor of 2-3 for most of elements like C, O, Ti and Fe. The rate coefficients with errors smaller than a few tens of percent are required in tokamak research. In applications of the long-wavelength forbidden lines of highly ionized ions for plasma diagnostics, we need to know the accurate wavelength. Also it is important to have accurate wavelength prediction for rare gas ions like Ar and Kr. Finally, the cross-sections for charge transfer of impurity ions like C, O, Ti, Fe, Ar and Kr with hydrogen and deuterium are required in order to apply spectral emissions due to this atomic process to plasma diagnostics.

Acknowledgments

The author would like to express his thanks to all the members of Plasma Physics Laboratory and ISX-B Group in Oak Ridge National Laboratory, and to Drs. R.C. Isler and T. Sugie for their support and useful discussion during these experiments. The author would also like to acknowledge Drs. Y. Tanaka, M. Tanaka and Y. Obata for their continuous encouragement.

References

(1) R.C. Isler, S. Kasai, L.E. Murray, M. Saltmarsh and M. Murakami: Phys, Letters 3 (1981) 333.

(2) S. Kasai, T. Hirayama, T. Yamauchi, T.Sugie, S. Yamamoto et al. : JAERI-M 82-164 (November, 1982)

(3) T. Sugie : private communication.

(4) R.C. Isler, L.E. Murray, S. Kasai, J.L. Dunlap, S.C. Bates et al. : Phys. Rev. A24 (1981) 2701.

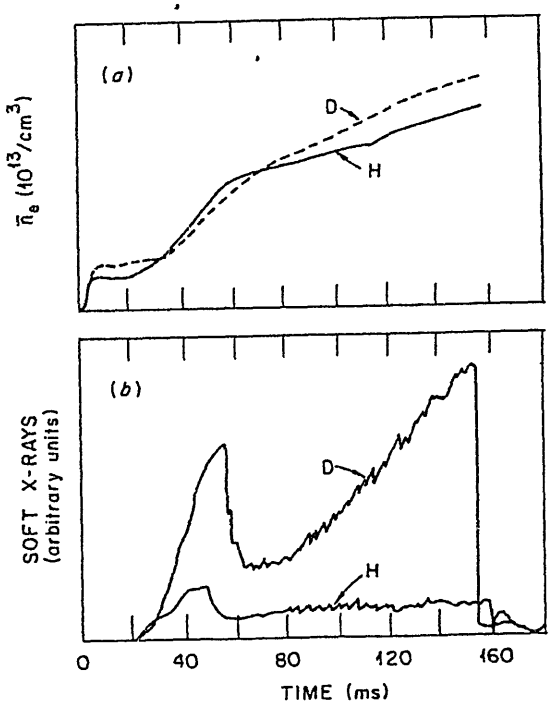

Fig. 1 The line-averaged electron densities and the soft X-ray signals during ohmically heated deuterium (D) and hydrogen(H) discharges.

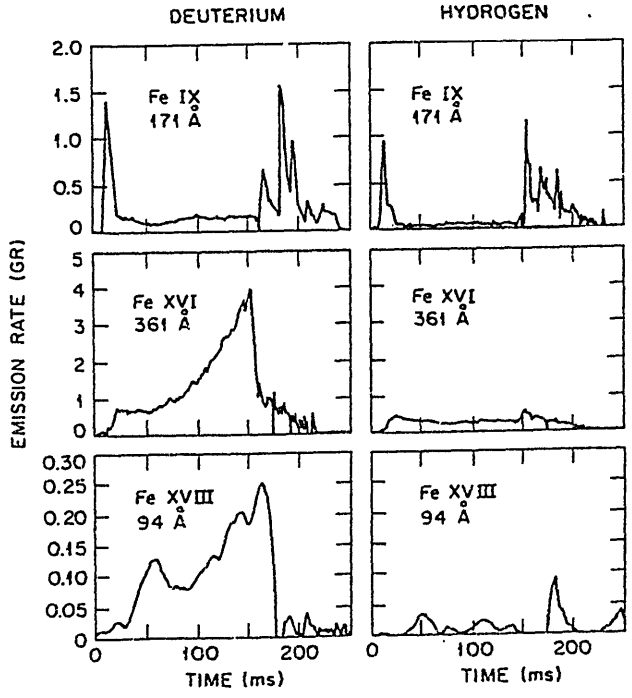

Fig. 2 Comparisons of emission rates (1 giga-rayleigh = 10^{15} photons/cm^2.s) from several iron lines during ohmically heated deuterium and hydrogen discharges.

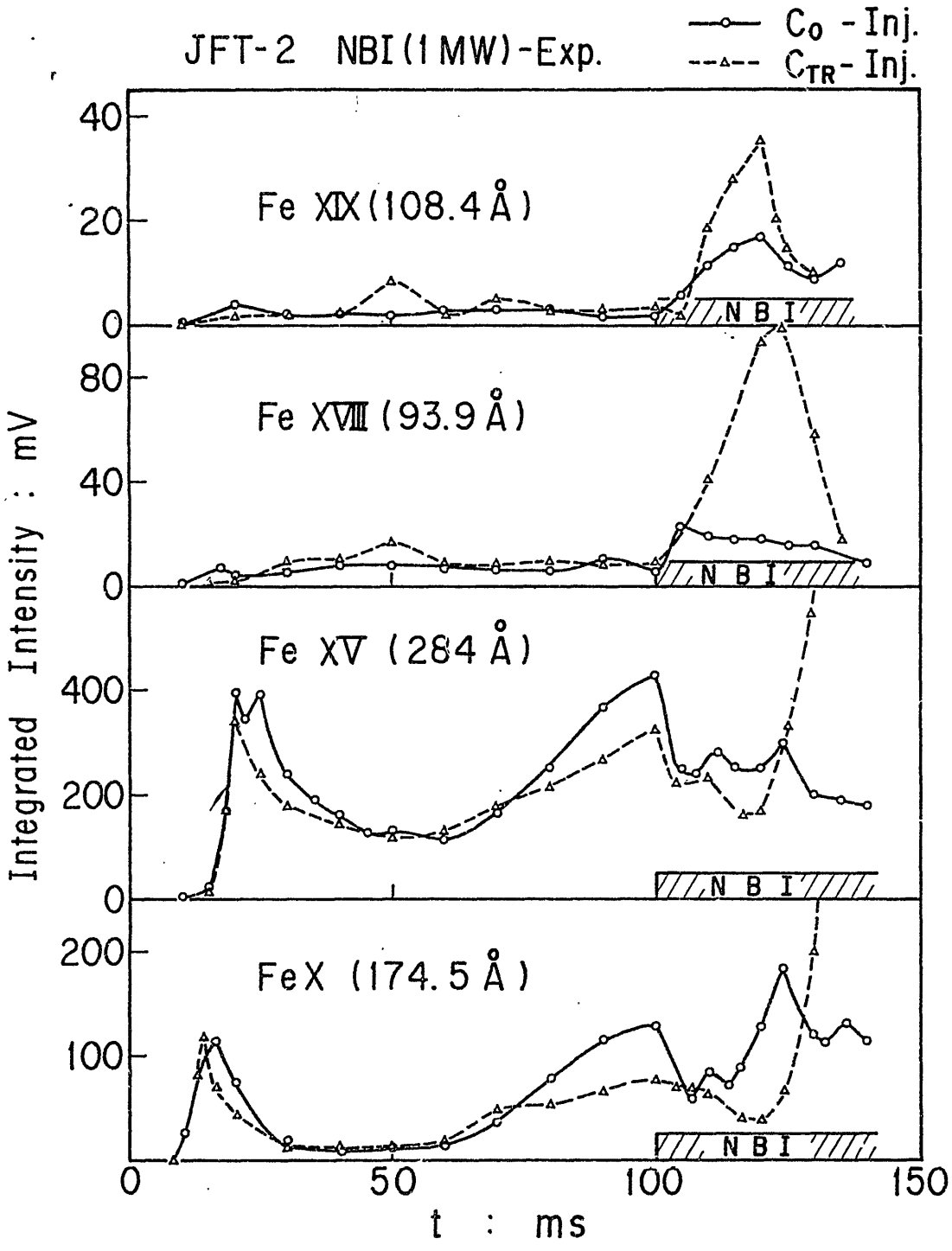

Fig. 3 Time-behaviors of line-integrated intensities of Fe XIX, Fe XVIII, Fe XV and Fe X lines during co- and counter- injection.

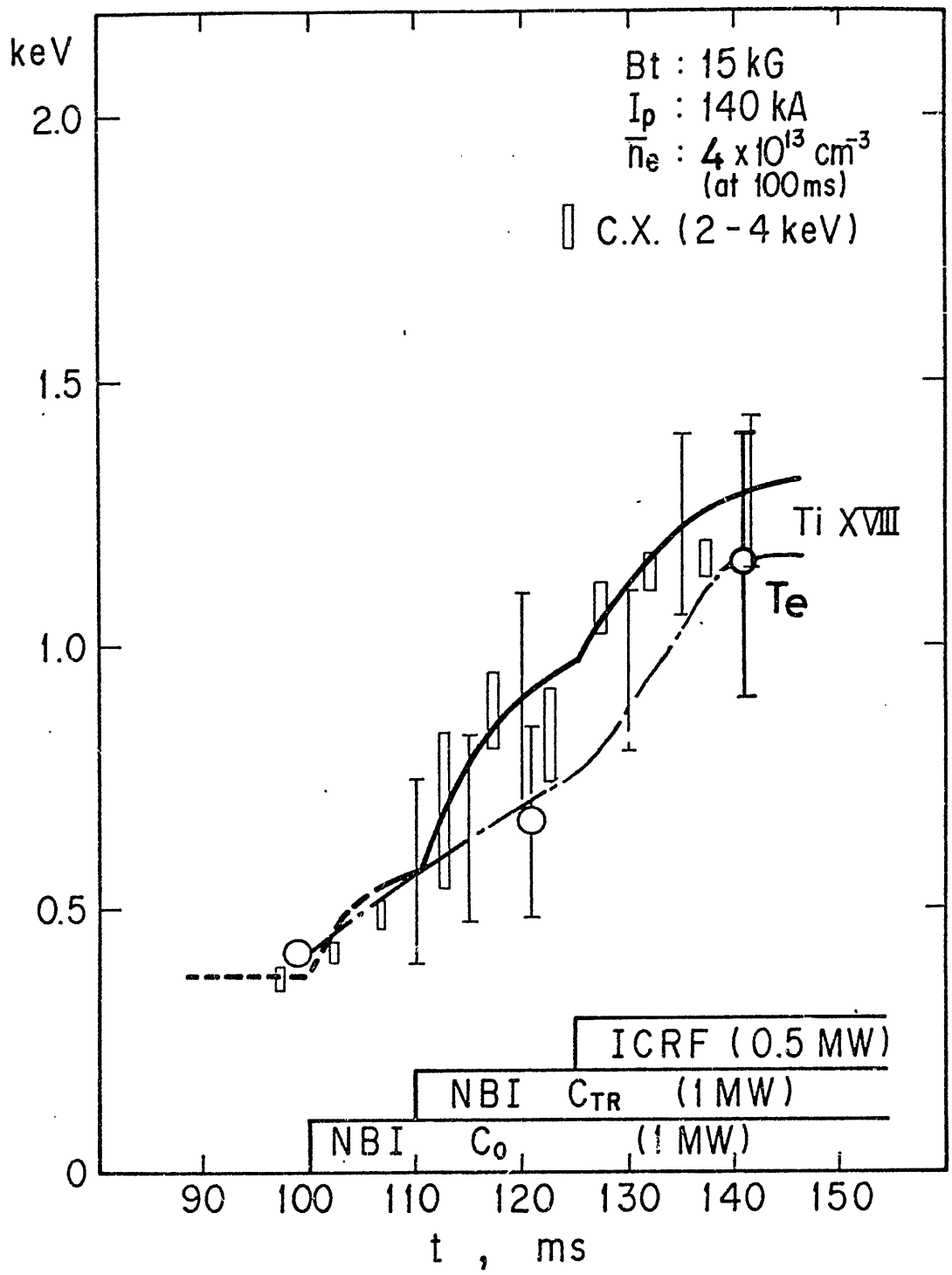

Fig. 4 Temporal plasma temperature (electron and ion) during supplementary heating (NBI : 2 MV, ICRF : 0.5 MW).

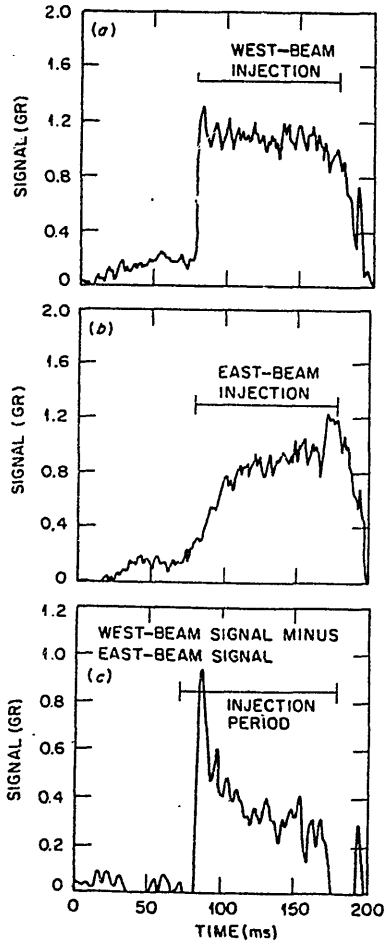

Fig.5 Comparison of the n=3 → n=2 transition of O^{7+} when the neutral beams are injected only from the east beam or from the west beam. The difference signal is due to charge transfer process.

Impurity Transport in Tokamaks

Tsuneo Amano
Institute of Plasma Physics,
Nagoya University

The development of tokamaks into efficient fusion reactors will be seriously impeded, unless tokamak plasmas can be maintained relatively impurity free. Consequently, much theoretical and experimental effort is being extended in order to understand impurity behavior in tokamaks.

In the Alcator tokamak experiments, laser blow-off technique has been used to introduce trace amounts of impurities into the ohmically heated plasmas[1]. After a series of the experiments in which they injected Si, Al, Fe, Mo impurities, they have obtained the following empirical impurity confinement time

$$\tau_I(\mathrm{ms}) = \frac{0.075\, a_L m_{bg}}{q_L} R^{0.75} \frac{Z_{eff}}{Z_{bg}} , \qquad (1)$$

with R and a_L in cm, and where m_{bg} is the background plasma mass in amu and Z_{bg} is the charge of the background ion. The scaling of Eq. (1) was compared with the results of impurity injection experiments on the other tokamaks, FT-I, PDX, TFR, ISX-B. Impurity confinement times in all these cases agree remarkably well, except for the TFR confine-

ment times, which are about a factor of two larger than predicted by Eq. (1). In the TFR tokamak experiments, Cr, Ni and V have been injected into the ohmic plasmas[2]. To interpret the measured impurity emission profiles, they have used the following empirical expression for the diffusion flux of the impurity with charge Z :

$$\Gamma_Z = - D_A \frac{dn_Z}{dr} - \frac{r}{a} v_A n_Z \quad , \tag{2}$$

where n_Z is the number density, a is the radius of the cylindrical plasma and D_A and v_A are independent of the radius. They have solved numerically the equations,

$$\frac{\partial n_Z}{\partial t} = - \frac{1}{r} \frac{\partial}{\partial r} r\Gamma_Z + A_Z \quad , \tag{3}$$

where A_Z represents the ionization and recombination terms, and compared with the measured emissivity profiles $E_Z(r)$. They selected the value of D_A, by matching the peak position of $E_Z(r)$, and selected the value of v_A by matching the radiances of two ions of the same element located at different radii. Typical D_A and v_A thus obtained are $2 \times 10^3 \sim 4 \times 10^3 cm^2 s^{-1}$ and $400 \sim 800$ cm s^{-1}, respectively. It should be noted, in the Alcator injection experiments, a similar analysis has been made with $v_A = 0$.

In the presence of intense neutral beam injection, impurity ions seem to behave differently. Specifically, in the ISX-B experiments, they have observed a marked accumulation of the injected impurity ions toward the center of the plasma for the case of counter neutral

beam injection[3]. This enhanced inward diffusion has been interpreted semi-quantitatively by the neoclassical effect of the rotation of the plasma driven by the NB[4]. For the co-injection case, the outward diffusion of the impurity is predicted by the neoclassical theory. However, this effect is not so significant as in the counter-injection case, in agreement with the observation.

To summarize, impurity transport is understood only empirically, although there is an indication that the neoclassical effect is significant in the case of intense neutral beam counter injection. In the future large and long pulse tokamaks, it is crucial to know the precise value of v_A/D_A, since for sufficiently large v_A/D_A value impurity will tend to accumulate toward the center. Unfortunately, there is little hope that plasma physics will provide the accurate value of this quantity in the near future. Therefore, we hope atomic physics will provide as accurate atomic data as possible (say accurracy within 20%). Then we will be able to deduce v_A/D_A from the comparison of the impurity diffusion experiments and the results of numerical simulations.

Recently, much progress has been made in the divertor experiments in D-III[5], ASDEX and PDX tokamaks. On the other hand, a two dimensional computer model of the divertor dynamics, including plasma streaming parallel to the magnetic field and a Monte-Carlo description of the neutral particle behavior has been developed[6]. By combining such a model with the tokamak plasma and impurity transport codes[7], it will become possible to obtain the overall impurity behaviors in tokamaks self-consistently.

References

1) E.S. Marmar et al.: Nuclear Fusion 22 (1982) 1567.

2) TFR GROUP : Nuclear Fusion 23 (1983) 559.

3) R.C. Isler et al.: Nuclear Fusion 23 (1983) 1017.

4) K.H. Burrel et al.: Phys. Rev. Lett. 47 (1981) 511.

5) M. Shimada et al.: Nuclear Fusion 22 (1982) 643.

6) M. Petravic et al.: Phys. Rev. Lett. 48 (1982) 326.

7) T. Amano et al.: IPPJ-616 (1982).

NUMERICAL ANALYSES FOR SCRAPE-OFF PLASMAS IN FER DIVERTOR CHAMBER

Masayoshi SUGIHARA, Seiji SAITO*, and Noboru FUJISAWA

Japan Atomic Energy Research Institute

Naka-machi, Naka-gun, Ibaraki, Japan

Numerical analyses of characteristics of poloidal divertors in Fusion Experimental Reactor (FER) of JAERI are presented. Diverted scrape-off plasmas are formulated and analyzed based on a fluid model including the interactions with the neutral particles through ionization and charge exchange reactions. The neutral particle behavior is calculated by Monte Carlo method. The possibility of high density operation of the FER divertor is examined numerically and the pumping requirement for the helium ash exhaust is discussed. It is also shown that the same numerical model gives results qualitatively consistent with the DIII divertor experiments.

---

* Hitachi Energy Research Laboratory, Hitachi, Japan

1. Introduction

Recent design works of the experimental fusion reactors [1,2,3] have stimulated experimental [4-7] and theoretical [8-12] studies on the heat removal and related impurity control measures. A possibility of the helium ash exhaust using a model poloidal divertor was discussed in earlier reports [8,9] by means of a Monte Carlo simulation of the neutral particles and ions in the divertor chamber. Their model [8] was based on the simple sheath theory as to the estimation of the scrape-off variables that were assumed to be uniform along the magnetic field line. The observations of the cold and dense divertor plasmas in DIII [4,5] and ASDEX [6] experiments have indicated the strong inhomogeneity of the scrape-off plasma along the field line. This feature has also been numerically investigated on the basis of the fluid model of the scrape-off plasma [10-12].

In this paper, possiblities of attaining the high density operation in the FER divertor are investigated using a self-consistent treatment for the scrape-off plasma and neutrals. The scrape-off plasmas are described by the fluid equations consisting of the particle, momentum and energy conservation equations along the magnetic field line. The neutral particle transport is simulated by the Monte Carlo method. Their interactions through ionization and charge exchange processes are solved self-consistently with the scrape-off plasma by an iterative procedure. The ion flux in the scrape-off layer is amplified between the divertor throat and the divertor plate due to the recycling of the neutral particles.

The present study concentrates on the range of the incoming ion flux which can cause high flux amplification for FER divertor. The effects of the radiations from the recycling neutrals and the oxygen impurities are

roughly estimated. The relations between the effective conductance of the exhausting system and the neutral particle transmission probability through the divertor are evaluated to obtain the pumping requirement for the FER divertor. Finally the scrape-off plasmas in DIII divertor chamber are numerically simulated for qualitative comparison with the experiments.

2. Model of Neutral Particle Transport [13]

2.1 The Particle Tracking Method

The neutral particle motions initiated at the neutralizer plate are followed by the Monte Carlo simulation method. The particle trajectories are traced at the space intervals between space lattices shown in Fig. 1. Neutral particles traversing the scrape-off plasma have chance for ionization and charge exchange reactions with plasmas. The reaction points are searched within the space interval by generating a random number according to the reaction probability.

After ionization of neutral particles, the tracking is terminated, while after the charge exchange a new velocity is assigned to the neutral particle by generating a random number according to the Maxwellian velocity distribution of the back-ground ions. A new velocity is also given to a reflected neutral in collision with the divertor chamber wall.

The tracking of neutral particles is terminated when they return to the main plasma region across the entrance of divertor throat or leave the bottom of the exhausting duct.

2.2 The Physical Model

The ionization process of neutral atoms is described on the basis of the ionization rate coefficients using the Freeman and Jones formula[14] for fuel particles and Lotz's formula[13] for heliums. As for the charge exchange, the Riviere formula[16] is used. Neutral particles colliding with the chamber wall are assumed to be reflected at the rates given by

$$R_N(E_{in}, \theta) = 1 + (1 - \frac{\theta}{90°})(R_N^0(E_{in}) - 1) \quad , \tag{2-1}$$

where E_{in} is the incident energy, θ is the incident angle measured from the normal to the surface and

$$R_N^0(E_{in}) = -0.24 \log_{10}(\frac{E_{in}}{E_L}) + 0.19 \quad , \tag{2-2}$$

where E_L is the reduced energy factor having typical value[17] of

$$E_L = \begin{matrix} 2990 \text{ eV for D, T} \\ 6290 \text{ eV for He} \end{matrix} . \tag{2-3}$$

On the other hand, reflected particles have an energy E_{ref} given as

$$E_{ref} = \frac{R_E(E_{in}, \theta)}{R_N(E_{in}, \theta)} E_{in} \quad , \tag{2-4}$$

where

$$R_E(E_{in}, \theta) = 1 + (1 - \frac{\theta}{90°})(R_E^0(E_{in}) - 1) \quad , \tag{2-5}$$

and

$$R_E^0(E_{in}) = -0.22 \log_{10}(\frac{E_{in}}{E_L}) + 0.06 \quad . \tag{2-6}$$

There are few experiments and theories concerning the dependence on θ of the reflection coefficients R_N and R_E, except for the normal incidence[17]. The numerical calculation shows that the reflection coefficients approach unity as θ goes to 90°[18]. Therefore we assume for simplicity the linear angular dependence in Eqs. (2-1) and (2-5). Particles which are not reflected are adsorbed and then desorbed at wall temperature. The angle of reflected or desorbed particles is determined by cosine distribution based on the assumption of rough surface in molecular level. There is still large uncertainty in this reflection model, especially in low incident energy. If, for instance, mirror reflection is dominant, the estimation of the effective conductance of the evacuating duct will be much altered. Deuterium and tritium particles desorbed from the wall are in molecular forms. Dominant processes for these molecules are [19]

$$e^- + H_2^0 \longrightarrow H_2^+ + 2\ e^- \quad , \tag{2-7}$$

and

$$e^- + H_2^+ \longrightarrow H^0 + H^+ + e^- \quad . \tag{2-8}$$

Incorporation of these processes is now in progress. Instead, in the present paper, we assume that all D and T particles are desorbed as an atom with the Frank-Condon energy of 3 eV.

2.3 The Scoring Method for the Neutral Distributions

Mean flight time of particles in each space lattice is obtained by following the particle trajectories at every space lattice. The neutral density distributions are calculated from the mean flight times of test particles, the total particle flux from the neutralizer plate and the volume of the space lattice[20] as follows:

$$n_{OD}(ij) = \frac{1}{\Delta V_{ij}} \{ \Gamma_D \frac{1}{N_D} \sum_{n=1}^{N_D} \tau_{DDn}(ij) + \Gamma_T \frac{1}{N_T} \sum_{n=1}^{N_T} \tau_{TDn}(ij) \} \quad , \quad (2\text{-}9)$$

$$n_{OT}(ij) = \frac{1}{\Delta V_{ij}} \{ \Gamma_D \frac{1}{N_D} \sum_{n=1}^{N_D} \tau_{DTn}(ij) + \Gamma_T \frac{1}{N_T} \sum_{n=1}^{N_T} \tau_{TTn}(ij) \} \quad , \quad (2\text{-}10)$$

$$n_{O\alpha}(ij) = \frac{1}{\Delta V_{ij}} \{ \Gamma_\alpha \frac{1}{N_\alpha} \sum_{n=1}^{N_\alpha} \tau_{\alpha\alpha n}(ij) \} \quad , \quad (2\text{-}11)$$

where $n_{OA}(ij)$'s$(A = D, T, \alpha)$ are the neutral densities for D, T and α particles in space lattice (ij). $\tau_{ABn}(ij)$ is the flight time in space lattice (ij) for particle B launched on the neutralizer plate as particle A. It takes into account particle exchanges between D and T particles on the charge exchange reaction and the adsorption-desorption process in collision with the duct wall. N_A's$(A = D, T, \alpha)$ are the test particle numbers in the Monte Carlo simulation, and Γ_A's$(A = D, T, \alpha)$ are the actual neutral particle fluxes emitted on the neutralizer plate. ΔV_{ij} is the volume of the space lattice (ij).

3. Fluid Model

The fluid equations in conservation form derived by Braginskii [21] can be reduced to the equations along the field line, neglecting the perpendicular diffusion to the field line [22]. The particle, momentum and energy conservation equations projected on the poloidal cross section shown in fig. 2 are given by

$$\frac{\partial}{\partial z} f_{k,z}(x,z) = S_k(x,z) \quad : \quad (k = D,T,\alpha) \quad , \quad (3\text{-}1)$$

$$\frac{\partial}{\partial z}\left[n_p(x,z)(2U(x,z) + z_p T_e(x,z) + T_i(x,z))\right] = \frac{B_T}{B_p} S_p(x,z) \quad , \qquad (3\text{-}2)$$

$$\frac{\partial}{\partial z}\left[f_z(x,z)(U(x,z) + \frac{5}{2} T_i(x,z)) + q_i(x,z)\right]$$

$$= - V_z \frac{\partial}{\partial z} P_e(x,z) + P_{ei}(x,z) + S_{Ei}(x,z) \quad , \qquad (3\text{-}3)$$

$$\frac{\partial}{\partial z}\left[\frac{5}{2} f_z(x,z)\ T_e(x,z) + q_e(x,z)\right]$$

$$= V_z \frac{\partial}{\partial z} P_e(x,z) - P_{ei}(x,z) + P_r(x,z) + S_{Ee}(x,z) \quad , \qquad (3\text{-}4)$$

where, for simplicity, the ratio of the poloidal to toroidal magnetic field is assumed to be constant along the field line. $f_{kz}(x,z)$ denotes the ion flux parallel to the z direction for D, T and α particles and $f_z(x,z)$ the total ion flux. $U(x,z)$ is expressed in terms of the average ion mass m_p and the ion flow velocity along the field line $V_{/\!/}(x,z)$ as follows:

$$U(x,z) = \frac{1}{2} m_p V_{/\!/}^2 (x,z) \quad . \qquad (3\text{-}5)$$

In eqs. (3-3) and (3-4), q_i and q_e are the conduction heat fluxes in the z direction for the ions and electrons, where the heat conductivities along the field line are assumed to be classical.

The first terms on the right-hand side of eqs. (3-3) and (3-4) represent energies due to the ambipolar electric field produced by the gradient of the electron pressure $P_e(x,z)$. The second terms express the collisional energy transfer between the electrons and ions. In eq. (3-4), P_r denotes the radiation loss power from the recycling hydrogen neutral and oxygen impurities. As for the hydrogen line radiation, only the first excitation level is taken into account using the

excitation rate coefficient given by Johnson [23]. The power density of the oxygen radiation is calculated using a numerical fit to the calculation by Shimada [24]. The particle, momentum and energy sources due to ionization and charge exchange of the neutral particles are denoted by $S_k(x,z)$ $(k = D,T,\alpha)$, $S_p(x,z)$, $S_{Ei}(x,z)$ and $S_{Ee}(x,z)$. The source densities are calculated by the Monte Carlo simulation method presented in the previous section.

The boundary conditions used are as follows. A part of them are given at the divertor throat entrance, that is, the incoming ion fluxes $f_{kz}(x,o)$, $(k = D,T,\alpha)$, the incoming total heat flux $Q_{TOT}(x,o)$ and the ratio of the ion to electron temperature. More restrictive conditions characterizing the scrape-off plasma come from the existence of the electronstatic sheath formed in front of the divertor plate. The first condition is the heat flux limitation [25] imposed by the sheath electric field given by

$$Q_{TOT}(x,L) = \gamma_{TOT}\, T_e(x,L)\, f_z(x,L) \quad , \tag{3-6}$$

where γ_{TOT} is the total heat transmission coefficient. The second one is the sound speed condition [26] in the following:

$$U(x,L) = \frac{1}{2} \{ z_p T_e(x,L) + T_i(x,L) \} \quad . \tag{3-7}$$

In addition, the following continuity condition for the ion heat flux by conduction is included,

$$\left. \frac{\partial q_i}{\partial z} \right|_{z=L} = 0 \quad , \tag{3-8}$$

since the convection heat flow is dominant for ions near the divertor plate so that the boundary condition (3-8) only weakly affects the solution of the fluid equations.

4. Evaluation of FER divertor characteristics [27]

The scrape-off plasmas in the outboard-side divertor chambers of FER are estimated numerically using a simplified model configuration illustrated in fig. 3(a).

The ion flux reaching the divertor plate increases due to reionizations of the recycling neutral particles. The neutral ionization rate is further intensified by the increase of the scrape-off plasma density resulting from the increased ion flux. Therefore the ion flux continues to be amplified until a steady state is reached. The flux amplification becomes higher as it becomes more difficult for the neutrals to escape from the divertor. The dependence of the scrape-off plasma variables on the incoming ion flux is analyzed with the use of the divertor chamber with the short length of 50 cm and relatively large width of 30 cm and with the high pumping speed of 2.5×10^5 ℓ/s.

The calculated results of the peak electron density and temperature at the divertor plate are shown in fig. 3 as a function of the incoming ion flux I under FER baseline condition of the heat flux of 20 MW to the outboard-side of each divertor. The heat and particle flux are assumed to have exponential distributions whose e-folding distances are 7 cm. The ratio of the poloidal to toroidal magnetic field is set to B_p/B_T = 0.1. It should be noted that the high density at the divertor plate ($> 10^{14}/cm^3$) can be obtained even for a rather low value of the incoming ion flux of a few times 10^{22} /s. For higher incoming ion flux, the electron temperature near the divertor plate is less than 10 eV due to larger ion flux amplification. The temperature reduction hinders further increase of the ion flux at the divertor plate because of the decrease of the ionization rate coefficient. As a result, the electron temperature at the divertor plate depends only weakly on the

incoming ion flux in high density region as shown in Fig. 3(b).

Cases (A) and (B) in Fig.3(b) show the case without and with the line radiations from the recycling hydrogen neutrals and 1% oxygen impurities, respectively. The corresponding radiated power amounts to 40% of the total power for the hydrogen and 25% for the 1% oxygen impurities as shown in Fig. 3(c). The effect of the radiation cooling is to reduce the electron density with little variation of the electron temperature, as shown in fig. 3(b). This effect can be explained by the following physical mechanism. The ionization rate coefficient by the electron impact strongly depends on the electron temperature in the region less than 10 eV. The radiation cooling reduces the electron temperature so that the ion flux at the divertor plate is reduced by the decrease of the ionization rate. The small variation of the electron temperature produces large variation of the ion flux at the plate because of the strong temperature dependence of the ionization rate coefficient. Therefore a new steady state can be reached with the large variation of the electron density as well as the ion flux and with small variation of the electron temperature. Further study will, however, be needed concerning more elaborate estimation of the radiation loss power in very high density and low temperature region [28].

The two-dimensional plots of the electron temperature and density obtained with the radiation losses are shown in figs. 4(a) and (b) for the incoming ion flux $I = 2.5 \times 10^{22}/s$. The electron temperature on the separatrix line is about 40 eV at the divertor throat entrance and rapidly decreases to about 3 eV in front of the divertor plate. The electron density varies from about $3 \times 10^{13}/cm^3$ at the throat entrance up to about $2 \times 10^{14}/cm^3$ along the separatrix line.

In order to evaluate the pumping requirement for the helium ash exhaust, we obtain the relation between the effective conductance of the exhaust system and the backflow fraction of the neutrals, f_{bf}. The backflow fraction is defined as the ratio of the neutral flux returning to the main plasma to the incoming ion flux. Since the required pumping speed is expected to be higher for lower incoming ion flux, we investigate it for the low incoming ion flux of 2.5×10^{22}/s. The results are shown in fig. 5. The helium backflow fraction, f_{bf}, must satisfy the following relation to keep the helium concentration in the main plasma to the desired value N_α/N_i:

$$1 - f_{bf} = \frac{\Gamma_\alpha}{2\dot{I}} \left(\frac{N_\alpha}{N_i} \right)^{-1} , \qquad (4\text{-}1)$$

where Γ_α is the helium production rate due to DT reactions. FER standard condition gives the backflow fraction, $f_{bf} = 0.94$ for $2\dot{I} = 5 \times 10^{22}$/s and $N_\alpha/N_i = 0.05$. Figure 5 shows that the effective pumping speed must be larger than 2.5×10^4 ℓ/s to keep the helium concentration lower than 5%. The required pumping speed is reduced by a factor of 10, due to the density enhancement in scrape-off layer, from a previous estimation ($\sim 2 \times 10^5$ ℓ/s)[8], where the scrape-off plasma density ($\sim 2 \times 10^{12}$/cm^3) and temperature (250 eV) are assumed based on the simple sheath theory. Those results, however, depend on the model divertor configuration used here, where the divertor plate is set perpendicularly to the poloidal field line. The neutral particles are emitted on the cosine distribution with respect to the normal direction to the divertor plate so that they have large velocity component toward the throat entrance. When the plate is inclined to the exhaust duct opening, the backflow of the neutral particles is reduced so that the required pumping speed will become lower.

5. Numerical simulation of DIII divertor

The high density ($\sim 10^{14}/cm^3$) and low temperature (3 ~ 10 eV) plasmas in front of the divertor plate have been measured on DIII experiments under 1.0 MW beam heated condition [5]. In this experiment, the incoming ion flux was observed to be in the range $2 \sim 4 \times 10^{21}/s$. Here a comparison is made of the calculated and experimentally observed results of the incoming ion flux, which can produce high density and low temperature plasma near the divertor plate.

The configuration used for the simulation is shown in the insert of fig.6. The experiments indicate that the heat flux into the divertor throat is about 0.5 MW and the e-folding distances of the heat flux and particle flux are 1.8 cm and 3 cm, respectively. Figure 6 shows the results obtained under these flux conditions. The calculated peak electron densities and temperatures are plotted by the closed and open circles. The results without and with the radiation loss from the neutral hydrogen and 1% oxygen impurities are denoted by case (A) and (B), respectively. The calculated values of the density and the incoming ion flux are roughly consistent with the observed values ($n_{ed} \sim 10^{14}/cm^3$, $I = 2 \sim 4 \times 10^{21}/s$) [5].

Another important feature of DIII experiment is the nonlinear dependence of the density at the divertor plate n_{ed} on the main plasma density $\bar{n}_{main}$ which is roughly given by $n_{ed} \propto \bar{n}^3_{main}$ [4, 5, 29]. This feature can well be understood on our numerical model. By using the momentum conservation equation (3-2) and by neglecting the momentum source term, the following scaling can be easily derived in the high density and low temperature region:

$$n_{ed} \propto Q(L)^{-2}\, n^3_{eth} \quad , \tag{5-1}$$

where Q(L) is the total heat flux to the divertor plate and n_{eth} is

the electron density at the throat entrance. The scaling (5-1) is also satisfied by the numerical results shown in fig.7. It explains fairly well the observed nonlinear dependence provided that the density at the throat n_{eth} is proportional to the main plasma density $\bar{n}_{main}$. It should also be remarked that the radiation cooling introduces a more rapid variation of the density at the plate n_{ed} with the density at the throat entrance n_{eth}.

6. Concluding remarks

The self-consistent numerical evaluation for the transport of the scrape-off plasmas and the neutral particles was carried out to elucidate the performance of the divertor in FER of JAERI. The analyses for FER baseline condition indicated the possibility of the high-density and low-temperature plasma in front of the divertor plate even in the case of the low incoming ion flux. The main features of the numerical results are the large gradient of the electron temperature that varies from 40 eV at the divertor throat entrance down to a value less than 10 eV at the divertor plate, and the enhanced plasma density of the order of $10^{14}/cm^3$ in front of the divertor plate. The numerical calculations for FER divertor also suggest the intense radiative cooling (about 40% to 65% of total incoming heat flux is radiated in the divertor chamber) and the low required pumping speed for helium ash exhaust (about 2.5×10^4 ℓ/s). However, the key parameters to determine these quantities in detail are the incoming ion flux that cannot be assigned without considering the main plasma and the diverted plasma consistently. We will discuss this problem in future.

The numerical calculation for DIII under 1.0 MW beam heated condition yielded the electron density and temperature roughly consistent with the experiments. The incoming ion flux that gives the high density operation

also agrees with the observed range.

Acknowledgement

The authors would like to express their sincere gratitude to Drs. M. Yoshikawa, T. Hiraoka and T. Tone for their supports and encouragements. They are also indebted to Drs. Y. Shimomura, M. Azumi, T. Takizuka, T. Hirayama, M. Shimada, M. Nagami, S. Sengoku and T. Sugie for several useful discussions and helpful advices.

References

[1] K. Tomabechi et al., : Proc. Ninth Int. Conf. on Plasma Physics and Controlled Nuclear Fusion Research, Vol. 1, Baltimore, 1982 (IAEA, Vienna, 1983) p.399.

[2] INTOR Group, International Tokamak Reactor, Phase One, IAEA Vienna (1982).

[3] FED team, "Fusion Engineering Device", Vols. I-VI, DOE/TIC-11600 (1981).

[4] M. Shimada et al., Phys. Rev. Lett. 47, 796 (1981).

[5] S. Sengoku et al., to be published in Nucl. Fusion.

[6] Y. Shimomura, M. Keilhacker, K. Lackner, H. Murmann and G. Siller, IPP III/80 (1982).

[7] R.J. Fonk et al., J. Nucl. Mater. 111 & 112, 343 (1982).

[8] Y. Seki, Y. Shimomura, K. Maki, M. Azumi, and T. Takizuka, Nucl. Fusion 20, 1213 (1980).

[9] D. Heifetz, D. Post, M. Petravic. J. Weisheit, and G. Bateman, J. Comput. Phys. 46, 309 (1982).

[10] M. Petravic, D. Post, D. Heifetz, and J. Schmidt, Phys. Rev. Lett. 48, 326 (1982).

[11] M. Petravic, D. Heifetz, D. Post, W. Langer and C. Singer, Proc. Ninth Int. Conf. on Plasma Physics and Controlled Nuclear Fusion Research, Baltimore, 1982, IAEA-CN-41/D-3-2.

[12] M.F.A. Harrison, P.J. Harbour, and E.S. Hotston, Nucl. Technol./ Fusion 3, 432 (1982).

[13] S. Saito, M. Sugihara, N. Fujisawa, T. Abe and K. Ueda, to be published in Nucl. Technol./Fusion.

[14] R.L. Freeman and E.M. Jones, CLM-R 137, Culham Laboratory (1974).

[15] W. Lotz, Z. Phys. 216, 241 (1968).

[16] A.C. Riviere, Nucl. Fusion 11, 363 (1971).

[17] G.M. McCracken and P.E. Stott, Nucl. Fusion 19, 889 (1979).

[18] O.S. One and M.T. Robinson, J. Nucl. Mater. 76 & 77, 370 (1978).

[19] D.E. Post, D.B. Heifetz and M. Petravic, J. Nucl. Mater. 111/112, 393 (1982).

[20] M.H. Hughes and D.E. Post, J. Comput. Phys. 28, 43 (1973).

[21] S.I. Braginskii, Reviews of Plasma Physics, Vol. 1, Consultants Bureau, New York, 1965.

[22] C.E. Singer and W.D. Langer, PPPL-1920 (1982).

[23] L.C. Johnson, Astrophys. J. 174, 227 (1972).

[24] M. Shimada et al., JAERI-M 9862 (1981).

[25] G.D. Hobbs and J.A. Wesson, Plasma Physics 9, 85 (1967).

[26] D. Bohm, Characteristics of Electrical Discharges in Mangetic Fields P.77 (A. Guthrie and R.K. Wakerling, Eds.), McGraw-Hill.

[27] S. Saito, M. Sugihara and N. Fujisawa, to be published in J. Nucl. Mater.

[28] J. Weisheit, J. Phys. B8, 2556 (1975).

[29] M.A. Mahdavi et al., J. Nucl. Mater. 111 & 112, 355 (1982).

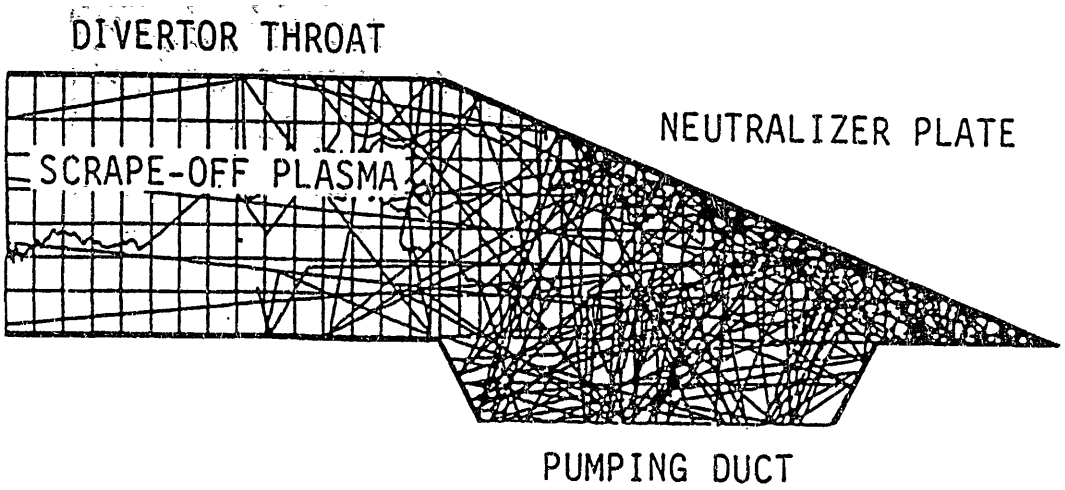

Fig. 1 Calculation model of neutral particle transport by Monte Carlo method for divertor chamber. The particle trajectories are tracked at intervals between the space lattices.

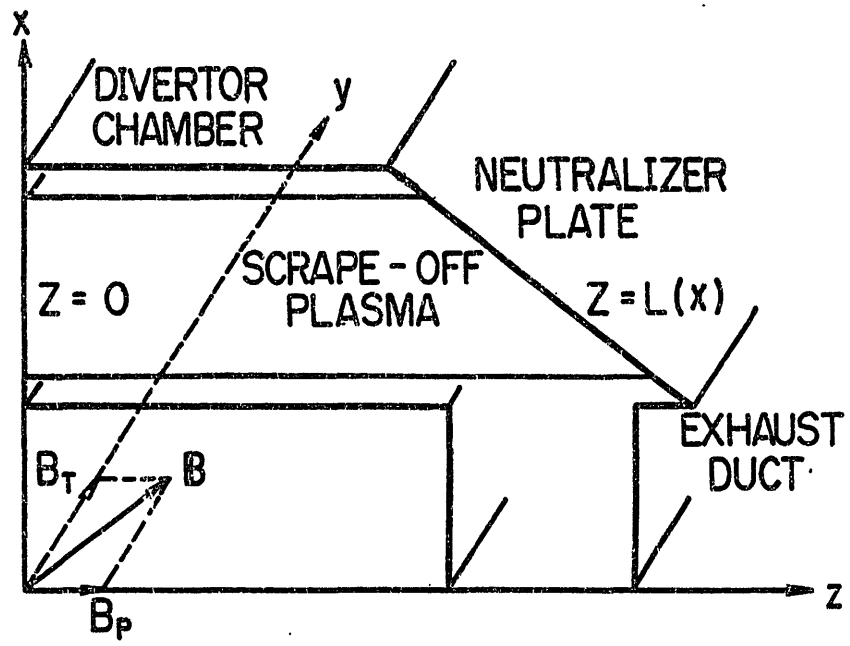

Fig. 2 Schematic drawing of divertor chamber.

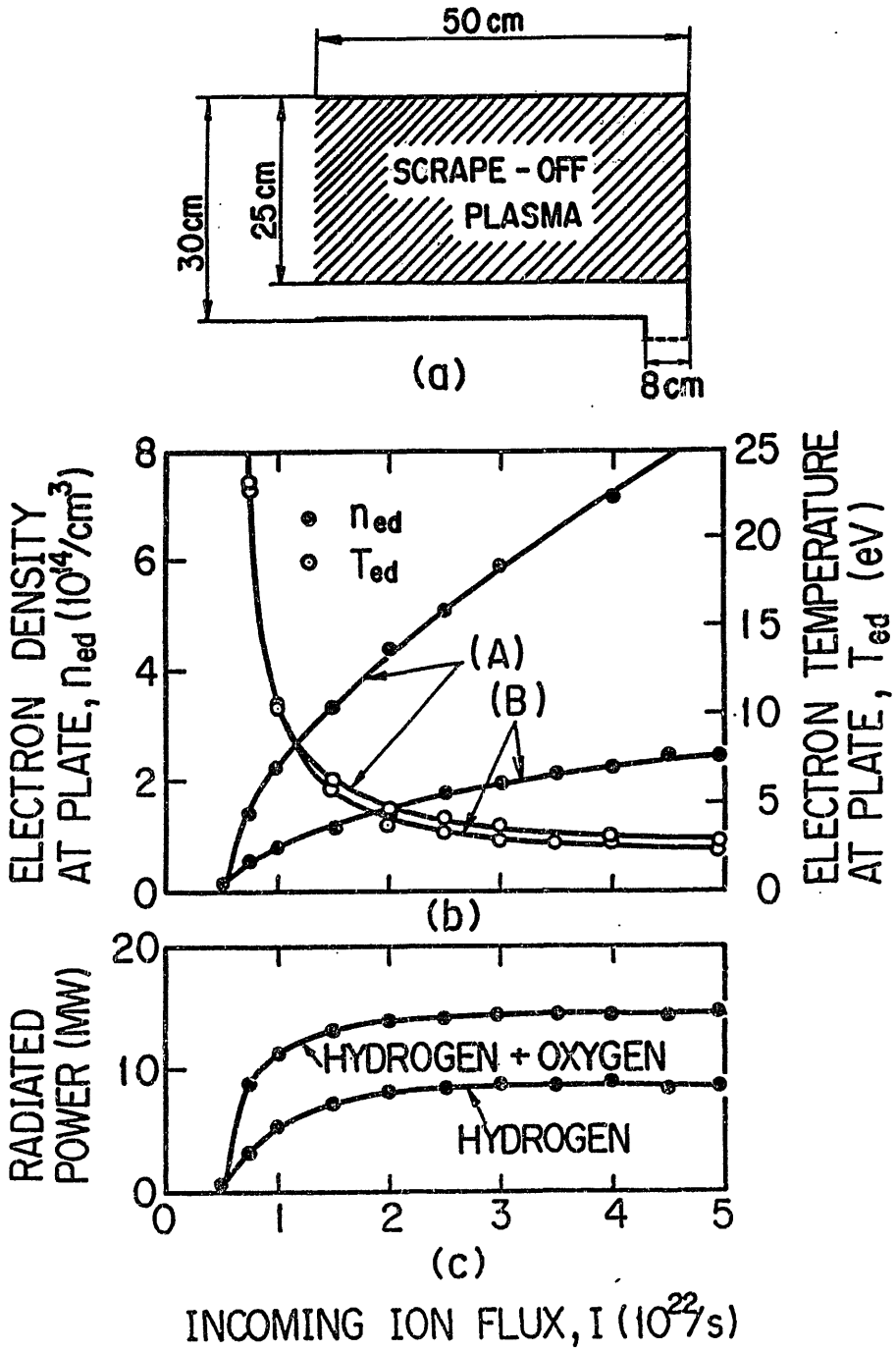

Fig. 3 Characteristics of the scrape-off plasmas in FER divertor chamber:

(a) Model divertor chamber for FER.

(b) Peak electron densities and temperatures at the divertor plate as a function of the incoming ion flux. Case (A) and (B) show the results calculated without and with the radiation loss from the neutral hydrogen and 1% oxygen impurities.

(c) Corresponding radiation loss power as a function of the incoming ion flux.

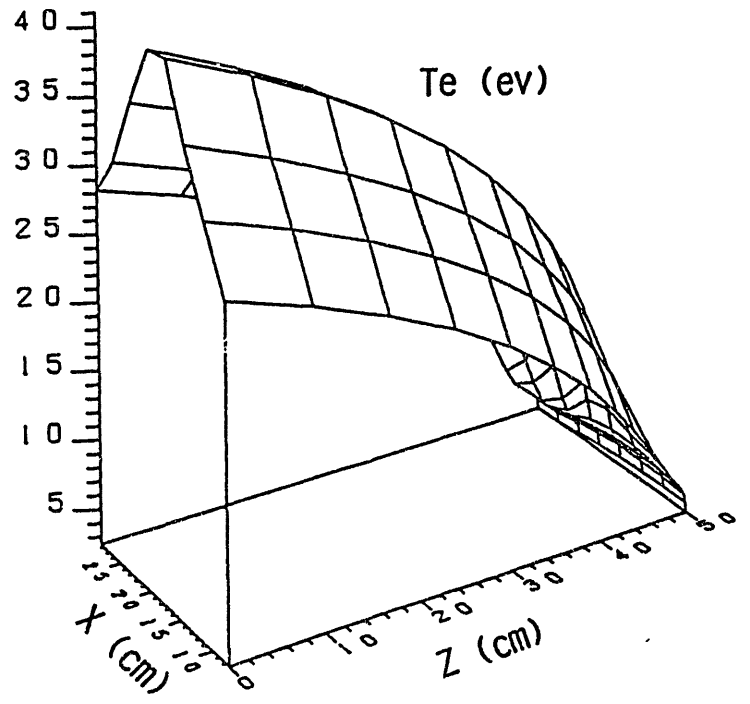

(a)

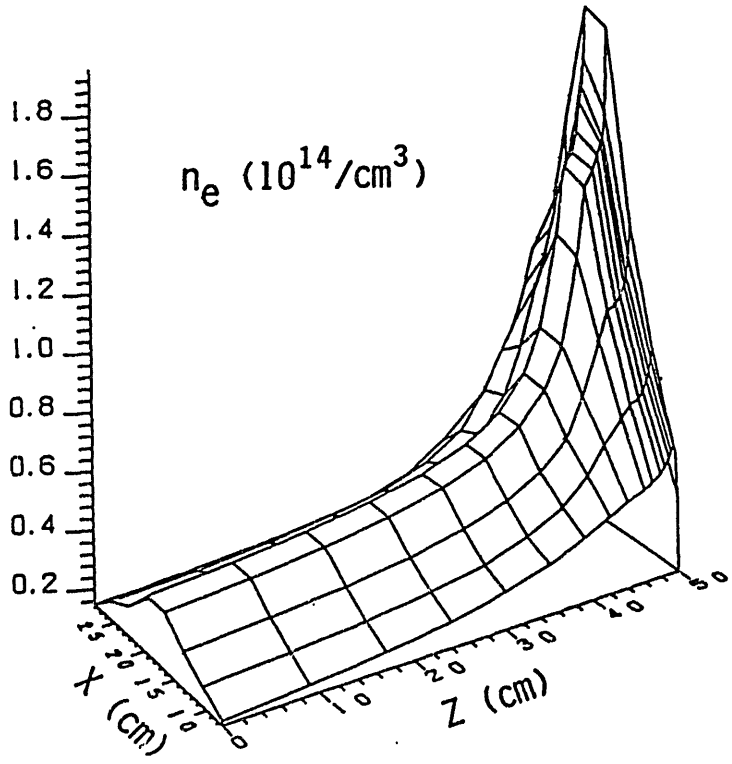

(b)

Fig. 4 Two-dimensional plots: (a) electron temperature distribution, (b) electron density distribution in the FER divertor chamber.

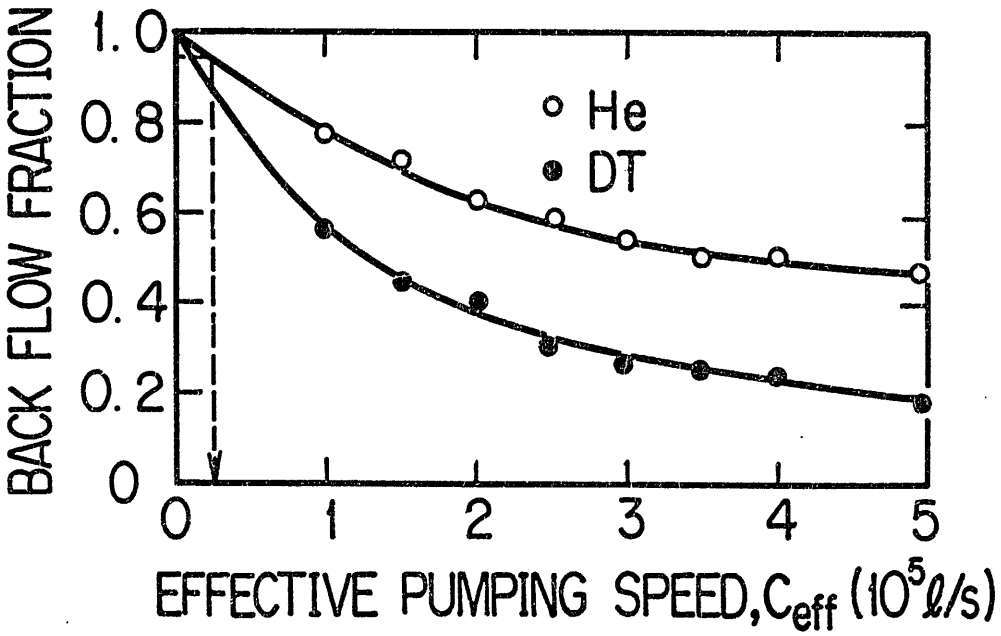

Fig. 5 Relation between the backflow fraction and the effective pumping speed for the FER divertor ($I = 2.5 \times 10^{22}$/s).

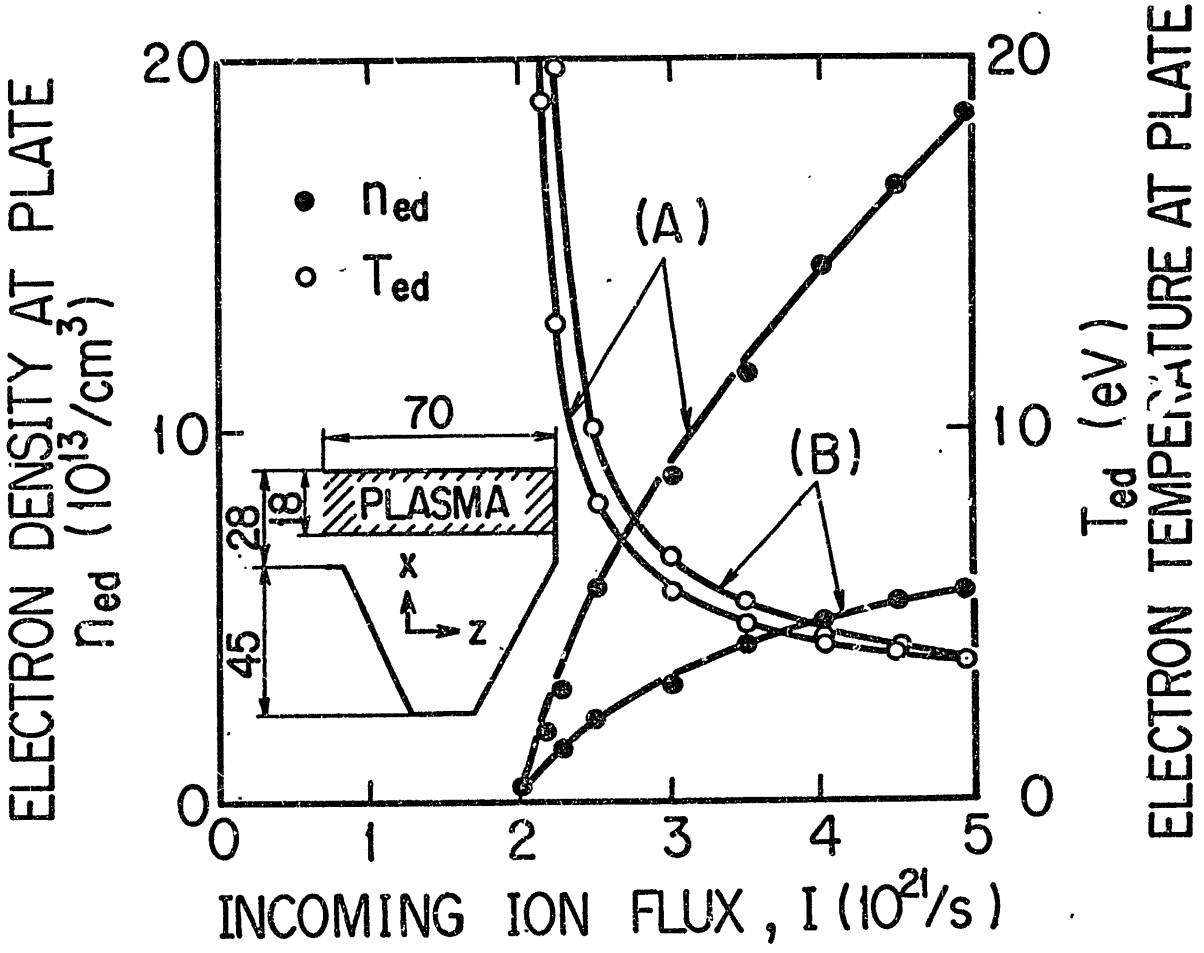

Fig. 6 Peak electron densities and temperatures at the divertor plate as a function of the incoming ion flux (DIII). Case (A) and (B) show the results calculated without and with the line radiation loss from the neutral hydrogen and 1% oxygen impurities.

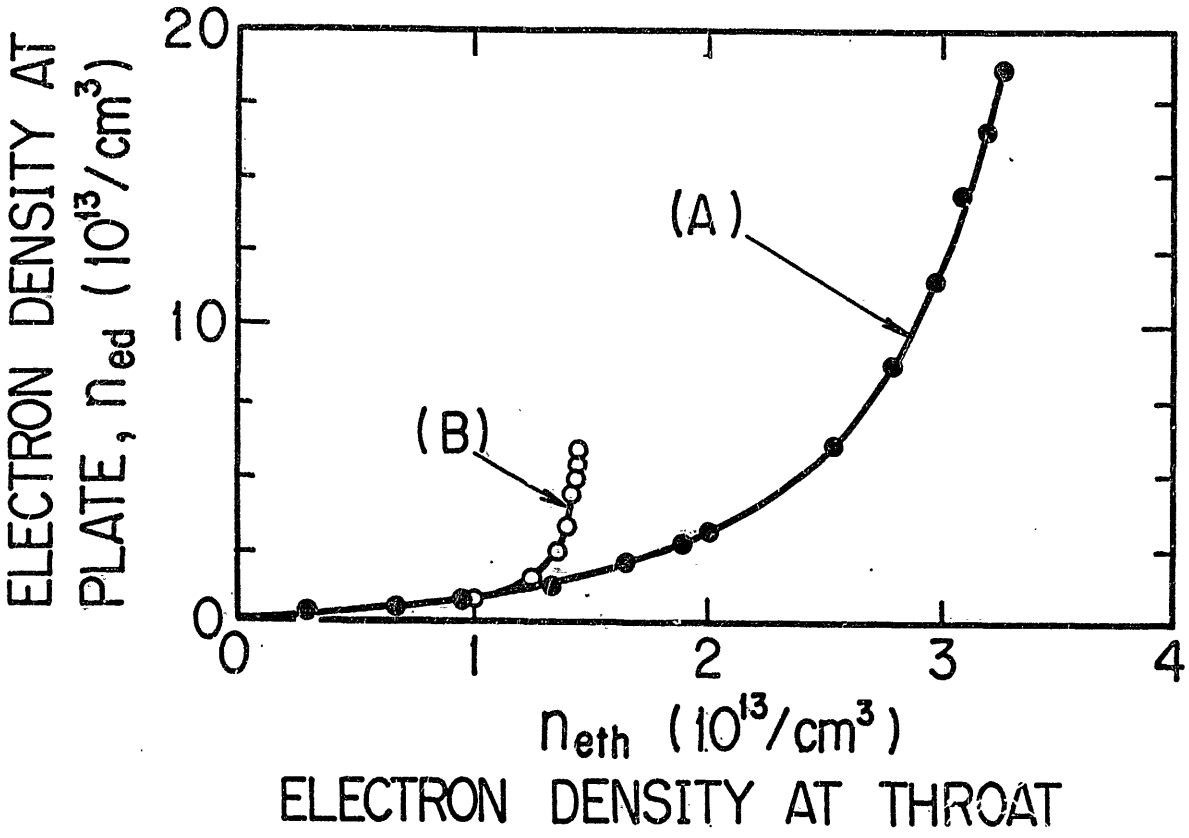

Fig. 7 Relation between the peak electron density at the divertor plate and the peak electron density at the throat entrance (DIII).

Emission Properties of Highly Ionized Iron Spectra for Spectroscopic Plasma Diagnostics

Kuninori SATO, Masamoto OTSUKA
Institute of Plasma Physics, Nagoya University,
Nagoya 464, Japan
and
Mikio MIMURA
Research Institute for Atomic Energy, Osaka City University,
Osaka 558, Japan

ABSTRACT

Three selected transitions of highly ionized iron in n = 2 level, i.e., the forbidden transition within the ground state configurations, $\Delta n = 0$ transition, and $\Delta n = 1$ transition are primarily sensitive to a single or particular plasma parameters. Measurement of these three transitions makes it possible to diagnose local plasma parameters. This method is useful to estimate the plasma parameters in the case of additional heating in plasmas. Preliminary experimental results are shown for Fe XVIII spectra during ICRF heating in JIPP T-IIU TOKAMAK.

I. Introduction

Spectral line intensity from a plasma is generally given by a complicated function of plasma parameters (for example, electron temperature T_e, electron density n_e and ion density n_i), and in transient plasmas, it also depends on a previous history. In TOKAMAK plasmas, low electron density ($n_e(0) < 10^{14}$ cm^{-3}) and high electron temperature ($T_e(0) > 1$ keV) ensure applying a simple coronal model to the emissivities of the allowed resonance lines.[1)]

The local emissivity J(r) of an allowed resonance line at the radial distance of r is simply given by

$$J(r) = n_e(r) \cdot n_i(r) \cdot S_x(T_e) \quad \text{photons/cm}^3 \cdot \text{sec} , \qquad (1)$$

where n_i is the population of the ground state of the ions, and S_x is the electron impact excitation rate coefficient.

The radial distribution of the ions with the ionization potential Ei is usually fairly limited in a region where the electron temperature nearly equals Ei. When $T_e(r)$ and $n_e(r)$ are known, the spatial distribution of spectral line intensity yields the ion density of interest.

However, when a plasma is in a transient phase (for example, due to additional heating by NBI or RF, and high density regime by gas puffing), it is hard to understand the physical mechanism of the change of line emission, because the plasma parameters and the distribution of ions change temporally and spatially.[2-8)]

Furthermore, additional heating brings more impurities.

Here we present a method of determining localized plasma parameters, which makes it possible to explain the behavior of spectral line emission in a transient plasma.

This method is based on measurement of three particular lines : a forbidden line for the transition within the ground state configuration (sensitive only to n_i), an allowed transition line with $\Delta n = 0$ (sensitive to n_i and n_e), and a line with $\Delta n = 1$ transition (sensitive to n_i, n_e, and T_e). In the next section, we will discuss in more detail properties of these three lines of interest. In section III, preliminary experimental results are shown for Fe XVIII spectra during ICRF heating.

II. Properties of forbidden, $\Delta n = 0$ and $\Delta n = 1$ transitions of highly ionized iron in the n = 2 levels

II-1 Forbidden lines in the ground state configuration

Measurements of the forbidden lines, especially in the visible region, allow us to use conventional optical techniques. These forbidden lines of iron, chromium and titanium atoms have been widely used in TOKAMAKS to measure the ion temperature and drift motion through the Doppler width and shift [9-11]. Another aspect of the forbidden lines is that the population of the upper level is close to equilibrium with that of ground state. Because of such low transition-probabilities as 10^2-10^5 sec^{-1}, the radiative rates of the forbidden line are smaller than the collisional rates, which of course depend on the electron density

but the above condition is usually fulfilled in TOKAMAKS ($n_e > 10^{13}$ cm^{-3}). The fine-structure levels in the ground state configuration have a population distribution which may be in equilibrium with the ground state populations.

The relative populations of the ground state configuration have been calculated for different electron densities and temperatures. From these calculations the level population of the ground state configuration is found to be nearly independent of the electron density and temperature over their wide ranges in $n_e > 10^{13}$ cm^{-3} and $T_e > 100$ eV[12-14].

Thus, the measured absolute intensity of the forbidden line, the radiative transition probability, and the knowledge of radial distribution of T_e and n_e allow us to evaluate the ion density of interest.[15]

II-2 Allowed $\Delta n = 0$ transitions

The excitation potentials for the transitions with $\Delta n = 0$ are much smaller than the ionization potentials from the $n = 2$ shell.[1] The ratio is about one tenth. High excitation rate from the ground state and high transition probability cause a strong line-emission. The radiation loss of TOKAMAKS is dominated by these $\Delta n = 0$ transitions. In TOKAMAK plasmas, spatial distribution of highly ionized ions is localized approximately at the position where $E_i \approx T_e(r)$. Then the excitation rate is almost independent of the electron temperature. Feldman and Doschek have proposed to use the relative intensities of forbidden to allowed lines as density-sensitive line ratios.[16,17] Their result for Fe XVIII shows that the ratio is almost inversely proportional to the

electron density in the region above 10^{13} cm^{-3}.[18]

II-3 Allowed $\Delta n = 1$ transitions

The energy of the transitions with $\Delta n = 1$ are about a half the ionization potential.[1] The line emission associated with these transitions may be strongly temperature-dependent.

Figure 1 shows the results of calculation of excitation rate coefficients of selected Fe XVIII levels.

The electron impact excitation rates (S_{ij} $cm^3 \cdot sec^{-1}$) for allowed transitions between the levels i and j is obtained using the expression given by Van Regemortor,[19] i.e.,

$$S_{ij} = \frac{1.57 \times 10^{-5} f_{ij} \cdot \bar{g} \cdot \exp(-\Delta E_{ij}/kT_e)}{(kT_e)^{-1/2} \cdot \Delta E_{ij}} \quad , \qquad (2)$$

where f_{ij} is the absorption oscillator strength, ΔE_{ij} is the transition energy in eV, and kT_e is the electron temperature in eV. For the effective Gaunt factor $\bar{g}$, empirical formula by Mewe[20] is used. The oscillator strength is available from the multi-configuration Dirac-Fock calculations of Cheng et al.[21]

The electron impact excitation rate for forbidden transition is obtained using the expression of collision strength,

$$S_{ij} = \frac{8.0 \times 10^{-8}}{\omega_i} \bar{\Omega} \, (kT_e)^{-1/2} \exp(-\Delta E_{ij}/kT_e) \quad , \qquad (3)$$

where ω_i is the statistical weight for the lower state, $\bar{\Omega}$ is the averaged collision strength, and kT_e is the electron temperature in eV . The averaged collision strength is extrapolated from

Blaha's calculations.[22,23] The proton impact excitation rate are negligible compared to electron rates for the allowed transition, but the proton rates between levels of the $2s^2 2p^x$ configuration are generally comparable to or even higher than the electron rates.[24] Proton collisions should have a noticeable effect on the excitation rate of forbidden transitions.

In addition, in the $2s^2 2p^x$ (x = 1-5) ground state configuration sequence, there are metastable levels in LS coupling. However, in heavy elements like iron, the radiative lifetimes of these metastable levels become short compared to collisional life times, and the population of metastable level is therefore small and does not affect the above mentioned line emissions.[1] Of course, the populations of metastable levels are important when the simple corona model is replaced by a collisional-radiative model.

III. Preliminary Experimental Result

We have concentrated on observation of Fe XVIII line intensities during an ICRF heating experiment. Under our experimental conditions, the central electron temperature before heating was about 500 eV. Fe XVIII ions (ionization potential 1358 eV) are assumed to be localized with its maximum density at the center. Also low intensities of Fe XIX spectra indicate that the Fe XVIII ion is the highest ionization stage of iron. Then, Fe XVIII spectra are expected to reflect the central part of plasma.

The measured lines of Fe XVIII are: 978.4 Å $2s^2 2p^5\ ^2P_{1/2} \rightarrow$

$2s^2 2p^5\ ^2P_{3/2}$(magnetic dipole transition), 93.94 Å $2s2p^6\ ^2S_{1/2} \rightarrow 2s^2 2p^5\ ^2P_{3/2}$ ($\Delta n = 0$), 16.00 Å $2s^2 2p^4 3s\ ^4P_{3/2} \rightarrow 2s^2 2p^5\ ^2P_{3/2}$ ($\Delta n = 1$). In Fig.2, a partial Grotrian diagram of Fe XVIII is shown. The time behavior of these three lines during ICRF heating is shown in Fig.3 with the change of the central electron temperature, averaged density and ion density.

The intensity of 978.4 Å increases threefold during heating. This increment shows threefold increase in the concentration of Fe XVIII. The intensity of 93.94 Å line shows a similar or slightly more increase which means the increase of electron density at the central part, agreeing well with a small density rise of the plasma. On the other hand, a sharp increase in the intensity of 16.00 Å is observed after the ICRF heating begins. Sixfold increase of the 16.00 Å line exceeds the product of the increment of the concentration of Fe XVIII ion and the electron density. This fact means a sharp rise in the electron temperature.

In principle, absolute measurement of 16.00 Å makes it possible to determine a rapidly changing electron temperature, although in the present experiment such a measurement was not attempted.

We should note that the identification of Fe XVIII 16.00 Å line is still questionable. The intensity of this line were measured with a grazing incidence monochromator with an angle of incidence of 86 degree. In the short wavelength region $\lambda < 20$ Å, stray light from 0-th order light was so high that the first order spectra below 18 Å were unclear. We measured 6-th order spectrum of

Fe XVIII 16.00 Å, but background was still high. A crystal spectrometer would be feasible for a measurement of such a short wavelength light.

A particular problem arises in the case of measurement of 16 Å. O VIII resonance line 3p → 1s at 16.00 Å overlaps Fe XVIII line at 16.00 Å. Therefore some part of measured intensity may be affected by the O VIII spectrum.

IV. Discussion

The above mentioned method requires the following conditions: (1) Intensities of appropriate lines should be measured absolutely with sufficient accuracies. (2) The corresponding rate coefficients, electron impact excitation rate coefficients, proton impact excitation rate coefficients and radiative transition probabilities have to be adequately known.

The first condition represents a serious problem since the intensities of lines with different wavelengths are to be compared. In the past decade, calibration methods in the vacuum ultraviolet region have much progressed in two ways.

One is the absolute calibration by using a synchrotron radiation and the other is the atomic branching ratio method which can be used as in-situ calibration based on the known transition probabilities . However, the calibration of such a spectroscopic system in the extreme ultraviolet and soft X-ray region has problems to be solved.

The second condition restricts the applicability of the

method to very few simple systems especially such as lithium and beryllium-like ions, e.g., Fe XXIV and Fe XXIII. The cross-sections are directly measured in a few cases, but generally it is necessary to rely on the calculation based on various degrees of assumption.

Acknowledgments

The authors wish to thank our colleagues from JIPP T-IIU and Dr. M. Ono from PPPL for their cooperation in experiments and analysis of the data.

References

1) E. Hinnov, NATO ADVANCED STUDY INSTITUTE SERIES, Atomic and Molecular Processes in Controlled Thermonuclear Fusion, ed., M. R. C. McDowell and A. M. Ferendeci (Plenum Press, New York and London, 1980) p.449.

2) S. Suckewer, E. Hinnov, M. Bitter, R. Hulse and D. Post, Phys. Rev. A22 (1980) 725.

3) S. Suckewer, Physica Scripta 23 (1981) 72.

4) R. C. Isler, L. E. Murray, S. Kasai, J. L. Dunlop, S. C. Bates, P. H. Edmonds, E. A. Lazarus, C. H. Ma and M. Murakami, Phys. Rev. A24 (1981) 2701.

5) J. L. Terry, K. I. Chen, H. W. Moos and E. S. Marmar, Nucl. Fusion 184 (1978) 485.

6) D. Meisel, O. Klüber, B. Cannici, W. Engelhardt, G. Fussmann, J. Gernhardt, E. Glock, F. Karger, G. Lisitano, K. McCormick, H. M. Mayer, P. Morandi, S. Sesnic and F. Wagner, Plasma Physics and Controlled Nuclear Fusion Research (Proc. 7th Int. Conf. Innsbruck, 1978) IAEA-CN-35/A-6, IAEA, Vienna.

7) J. Hosea et al., Princeton Plasma Physics Laboratory Report, PPPL-1588 (1979).

8) R. C. Isler, Phys. Rev. Lett. 38 (1977) 1359.

9) S. Suckewer and E. Hinnov, Phys. Rev. Lett. 41 (1978) 756.

10) S. Suckewer, H. P. Eubank, R. J. Goldston, E. Hinnov and N. R. Sauthoff, Phys. Rev. Lett. 43 (1979) 207.

11) E. Hinnov, R. Fonck and S. Suckewer, Princeton Plasma Physics Laboratory Report, PPPL-1669 (1980).

12) A. K. Bhatia, U. Feldman and G. A. Doschek, J. Appl. Phys. 51 (1980) 1464.

13) U. Feldman, G. A. Doschek, Chung-Chieh Cheng and A. K. Bhatia, J. Appl. Phys. 51 (1980) 190.

14) U. Feldman, G. A. Doschek and A. K. Bhatia, J. Appl. Phys. 53 (1982) 8554.

15) S. Suckewer, E. Hinnov, K. Bol, R. Fonck, R. J. Hawryluk, R. A. Jacobsen, D. M. Meade, M. Okabayashi, G. L. Schmidt, E. H. Silver and J. C. Sinnis, Nucl. Fusion 19 (1979) 1681.

16) U. Feldman and G. A. Doschek, J. Opt. Soc. Am. 67 (1977) 726.

17) G. A. Doschek, U. Feldman, J. Davis and R. D. Cowan, Phys. Rev. A12 (1975) 980.

18) G. A. Doschek and U. Feldman, J. Appl. Phys. 47 (1976) 3083.

19) H. Van Regemorter, Astrophys. J. 136 (1962) 906.

20) R. Mewe, Astron. and Astrophys. 20 (1972) 215.

21) K. T. Cheng, Y. K. Kim and J. P. Desclaux, Atom. Data & Nucl. Data Tables 24 (1979) 111.

22) M. Blaha, Astrophys. J. 157 (1969) 473.

23) M. Blaha, Astron.& Astrophys. 1 (1969) 42.

24) S. Suckewer and E. Hinnov, Phys. Rev. A20 (1979) 578.

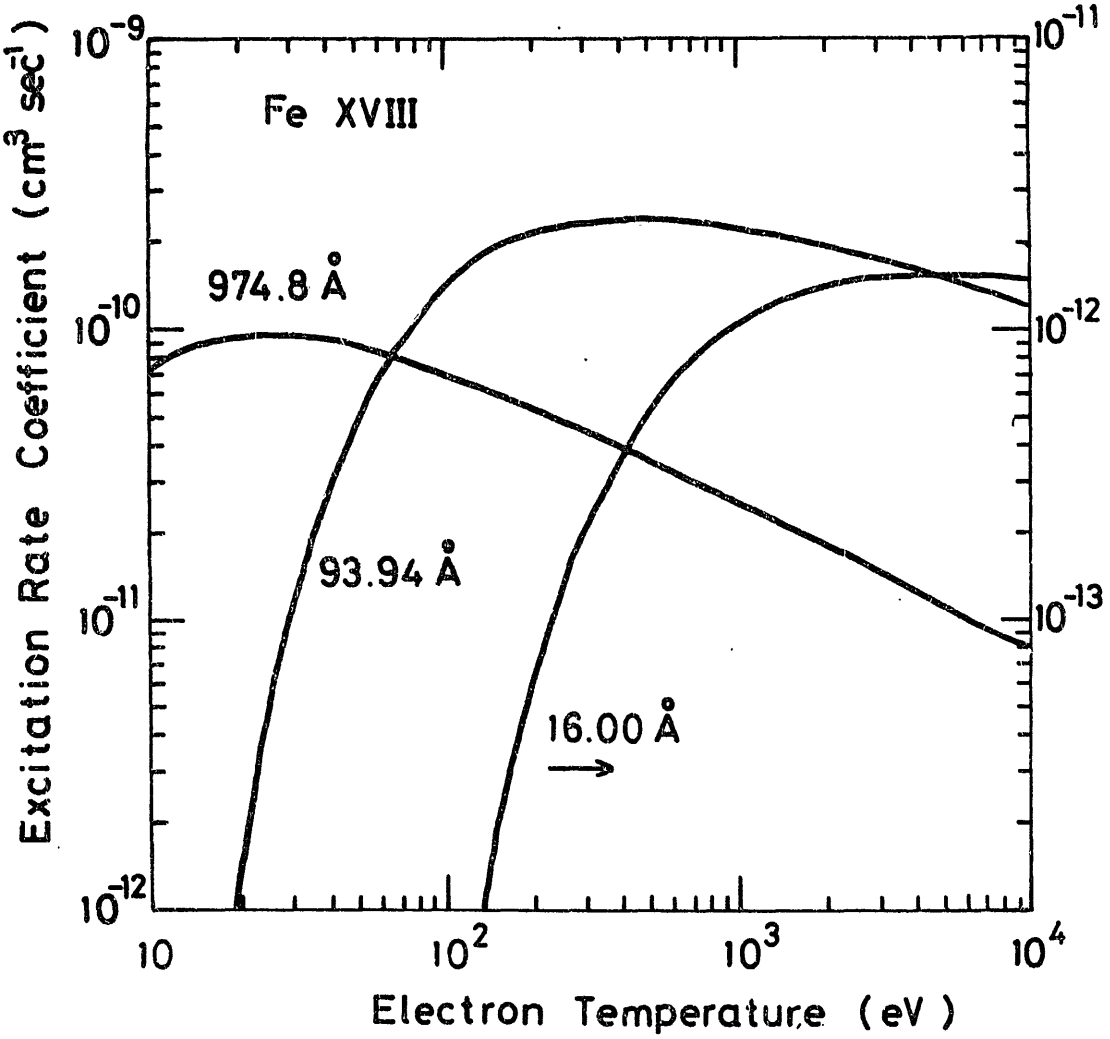

Fig.1 Electron impact excitation rate coefficient as a function of temperature. For the transitions:

Fe XVIII 978.4 Å $2s^2 2p^5\ ^2P_{1/2} \rightarrow 2s^2 2p^5\ ^2P_{3/2}$

Fe XVIII 93.94 Å $2s^2 2p^6\ ^2S_{1/2} \rightarrow 2s^2 2p^5\ ^2P_{3/2}$

Fe XVIII 16.00 Å $2s^2 2p^4 3s\ ^4P_{3/2} \rightarrow 2s^2 2p^5\ ^2P_{3/2}$

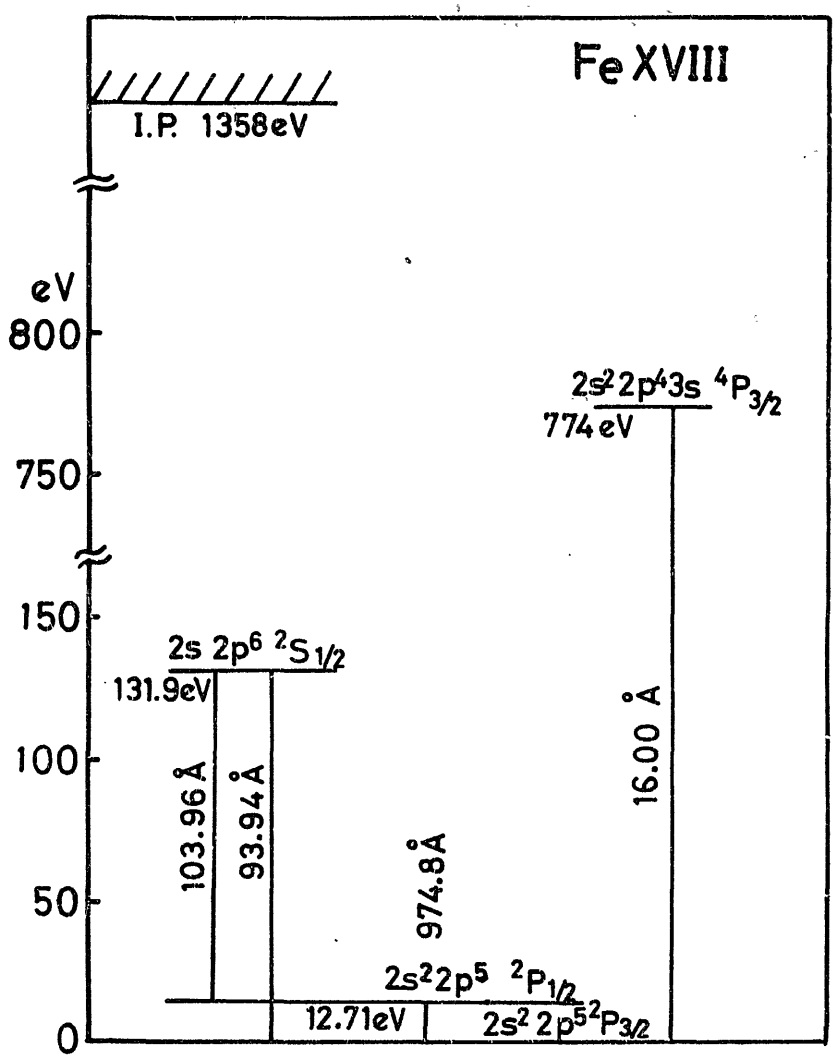

Fig.2 Partial energy level diagram for Fe XVIII.

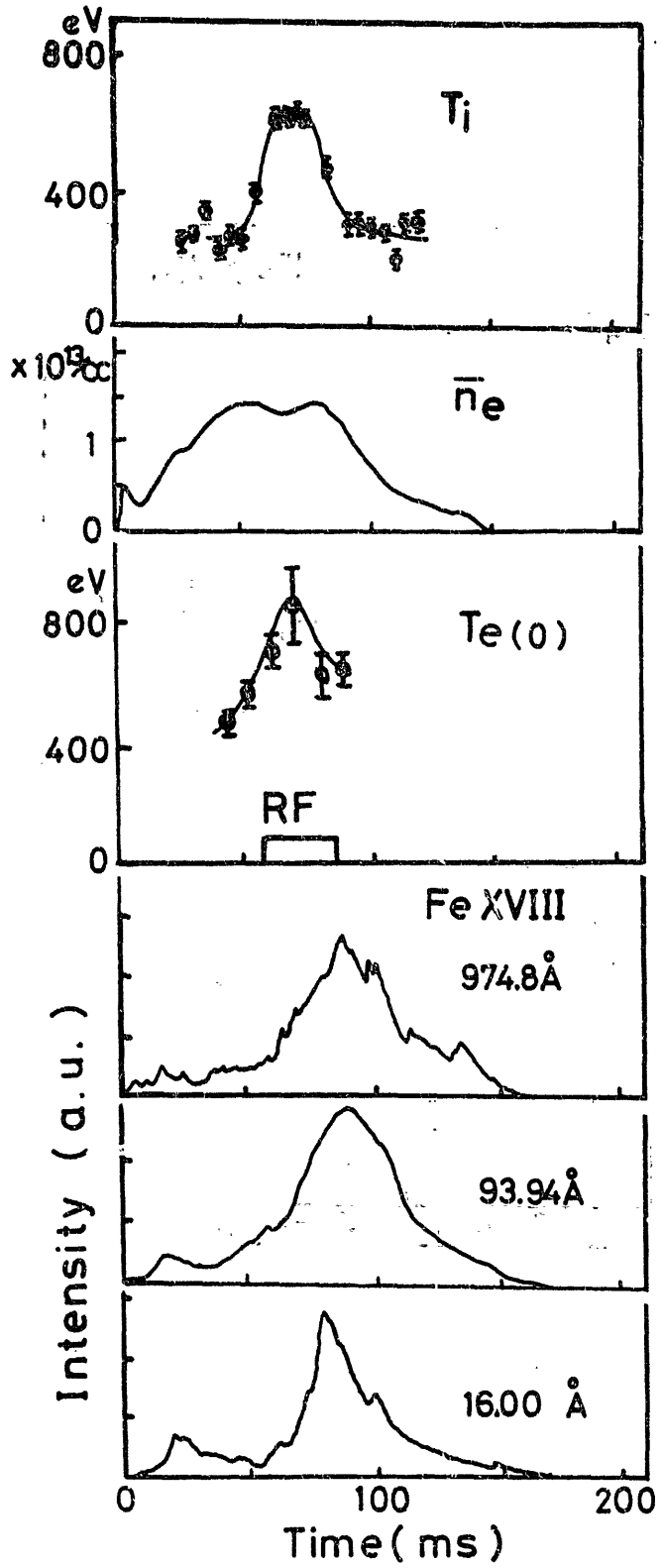

Fig.3 Time evolution of Fe XVIII line intensities during 80 kW ICRF heating. Central electron temperature and averaged electron density determined by Thomson scattering and microwave interferometer, and ion temperature by fast neutral energy analyzer are shown in upper part of the figure.

Evaluation of excitation cross sections by plasma spectroscopy

Takako KATO and Takashi FUJIMOTO*

Institute of Plasma Physics, Nagoya University, Nagoya
*Dept. of Engineering Science, Kyoto University, Kyoto

Abstract

The excitation cross sections by electron impact for highly ionized ions are evaluated using the spectroscopic data from plasmas. A computer code of the collisional radiative model for He-like ions is constructed and is applied to the estimation of the emission line intensities from the solar corona and theta-pinch plasmas. The evaluation of the excitation cross sections as well as of the plasma state for He-like ions has been made.

1. Introduction

The cross sections by electron impact for highly ionized ions are necessary for diagnostics of nuclear fusion plasmas and astrophysical plasmas. But we often encounter the cases that there are no atomic data when we analyze spectroscopic data.

Recently the measurements of the cross section by the crossed beam method have been performed actively for the ionization processes. But for the excitation processes, only a few data of highly ionized ions are available. Although the accuracy is less than the crossed beam method, the measurements of the emission from plasmas give useful information about cross sections, because highly ionized ions can be easily produced in plasmas.

Various experiments have been performed to derive the rate coefficients for both ionization and excitation from line intensities. We are going to discuss mainly the excitation process here. There have been about 14 experiments for excitation rates so far as listed in Table I.

The problems in spectroscopic diagnostics of the plasmas are

1) Generally the electron density and temperature in plasmas are not uniform. Spatial and time information on electron density and temperature is necessary.

2) Plasma states and ion abundances are to be known; we have to know whether the plasma under study is predominantly ionizing, equilibrium or recombining plasma. If the plasma is

not in a steady states, it is also necessary to know a time evolution as well.

3) The cascades from higher excited states have to be taken into account. It is considered that to analyze with the collisional radiative model is the best way.

2. Collisional radiative model for He-like ions

We have constructed a computer code of the collisional radiative model for He-like ions of Z=5 - 26[15].

The population density of an excited level p of a He-like ion is given as a superposition of the two components; the contribution connected to the hydrogenic ions $n_H(^2S)$ and that to the ground level of He-like ions;

$$n(p) = n_0(p) + n_1(p)$$
$$= Z(p) r_0(p) n_H(^2S) n_e + \{Z(p)/Z(1)\} r_1(p) n_{He}(^1S)$$

with

$$Z(p) = g(p) (h^2/2mkT_e)^{3/2} \exp\{I(p)/kT_e\}/2g_H.$$

Here g(p) and I(p) are the statistical weight and the ionization potential of level p, respectively, g_H is the statistical weight of the ground-state hydrogenic ion. $r_0(p)$ and $r_1(p)$ are functions of n_e and T_e and called the population coefficients.

We have taken into account the energy levels up to n=20. The levels having a principle quantum number $n \leq 7$ are treated separately; e.g. 2^1S, 2^1P, 2^3S, 2^3P. The levels of the orbital

angular momentum L>3 with the same n are grouped together to form a single level. The level 1s2s ^{3}P is resolved into the fine-structure components.

In order to obtain the population density n(p), the value of n_H and n_{He} have to be specified. We introduce the quantity

$$q = \left[n_H(1^2S)/n_{He}(1^1S)\right] / \left[n_H(1^2S)/n_{He}(1^1S)\right]_E$$

where E means the ionization equilibrium which is given by the ratio of the direct ionization and recombination rate in the low-density limit. For q=0, the plasma is purely ionizing. The conventional corona model assumes this situation. A theta-pinch plasma is one of such plasmas. On the other hand, the purely recombining plasma is defined as $q=\infty$ and the population density is entirely determined by $r_0(p)$. Generally real plasma is described by $0<q<\infty$. In a special case, an equilibrium plasma is defined as q=1.

3. Application to real plasmas

We have applied this computer code to the investigation of the emission lines from the solar corona and theta-pinch plasmas. Comparing the calculated line-intensity ratios with the observed results, we have made the evaluation of the excitation cross sections as well as of the plasma state.

In the low density plasma, the resonance line R($2^1P - 1^1S$) and the forbidden line F($2^3S - 1^1S$) are strong. Due to the decay from 2^3P levels, the forbidden line F is much stronger

than the intercombination line I($2^3P - 1^1S$). A diagram of the low-lying energy levels for O^{6+} is shown in Fig.1. When the electron density increases, the forbidden line F decreases whereas the intercombination line I increases. This is because of the collisional excitation from the state $2^3S - 2^3P$. For the electron density greater than $10^{16} cm^{-3}$, which is a typical density of theta-pinch plasmas, the collisional ionization from 2^3P level becomes dominant in comparison with the radiative decay from 2^3P level and, then, the intensity I decreases. The electron density dependence of the line intensity ratio is shown in Fig.2.

In the following, firstly, we see the line intensity ratio from the solar corona where the line intensity ratio is independent of the density. Next, we see the case of theta-pinch plasmas where line intensities change significantly with the density.

(a) Solar corona

The emission line intensity of He-like ions from the solar corona has been analysed[16] and we tried to evaluate the excitation cross section of $1^1S - 2^3S$ and of $1^1S - 2^1P$ using the observed line intensity ratio I/F and (I+F)/R. The results are summarized here and detailed description are given in Ref. 16).

1) We consider the line intensity ratio F/I which is determined essentially by the excitation cross sections of $1^1S - 2^3S$ and $1^1S - 2^3P$.

When we see the existing cross section data for $1^1S - 2^3P$ of O^{6+}, all data except for those by CB method are found to be consistent within 10%. We rely on the average values of the cross section.

For the excitation $1^1S - 2^3S$, there exists disagreement with a factor of 2 at the threshold energy among the data. We take the two extrema; σ_1 as the upper bound of the existing data and σ_2 as the lower bound. But the effect in the difference between σ_1 and σ_2 on the ratio F/I is almost negligible. This is due to the fact that, in the case of O^{6+}, 58% of the population density of 2^3S level comes from the cascade from 2^3P levels, and the contribution from the direct excitation from the ground state to 2^3S level is only 20%, because the cross section of $1^1S - 2^3S$ is small compared with that of $1^1S - 2^3P$. Thus we cannot decide which cross section, σ_1 or σ_2, is more reasonable. Therefore for $\sigma(1^1S - 2^3S)$ we used the values which reproduce the rate coefficients calculated by Pradhan et al.[17]; that is about 5% smaller than the upper bound σ_1.

2) We next examine the resonance line intensity R in connection with the excitation $1^1S - 2^1P$. In Fig.3, the existing theoretical data are summarized. The cross sections σ_1' and σ_2' give the upper and lower bound, respectively. The line intensity ratio (F+I)/R for equilibrium plasma (q=1) is shown in Fig.4. The ratios are also given for the purely ionizing (q=0) and purely recombining ($q=\infty$) plasmas for σ_2'. It is noted that the ratio for $q=\infty$ is independent of the

magnitude of the cross section. The observed results are also plotted in this figure.

In order that the observed results are to be consistent with the cross section σ_1', all of the plasma observed would have to be strongly recombining; this is unlikely to be the case. For the cross section σ_2', the data for OVII are consistent on the assumption of the equilibrium plasma (q=1). Thus, it is well expected that the cross section should be close to σ_2', that is the distorted wave calculations[18]. For the data of other elements are given the discussions in Ref. 16).

(b) Theta-pinch plasmas

The electron density is relatively high in theta-pinch plasmas, and therefore the excitation or ionization cross sections from the metastable levels become essential in determining the population densities of the line-emitting levels.

We start with the assumption that the plasmas for which the line intensities have been observed are in the ionizing phase, or n_H/n_{He}, the ratio of the hydrogenic ion density to the helium-like ion density is much smaller than that given under the ionization equilibrium condition, S_{CR}/A_{CR}, where S_{CR} and A_{CR} are the ionization and recombination rate coefficients, respectively.

1) For $1^1S - 2^1S$ process, the existing calculations are summarized in Fig.5, and the upper bound, σ_1", and the lower bound, σ_2" are defined as shown in Fig.5.

Figure 6 shows the intensity ratio R/(R+I). Experimental values are given by the three groups; Elton and Köppendörfer (1967)[2], Kunze at el. (1968)[3], and Pospieszczyk (1975)[19]. The number associated with each of the data point represents the electron temperature given in the original papers. The results of the calculation corresponding to these two cases are shown in Fig.6 for two temperatures, 200eV and 300eV. For $n_e < 10^{16}cm^{-3}$, the gradual increase in the ratio corresponds in part to the increase in the 2^1P population due to the stepwise excitation via 2^1S and in part to the gradual decrease in the 2^3P level population due to the depletion by ionization from this level.

The data by Kunze et al[3] favor the upper bound σ_1", while that by Elton and Köppendörfer favor the lowest bound σ_2". However, if we take into account the experimental uncertainty both the data are consistent with either of the cross sections, σ_1" or σ_2". This ambiguity comes partly from the fact that the contribution from the excitation $1^1S - 2^1S$ to the intensity R is small, i.e. 17% for σ_1" or 15% for σ_2" for the condition of T_e=250eV and $n_e=6.2 \times 10^{16}cm^{-3}$.

2) In the high-density region, $n_e > 10^{16}cm^{-3}$, with an increase in n_e the stepwise ionization from the 2^3P level makes the relative population density of this level decrease and results in an increase in the ratio. Kunze et al. assume that this

increase is due to the singlet-triplet excitation transfer, and they give the excitation rate coefficient of $1.1 \times 10^{-9} cm^3 s^{-1}$ for O^{+6}. In our calculation, however, the corresponding rate coefficient is about $1 \times 10^{-10} cm^3 s^{-1}$ and the ionization has $1.6 \times 10^{-9} cm^3 s^{-1}$ instead. We can determine the ionization rate coefficient using the experimental data in the high electron density region. Elton and Köppendörfer (1967) derived the rate coefficients $31 \times 10^{-12} cm^3 s^{-1}$ for $1^1S - (2^1S+2^1P)$ and $15 \times 10^{-12} cm^3 s^{-1}$ for $1^1S - (2^3S+2^3P)$. Our calculation gives about half of their values; 19×10^{-12} and $9 \times 10^{-12} cm^3 s^{-1}$, respectively, whereas our calculation gives the absolute intensity of the lines $2^3S - 2^3P$ being consistent with the observation. The difference of the factor of 2 in excitation rate coefficients is interpreted as partly due to the neglect of the cascading contribution in the original paper and partly due to the different rate coefficients for ionization from the 2^3S and 2^3P levels.

3) We examine the experiment for carbon. The critical electron density for which the ionization rate and radiative decay from the 2^3P level become comparable in magnitude is smaller for carbon than for oxygen. It is about $5 \times 10^{15} cm^{-3}$. The intensity ratio I/R is sensitive to the ionization rate coefficient at this density. Figure 7 compares the experiments with our calculation. The experiments give lower values of the ratio R/(R+I) than the calculation. This discrepancy is thought to be due to the following origins.

i) If the ionization cross sections from the 2^3S and 2^3P levels were decreased by a factor of 2, the calculated result would shift toward higher density by almost the same amount. The experimental data for $T_e > 200$eV would then become consistent with the calculation. However, the error of a factor of 2 appears unlikely to occur in our ionization cross section and the lower temperature data remain in consistent with the calculation. We rule out this possibility.

ii) Next is the excitation cross sections $1^1S - 2^1P$ and $1^1S - 2^3P$, by which the intensity ratio is determined. If we decrease $\sigma(1^1S - 2^1P)$ by 20% or increase $\sigma(1^1S - 2^3P)$ by the same amount, an agreement within the experimental uncertainty would be obtained for the data for $T_e > 200$eV. This large modification to the cross section, however, appears unrealistic and then a strong doubt would have to be cast on the scaling law of the cross section, since good agreement has been obtained for oxygen ions.

iii) Another possibility is as follows; the assumption that the plasma condition is in the ionizing phase is not valid. If we assume that the plasma is slightly ionizing and is close to equilibrium, all of the data except for those for T_e=130eV and 79eV are well interpreted. The intensity ratio for the equilibrium plasma is plotted in Fig.7 as well as that for the recombining plasma. We suppose that the plasmas for carbon experiment are not predominantly ionizing, but they have appreciable contributions from the recombining plasma

component. Thus it should be stressed to be very important to know the plasma condition of the plasma under study.

4. Summary

A method evaluating the cross sections using the collisional radiative model for He-like ions has been discussed. With this method the plasma state as well as the collisional rate coefficients can be known.

We have gotten the result for excitation cross section of $1^1S - 2^1P$ that the distorted wave calculation by McDowell[18] is found to give reasonable values.

We have found that it is very important to know the plasma state when we analyze the spectroscopic data; the ionizing plasma, equilibium plasma or recombining plasma.

In order to make the collisional radiative model reliable, are necessary more atomic data especially, data of excitation and ionization processes from the metastable levels.

References

1) E.Hinnov, J.Opt.Soc.Am. 56,1179(1966)

2) R.C.Elton and W.W.Köppendörfer, Phys.Rev. 160, 194 (1967)

3) H.-J.Kunze, A.H.Gabriel and H.R.Griem, Phys.Rev. 165, 267 (1968)

4) A.N.Prased, M.F.El-Menshawy, J.Phys. B1, 471 (1968)

5) I.L.Beigman, L.A.Vainshtein, A.P.Dronov, E.M.Kudryavtsev, JETP USSR 59, 1991 (1970), Sov.Phys.JETP 32, 1079 (1971)

6) H.-J.Kunze and W.D.Johnston III, Phys.Rev. A3, 1384 (1971)

7) W.D.Johnston III and H.-J.Kunze, Phys.Rev. A4, 962 (1971)

8) H.-J.Kunze, Phys.Rev. A4, 111 (1971)

9) G.Tondello and R.W.P.McWhirter, J.Phys. B4, 715 (1971)

10) R.U.Dalta, H.-J.Kunze and D.Petrini, Phys.Rev. A6, 38 (1972)

11) W.Engelhardt, W.Köppendörfer and J.Sommer, Phys.Rev. A6, 1908 (1972)

12) G.N.Haddad and R.W.P.McWhirter, J.Phys. B6, 715 (1973)

13) R.U.Dalta, M.Blaha and H.-J.Kunze, Phys.Rev. A12, 1076 (1975)

14) Jieh-Shan Wang and H.R.Griem, PL83-032 (1982) Univ. Maryland

15) T.Fujimoto and T.Kato, IPPJ-647 (1983), Institute of Plasma Physics, Nagoya Japan

16) T.Fujimoto and T.Kato, Astrophys.J. 246, 994 (1983)

17) A.K.Pradhan, D.W.Norcross and D.G.Hummer, Astrophys.J. 246, 1031 (1981)

18) M.R.C.McDowell, L.A.Morgan, V.P.Myercough and T.Scott, J.Phys. B10, 2727 (1977)

19) A.Pospieszczyk, Astron. & Astrophys. 39, 357 (1975)

20) H.-J.Kunze, Phys.Rev. A24, 1096 (1981)

Table I

Measurements of excitation rate coefficients by plasma spectroscopy

Author(s)		Ion(s)
Hinnov[1]	(1966)	Ne^{n+} (n=1-7)
Elton, Köppendörfer[2]	(1967)	O^{6+}
Kunze, Gabriel, Griem[3]	(1968)	C^{4+}
Prased, El-Menshawy[4]	(1968)	C^{4+}
Beigman et al.[5]	(1971)	Ba^{+}, Sr^{+}
Kunze, Johnston III[6]	(1971)	N^{4+}, O^{5+}, Ne^{7+}
Johnston III, Kunze[7]	(1971)	N^{3+}, O^{4+}, Ne^{6+}, Si^{8+}
Kunze[8]	(1971)	Ne^{7+}
Tondello, McWhirter[9]	(1971)	Ne^{6+}
Dalta, Kunze, Petrini[10]	(1972)	Ar^{7+}
Engelhardt et al.[11]	(1972)	C^{4+}, N^{5+}, O^{6+}, F^{7+}, Ne^{8+}
Haddad, McWhirter[12]	(1973)	Ne^{7+}
Dalta et al.[13]	(1975)	$Fe^{7+,8+,9+}$
Wang, Griem[14]	(1982)	Fe^{9+}

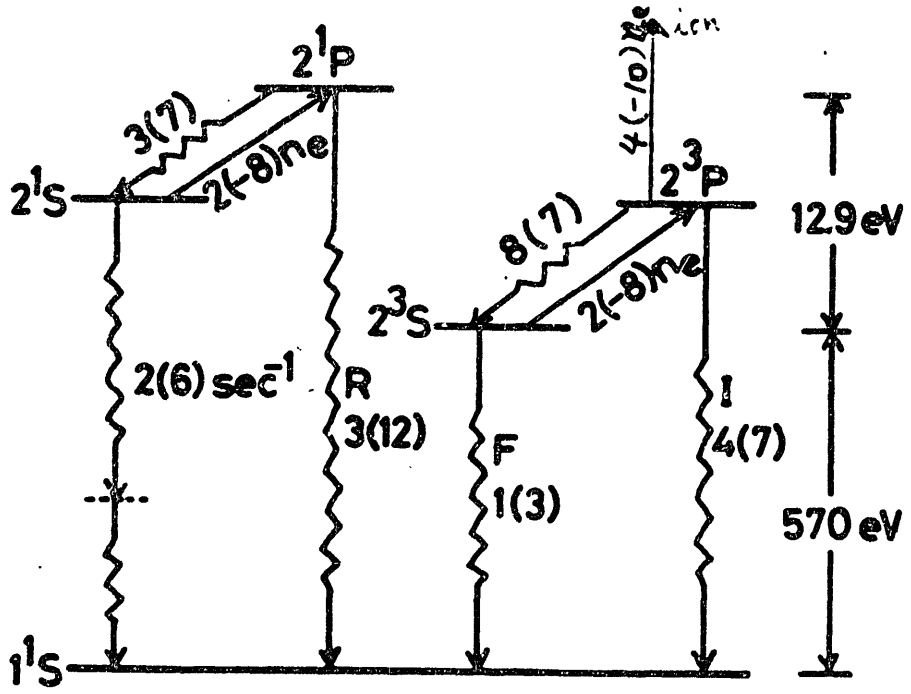

Fig.1 An schematic energy level diagram of He-like oxygen ion O^{6+}. The numbers attached to the transition lines indicate the values of transition probabilities or collisional rate for $T_e = 2.9 \times 10^6$ K.

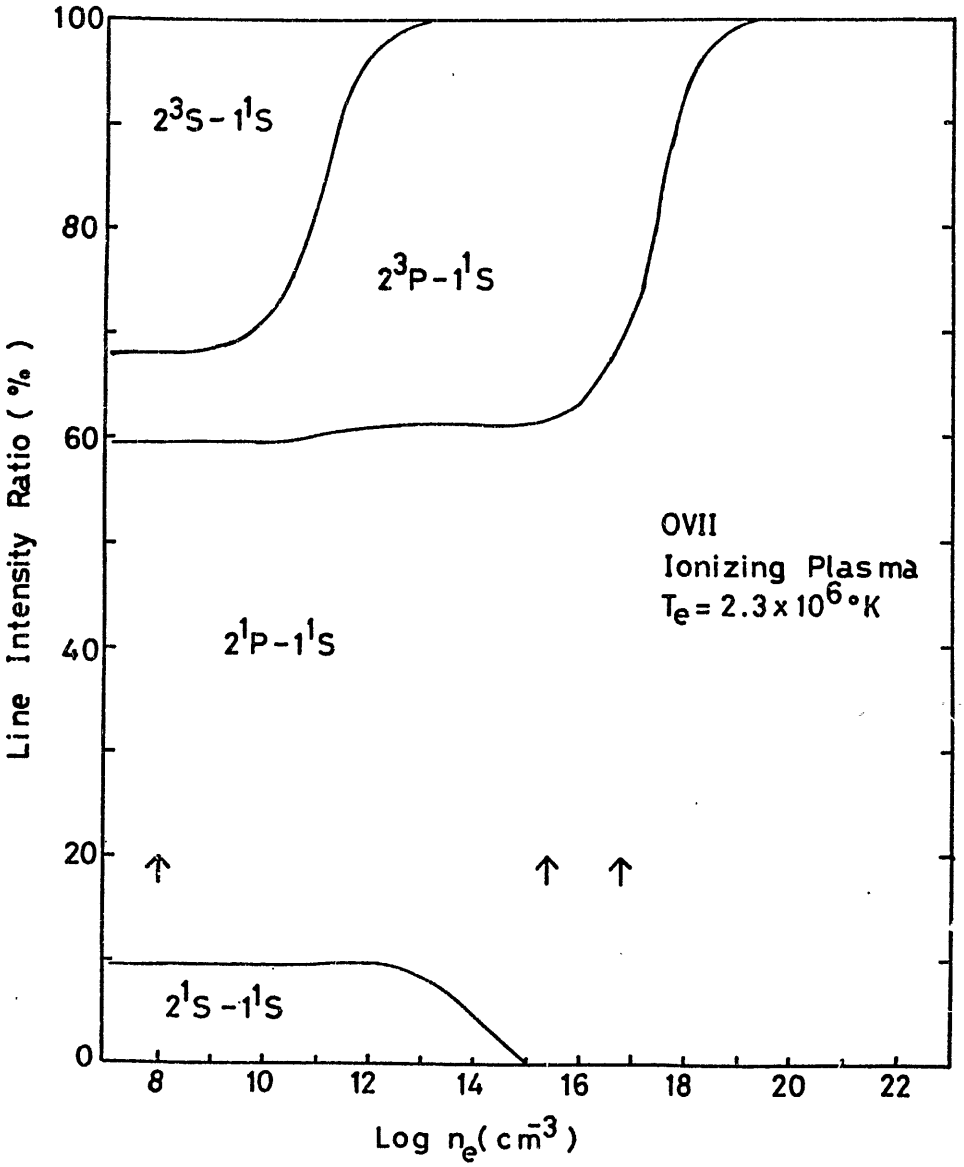

Fig.2 Line intensity ratios of O VII as a function of electron density in the ionizing plasma of $T_e=2.3 \times 10^6$°K. ↑ indicates the electron density for solar corona and theta-pinch plasmas, respectively.

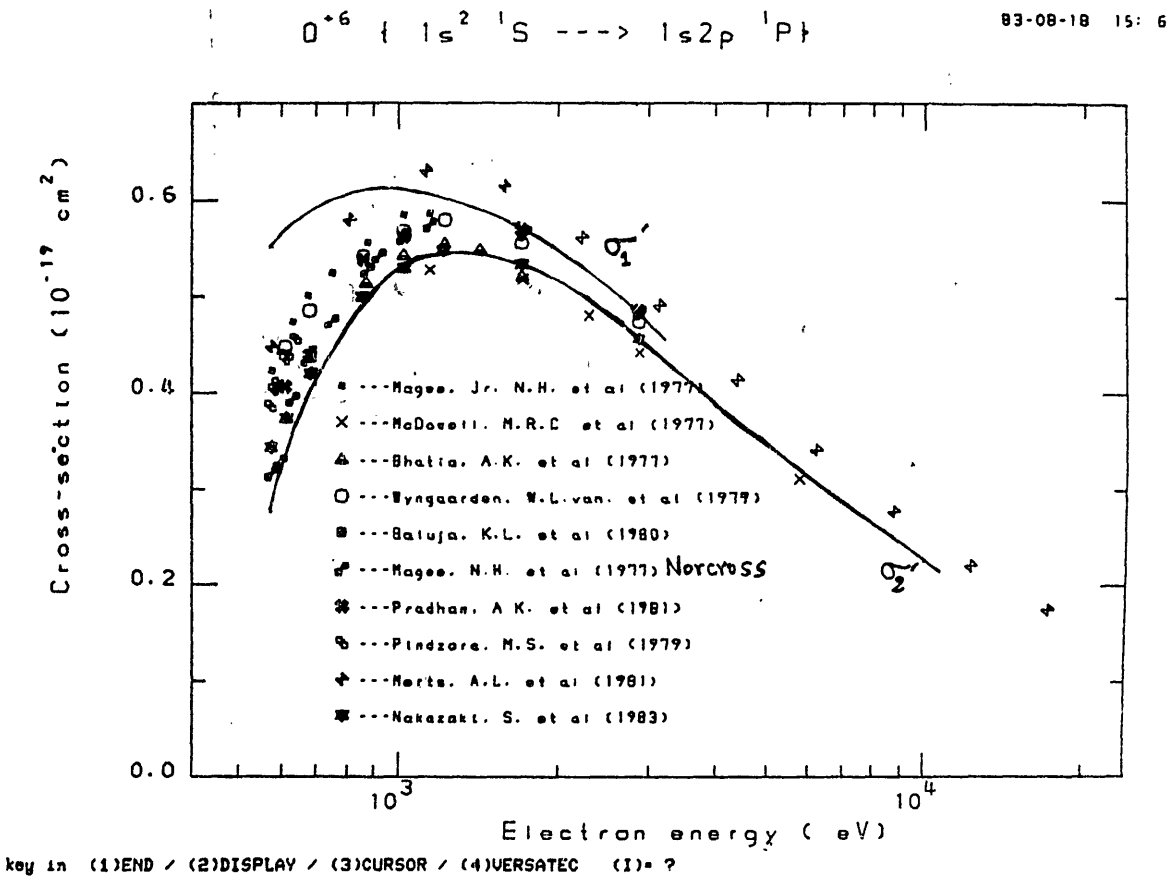

Fig.3 Summary of the existing cross section data for excitation of $1^1S - 2^1P$ of O^{6+}. The cross sections σ_1' and σ_2' pose the upper and lower bound, respectively.

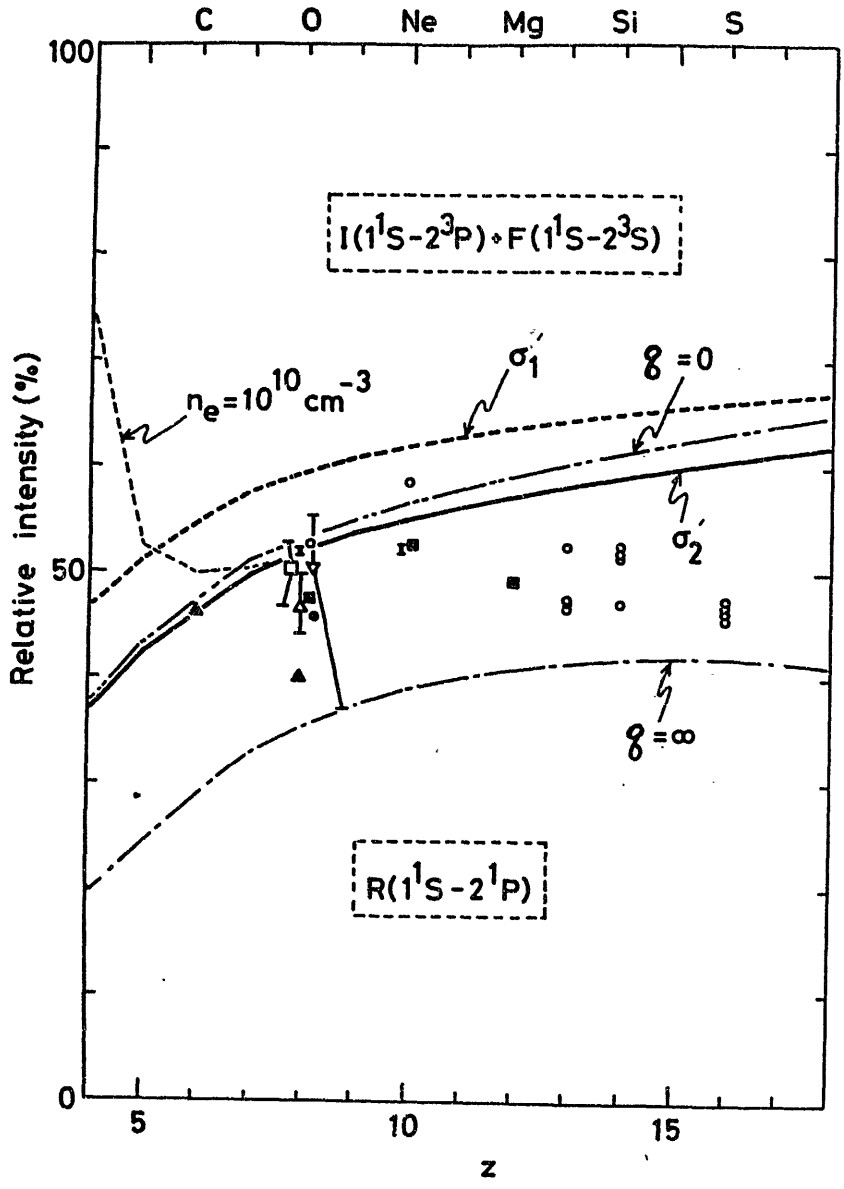

Fig.4 Percentage contributions from (F+I) and R to their sum VS. nuclear charge. Calculated results for σ_1' (dotted line) and σ_2' (solid line) are shown for q=1, the equilibrium plasma. For the cross section σ_2' the results for q=0 (purely ionizing plasma), and q=∞ (purely recombining plasma) are given as well as the results for $n_e=10^{10}cm^{-3}$ with q=1. Observed results are compared.

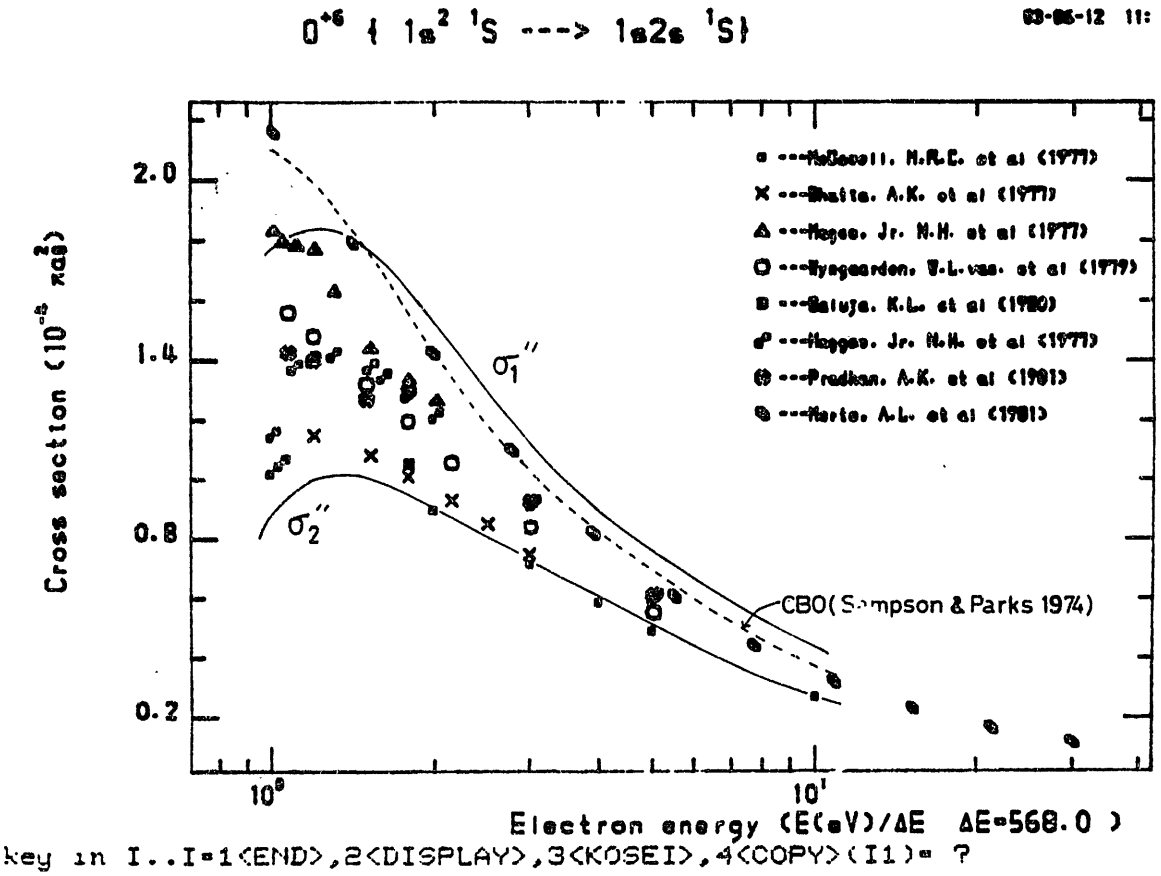

Fig.5 Summary of the existing cross section data for excitation of $1^1S - 2^1S$ of O^{6+}. The cross sections σ_1'' and σ_2'' are the upper and lower bound, repectively.

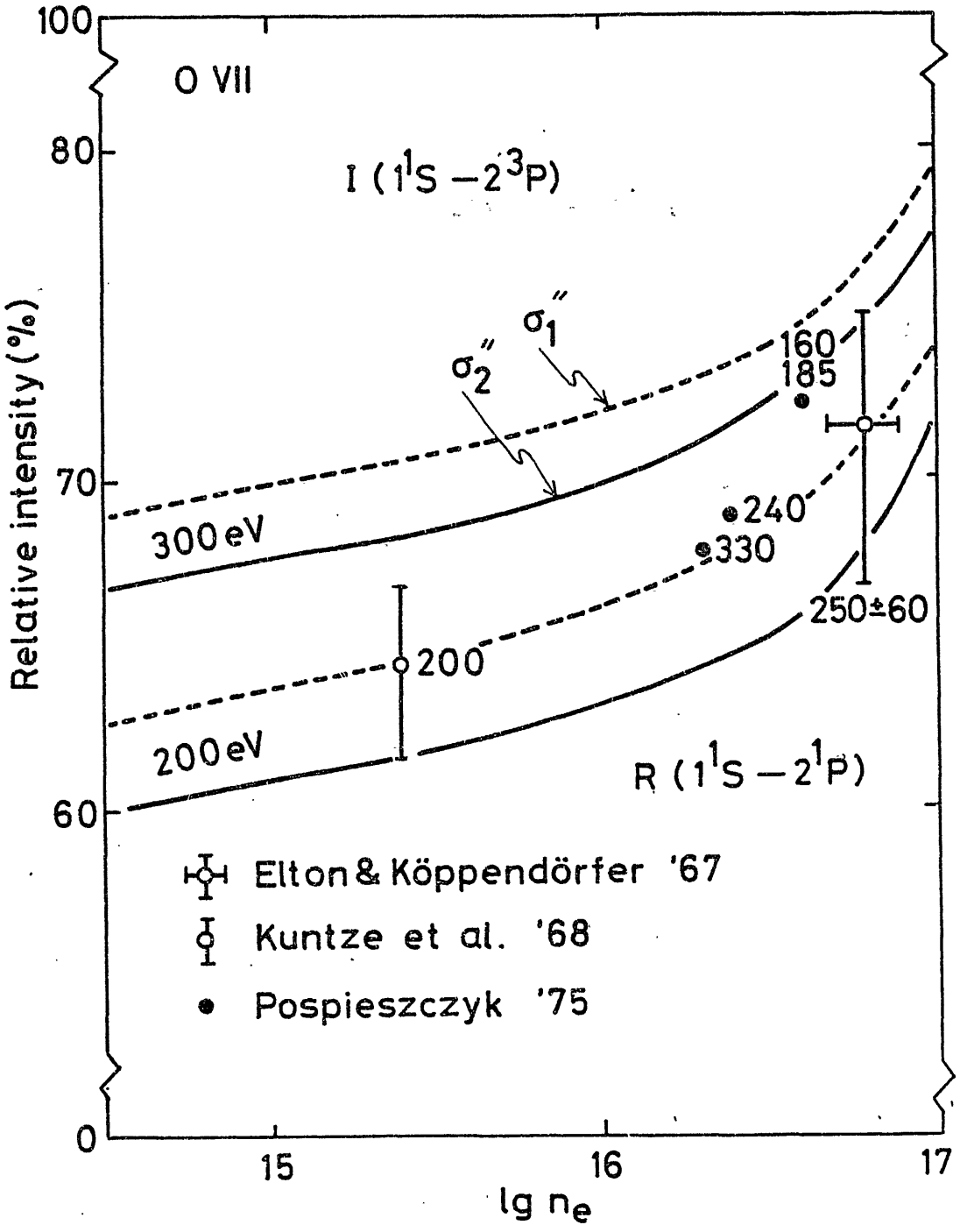

Fig.6 The intensity ratio R/(R+I) for O^{6+}. Dotted line and solid line are the calculated results using the cross section of upper bound σ_1'' and lower bound σ_2'' in Fig.5, respectively.

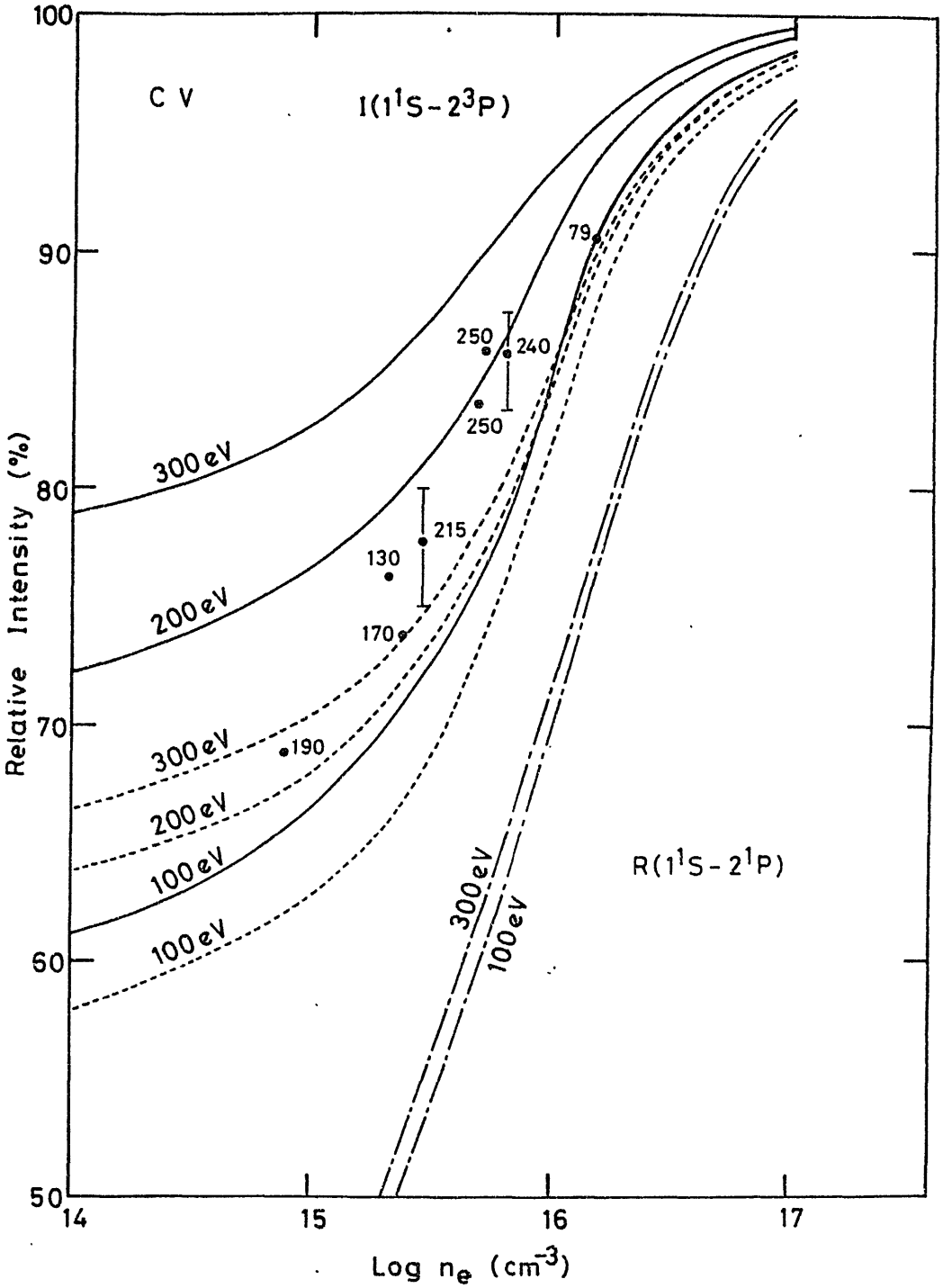

Fig.7 The intensity ratio R/(R+I) for C^{+4}. Solid lines show the results for the ionizing plasma, whereas the dotted lines and dott-dashed lines indicate the results for the equilibrium and recombining plasma, respectively.

Diagnostics and Simulation in G-XII Implosion Experiments

Yoshiaki KATO and Katsunobu NISHIHARA
Institute of Laser Engineering, Osaka University
Suita, Osaka 565, Japan

Abstract

High density implosion experiments become feasible with the completion of Gekko XII glass laser system. We review some of the important aspects on diagnostics and simulation in G-XII implosion experiments.

We are developing Gekko XII Glass Laser System (G-XII) for high density implosion experiments. G-XII is a twelve beam system with an output aperture of each beam of 35cm. It is capable of delivering an output energy of 20kJ in 1ns and a peak power of 40TW in 0.1ns at a wavelength of 1.052μm. Two target chambers are available for different types of experiments with different target irradiation geometries. It is planned that the laser frequencies are converted to the second harmonic (0.53μm) and the third harmonic (0.35μm) for target irradiation with the conversion efficiency of ∿70%.

Based on 1-D simulation calculations of the implosion processes with different types of target structures[1], it is expected that the neutron yield Ny of $\sim 10^{12}$/shot is obtained with an exploding pusher type target. By using the cannonball target $Ny=10^{11}-10^{12}$ and $\rho R \sim 0.1 g/cm^2$ are expected. In order to achieve the good implosion symmetry, we have proposed and experimentally tested random-phasing[2] of the laser beams for direct target irradiation and cannonball target[3] for indirect irradiation. Major issues in the G-XII implosion experiments, among various issues, are implosion uniformity (including irradiation uniformity, symmetry breaking instabilities such

as Rayleigh-Taylor instability, and fuel mixing), implosion efficiency, preheating of the fuel, and the final compression parameters.

The laser energy and the power available from G-XII are approximately 2 orders of magnitude larger than that we have experienced so far. Accordingly we enter into a new region of plasma parameters ; higher temperature, higher density, larger opacity and larger reaction products. It is very interesting to produce and study various kinds of high density plasma effects. However, on the other hand, this is a region that is difficult to make accurate diagnostics. In order to compress the fuel to a high density, the density-radius product (ρR) of the pusher becomes high ($10^{-3} \sim 10^{-1} g/cm^2$). At this condition the transmission coefficient of the X-ray and the charged reaction products such as protons and α-particles are significantly reduced ($10^{-1} \sim 10^{-2}$). For diagnostics of highly compressed fuel, neutron is probably the most useful particle in the forms of neutron yield, neutron activations, and neutron imaging. Development of new diagnostics techniques for high density implosion experiments, such as X-ray backlighting at high X-ray energy ($\gtrsim$5keV), is planned.

We have to collect as many diagnostic data as

possible for each target shot. Simultaneous measurement on various aspects of the plasma (such as temporal, spectral and spatial) is important since analysis of the data of one diagnostic instrument has to rely on other supplementary information . As to the reliability of the data, various diagnostic instruments have to be accurately calibrated. Also we need accurate data base for analysis of the experimental data ; for example, the accurate neutron activation cross section, stopping power of charged particles in dense plasmas, opacity, refractive index, and scattering cross section of X-ray.

As to the simulation of the implosion process, it depends on various models that the code uses. Since the ability to directly diagnose the high density plasmas is limited, the accuracy of the code is more required than it has been so far. Recently the accuracy and the options of the codes have been remarkably improved. However, since we are entering a new region of plasma parameters, further basic experiments are required which model can simulate certain aspects of the high density implosion experiments. The following items were selected as the cooperative research[4] among scientists from various universities, mainly from the viewpoint of the energetics of the

implosion process.

1. X-ray transport, esp. line profile (broadening and edge shift), oscillator strength, and Gaunt factor.
2. Electron transport, esp. Fokker-Planck equation with the high density effect, and determination of the thermal conductivity.
3. Stopping power of high energy electrons and α-particles, esp. scattering by ions and energy transport to electrons, and effect on the ignition condition.
4. Inclusion of the above effects into the implosion simulation code.

Figures 1(a) and 1(b) show ion density, electron temperature, and pressure at the laser peak (a) and maximum compression (b) of a cannonball target irradiated by the 20kJ, 1ns laser.[5]

References

1. T. Yabe, unpublished.
2. Y. Kato et al., IEEE Internatl. Conf. Plasma Science, May 23-25, 1983, San Diego.
3. N. Miyanaga et al., to appear in Jap. J. Appl. Phys. Sept. 1983.
4. K. Mima et al., Grant-in-Aid for Fusion Research, the Ministry of Education, Science and Culture.
5. K. Nishihara, unpublished.

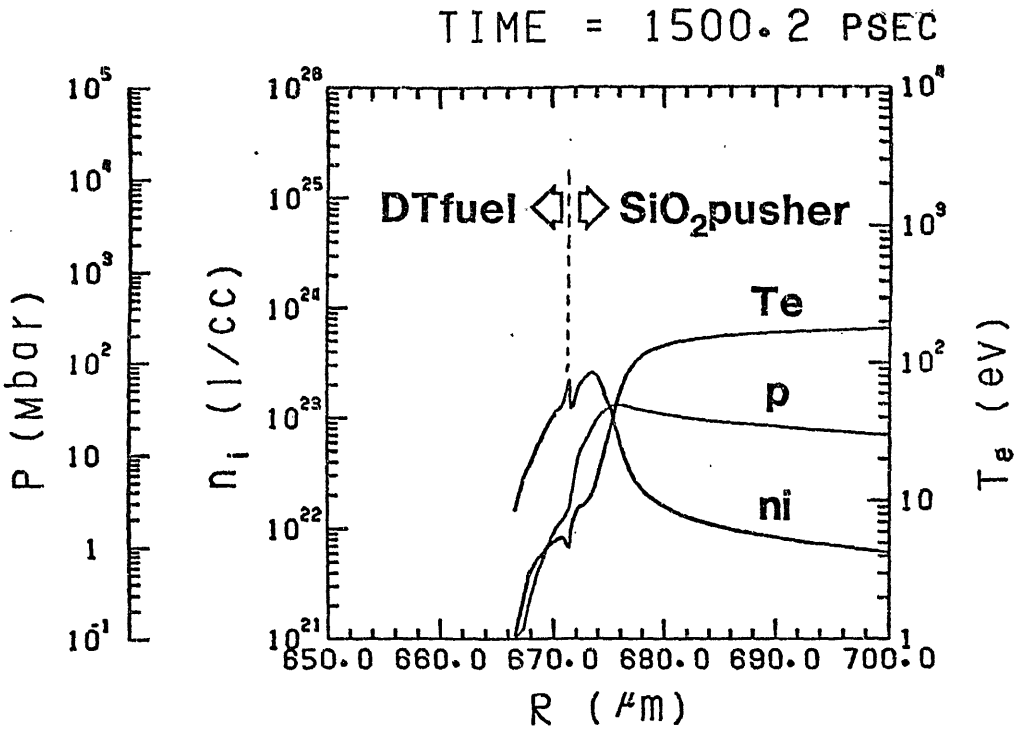
TIME = 1500.2 PSEC
P (Mbar)
n_i (1/cc)
T_e (eV)
DTfuel ◁ ▷ SiO_2pusher
Te
p
ni
650.0 660.0 670.0 680.0 690.0 700.0
R (μm)

Fig. 1 (a)

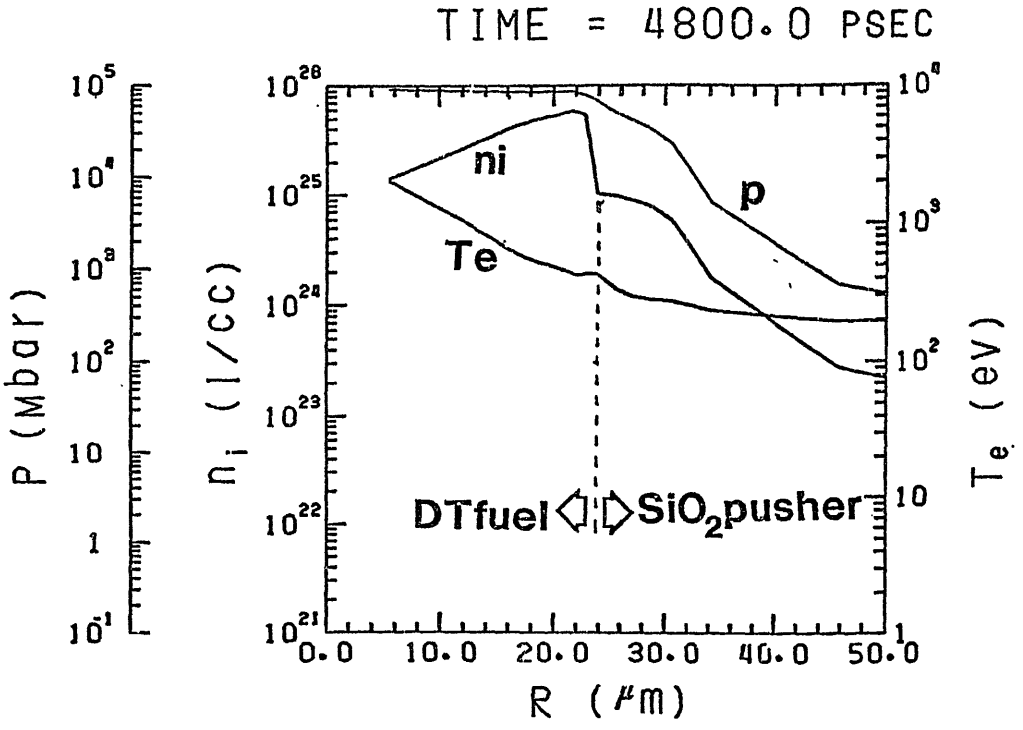
TIME = 4800.0 PSEC
P (Mbar)
n_i (1/cc)
T_e (eV)
ni
p
Te
DTfuel ◁ ▷ SiO_2pusher
0.0 10.0 20.0 30.0 40.0 50.0
R (μm)

Fig. 1 (b)

Atomic Processes for Modeling of Inertial Confinement Fusion Plasma

Katsunobu Nishihara

Institute of Laser Engineering, Osaka University,
Suita, Osaka 565, Japan

Abstract

The density and temperature of hot dense plasma that will be achieved in the cannonball target compression by the Gekko XII laser system are predicted by means of computer simulation. It is shown that the plasma is characterized by the two parameters as $kT \sim \varepsilon_F$ and $\Gamma \equiv Z^2e^2/R_o kT \sim 1$, where ε_F and R_o are the zero temperature Fermi energy and the mean ion distance, respectively. Model of the code and reguired atomic properties are also briefly overviewed.

1. Introduction

To clarify the problems in modeling of inertial confinement fusion plasmas, it is necessary to know their density and temperature. By choosing an example of a target and a laser energy, this report presents simulation predictions of plasma density and temperature which will be achieved in near future. The two important parameters characterizing the hot dense plasma are the ratios of the plasma kinetic energy to the zero temperature Fermi energy and to the Coulomb interaction energy. The predicted values of the two parameters show that the hot dense plasma is far anything previously achieved in the laboratory.

Accurate computer simulation requires a variety of atomic properties of target materials. Atomic properties required in a computer code are discussed including structrure of ions (equation of state), transport coefficients (thermal conductivity, collision frequencies) and x-ray transport coefficients.

2. Hot Dense Plasma in Inertial Confinement Fusion

The HISHO computer code is used to predict plasma density and temperature of hot dense plasma that will be achieved by large cavity cannonball target[1] with the Gekko XII laser system. The cannonball target is a double-shell target, with holes on the outer shell, through which laser beams are injected. The cannonball target is classified into two types according to the cavity size between the inner and outer shell. The outer shell of the large cavity cannonball target is composed

of high-z material, such as gold, and laser beams are irradiated mainly onto the inner sunface of the outer shell. Then the outer shell emits x-rays which ablate the inner shell. Thus, the radiation driven ablation[2,3] plays an important role in the large cavity cannonball target.

The laser and target parameters used are summarized in Table 1. We assume the laser absorption of 90% at the critical density of the inner surface of the outer shell. Figure 1 shows implosion dynamics on r-t diagram. Laser peak is achieved at 1.5 ns in the figure. Since the laser absorption is assumed only by the outer shell, the ablation and implosion of the inner shell are drived by the x-ray radiation emitted from the outer shell. The spatial profiles of the plasma density, temperature and pressure are shown in Fig. 2 (a) at the laser peak 1.5 ns and Fig. 2 (b) at the maximum compression 4.8 ns. Figure 2 (c) also shows the inward and outward radiation fluxes at the laser peak. As shown in the figure, the x-ray radiation is absorbed near the surface of the inner shell mainly by the bound-free transition. It heats plasma and drives plasma ablation. The high pressure thus generated drives the implosion of the inner shell. The ablation pressure becomes about 40 Mbar.

Both the plasma density and temperature change very rapidly through the ablation region, while the pressure remains almost constant as shown in Fig. 2 (a) and 2 (c). In the front of the ablation the plasma density is higher than the solid density because of the compression and the temperature remains

relatively cold. The density and temperature in the front are shown in the dotted region 1 in Fig. 3. As clearly seen from the figure, the plasma are characterized by the two parameters as

$$kT \sim \varepsilon_F \text{ and } \Gamma \equiv \frac{Z^2 e^2}{R_o kT} \sim 1. \qquad (1)$$

Here ε_F and R_o are the zero temperature electron Fermi energy and the mean ion distance, respectively. Thus the electrons are partially degenerate and the Coulomb interaction energy becomes comparable to the kinetic energy. When the parameter Γ is much less unity, the the plasma is called an ideal plasma, while when $\Gamma >> 1$, it is called a strong coupled plasma. Thus the plasma in the region 1 is the two-component intermediate coupled plasma. In the rear side of the ablation region, the plasma density is relatively low because of the ablation and the temperature is high due to the heating. This plasma is an ideal one.

The plasma density and temperature at the final compression is shown in the dotted region 2 in Fig. 3. The fuel density becomes 1000 times greater than its solid density. The fuel ρR, the product of fuel mass density and its radius, reaches approximately 0.3 gr/cm^2 which can satisfy one of the ignition conditions. However, the laser energy of 20 kJ is not large enough to heat plasma to satisfy the other ignition condition. Thus the plasma parameters remain almost the same as those given by eq. (1). It should be noted that although the parameter

Γ for fuel is less than unity, that for glass pusher is of the order of unity because of higher ionization state.

3. Model Overview and Required Atomic Properties

The HISHO computer code was developed at Institute of Laser Engineering to study the many interrelated physical processes important in achieving the laser inertial fusion. The code is essentially one-fluid and two-temperature (thermal electrons and ions) model. In addition to these fundamental parts, it calculates laser absorption, equation of state, high energy electron transport and x-ray radiation transport. The high energy electrons are generated by the anomalous laser absorption and their energy is typically of the order of 10 to 100 keV.

Equation of motion for the ion-fluid requires the pressures of thermal electrons, ions and high energy electrons. Energy conservation equation for thermal electrons is given by

$$C_{ve} \frac{dT_e}{dt} + (B_{Te} + p_e) \frac{dV}{dt} = S, \qquad (2)$$

where

$$C_v \equiv \frac{de}{dT}\Big|_v, \quad B_T \equiv \frac{de}{dv}\Big|_T.$$

Here e(ni,Te), p(ni, Te) and V are thermal electron internal energy density, its pressure and specific volume. The source terms include thermal conduction, energy relaxations from high

energy electrons to thermal electrons and from thermal electrons to ions, laser absorption, x-ray emission and absorption. Energy conservation for ions is also given in the same type as eq.(2).

The average-atom equation of state[4,5] is used to calculate C_V, B_T, p, the ionization state Z*, the electron population of n-th principal quantum state P_n, and its ionization energy I_n. The latter three values, Z^*, P_n and I_n are necessary to obtain thermal conductivities and energy relaxation rates of thermal electrons and ions, the scattering frequencies and energy relaxation rates of high energy electrons and x-ray absorption coefficients. In the average-atom model we consider a fictitious ion of which the ionization state is given by

$$Z^* = Z - \sum_n P_n, \tag{3}$$

where Z is the atomic number. In the hot dense plasma as shown in the previous section, the orbit radius of large principal quantum number becomes larger than the mean ion distance. This results in the pressure ionization. As discussed in the previous section, the electron Fermi degeneracy becomes important and we have to use the Fermi distribution function. The Coulomb interaction leads to lowering the ionization energy and the excess interaction energy. Mixed ions such as a glass are often used for target materials. For mixed ions the chemical potentials for each species can be assumed to be equal.

Frequency dependent absorption coefficients are obtained

from the average-atom model, for bound-bound, bound-free and free-free transitions. The photons are transported with a multigroup ray-trace model. Namely, photons are divided into groups according to their energies and their intensities are calculated along their trajectories in target.

High energy electron transport is calculated with a multigroup flux-limited diffusion model, which is derived from the Fokker-Planck transport equation. As their energy is lost, we consider the ionization and excitation loss and energy relaxation to thermal electrons. We also take the Rutherford scattering with the partially ionized ions into account[6].

As a summary, we have shown that the hot dense plasma produced by laser compression can be characterized by the two parameters as $kT \sim \varepsilon_F$ and $\Gamma = Z^2e^2/R_okT \sim 1$. More precise knowledge of atomic properties is required to calculate the equation of state, transport coefficients and x-ray absorption coefficients.

References

1) K. Nishihara and T. Yuchi, ILE Quarterly Progress Report on Inertial Fusion Program, Inst. of Laser Eng., Osaka Univ., ILE-OPR-83-5, p 24 (1983).

2) K. Nishihara, Jpn. J. Appl. Phys. 21, L571 (1982).

3) T. Mochizuki, S. Sakabe, K. Okada, H. Shiraga, T. Yabe and C. Yamanaka, Jpn. J. Appl. Phys. 22, L133 (1983).

4) G. B. Zimmerman and B. M. More, J. Quant. Spectrosc. Radiat. Transfer 23, 517 (1980).

5) T. Yuchi and K. Nishihara, Tech. Repts., Osaka Univ., 32, 295 (1982).

TABLE 1 Laser and Target Parameters

laser parameters	
energy	E_L = 20 kJ
pulse width	τ_L = 1 ns (FWHM)
wavelength	λ_L = 1.06 μm
target size and material	
radius of outer shell	R_o = 1400 μm
radius of inner shell	R_i = 700 μm
tamper (outer shell)	Au
pusher	SiO_2
fuel	DT (0.2gr/cm^3)
thickness of tamper	ΔR_t = 15 μm
thickness of pusher	ΔR_p = 18 μm
thickness of fuel	ΔR_f = 8 μm

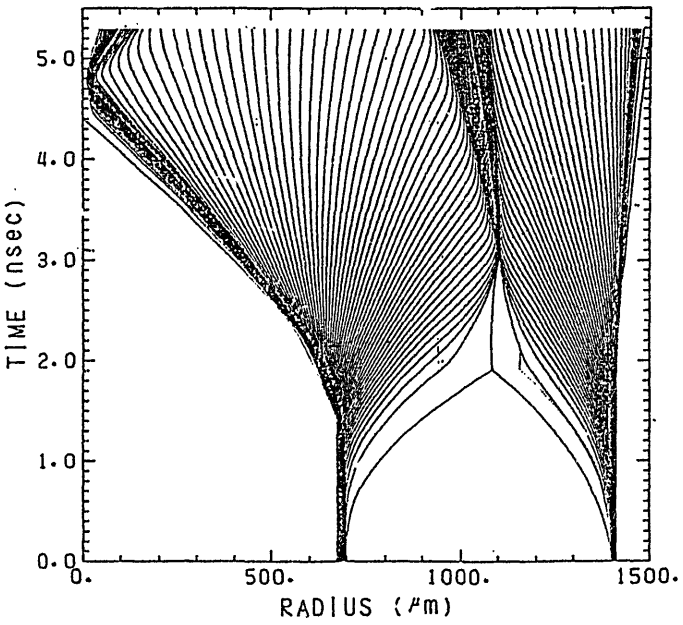

Fig. 1 Implosion dynamics of large cavity cannonball target on r-t diagram. Laser energy is assumed to be absorbed only by the outer shell. Laser peak is achieved at 1.5 ns.

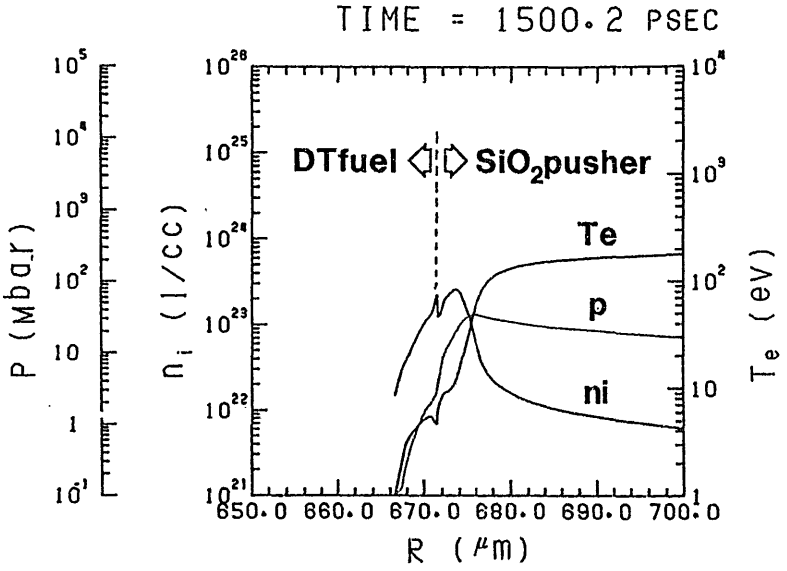

Fig. 2(a)

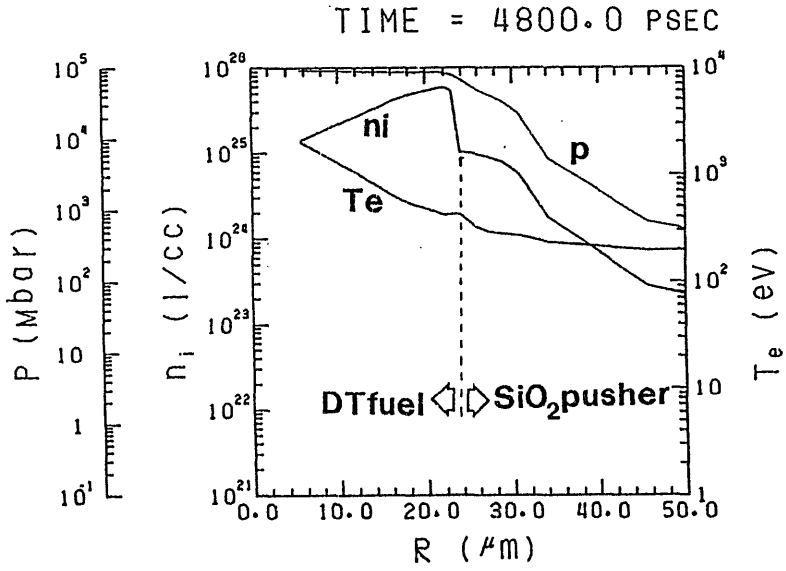

Fig. 2(b)

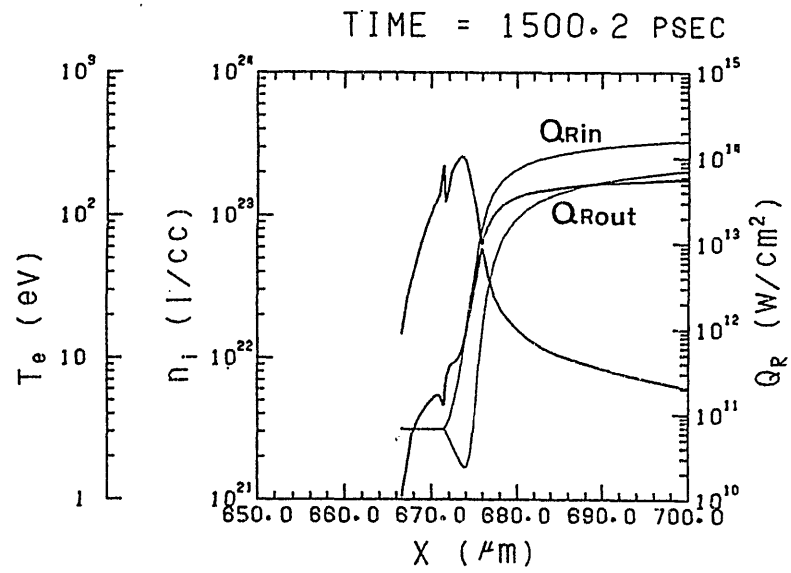

Fig. 2(c)

Fig. 2 Spatial profiles of ion density, electron temperature and pressure. (a) at laser peak 1.5 ns, (b) at maximum compression 4.8 ns, and (c) inward and outward x-ray flux at 1.5 ns.

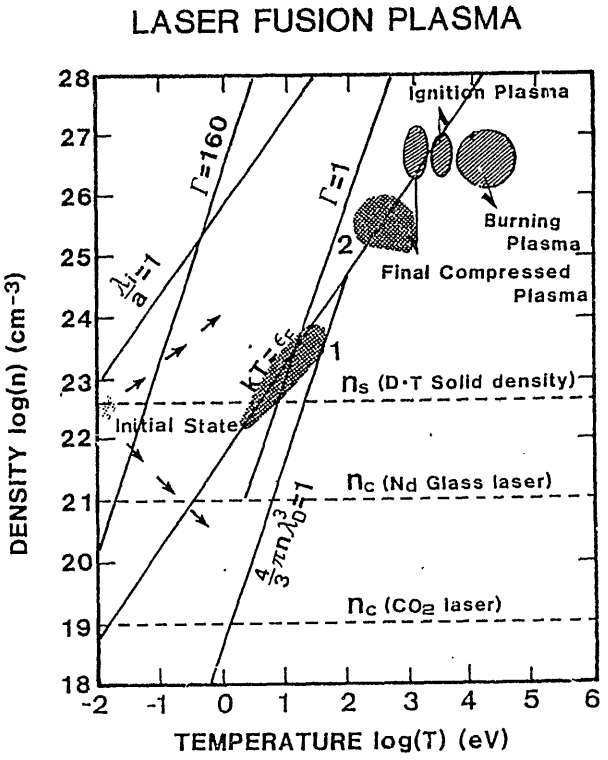

Fig. 3 Hot dense plasma in inertial confinement fusion plasma. Dotted region 1 corresponds to density and temperature at laser peak 1.5 ns, and region 2 to those at maximum compression 4.8 ns.

Atomic Collision Data for Beam Probe Diagnostics of Magnetically Confined High Temperature Plasmas

Kiyoshi Kadota

Institute of Plasma Physics, Nagoya University
Nagoya 464, Japan

Abstract

Beam probe methods for high temperature plasma diagnostics, in which atomic collision data play a very important role, are reviewed briefly. The cross sections for electron impact excitation and ionization of the probing particles are of use for the measurements of electron density and temperature. On the other hand, those for charge transfer between various plasma ions and the probing particles are useful for the measurements of proton and multiply charged impurity ion densities. The atomic collision data, which should be evaluated and compiled, are summarized.

1. Introduction

In the early phase of studies on plasma physics, Langmuir probes were mainly used as diagnostic tools. With the progress of fusion research, the temperatures of plasmas to be studied become much higher than the early ones and the Langmuir probes are no longer usable. Instead, diagnostic techniques using lasers and/or particle beams as probes have received much attention. The lasers are being used as powerful diagnostic tools.[1] The usefulness of particle beam probes is also recognized and their studies are gradually increasing.[2]

We will give an outline of the particle beam probe diagnostics which are closely related to atomic collision processes and discuss about the atomic collision data which are useful for them. The atomic data relevant to beam probe diagnostics of the high energy α-particles produced by D-T reaction will be discussed separately in this proceedings.

2. Particle Beam Probe Diagnostics

2.1. Principle of the methods

Neutral or ion beams can be used to probe plasmas with spatial and temporal resolution. Particles or photons are detected, which are locally emitted by interactions between the probing particles and plasma particles. They give information on plasma parameters as seen in Fig.1. The useful atomic processes for the beam probing, the physical quantities observed and the plasma parameters obtained are listed in Table 1.

In the application to magnetically confined plasmas, the use

of a neutral beam may be easier than an ion beam, because of its simple beam trajectory which is independent of magnetic fields. In the case of the ion beam, heavy ions with a relatively high energy must be used to keep the condition in which the ion gyroradius is larger than the size of devices. For the neutral beam, generally light atoms are suitable, because the plasma contamination by the impurity injection can be minimized and it is relatively easy to get higher beam velocities necessary for the penetration of the probe beam into the center of the plasma column.

In some cases of the particle detection, the attenuation of the detected secondary particles in the plasma must be considered in addition to that of the probing beam. It seems that the techniques of the photon detection (we may call the "Beam Probe Spectroscopy") in which the data analysis is simplified are advantageous in comparison with those of the particle detection, although there may be some exceptions.

The attenuation (or penetration) of the beam in the plasma is an important factor for the beam probing. The beam attenuation is given by the following formulae,

$$\frac{1}{I_A(x)} \frac{dI_A(x)}{dx} = -\sum_{jk} n_j(x) \frac{\langle \sigma v \rangle_{jk}}{v_A} , \qquad (1)$$

or

$$I_A(x) = I_A(0) \exp\{-\int_0^x \sum_{jk} n_j(x) \frac{\langle \sigma v \rangle_{jk}}{v_A} dx\} , \qquad (2)$$

where $I_A(x)$ is the beam intensity of the probing particles A with the velocity v_A at the distance x along the beam axis in the plasma, $n_j(x)$ the local density of the plasma particles of species j and $\langle\sigma v\rangle_{jk}$ the rate coefficient for the collision process k between the probing and plasma particles. The effective cross section $\langle\sigma v\rangle_{jk}/v_A$ which is a very useful physical quantity for the beam probe diagnostics is defined by the following formula,

$$\frac{\langle\sigma v\rangle_{jk}}{v_A} = \frac{1}{v_A}\int\sigma_k(|\vec{v}_j-\vec{v}_A|)\,|\vec{v}_j-\vec{v}_A|\,f(\vec{v}_j)\,d\vec{v}_j \ , \qquad (3)$$

where $\sigma_k(|\vec{v}_j-\vec{v}_A|)$ is the collision cross section at the relative velocity $|\vec{v}_j-\vec{v}_A|$ and $f(\vec{v}_j)$ the velocity distribution function of the plasma particles which is assumed to be Maxwellian under ordinary circumstances.

As an example, the effective cross sections for various collision processes between the neutral lithium beam and the hydrogen plasma particles with the electron and proton temperatures of 100 eV are shown as a function of the Li°-beam energy in Fig. 2. The cross section data compiled in Refs. 3 and 4 are used. Figure 2 gives useful information on the beam probe diagnostics. We see that electron impact excitation and ionization are the dominant processes at beam energies below several keV, which means that we can have information on the electrons with the beam of an energy in this range. On the other hand, at energies around several tens of keV charge transfer becomes important and we can have information on the protons.

This situation strongly depends upon species of the probing beam. For instance, in the case of hydrogen atoms charge transfer is important even if at low energies[5]. This means that in the beam probe diagnostics we can selectively determine the plasma parameters by using the beam of a suitable species and energy.

2.2. Diagnostics using electron impact excitation

Techniques of the beam probing combined with spectroscopy can be used. As an example, the experimental setup used for the electron density measurement in the Nagoya Bumpy Torus (NBT) at IPP, Nagoya University, is shown in Fig. 3.[6] The Li°-beam produced by neutralization of a 3.6 keV Li^+-beam passing through Li-vapour is injected into the plasma. A part of the injected Li-atoms is excited by electron impact, which is the dominant excitation process at beam energies below 10 keV (see Fig. 2), and then emits photons. The local photon flux $N_{\nu p}(x)$ of the lithium resonance line (2^2S-2^2P, 670.8 nm) is given by the following formula,

$$N_{\nu p}(x) = n_{Li}(x)\ n_e(x)\ \langle\sigma_{ex}v\rangle\ , \qquad (4)$$

where $n_{Li}(x)$ and $n_e(x)$ are the local densities of the beam and the plasma electrons, respectively, and $\langle\sigma_{ex}v\rangle$ the rate coefficient for the electron impact excitation which is insensitive to electron temperature T_e in the region of 10 to 100 eV [4,7] (excitation energy is 1.85 eV). One can obtain n_e by measuring $N_{\nu p}$ and n_{Li}, when $\langle\sigma_{ex}v\rangle$ is known. The beam density n_{Li} was measured by using the collision process between Li and

H_2,

$$Li(2s) + H_2 \rightarrow Li^*(2p) + H_2. \qquad (5)$$

The local photon flux $N_{\nu g}(x)$ produced by process (5) is given by the following formula,

$$N_{\nu g}(x) = n_{Li}(x)\ n_g\ Q\ v_{Li}, \qquad (6)$$

where n_g is the density of molecular hydrogen, Q the cross section for process (5) and v_{Li} the Li°-beam velocity. From formulae (4) and (6), we have the following formula,

$$n_e(x) = \frac{Q}{\langle\sigma_{ex}v\rangle/v_{Li}} \frac{N_{\nu p}(x)}{N_{\nu g}(x)}\ n_g\ . \qquad (7)$$

The local electron density $n_e(x)$ can be obtained from the measurements of the ratio $N_{\nu p}/N_{\nu g}$ and n_g, as Q and $\langle\sigma_{ex}v\rangle/v_{Li}$ are known.[7] The cross section Q was measured and $\langle\sigma_{ex}v\rangle/v_{Li}$ was calculated with the experimental data of σ_{ex} by Leep and Gallagher.[8]

Typical spatial profiles of the both photon fluxes, which were obtained by tilting a mirror (see Fig. 3), are shown in Fig. 4. The spatial profiles of n_e are shown in Fig. 5. They give useful information on the plasma confinement in the Bumpy Torus. In this experimental phase of NBT, the plasma parameters n_e and T_e are of the order of $10^{11}cm^{-3}$ and several tens of eV,

respectively. The attenuation of the probing beam in the plasma can be neglected. If it is not negligibly small, the measurement of the local density $n_{Li}(x)$ can be done with the laser-induced fluorescence method.[4)]

There is a possibility of using a Ba^+-ion beam[9)] on which the cross section for electron impact excitation is large.

2.3. Diagnostics using electron impact ionization

The beam probe diagnostics using electron impact ionization has extensively been developed with the beams of singly charged heavy ions like Tl^+, Cs^+ and Rb^+ of which the ions can easily be produced with ion sources of the thermionic emission type. Figure 6 illustrates the principle of the ion beam probing.[10)] A monoenergetic ion beam (R^+) is injected into a plasma confined by magnetic fields. Some of the ions are ionized to multiply charged states (R^{q+}) by collisions with plasma electrons. The magnetic fields cause the secondary R^{q+}-beams to be separated from the primary R^+-beam. The energy E_1 of the primary R^+-beam changes to $E_1 - e\phi$ in the plasma of the potential ϕ, and the energy E_2 of the secondary R^{2+}-beam becomes $(E_1 - e\phi) + 2e\phi = E_1 + e\phi$ outside the plasma. Then ϕ can be determined by measuring E_2 as E_1 is known[10-12)]. In principle, the spatial profile of ϕ can be obtained by moving the energy analyzer for the R^{2+}-beam.

The electron density n_e and the electron temperature T_e can also be determined from the measurements of the R^+-beam intensity I_1 and the R^{q+}-beam intensities I_q with the following formulae,

$$I_q = I_1 \, n_e \langle \sigma_i^q \, v \rangle / v_1 = I_1 \, n_e \, f_q(T_e) \ , \qquad (8)$$

(for the unit observation length)

and

$$\frac{I_2}{I_3} = \frac{I_1 \, n_e \, \langle \sigma_i^2 \, v \rangle / v_1}{I_1 \, n_e \, \langle \sigma_i^3 \, v \rangle / v_1} = f(T_e) \ , \qquad (9)$$

where $\langle \sigma_i^q \, v \rangle / v_1$ is the effective cross section for electron impact ionization to the charge state q of the R^+-ions, which is a function of T_e. The feasibility of this diagnostic technique has been demonstrated with 10 - 30 keV Cs^+-beams in RENTOR which is a small tokamak of the toroidal magnetic field of 4.32 kG at the Rensselaer Polytechnic Institute[13]. Figure 7 shows the ratio of the effective ionization cross section for 1+ →2+ of Cs to 1+ →3+ as a function of T_e. The experimental data by Feeney and Hertling [14] were used in the calculation. The ratio is suitably sensitive to T_e below about 200 eV. The experimental apparatus is shown in Fig. 8. The scanning of the observed position was done by deflecting the beam and changing its energy. The obtained T_e and n_e profiles are shown in Fig. 9.

A method involving the use of two kinds of singly charged ion beams (A^+ and B^+) was applied to measure T_e of hollow cathode discharge.[15,16] The technique is similar to that mentioned above, as it uses the following formula,

$$\frac{I_{A2}/I_{A1}}{I_{B2}/I_{B1}} = \frac{n_e \, \langle \sigma_i^{A2} v \rangle / v_A}{n_e \, \langle \sigma_i^{B2} v \rangle / v_B} = h(T_e) \ . \qquad (10)$$

In this formula, I_{A1} and I_{A2} are the intensities of the A^+- and A^{2+}-beams of the velocity v_A, respectively, I_{B1} and I_{B2} those of the B^+- and B^{2+}-beams of v_B, and $\langle\sigma_i^{A2}v\rangle/v_A$ and $\langle\sigma_i^{B2}v\rangle/v_B$ the effective cross sections for electron impact ionization on $1+ \rightarrow 2+$. The ratios of the effective cross sections for some pairs of the species are shown as a function of T_e in Fig.10. Since there are no experimental data for Rb, the solid curves were calculated with the Gryzinski formula[17] and the dashed curve(K/Na) with the experimental data compiled by Kieffer[18]. From the comparison between both the curves for K/Na, we see that the accuracy of the collision data is very important for the determination of T_e. In the experiments, the intensities of the primary and secondary ions of the two beams (Na^+-K^+ and K^+-R_b^+) were measured.

A demerit of using ion beams is that the beams of very high energy are required to apply to fusion research devices with strong magnetic fields like tokamaks above the medium size (toroidal magnetic field $B_T \gtrsim 20$kG). In order to overcome this difficulty, a method using two kinds of neutral beams has been proposed to measure n_e and T_e of the boundary layer plasma in tokamaks[4]. The electron density can be measured with the method using electron impact excitation of a Li°-beam. The electron temperature can be determined by measuring the differential attenuations of the two probing beams in the plasma. Their ratio which is dominated by electron impact ionzation, is given by the following formula,

$$\frac{\frac{1}{I_{A0}}\frac{dI_{A0}}{dx}}{\frac{1}{I_{B0}}\frac{dI_{B0}}{dx}} = \frac{-n_e\langle\sigma_i^{A1}v\rangle/v_A}{-n_e\langle\sigma_i^{B1}v\rangle/v_B} = g(T_e) \ . \qquad (11)$$

In formula (11), I_{A0} and I_{B0} are the probing beam intensities, $\langle\sigma_i^{Al}v\rangle / v_A$ and $\langle\sigma_i^{Bl}v\rangle/v_B$ are the effective ionization cross sections for 0 → 1+. The differential beam attenuation may be measured by laser-induced fluorescence with two tunable dye lasers incident along the probing beam axis. The ratios of the effective ionization cross sections for the pairs of Li-Al and Li-Ti are shown in Fig.11. The experimental data are used for Li[19,20] and Al[21], and the Lotz formula[22] for Ti. For Li-Al, the uncertainties indicated by the solid and dashed curves are due to an incomplete set of the experimental data for Al, as mentioned in Sec.3.2. This method, however, is still usable below about 50eV which is of the order of T_e in the boundary layer of tokamaks.

In the cases of the techniques detecting secondary ions, it may be possible to use heavy neutral beams like Xe[23]. An Au^--beam has also been used to measure plasma potential[24]. The energy of the secondary Au^+-beam produced by electron detachment was analyzed.

2.4. Diagnostics using charge transfer

Charge transfer processes are very useful for diagnostics of various ions with neutral beam probes, especially for fully stripped ions because they can not be observed by passive spectroscopy which is normally used to diagnose multiply charged

impurity ions. In this beam probing, there are two possibilities. One of them is the detection of the photons emitted from the plasma neutrals or ions produced by the electron capture, and the other is of the produced neutrals which escape from the plasma. For fully stripped ions with low nuclear charge like H^+ and He^{2+}, the latter is possible[25]. In the case of the application to higher density plasmas, however, the efficiency with which the produced neutrals escape from the plasma must be considered in addition to the attenuation of the probing beam. It seems that the former is advantageous in comparison with the latter.

A technique of atomic hydrogen beam probing combined with spectroscopy has been developed to measure the densities of fully stripped light impurity ions (C^{6+} and O^{8+}) and applied to tokamaks[26-28]. The experimental setup which was used in the PDX tokamak[28] is shown in Fig.12. A 25keV H-beam is tangentially injected into the plasma. The C^{6+} and O^{8+} ions in the plasma capture electrons into excited states from the hydrogen atoms, and emit photons. The emitted photon flux $N_{\nu p}(r)$ at the radial position r is given by the following formula,

$$N_{\nu p}(r) = n_H(r) n_z(r) \langle \sigma_{ct} v \rangle \simeq n_H(r) n_z(r) \sigma_{ct} v_H, \qquad (12)$$

where n_H is the density of the H°-beam of the velocity v_H, n_z the density of the impurity ions with charge state z, and $\langle \sigma_{ct} v \rangle$ the rate coefficient for charge transfer followed by emission. The rate coefficient $\langle \sigma_{ct} v \rangle$ can be replaced by $\sigma_{ct} v_H$, because the

beam velocity v_H is much larger than the impurity ion velocities v_z. The local impurity ion density $n_z(r)$ can be determined from the measurements of $N_{\nu p}$ and n_H when σ_{ct} is known. The radial profiles of n_z were measured by tilting the probing beam injector. The radiations of the transitions $n=4 \rightarrow 3$ or $3 \rightarrow 2$ were detected. Since there are few experimental data of σ_{ct} for H + C^{6+} and H + O^{8+} systems, they were estimated with theoretically calculated values[29-31]. In this measurement, the beam density n_H at the observed position was estimated with a computer code for the beam attenuation in which atomic collision data also play an important role. The obtained density profiles for the C^{6+} and O^{8+} ions are shown in Fig. 13, which give useful information on the impurity transport in the tokamak plasma.

In the measurement of partialy stripped ions by passive spectroscopy, there are also some problems. It is difficult to estimate the impurity ion densities from spectroscopic data, because n_e and T_e in the edge plasma region, where such ions are mainly located, are not well known. The measurement of highly stripped ions diffusing to the edge plasma region is also difficult due to no emission by relatively low electron temperature. The possibility to use a Li°-beam for the density measurement of multiply charged impurity ions in the edge plasma region has been proposed[32]. The use of the Li°-beam is also promising to probe H^+ and He^{2+} ions,[33] because the cross sections for electron capture into excited states on the Li + H^+ [34,35] and Li + He^{2+} [35,36] systems are very large. As an example, the emission cross sections for the Li + He^{2+} system[36] are shown in

Fig. 14. The He^{2+} ions capture an electron very selectively into the n=3 state of He^{+} and the emission cross sections for the 30.4 nm (n=2 → 1) and 164.0 nm (n=3 → 2) are around 7 - 9 x $10^{-15}cm^2$ at 30 keV for Li which is suitable as the probing beam energy. The situations for C^{z+} and O^{z+} are similar to those for H^{+} and He^{2+} [37]. The disadvantage of using the Li°-beam is the strong beam attenuation in plasmas. It is not, however, a critical problem for diagnostics of the edge plasma. Besides the local Li°-beam density can be measured by laser-induced fluorescene with a tunable dye laser as mentioned before. For the application to plasmas of larger scale and higher density, the use of a He°-beam may be suitable in order to probe the core plasmas.

Another application of charge transfer processes to the beam probe diagnostics is the determination of the proton density n_i and the effective charge $Z_{eff} = \sum_{jz} z n_{jz}/n_e$ (n_{jz} :the density of the ions of species j with charge state z) by means of the attenuation of a H°-beam in the plasma. The beam attenuation is given by the following formula,[38,39]

$$I = I_0 \exp\{-\int(\sigma_c n_i + \frac{\langle\sigma_i v\rangle}{v_H} n_e + \sum_{jz} \sigma_{jz} n_{jz})dx\} \quad , \qquad (13)$$

when the contribution from collisions with the hydrogen molecules can be neglected. In this formula, I and I_0 are the intensities of the probing beam transmitted through the plasma and the incident probing beam, respectively, σ_c the capture cross section (charge transfer plus impact ionization) of protons, $\langle\sigma_i v\rangle/v_H$ the

effective cross section for electron impact ionization, and σ_{jz} the electron capture cross section for impurity ions of species j and charge z. When the concentration of impurities is small, the impurity term in formula(13) can be neglected and n_i is equal to n_e. In this case, formula (13) is simplified as the following formula,

$$I=I_0 \exp\{-(\sigma_c + \frac{\langle\sigma_i v\rangle}{v_H})\ \bar{n}_i\ L\}, \qquad (14)$$

where $\bar{n}_i$ is the line-averaged ion density and L the size of the plasma. From the measurement of I/I_0, the line integral density $\bar{n}_i L$ can be obtained[40,41] as the related cross sections are known[5] and $n_i(r)$ with multichord beam.[42] The beam attenuation measurement at several radial positions has been done with deuterium plasmas in the TFR tokamak (CEN, Fontenay-aux-Roses), in which the contribution by impurity ions can not be neglected[38,39]. The spatial profiles of n_i and Z_{eff} were evaluated by means of the best fitting to the measurement with formula(13) in which parameters are the concentration of impurities and Z_{eff}. They obtained the results which were consistent to those determined by other independent methods, although this method takes rather complicated steps on the data analysis.

3. Atomic Collision Data for the Beam Probe Diagnostics

3.1. Excitation

In Table 2 are listed the atomic collision processes of which the data-evaluation and -compilation (including the cross section measurement) are necessary for the beam probe diagnostics. For excitation processes, the most useful data are of electron impact excitation of Li-atoms (process 1) and Ba^{+}-ions(process 7). The data of proton (or deuteron) impact excitation (processes 3 and 9) are also needed for estimating the contribution of the emission by proton impact. These processes might be useful for the proton density measurement with a high energy probing beam. In Fig.2, the effective cross section for proton impact excitation of Li is calcuated with the Gryzinski formula which gives a much larger cross section for the He^{2+} + Li system at low energy than the measured one[43].

Those for H and He may also be useful for the core plasma diagnostics of large scale devices with an H°- or He°-beam.

3.2. Ionization

In the attenuation measurement with a beam of metallic atoms like Al and Ti, multiple ionization by electron impact must be considered. The beam attenuation is related to the sum of partial cross sections $\sum_q \sigma_i^q$, but not the total cross section $\sum_q q\sigma_i^q$. The ambiguity of the cross section ratio for the pair of Li-Al in Fig.11 is caused by the fact that no data exist of the partial cross sections for Al. The data of ionization processes (2) and (4) for H, He and Li are necessary for the estimation of the beam

attenuation and those for Xe, Rb, Cs and Tl would also be useful.

For heavy ion beam probing using electron impact ionization, the Rb^+, Cs^+ and Tl^+ ions have mainly been used. The partial cross sections are needed for the measurements of n_e and T_e, as seen in Sec. 2.3. In the cases in which the beam attenuations of the primary and secondary ion beams must be considered, the data of electron and proton impact ionization of A^+(processes 8 and 10) and A^{q+}(process 13) are necessary. Detachment processes of heavy negative ions like Au^- are also useful.

3.3 Charge transfer

Useful species as the probing beam are H-, He- and Li-atoms. The partial cross sections $\sigma_{ct}(n,l)$ and the total cross section $\Sigma_{nl} \sigma_{ct}(n,l)$ are needed. Collision partners are $H^+(D^+)$, He^{2+}, and multiply charged ions of impurities (B,C, N, O, Al, Si, Ti, Fe, Ni, Mo and so on) which are mainly relatd to the wall material like stainless steel, Inconel, Molybdenum , Aluminum, Carbon, TiC, SiC, TiN, TiB_2 and so on.

The process 11($A^+ + H^+ \rightarrow A^{2+} + H$) might also be useful for proton diagnostics[16]. A heavy ion beam of higher energy must be used for the application to large devices. Then the cross section for process 11 might be comparable to or larger than that for process 8 (electron impact ionization). The total cross sections for charge transfer between the plasma ions and all the species used as the probing beam (processes 5,6 and 11) are necessary for the estimation of the beam attenuation.

4. Concluding Remarks

There are the experimental data for some of the atomic collision processes discussed in this paper. The measurements should be made of the cross sections for the processes, if no experimental data available, including the refinement of the earlier works. The refinement of the theory is also needed, for instance, the formulae of Gryzinski and Lotz. It is requested that the data are not only evaluated but also compiled in the forms which are convenient for the users, for instance, like Fig. 2. The treatment with the Maxwellian velocity distribution for the plasma particles is most useful, although the velocity distribution may not always be Maxwellian.

Acknowledgements

The author would like to thank Prof. J. Fujita, Dr. H. Iguchi and Mr. K. Takasugi for helpful information and useful discussions.

References

1) Equipe TFR: Nucl. Fusion 18 (1978) 647.

2) A.I. Kislyakov and L.I. Krupnik: Sov. J. Plasma Phys. 7 (1981) 478.

3) K. McCormick: Report IPP III/40, Max-Planck-Institut für Plasmaphysik, Garching (1978).

4) K. Kadota, A. Pospieszczyk, P. Bogen and E. Hintz: Report Jül-1812, Institut für Plasmaphysik, KFA Jülich (1982).

5) R.L. Freeman and E.M. Jones: Report CLM-R137, Culham Laboratory, Abingdon (1974).

6) K. Kadota, K. Matsunaga, H. Iguchi, M. Fujiwara and K. Tsuchida and J. Fujita: Jpn. J. Appl. Phys. 21 (1982) L260.

7) K. Kadota, K. Tsuchida, Y. Kawasumi and J. Fujita: Plasma Physics 20 (1978) 1011.

8) D. Leep and A. Gallagher: Phys. Rev. A10 (1974) 1082.

9) J.A. Cobble and J.C. Glowienka: IEEE Trans. Plasma Sci. PS-7 (1979) 147.

10) R.L. Hickok and F.C. Jobes:AFOSR Report TR-72-0018 (1972).

11) J.C. Hosea, F.C. Jobes, R.L. Hickok and A.N. Dellis: Phys. Rev. Lett. 30 (1973) 839.

12) P.L. Colestock, K.A. Connor, R.L. Hickok and R.A. Dandl: Phys. Rev. Lett. 40 (1978) 1717.

13) P.M. Schoch: Report RPDL-83-23, Rensselaer Polytechnic Institute, Troy, New York (1983).

14) R.K. Feeney and D.R. Hertling: ORNL/Sub-7802 (1981).

15) R.E. Reinovsky, W.C. Jennings and R.L. Hickok: Phys. Fluids 16 (1973) 1772.

16) R.E. Reinovsky, J.C. Glowienka, A.E. Seaver, W.C. Jennings and R.L. Hickok: IEEE Trans. Plasma Sci. PS-2 (1974) 250.

17) M. Gryzinski: Phys. Rev. 138 (1965) A336.

18) L.J. Kieffer: Atomic Data 1 (1969) 19.

19) I.P. Zapesochnyi and I.S. Aleksakhin: Sov. Phys. JETP 28 (1969) 41.

20) R. Jalin, R. Hagemann and R. Botter: J. Chem. Phys. 59 (1973) 952.

21) L.L. Shimon, E.I. Nepiipov and I.P. Zapesochnyi: Sov. Phys. Tech. Phys. 20 (1975) 434.

22) W. Lotz: Z. Phys. 216 (1968) 241; 220 (1969) 466.

23) A.I. Hershcovitch, G.M. Gammel and J.W. Davenport: Nucl. Technology/Fusion 2 (1982) 700.

24) K.I.Ishii, T. Kawabe and S. Miyoshi: Proc. Int. Conf. on Plasma Phys., (Nagoya, 1980) p.100.

25) V.V. Afrosimov, E.L. Berezovskii, A.B. Izvozchikov and M.P. Petrov: Sov. J. Plasma Phys. 6 (1980) 133.

26) V.V. Afrosimov, Yu. S. Gordeev, A.N. Zinov'ev and A.A. Korotkov: Sov.J. Plasma Phys. 5 (1979) 551.

27) A.N. Zinov'ev, A.A. Korotkov, E.R. Krzhizhanovskii, V.V. Afrosimov and Yu. S. Gordeev: JETP Lett. 32 (1980) 539.

28) R.J. Fonck, M. Finkenthal, R.J. Goldston, D.L. Herndon, R.A. Hulse, R. Kaita and D.D. Meyerhofer: Phys. Rev. Lett. 49 (1982) 737.

29) T.A. Green, E.J. Shipsey and J.C. Browne: Phys. Rev. A23 (1981) 546.

30) A. Salop: J. Phys. B12 (1979) 919.

31) H. Ryufuku and T. Watanabe: Phys. Rev. A18 (1978) 2005.

32) H. Winter: Comments At. Mol. Phys. 12 (1982) 165.

33) W.P. West, E.S. Ensberg and K.H. Burrell: Bull. Am. Phys. Soc. 25 (1980) 697.

34) W. Grüebler, P.A. Schmelzbach, V. König and P. Marmier: Helv. Phys. Acta 43 (1970) 254.

35) W. Fritsch and C.D. Lin: J. Phys. B16 (1983) 1595.

36) K. Kadota, D. Dijkkamp, R.L. van der Woude, A. de Boer, Pan Guang Yan and F.J. de Heer: J. Phys. B15 (1982) 3275; Phys. Lett. 88A (1982) 135.

37) D. Dijkkamp, R.L. van der Woude, F.J. de Heer, A.G. Drentje, A. Brazuk and H. Winter: Abstracts of 13th Int. Conf. on the Physics of Electronic and Atomic Collisions, (Berlin, 1983) p.551.

38) TFR Group: Report EUR-CEA-FC-957, CEN Fontenay-aux-Roses (1978).

39) Equipe TFR: Nucl. Fusion 19 (1979) 1261.

40) H.P. Eubank, P. Noll and F. Tappert: Nucl. Fusion 5 (1965) 68.

41) V.V. Afrosimov, B.A. Ivanov, A.I. Kislyakov and M.P. Petrov: Sov. Phys. Tech. Phys. 11 (1966) 63.

42) V.V. Afrosimov, E.L. Berezovskii, A.I. Kislyakov, A.V. Khudoleev and S.G. Shchemelinin: Sov. J. Plasma Phys. 5 (1979) 423.

43) K. Kadota, D. Dijkkamp, R.L. van der Woude, Pan Guang Yan and F.J. de Heer: J. Phys. B15 (1982) 3297.

44) K.J. Nygaard: IEEE Trans. Plasma Sci. PS-5 (1977) 106.

45) K. Matsunaga, K. Kadota, M. Fujiwara and J. Fujita: Jpn. J. Appl. Phys. 20 (1981) L713.

46) K. McCormick, M. Kick and J. Olivain: Proc. 8th Europ. Conf. on Controlled Fusion and Plasma Physics (Prague, 1977) p.140.

47) K. Tsukuda, N. Aoki, Y. Itoh, S. Goto, M. Nunogaki and T. Ishimura: J. High Temp. Soc. 9 (1983) 141. (in Japanese)

48) R.J. Goldston: Phys. Fluids 21 (1978) 2346.

49) S. Masamune, M. Fukao and H. Nishihara: J. Phys. Soc. Jpn. 50 (1981) 2426.

50) E.V. Aleksandrov, V.V. Afrosimov, E.L. Berezovskii, A.B. Izvozchikov, V.I. Marasev, A.I. Kislyakov, E.A. Mikahailov, M.L. Petrov and G.V. Roslyakov: JETP Lett. 29 (1979) 1.

51) R.J. Fonck, R.J. Goldston, R. Kaita and D.E. Post: Report PPPL-1954, Plasma Physics Laboratory, Princeton University (1982).

52) M.G. Wickham, N.H. Lazar and N. Rynn: Bull. Am. Phys. Soc. 27 (1982) 1053.

53) J.F. Baur, W.P. West and E.S. Ensberg: Bull. Am. Phys. Soc. 25 (1980) 684.

54) N.J. Wiegart, U. Rebhan and H.-J. Kunze:Phys. Lett. 90A (1982) 190.

55) U. Rebhan, N.J. Wiegart and H. -J. Kunze: Phys. Lett. 85A (1981) 228.

56) K. Kawasaki, T. Usui and T. Oda: J. Phys. Soc. Jpn. 51 (1982) 3666.

Table 1. Useful atomic processes in the beam probing.

Atomic processes	Physical quantities observed	Plasma parameters obtained	References
$A + e \rightarrow A^* + e$	Intensity of the photons emitted from the excited particles	n_e, T_e	4, 6, 7, 9, 44
$A^+ + e \rightarrow A^{+*} + e$	Zeeman splitting or polarization, or Stark broadening of the emission	$\vec{B}$	9, 23+, 45, 46 47
$A + e \rightarrow A^{q+} + (q+1)e$	Attenuation of the probing beams; Intensity of the produced ions	n_e, T_e	4, 6 10, 13, 15, 16
$A^+ + e \rightarrow A^{q+} + qe$	Energy change of the produced ions	ϕ	10 - 13, 23
	Trajectry of the produced ions	$\vec{B}$,	10, 48, 49
$A + H^+ \rightarrow A^+ + H(n,l)$	Attenuation of the probing beam; Intensity of the hydrogen atoms or the photons emitted from the excited hydrogen atoms	n_i	38 -42 25
	Energy spectrum of the hydrogen atoms; Doppler broadening of the emission	T_i	25 23
$A + H^+ \rightarrow A + H^+$	Energy distribution of the scattered probing atoms	T_i	50
$A + I^{Z+} \rightarrow A^+ + I^{(Z-1)+}(n,l)$	Intensity of the photons emitted from the excited impurity ions	n_z	26 - 28, 32, 33
	Doppler broadenning of the emission	T_z	51
	Attenuation of the probing beam	Z_{eff}	38, 39
$A^- + e(H^+) \rightarrow A^+$	Energy change of the secondary ions	ϕ	24
$A + h\nu \rightarrow A^*$	Zeeman splitting or polarization, or stark shift caused by internal magnetic fields	$\vec{B}$	52, 53 54
$A^+ + h\nu \rightarrow A^{+*}$	Satellite lines or forbidden lines caused by fluctuating electric fields	$\vec{E}$	55, 56
($h\nu$: laser light)	Doppler shift caused by plasma potential (with techniques of laser spectroscopy)	ϕ	52

(+: In the case of Ref. 23, proton impact excitation of Xe-atoms is used.)

Table 2. Collision processes of which the data-evaluation and - compilation are necessary for the beam probe diagnostics.

	Collision processes		Collision energy range
(1)	$A + e$	$\rightarrow A^* + e$	$E_e \lesssim 100$ keV
(2)		$\rightarrow A^{q+} + (q+1)e$	
(3)	$A + H^+(D^+)$	$\rightarrow A^* + H^+$	$E_p \lesssim 100$ keV
(4)		$\rightarrow A^+ + H^+ + e$	
(5)		$\rightarrow A^+ + H(n,l)$	
(6)	$A + I^{z+}$	$\rightarrow A^+ + I^{(z-1)+}(n,l)$	$v_r \lesssim 3 \times 10^8$ cm/sec
(7)	$A^+ + e$	$\rightarrow A^{+*} + e$	
(8)		$\rightarrow A^{q+} + qe$	
(9)	$A^+ + H^+(D^+)$	$\rightarrow A^{+*} + H^+$	
(10)		$\rightarrow A^{2+} + H^+ + e$	
(11)		$\rightarrow A^{2+} + H$	
(12)	$A^- + e(H^+)$	$\rightarrow A, A^+$	
(13)	$A^{q+} + e(H^+)$	$\rightarrow A^{(q+p)+}$	

A : H, He, Li, Al, Ti, Xe, (C, K, Rb, Cs, Tl)
A^+ : Rb^+, Cs^+, Ba^+, Tl^+, (K^+, Xe^+)
A^- : Au^-
I : He, C, O, Al, Ti, Fe, (B, N, Si, Ni, Mo)

(E_e : electron energy, E_p : proton energy, v_r : relative velocity)

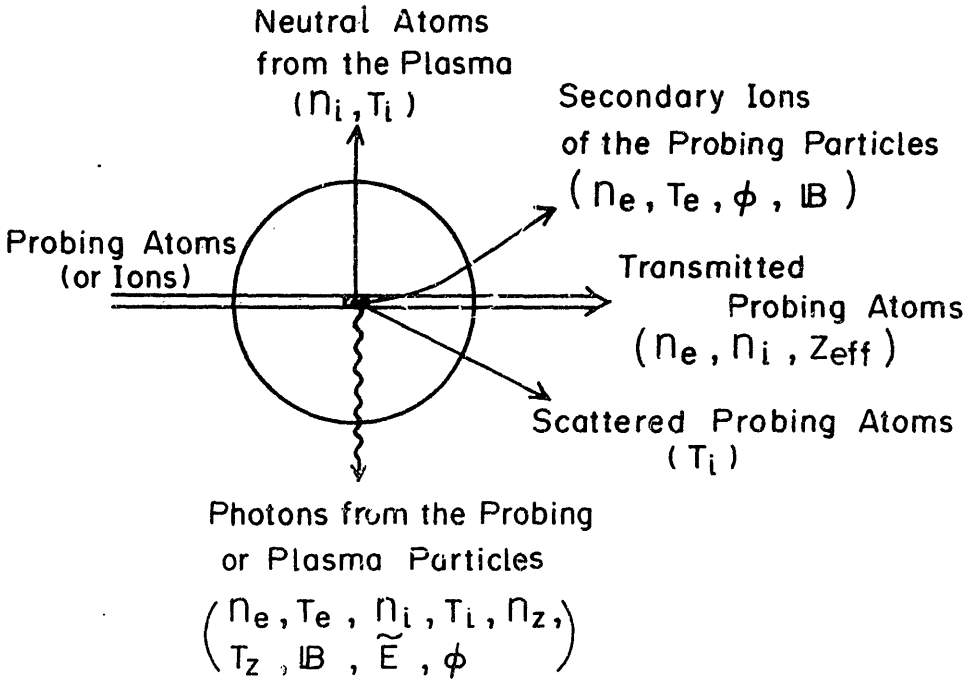

Fig. 1 Schematic representation of beam probe diagnostics.

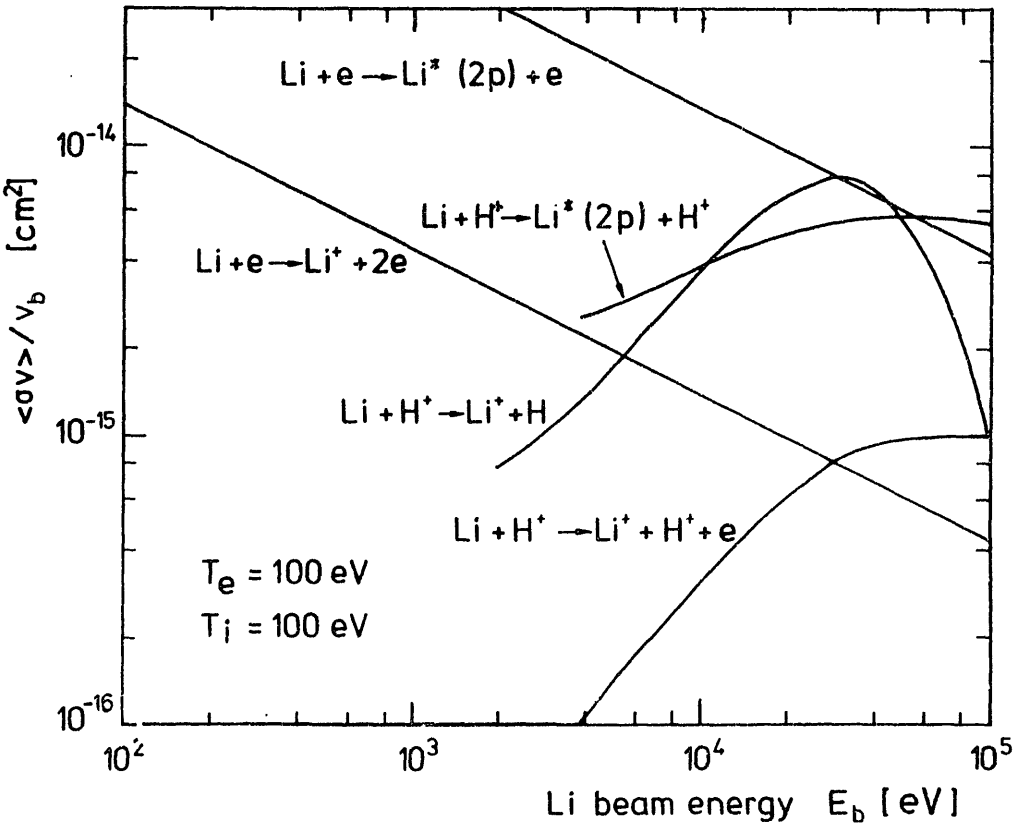

Fig. 2 Effective cross sections for various collision processes between the Li°-beam and the hydrogen plasma particles as a function of Li°-beam energy.

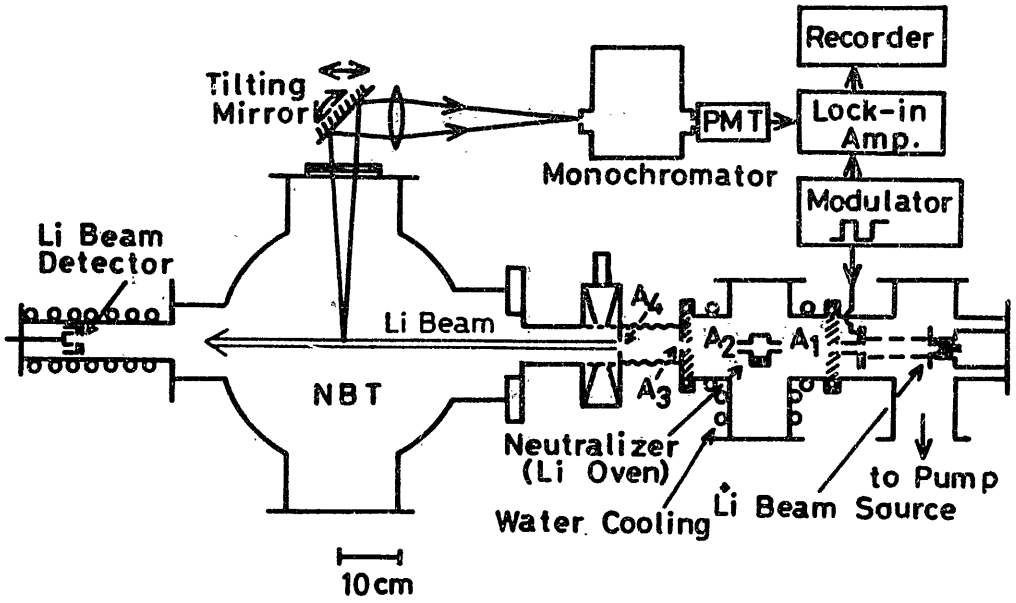

Fig. 3 Schematic diagram of the experimental setup for the electron density measurement by Li°-beam probe spectroscopy in NBT. (Ref. 6)

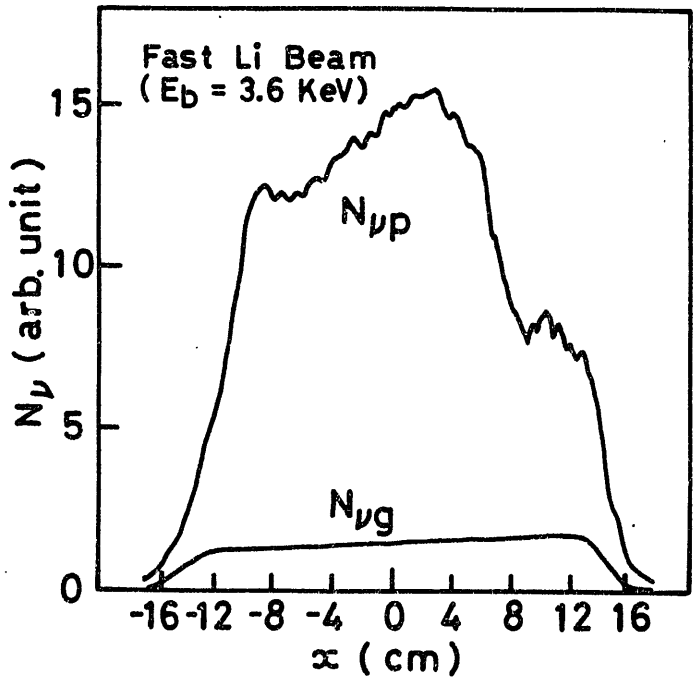

Fig. 4 Radial profiles of $N_{\nu p}$ and $N_{\nu g}$ which are the intensities of the resonance line emitted from the excited Li -atoms produced by collisions with plasma electrons and hydrogen molecules, respectively, in NBT. $N_{\nu g}$ was measured without the plasma. (Ref.6)

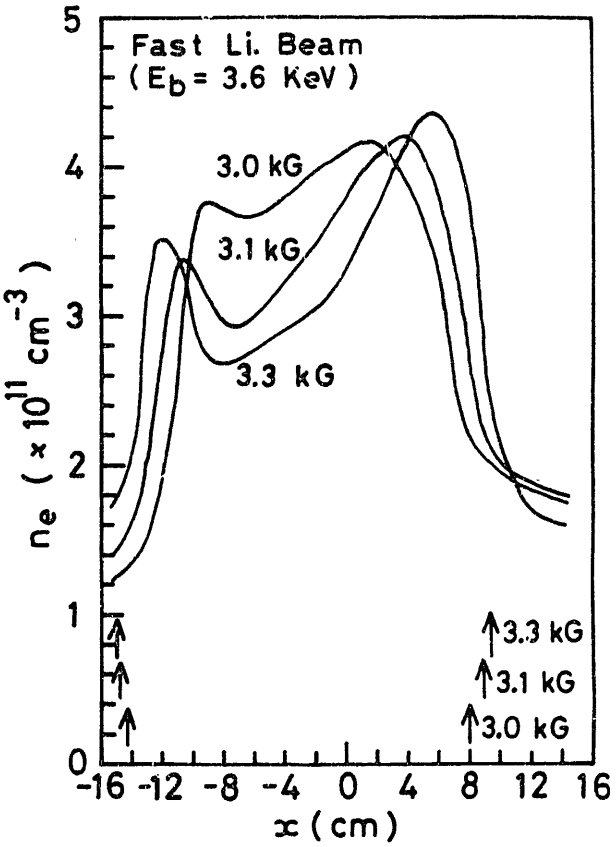

Fig. 5 Radial profiles of electron density by Li°-beam probe spectroscopy in NBT. Arrows indicate the positions of the hct electron ring produced by ECRH. (Ref. 6)

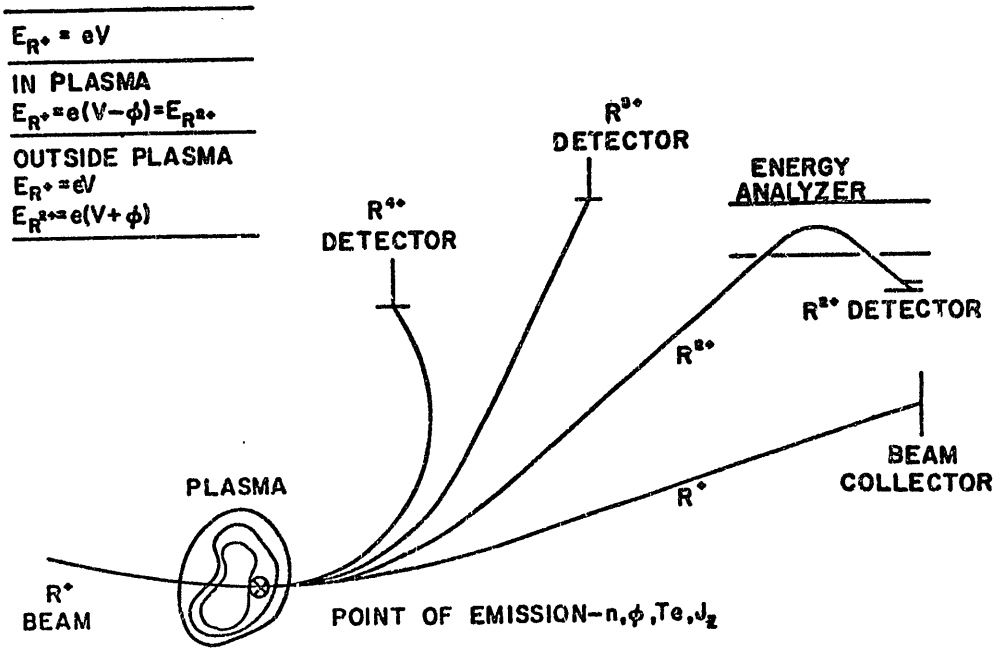

Fig. 6 Illustration of the principle of ion beam probing. (Ref. 10)

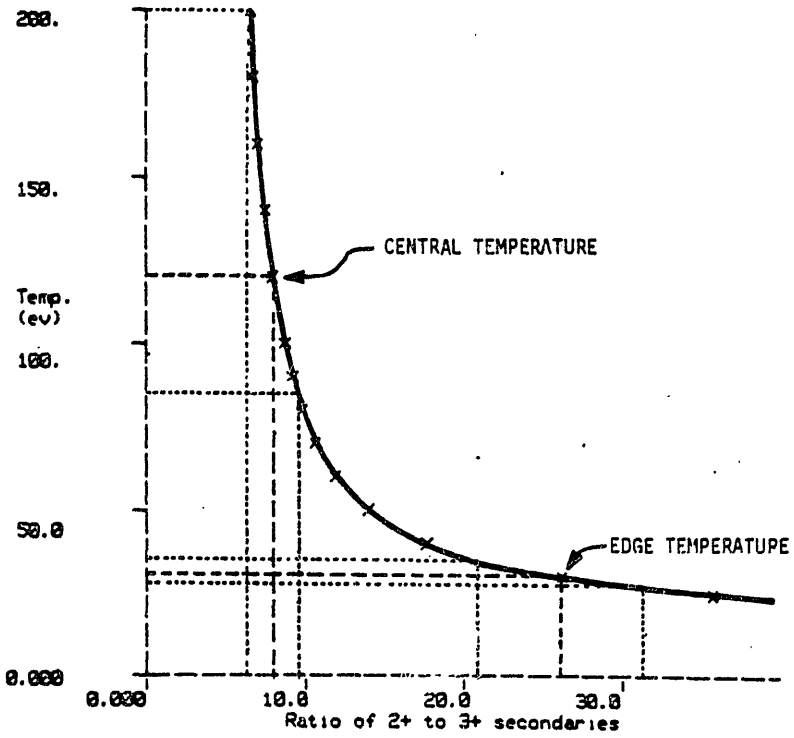

Fig. 7 Ratio of the effective cross section for the Cs^{2+} ion production by electron impact ionization of the Cs^{+} ions to that for Cs^{3+}, v.s. electron temperature. (Ref. 13)

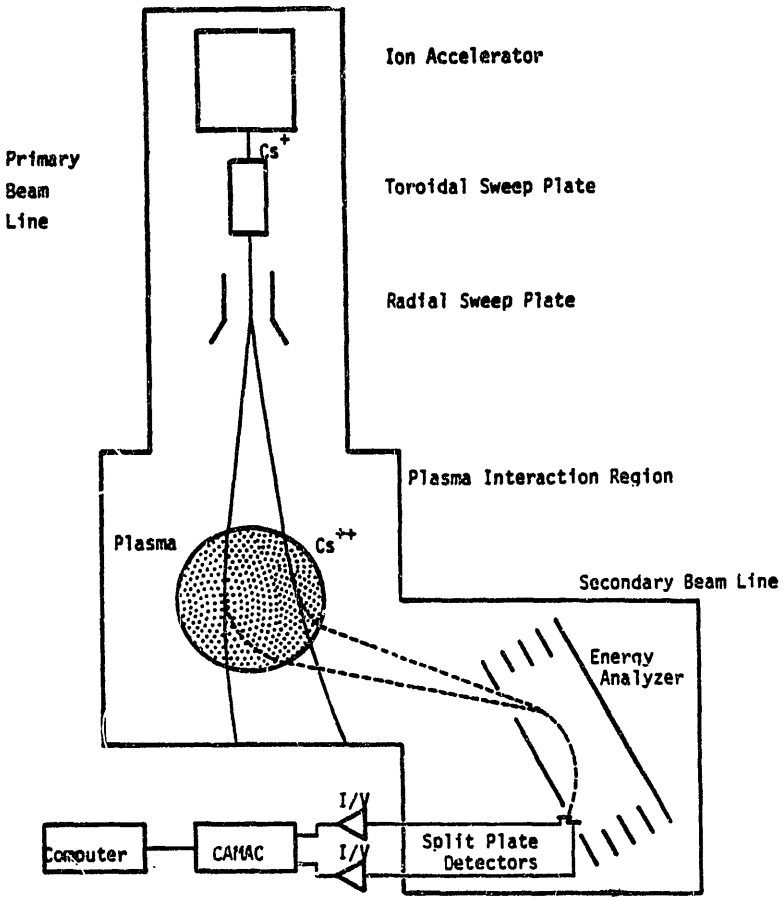

Fig. 8 Schematic arrangement of the apparatus for the measurements of plasma potential, electron temperature and electron density by Cs^+-ion beam probing in the RENTOR tokamak. (Ref. 13)

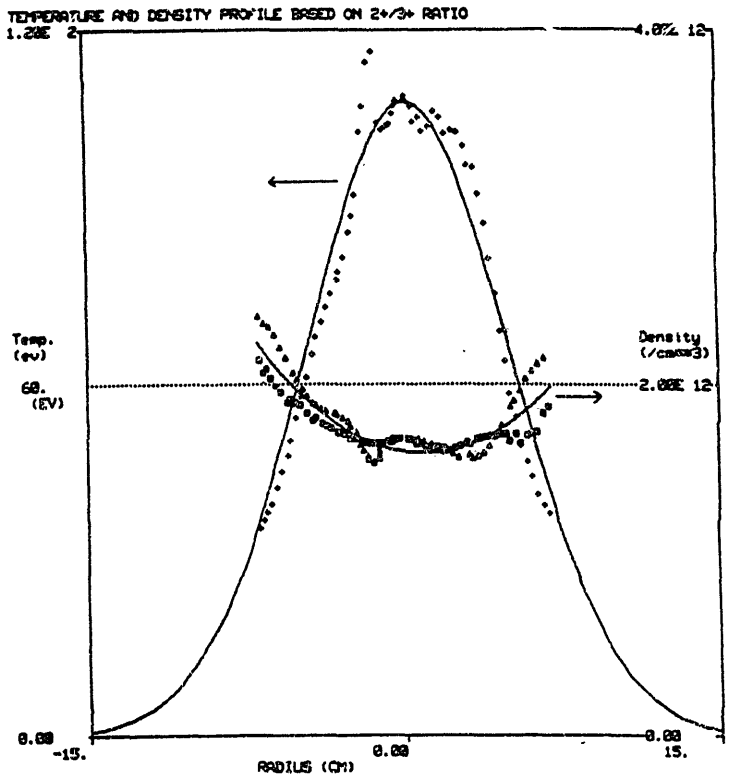

Fig. 9 Radial profiles of electron temperature and density by Cs^+ -ion beam probing in the RENTOR tokamak. (Ref. 13)

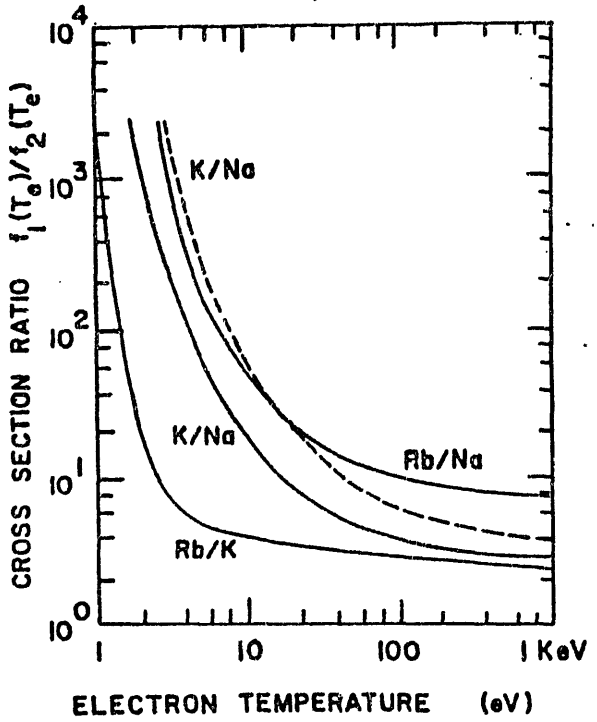

Fig. 10 Ratios of the effective cross sections for electron impact ionizatin (1+ → 2+) on various ion pairs as a function of electron temperature. Solid curves are calculated with the Gryzinski formula and dashed curve with the experimental data. (Ref. 16)

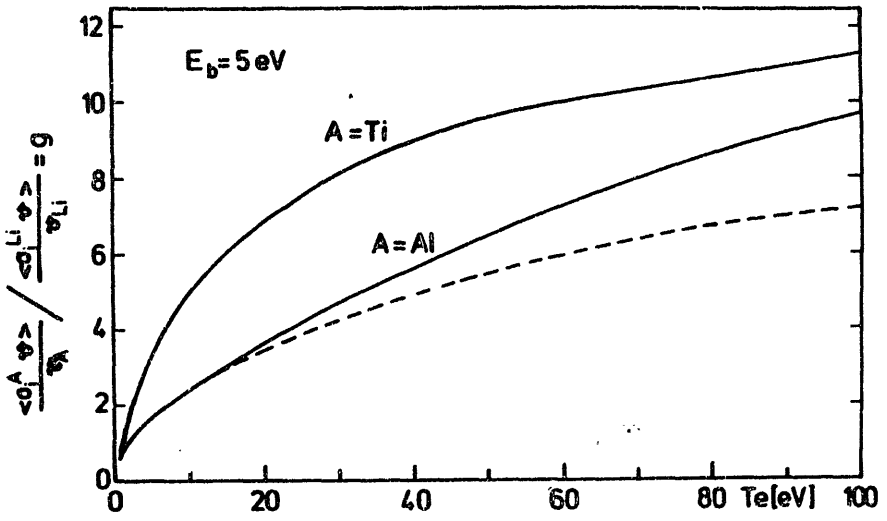

Fig. 11 Ratios of the effective cross sections for electron impact ionization ($0 \rightarrow 1+$) on Li-Al and Li-Ti as a function of electron temperature. Dashed curve for Li-Al indicates the ambiguity of the ratio. (Ref. 4)

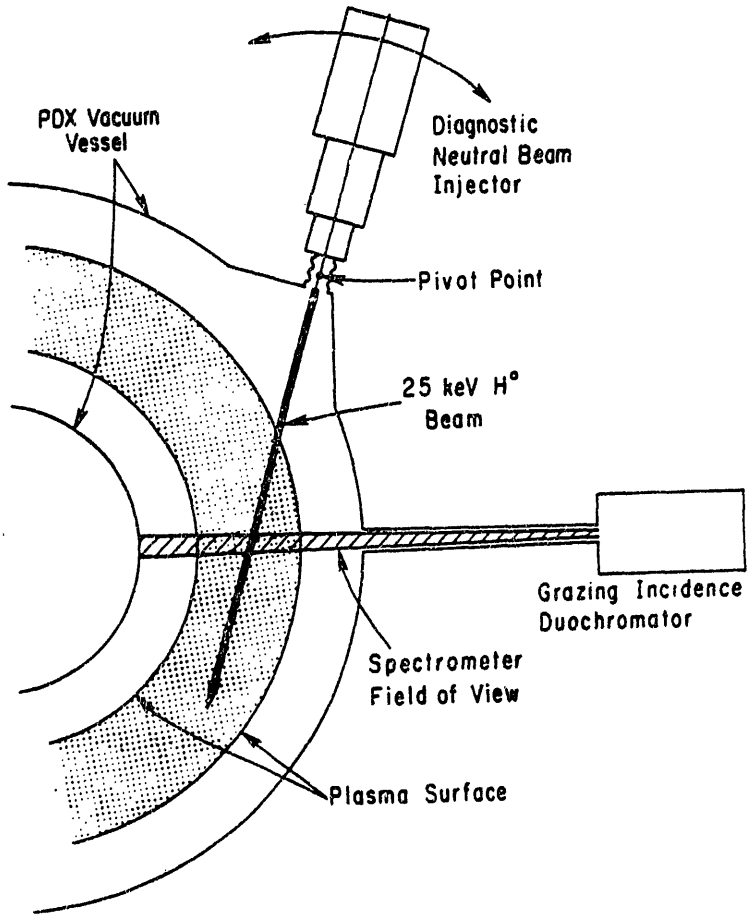

Fig. 12 Schematic diagram of the experimental setup for density measurements of the C^{6+}- and O^{8+}-ions by H°-beam probe spectroscopy in the PDX tokamak. (Ref. 28)

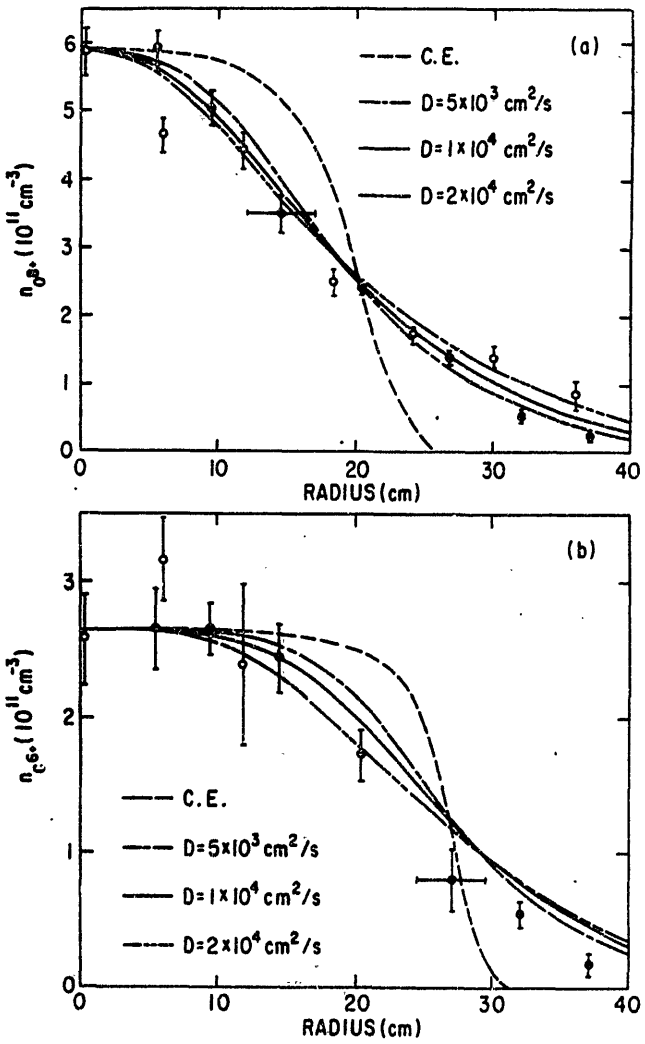

Fig. 13 Radial profiles of the C^{6+}- and O^{8+}-ion densities by H°-beam probe spectroscopy in the PDX tokamak. Various curves are the calculations (C.E.: corona equilibrium and D: diffusion coefficient). (Ref. 28)

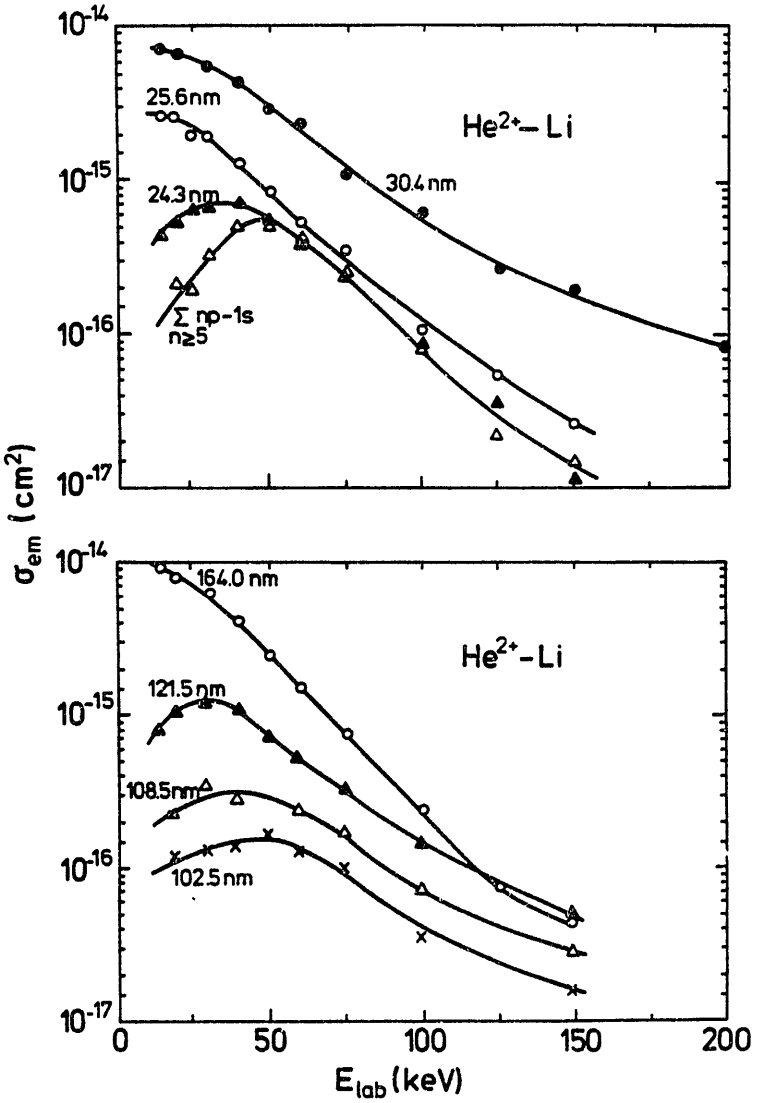

Fig. 14 Emission cross sections for the Lyman and Balmer series which are produced by the process $He^{2+} + Li \rightarrow He^{+}(n,l) + Li^{+}$ as a function of He^{2+} energy. (Ref. 36)

The effect of excitation anisotropy in the laser-induced fluorescence spectroscopy of plasmas

Takashi Fujimoto

Department of Engineering Science, Kyoto University, Kyoto 606 Japan

Abstract

The importance of the effect of alignment in the upper-level population and its collisional or radiative relaxation on the laser-induced fluorescence spectroscopy is pointed out. A method to take into account of the effect is presented.

The laser-induced-fluorescence spectroscopy (LIFS) method is a "potentially" powerful tool for plasma diagnostics as well as for study of atomic parameters like collisional and radiative transition rate coefficients for atomic and ionic species. However, there seems to be points that are important but draw little attention or even unrecognized yet.[1)] One of these problems is the effect of excitation anisotropy and its collisional and radiative relaxation.

In many LIFS experiments our prime concern is the population density of excited levels, and this is derived from the observed fluorescence. Suppose, for example, the determination of collitional excitation transfer rates for (3^1P or 3^1D) + 1^1S $\longrightarrow$ (3^3D + 1^1S) of helium by a pulsed LIFS experiment. Figure 1 shows the temporal changes in the population densities of the levels concerned as derived from the observed fluorescence intensities. (It is noted that this transfer process violates Wigner's spin conservation rule.) In the following we investigate how the excitation anisotropy and its relaxation manifest themselves in this kind of experiment.

In the above example the laser excites the transition $2^1S(J=0) \longrightarrow 3^1P(J=1)$, where J is the total angular momentum. (For helium as well as for neon and argon that are considered later, the nuclear magnetic moment is 0, and we need not take into account the hyper-fine structure.) Suppose we excite this transition with a linearly polarized light with the polarization direction angle θ to the direction of observation. (Fig. 2(a)) In the case of $\theta = 0$ or the π-light excitation (we take the quantization axis in the z-direction) only the Zeeman sublevel of $m_J = 0$ is populated, (Fig. 2(b)) where m_J stands for the projec-

tion of J onto the quantization axis. Then, this level emits only the π-polarized light for the same transition. This light is polarized in the θ-direction in the polar coordinate system and has a spatial intensity distribution according to $\sin^2\theta$. Thus, we don't observe any fluorescence even if we have the population in the upper level. If this level had another transition the lower level of which had the angular momentum J = 1, then we could observe the two σ-component transitions $m_J=0 \longrightarrow m_J=\pm 1$. (Fig. 2(c)) Thus, in this example if we were interested in the upper-level population we would derive <u>different</u> population densites for the same upper level. An example of this situation is shown in Fig. 3: a 5 ns laser pulse excites the transition 6164 A ($1s_3(J=0) \longrightarrow 2p_2(J=1)$) of neon in a mild glow discharge (pressure of 2 torr and current of 0.6 mA), and the fluorescent light of 6164 A($J=1 \longrightarrow J=0$) and 6599 A ($2p_2(J=1) \longrightarrow 1s_2(J=1)$) are observed. The above excitation scheme is indicated by "0°" in the figure. Actually the 6164 A fluorescence is hardly seen, but the 6599 A is intense. If we derive the "branching ratio" of the transition probabilities of these two lines, we would have an extremely large value. Figure 4 shows the result: the open circles correspond to the present case.

On the contrary, if the angle θ is π/2 the excited sublevels are coherent superposition of $m_J = \pm 1$ and we observe σ transitions for both the lines, 6164 A and 6599 A in the above example. The "branching ratio" in this case is indicated by the closed dircles in Fig. 4; in this case, it is smaller than the correct value by more than a factor of 2.

Thus, if we overlook the effect of excitation anisotropy we would have a variety of the "branching ratios", or in other

words, a variety of the population densities of the upper level depending on the observed line, the geometry of experiment, the angle θ and the sensitivity distribution of our detection system over the polarization directions of the observed light.

Figure 4 shows that with an increase in the filling pressure both the "branching ratios" for "0°" and "90°" tends to the correct value of 1.61. This is the result of the collisional relaxation of alignment, or the collisional excitation transfer among the Zeeman sublevels: In the case of the 0°-excitation the initial population in the m_J=0 level is collisionally transferred to the m_J=±1 levels resulting in the σ-lights. The small signal of 6164 A light in Fig. 3 for 0° corresponds to these σ-lights. We call this process the collisional disalignment, which has a cross section of the order of the geometrical cross section. If the collisional disalignment is sufficiently fast any excitation anisotropy would be destructed fast, and we would have a correct branching ratio or a population density independent of the various factors. Figure 4 suggests that this would be realized at the pressure of 100 torr or more.

One method to solve the problem of the excitation anisotropy is to employ the magic-angle excitation: in the above example, we take $\theta = 55°$. In this case, however, the fluorescent light is still polarized, and unless our detection system has the isotropic sensitivity distribution for any polarization direction, we would still have a problem. This situation is shown in Fig.5: The magic-angle excitation is applied to the 6164 A transition, and the same transition is observed with the detection system that is sensitive only to the polarization to the x-direction. If a magnetic field is applied to the direction of observation

the produced anisotropy or the dipole precesses around the magnetic field, and we have the sinusoidal oscillation on the observed signal. If the magnetic field is sufficiently strong, or 30 gauss in Fig. 5, the precession becomes too fast to be followed by our detection system having the time constant of ≃5 ns. Then, the sensitivity distribution of our detection system becomes effectively isotropic, and the observed fluorescence becomes directly proportional to the upper-level population. The signal intensities with "55°" in Fig. 3 and the triangles in Fig. 4 are the result of this method and give the correct branching ratio independent of the pressure. Thus, we have arrived at the method to obtain, without ambiguity, the upper-level population from the observed fluorescence.[2-4)]

The relative population densities in Fig. 1 are obtained by the above method. By adjusting the excitation transfer rates for $3^1P \rightarrow 3^3D$ and for $3^1D \rightarrow 3^3D$ we fitted our calculation to the observed 3^3D population using the observed 3^1P and 3^1D populations. The solid curve is the result of the fit, and Fig. 6 shows the pressure dependence of these rates. The slopes give the transfer rate coefficients or the cross sections; these are $(1.4 \pm 0.11) \times 10^{-18}$ cm^2 for $3^1P \rightarrow 3^3D$, and $(1.25 \pm 0.26) \times 10^{-17}$ cm^2 for $3^1D \rightarrow 3^3D$.[5)]

By applying the above method we obtained the natural lifetime for the ten neon $2p_j(2p^5 3p)$ levels;[3)] the result was consistent with the delayed-coincidence experiment except for $2p_8$ and $2p_{10}$. The depopulation collision rate coerricient was also determined for these levels,[4)] and we found that the depopulation is accounted for by the sum of the excitation transfer collisions among the $2p_j$ levels except for the $2p_{10}$ level. This is in contradiction

to the conclusion by Chang and Setser,[7] who did not take into account the effect of excitation anisotropy in their LIFS experiment.

The lifetimes of excited argon, though it is the most extensively studied so far, have been in dispute for many years.[8] For instance, the recent experiment by Erman and Huldt[9] by the high-frequency electron beam excitation gives smaller lifetime values for $2p_j$ ($3p^5 4p$) levels than the foregoing experiments, sometimes by more than a factor of 2. We employed the above method for the determination of the argon $2p_4$ level lifetime and obtained good agreement with the earlier delayed coincidence experiments rather than with ref. 9. We conjecture that, in Erman and Huldt's experiment, the heavy radiation trapping not only affected the decay of the upper-level population but also relaxed the alignment initially produced by the electron-collision excitation in the upper-level population. Thus, the directly observed decay of the emission-line intensity was different from the decay of the upper-level population. The fact that their results for $2p_1$ and $2p_5$ agree with other experiments appears to support our conjecture, since these levels have $J = 0$ and thus are free of the alignment problem. We assumed that the alignment relaxation in their experiment was brought about not by atomic collisions but by the trapped ratiations; this is the complementary process to the coherence narrowing in the Hanle effect experiment.

Using the neon 6164 A ($1s_3 - 2p_2$) transition we actually observed alignment relaxation by trapped radiations, and its rate was interpreted quantitatively by the theory of coherence narrowing.[10]

References

1) D. D. Burgess, V. P. Myerscough, C. H. Skinner and J. M. Ward: J. Phys. B 13 (1980) 1675.

2) T. Fujimoto, C. Goto and K. Fukuda: Opt. Comm. 40 (1981) 23.

3) T. Fujimoto, C, Goto and K. Fukuda: Physica Scripta 26 (1982) 443.

4) T. Fujimoto, C. Goto, Y. Uetani and K. Fukuda: J. Phys. Soc. Japan (to be submitted).

5) T. Fujimoto and K. Fukuda: J. Phys. Soc. Japan 50 (1981) 3476.

6) T. Fujimoto, C. Goto and K. Fukuda: J. Phys. Soc. Japan (to be submitted).

7) R. S. F. Chang and D. W. Setser: J. Chem. Phys. 72 (1980) 4099.

8) W. L. Wiese: "The Physics of Ionized Gases" (Invited Lectures, Review Reports and Progress Reports of SPIG-82), ed., G. Pichler (Institute of Physics of the University Zagreb, Yugoslavia) p. 435.

9) P. Erman and S. Huldt: Physica Scripta 17 (1978) 473.

10) T. Fujimoto, C. Goto, Y. Uetani and K. Fukuda: Physica Scripta (submitted).

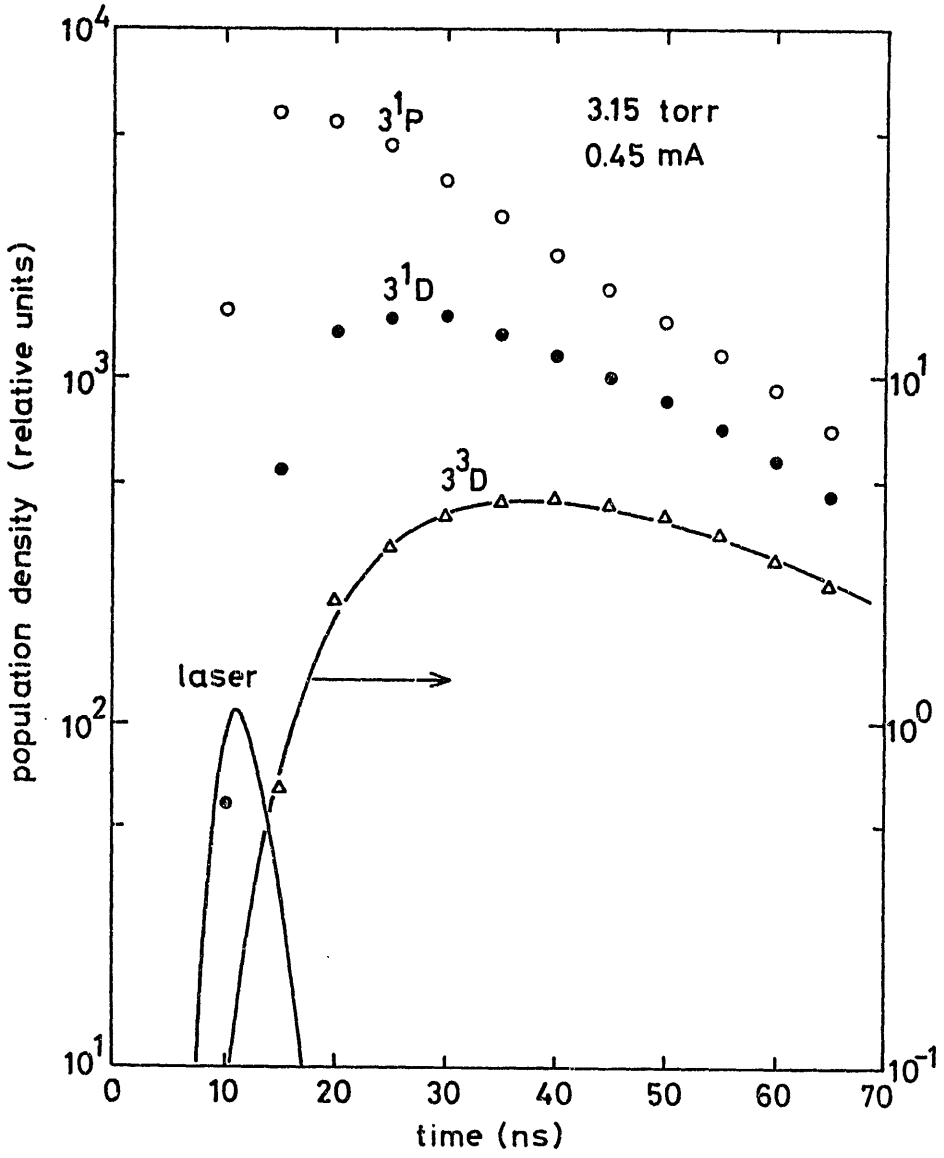

Fig. 1. Population perturbations accompanying the magic-angle excitation of 5016 A (2^1S - 3^1P) with a magnetic field of 39 gauss is applied in the direction of observation. The solid cureve is the result of fitting.

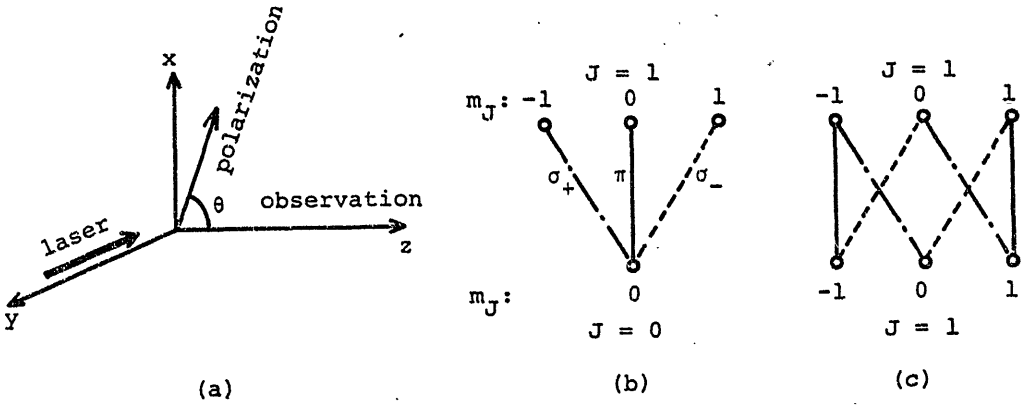

Fig. 2. (a), Geometry of excitation and observation. The laser light is polarized linearly in the direction having the angle θ to the direction of observation. (b), The Kastler diagram for the transition J=0 - J=1. (c), J=1 - J=1.

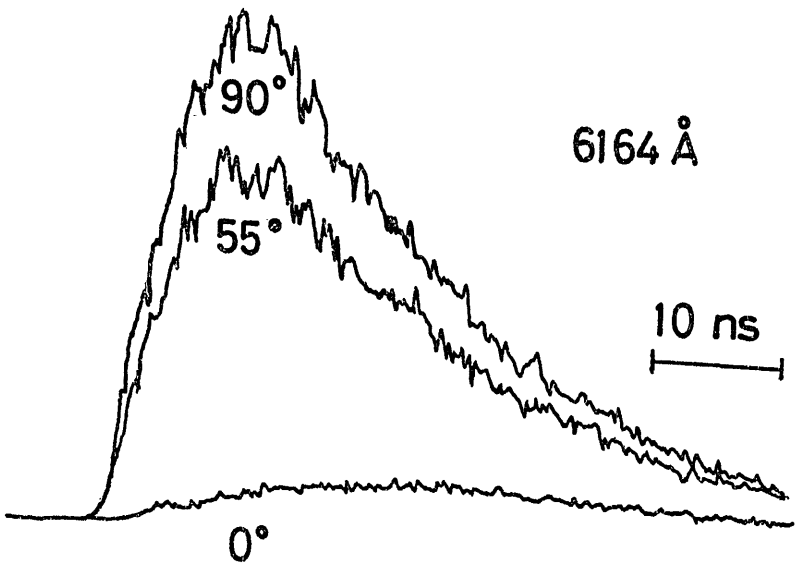

(a)

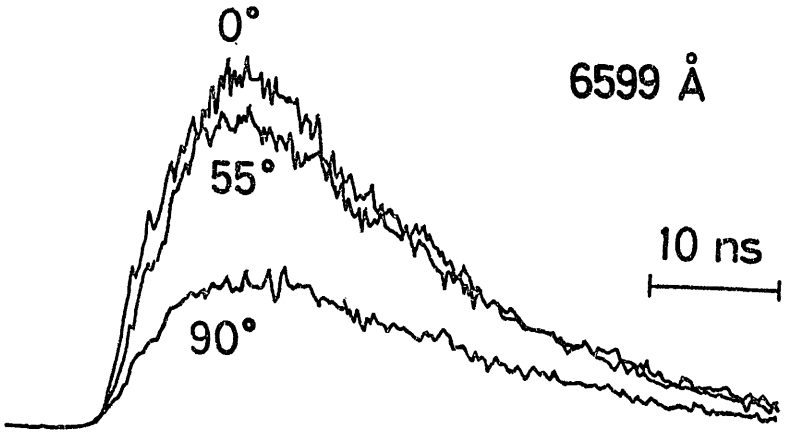

(b)

Fig. 3. The dependence of fluorescence intensities on the angle of excitation θ.

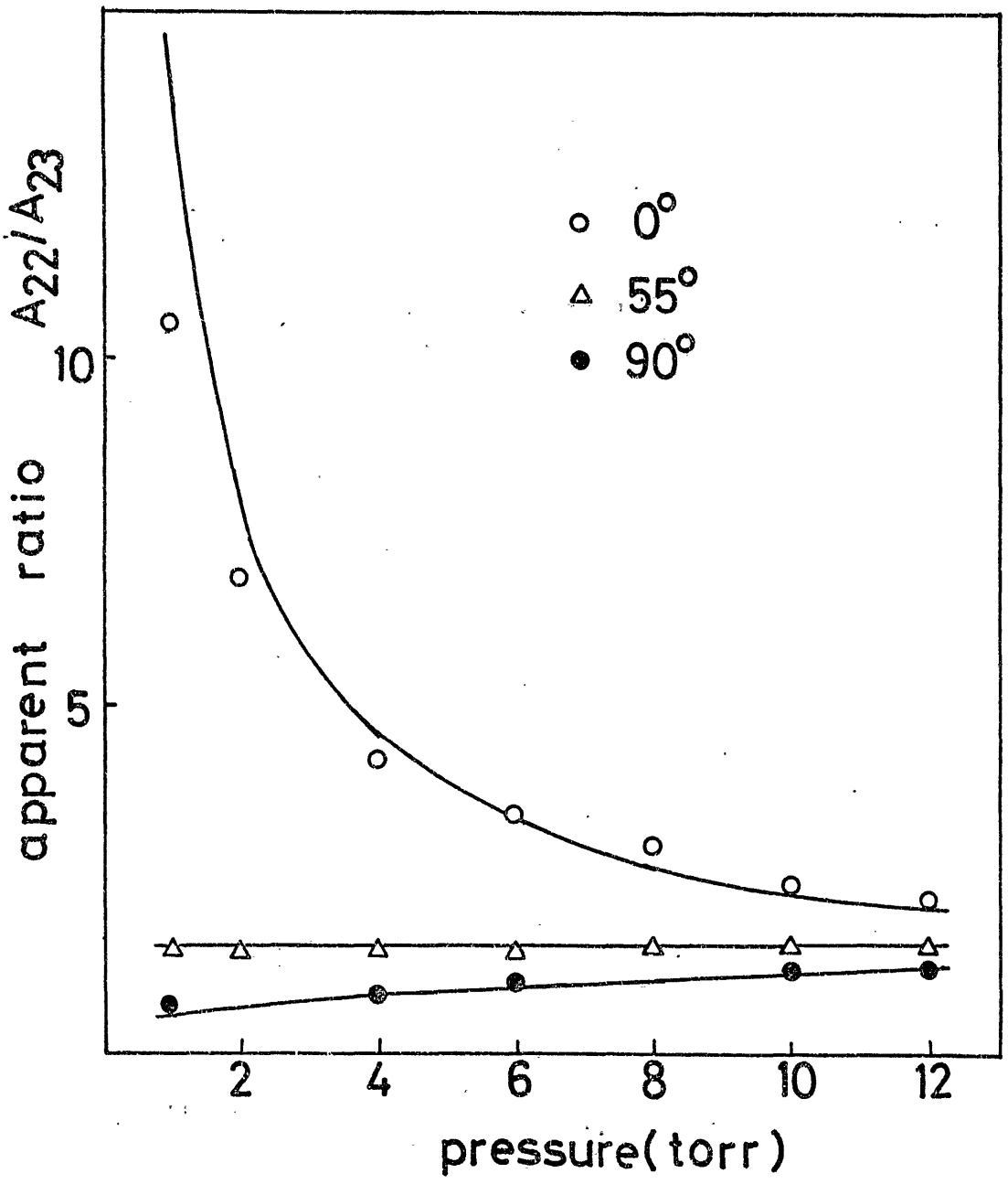

Fig. 4. The apparent "branching ratio" depending on the angle of excitation θ and as a function of pressure. The fluorescence intensity has been determined 25 ns after the onset of the signal in Fig. 3. The cureves are the prediction from the determined rate coefficient for collisional disalignment.

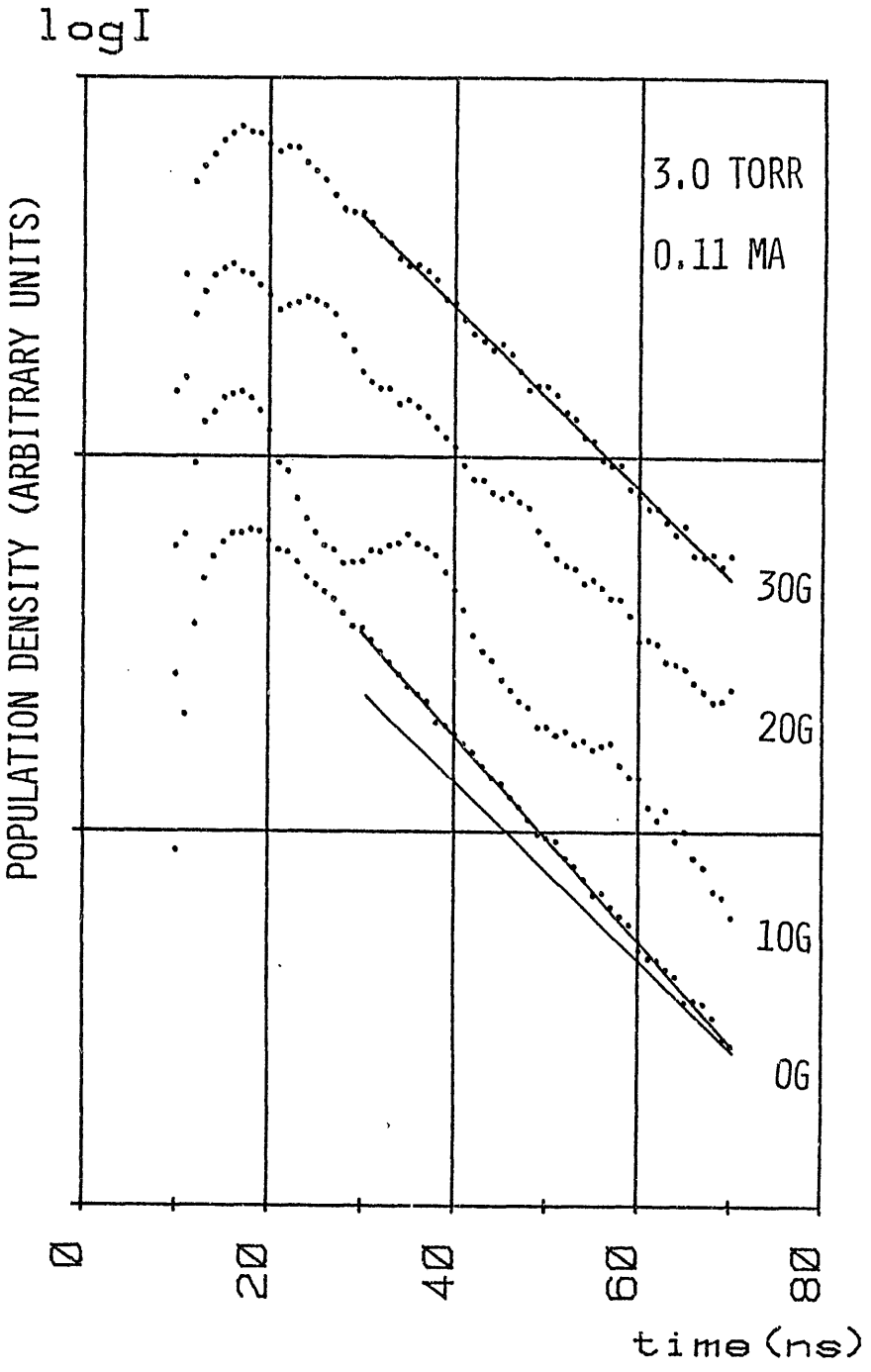

Fig. 5. Observed decay of fluorescence for the magic-angle excitation. The magnetic field is applied. The actual decay of the population is indicated by the slope at the bottom. The fluorescence without the magnetic field gives faster decay.

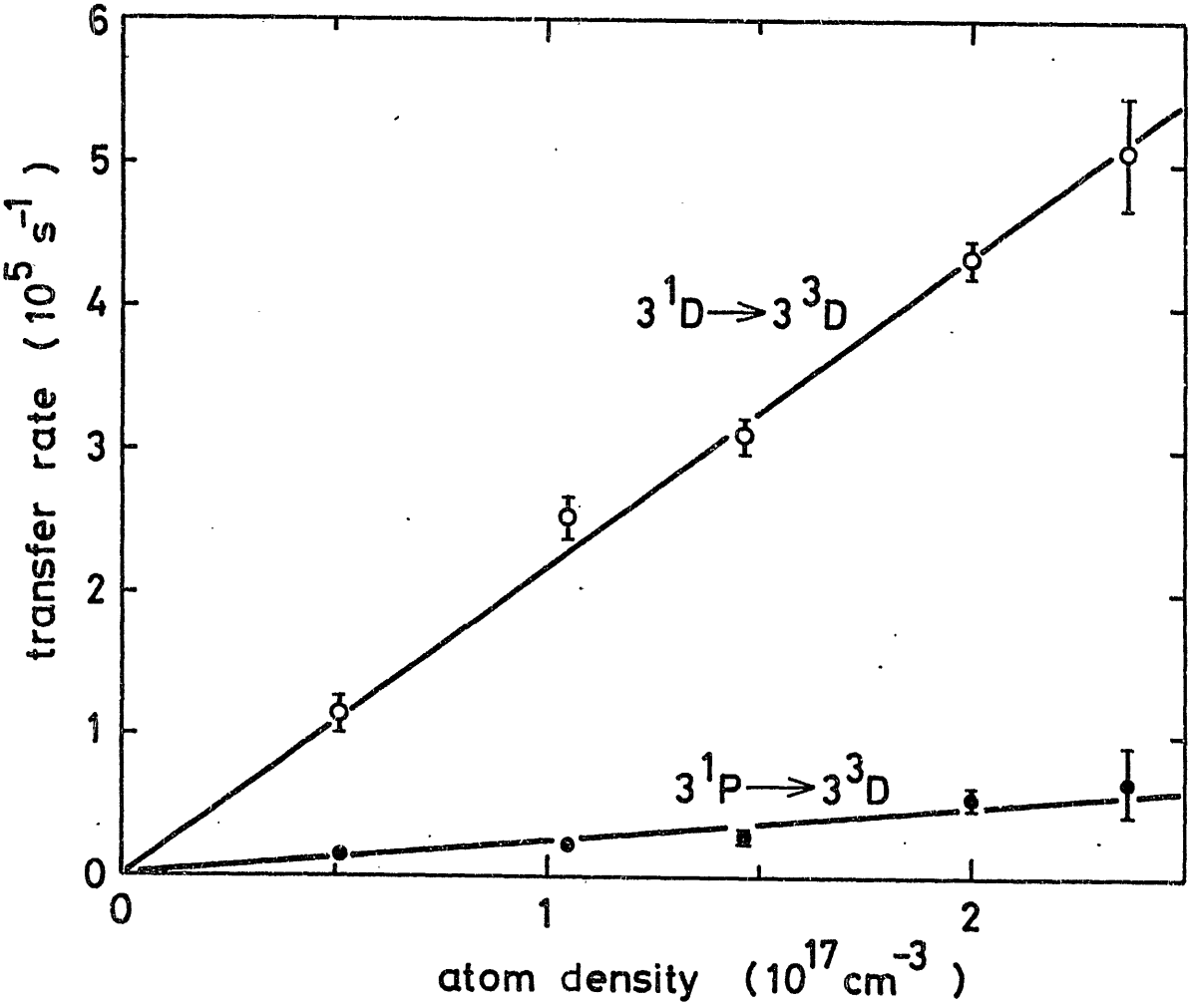

Fig. 6. The pressure dependence of the singlet-triplet excitation transfer rates.

Spectroscopy in Heliotron E

K.Kondo, N.Nishino, K.Magome, T.Mutoh, H.Kaneko, H.Zushi,
O.Motojima, T.Obiki, A.Iiyoshi, K.Uo

Plasma Physics Laboratory, Kyoto University
Uji, Kyoto, Japan

Abstract

Spectroscopic observations in visible and vacuum ultra violet region are presented.

The Doppler broadening measurements in the visible wavelength region are routinely used to estimate ion temperature.

Identification of the spectrum of VUV region is made and some trial to calibrate the sensitivity of the monochromator by using Ti XV emissions is described.

1. Doppler Broadening Measurements

The ion temperature is the most important parameter and the Doppler broadening measurement is easy method to estimate it.

We use a 1.26 m Cerny-Turner type scanning monochromator in the wavelength region above 2000 Å. It equips a vibrating mirror in front of the exit slit in order to scan the spectral line profiles many times during one plasma discharge in the Heliotron E device[1]. The scanning width of the wavelength and frequency of the vibrating mirror are controled by a waveform of a function generator.

The frequency is 50 Hz and scanning speed is 1 Å/msec in our case.

The output signals of a photomultiplier tube are introduced to AD convertor and stored in buffer memory.

After a plasma shot the calculation of the Doppler broadening width by the least square method is made and displayed by a data processing computer. Figure 1 shows a schematic drawing of this system.

An example of the experimental result is shown in Fig. 2. The line is CV 2270 Å. We also show the fitness to the Gaussian curve in Fig. 3. In the initial phase the ion temperature is about 100 eV and rises up about 300 eV by neutral beam injection heating. On the other hand the ion temperature derived by charge exchange fast neutral analyser is 700 eV and higher than the Doppler temperature.

This difference between charge exchange analysis and Doppler broadening is due to that C^{4+} ion radiates near the plasma

boundary. We have a plan to inject titanium into the plasma by laser blow-off technique and we will observe forbidden lines of ions with high ionization potential energies.

2. Vacuum Ultra Violet Spectroscopy

We installed the grazing incidence spectrometer (McPherson 247 V) to investigate impurity species.

The radius of the Rowland circle is 2.2 m. The grooves of the grating are 600 lines per 1 mm. The incidence angle is varied from 82 to 88 degrees. The observable wavelength region is from 10 to 1300 Å. The detectors are chosen either photographic plates or electron multiplier tube with Cu-Be photocathode.

The identification of the spectrum[2,3)]

Fig. 4 shows the spectrum observed in the Heliotron E plasma. The electron and ion temperatures are about 600 eV and the density is 3×10^{13} cm^{-3}. The glass plate (KODAK SWR) is exposed in about 140 shots plasma discharges.

The main components of the spectrum are oxygen, carbon, iron and titanium.

The iron is main component of the vacuum vessel, YUS 170. The titanium is flashed to the surface of the wall to control the recycling of the working gas and reduce the light impurity.

And the line emissions from Ti X to Ti XVI are distributed about 150 Å.

Absolute calibration of the sensitivity

It is necessary to perform an absolute calibration for the monochromator.

The branching ratios method is used widely because it can be made in-situ. The used line pairs are listed in Table 1. But calibrated points are limited, though. Therefore, the inter- and extra-polation should be made over a wide range of wavelength.

We have tried the above calibration by measuring the light intensities of Ti XV.

Titanium is a familiar element existed in the plasma. And in our plasma, lines of Ti XV are distributed around 150 Å. The line intensities of titanium are calculated by Bhatia et al.[4].

We can determine the relative sensitivity from 115 Å to 148 Å by comparing the experimental and calculated intensities as listed in Table 2. The absolute value is determined by matching the data at 150 Å from oxygen O VI.

We present the result of the calibration in Fig.5.

References

(1) K.Uo,A.Iiyoshi,T.Obiki,O.Motojima,S.Morimoto,A.Sasaki, K.Kondo, M.Sato,T.Mutoh,H.Zushi,H.Kaneko,S,Bessho,F.Sano, T.Mizuuchi,S.Sudo, K.Hanatani,M.Nakasuga,I.Ohtake,M.Iima, Y.Nakashima,N.Nishino : "Plasma Physics and Controlled Nuclear Fusion Reseach (Proc.9th Int.Conf.Baltimore) vol.II, 209 (1983).

(2) R.L.Kelly L.J.Palumbo:"Atomic and Ionic Emission Lines Below 2000 Angstroms: Hydrogen Through Krypton " NRL Report 7599,1973 .

(3) R.L.Kelly:"Atomic and Ionic Spectrum Lines Below 2000 Å: H through Ar " ORNL-5922, 1982.

(4) A.K.Bhatia,U.Feldman,G.A.Doshek: J.Appl.Phys. 51, 1464 (1980).

Table 1. Branching line pairs used
in the calibration experiment

	VUV Lines		UV and Visible Lines	
	Wavelength(Å)	Transition Probability ($\times 10^{8}$ s^{-1})	Wavelength(Å)	Transition Probability ($\times 10^{8}$ S^{-1})
O VI	150.09	259	3811.35	0.52
	150.127	259	3834.24	0.52
O V	220.352	453	3144.68	0.97
HeII	243.027	2.045	4685.682	1.438
C IV	312.42	45.7	5801.51	0.319
	312.46	45.5	581242	0.316
O III	320.98	190	3961.59	1.28
O II	515.50	15	4943.06	1.06
	515.64	12	4941.12	0.83
	515.64	2.4	4955.78	0.256
He I	537.0296	5.66	5015.6779	0.1338
H	1025.72	0.588	6562.8	0.441

Table 2. Line intensities from Ti XV

Wave Length (Å)	Conf.	Term	A (sec^{-1})	Relative Intensity
115.02	$2s^2 2p^4$-$2s2p^5$	$^1D_2$-$^1P^0_1$	1.20+11	1.91
134.61	$2s^2 2p^4$-$2s2p^5$	$^3P_2$-$^3P^0_1$	1.93+10	1.16
148.54	$2s^2 2p^4$-$2s2p^5$	$^3P_1$-$^3P^0_2$	8.43+9	1.00
2544.8	$2s^2 2p^4$-$2s^2 2p^4$	$^3P_2$-$^3P_1$	1.25+3	0.12

(A.K.Bhatia J.Appl.Phys. 51, 1464, 1980)

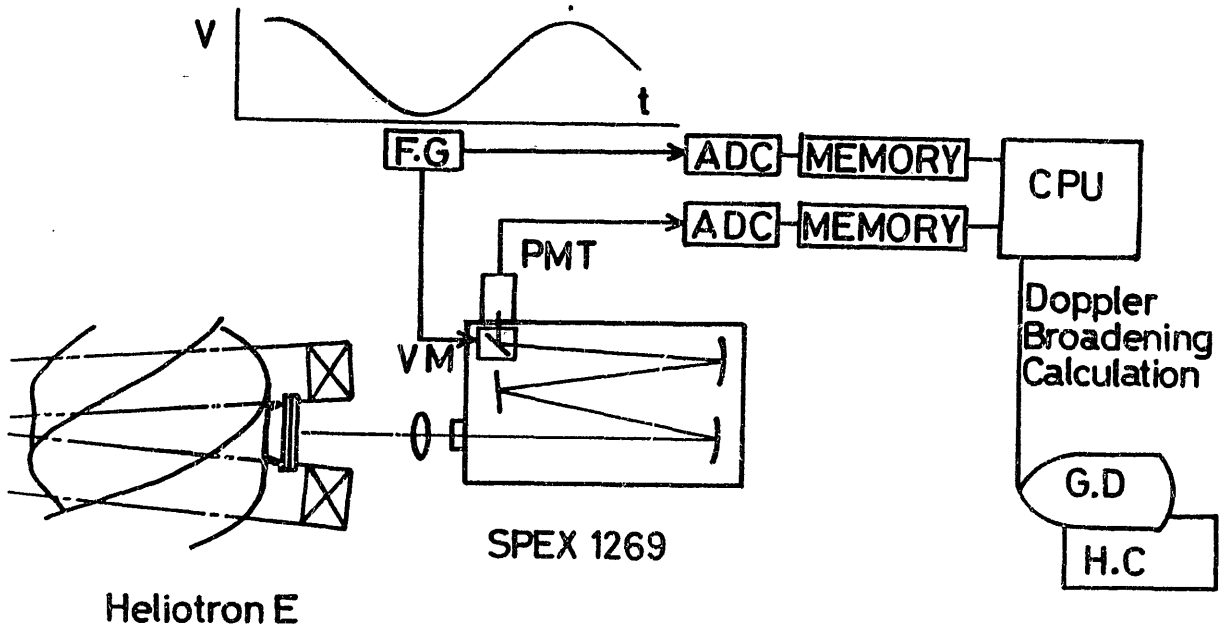

Fig.1. Schematic drawing of the Doppler broadening measurement system

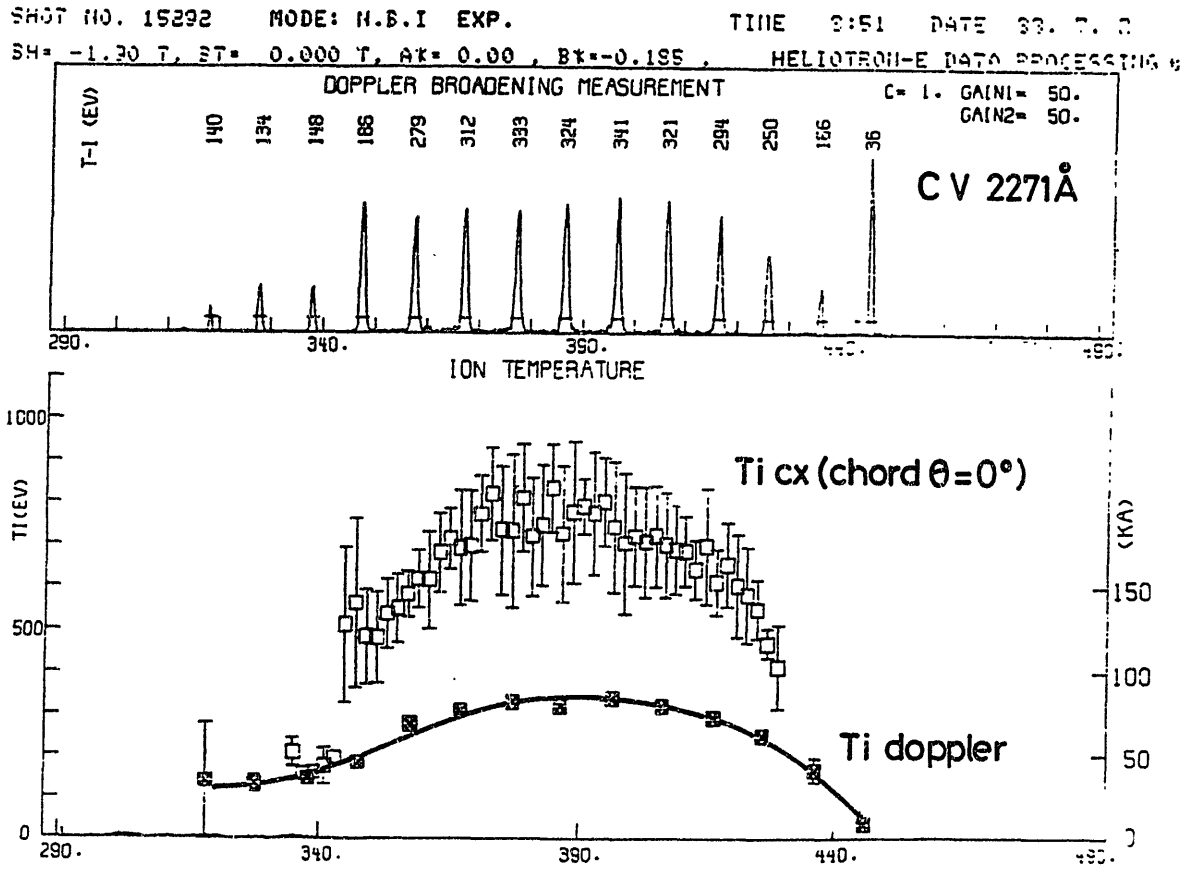

Fig.2. The result of the Doppler broadening measurement

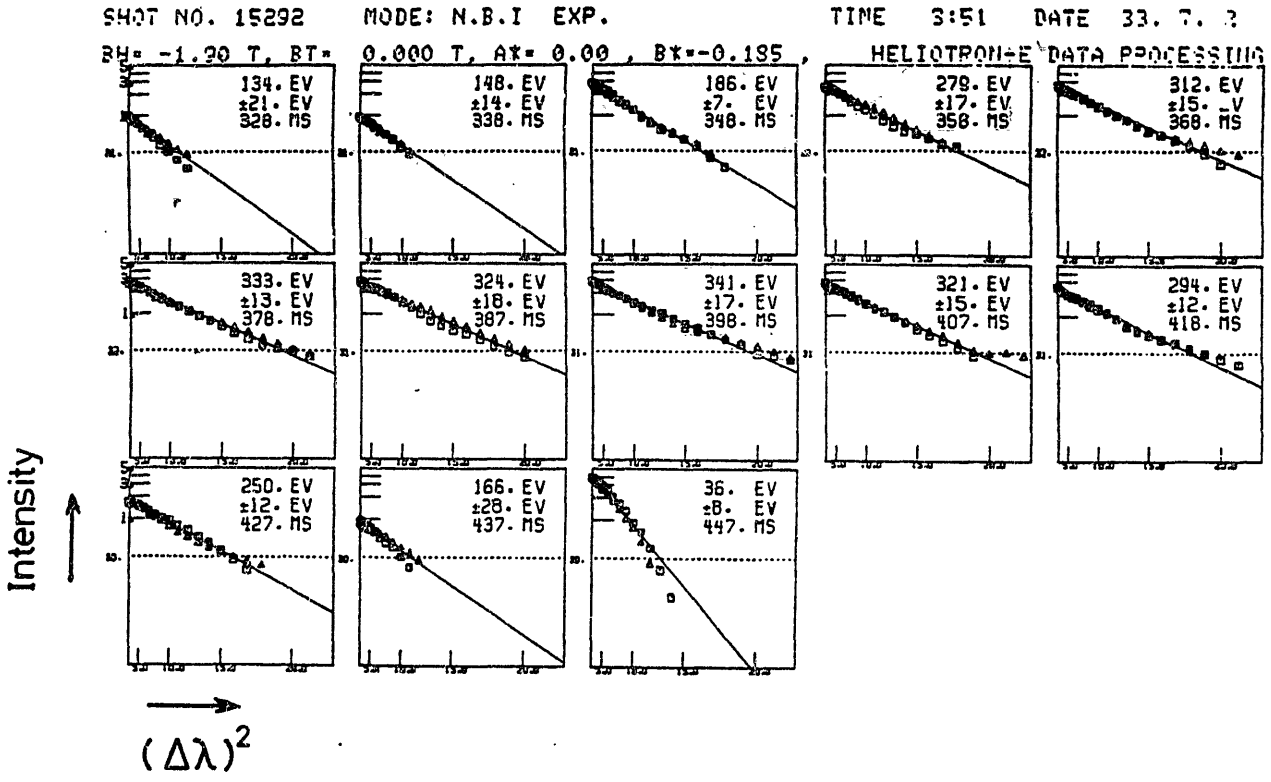

Fig.3. Fitness of the gaussian profile

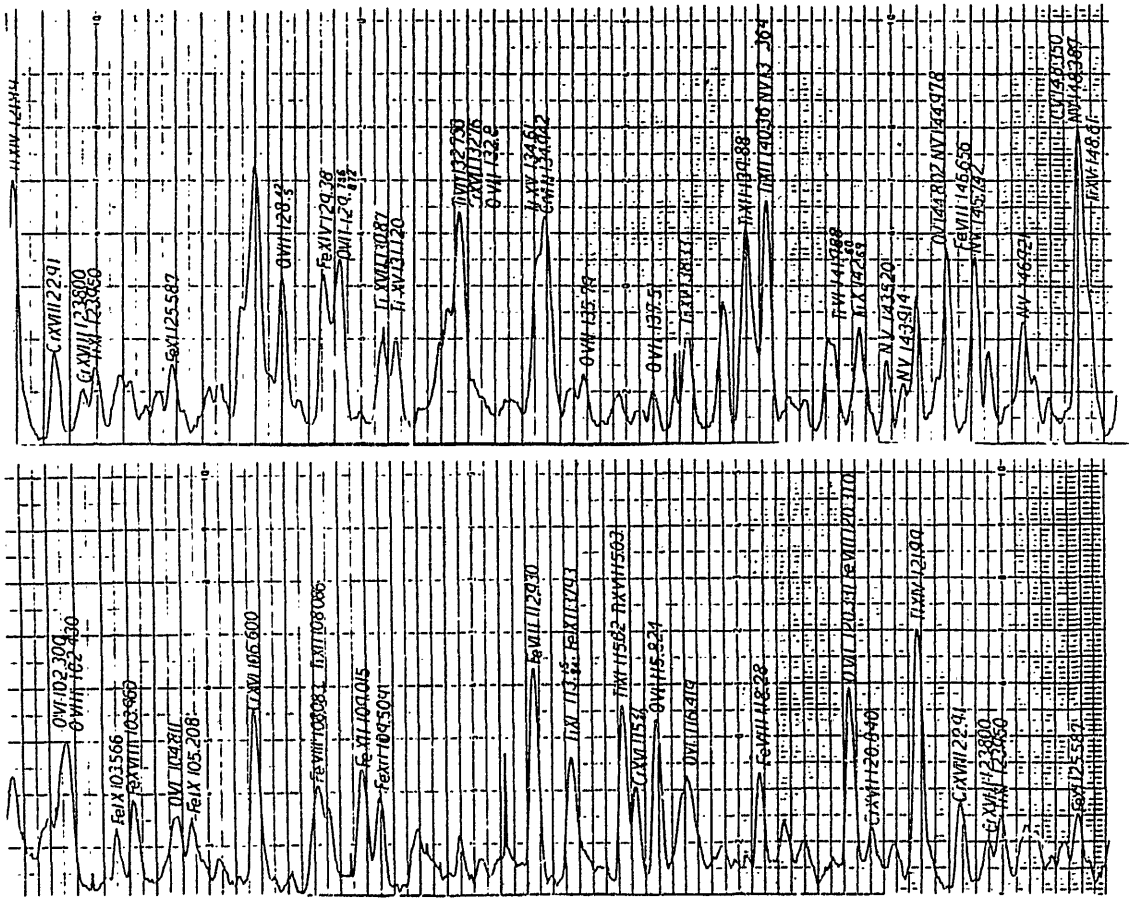

Fig.4. VUV spectra from 100 Å to 148 Å

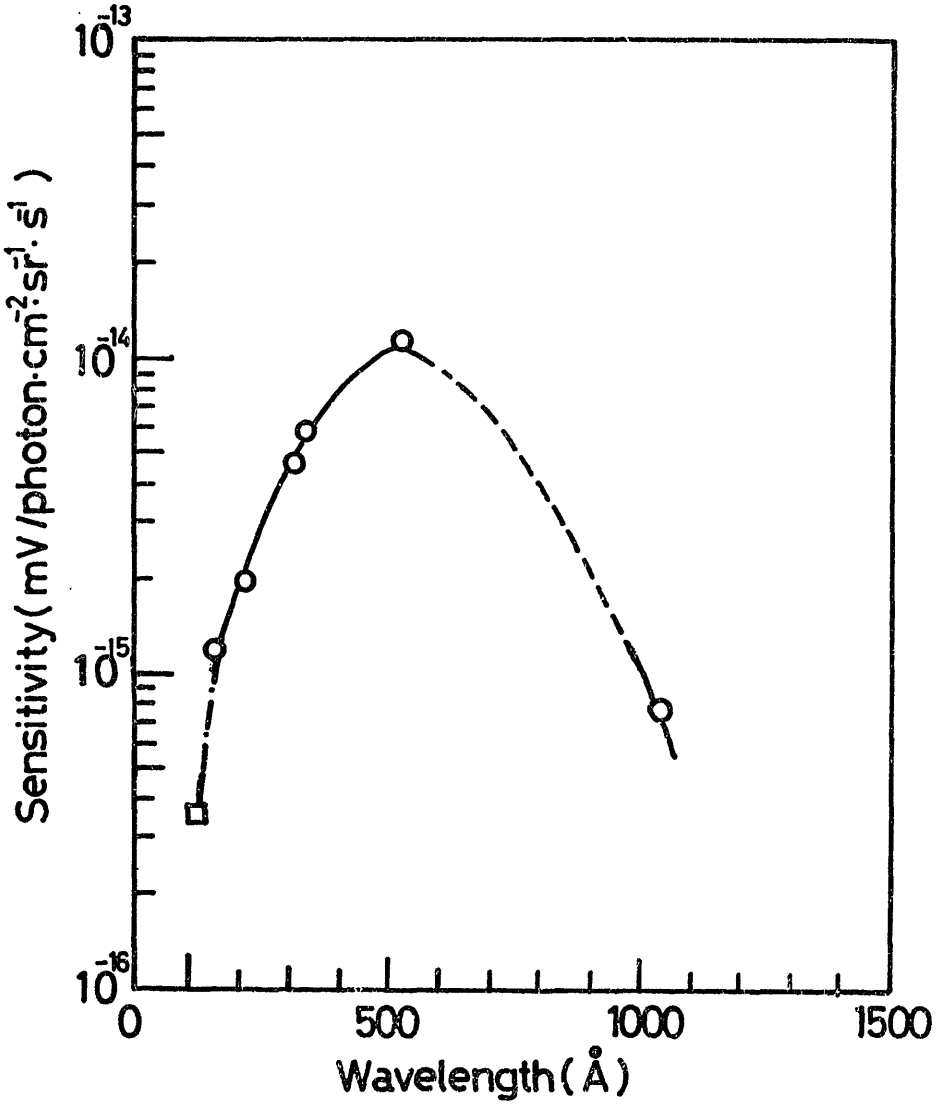

Fig.5. Sensitivity of the VUV system

High Resolution X-ray Spectra of H- and He-like Argon from the Alcator C Tokamak

J.E.Rice and E.S.Marmar, Plasma Fusion Center, M.I.T., Cambridge, Mass., U.S.A., 02139

and

E.Källne and J.Källne, J.E.T. Joint Undertaking, Abingdon, Oxfordshire OX14 3EA, United Kingdom

Abstract

A compact, spatially scanable, curved crystal spectrometer has been installed on the Alcator C tokamak. Spectra from highly ionized argon have been obtained and the spatial and temporal variations of several line ratios, as well as the ion temperature, have been determined.

Introduction

A compact curved crystal spectrometer in the Van Hamos geometry (R=53cm) with a quartz crystal (2d=6.687Å) has been installed on the Alcator C tokamak. The spectrometer system employs a high-count-rate, position sensitive proportional counter (1) capable of ~ 30 μ position sensitivity. Instantaneous counting rates of up to 200 kHz have been achieved without any spectral distortion. The data acquisition system utilizes a CAMAC time-to-digital-converter allowing individual spectra to be obtained in 20 msec or less. The detector is radially scanable, with a spatial resolution of ~ 4 cm, and profiles have been obtained.

The argon seed has been added with the pulsed working gas to reach convenient concentrations between 10^{-5} and 10^{-4} $\bar{n}_e$. Emission lines from H- and He-like Ar have been identified as well as satellites from the He- and Li-like states.

Argon spectra and radial profiles

Shown in fig.1 is a spectrum of Ar17+ obtained during the steady portion of an 80 kG, 375 kA deuterium discharge. The electron density was 2.4×10^{14} cm^{-3} and the central electron temperature was 1500eV. The most prominent feature is the doublet with components w1 at 3.730 Å and w2 at 3.735 Å. Also apparent are the satellites T at 3.754 Å and J at 3.771 Å as well as some features in between. A spectrum from Ar16+, obtained during a

discharge similar to the one for fig.1, is shown in fig.2. The dominant features are the resonance (W), intercombination (X,Y) and forbidden (Z) lines(2). There are several satellites from Li-like argon present, most notably q and k. The spectra in figs.1 and 2 are from central chord measurements, and have been obtained every 20 msec during the discharges. The time development of the He-like spectrum may be seen in fig.3. Spectral resolution of this instrument is sufficient to obtain the ion temperature from the doppler broadening of the resonance line. The ion temperature as a function time for a particular Alcator C discharge is shown in fig.4. The peak temperature of ~ 1 keV agrees favourably with values determined from charge exchange measurements (3) and the neutron flux (4). The error bars are large at the beginning and end of the shot because the observed doppler width is very close to the instrumental width.

Due to the compactness of the spectrometer, radial scans are easily achieved. Shown in fig.5 is the He-like argon spectrum at 8 cm for a discharge similar to those of figs.1 and 2. The minor radius of Alcator C is 16.5 cm and the electron temperature at 8 cm for this discharge was ~ 700 eV. Notice that the intensities of the forbidden line and the satellite lines (k in particular) have risen relative to the resonance line. The relative intensities of the satellites increase at this lower electron temperature due to an increase of the fractional abundance of the Li-like ionization state. The relative intensity of the forbidden line may have grown as a result of larger contributions of charge exchange and recombination at the outer radii. Shown in fig.6 are

the ratios of the satellite to resonance lines (k/W) and the intercombination lines (Y/X) as a function of radius in the plasma. The intercombination ratio remains constant (~ 1.2) while the relative contribution from the Li-like satellite k increases strongly in regions of lower electron temperature.

References

(1) J.Källne et al., Nucl.Instrum.Methods 203, 1155(1982)

(2) E.Källne et al., Phys.Rev.A 28, 1(1983)

(3) C.Fiore, private communication (1983)

(4) D.Pappas, private communication (1983)

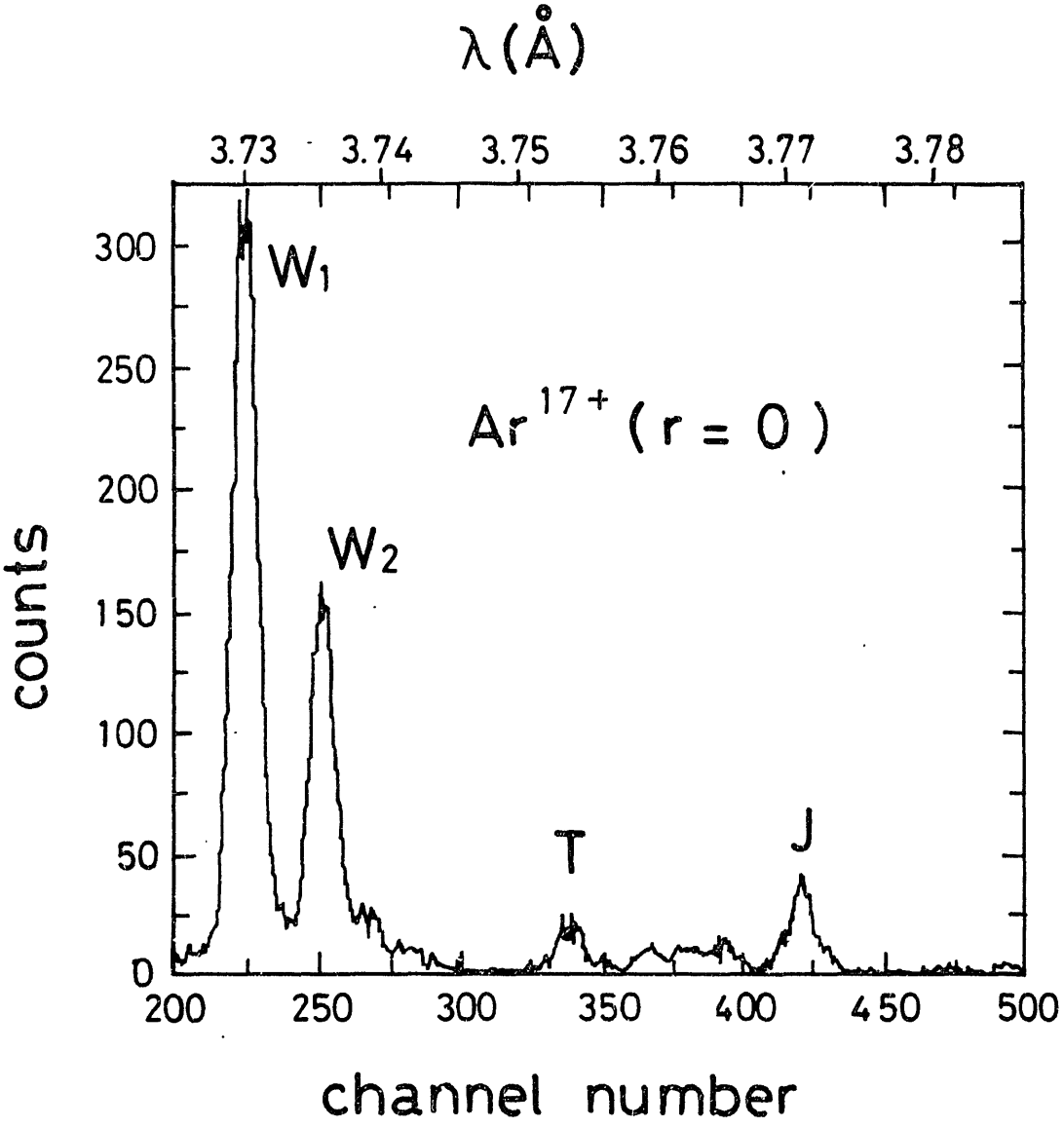

Fig.1. Spectrum of Ar17+ (r=0cm)

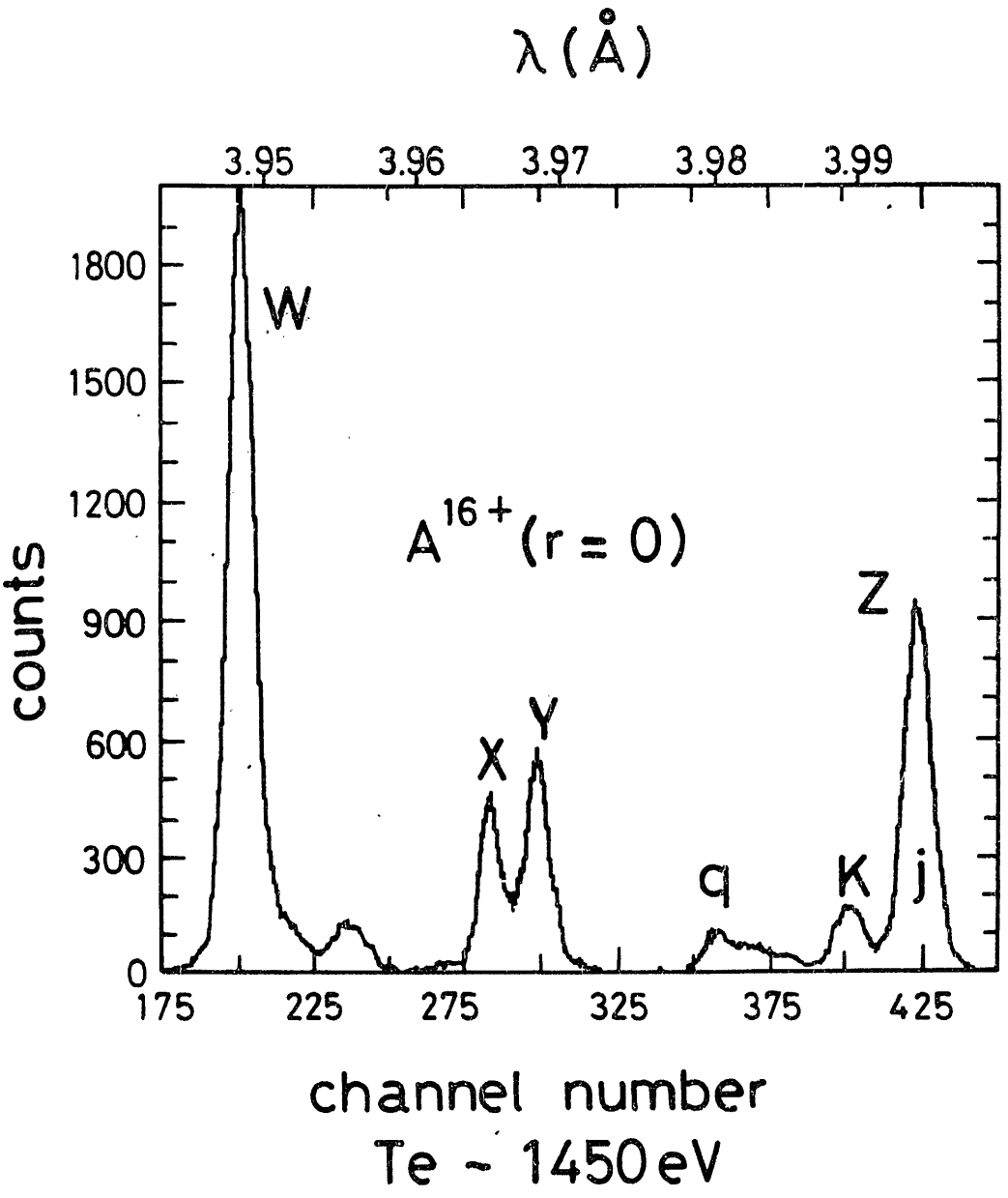

Fig.2. Spectrum of Ar16+ (r=0cm)

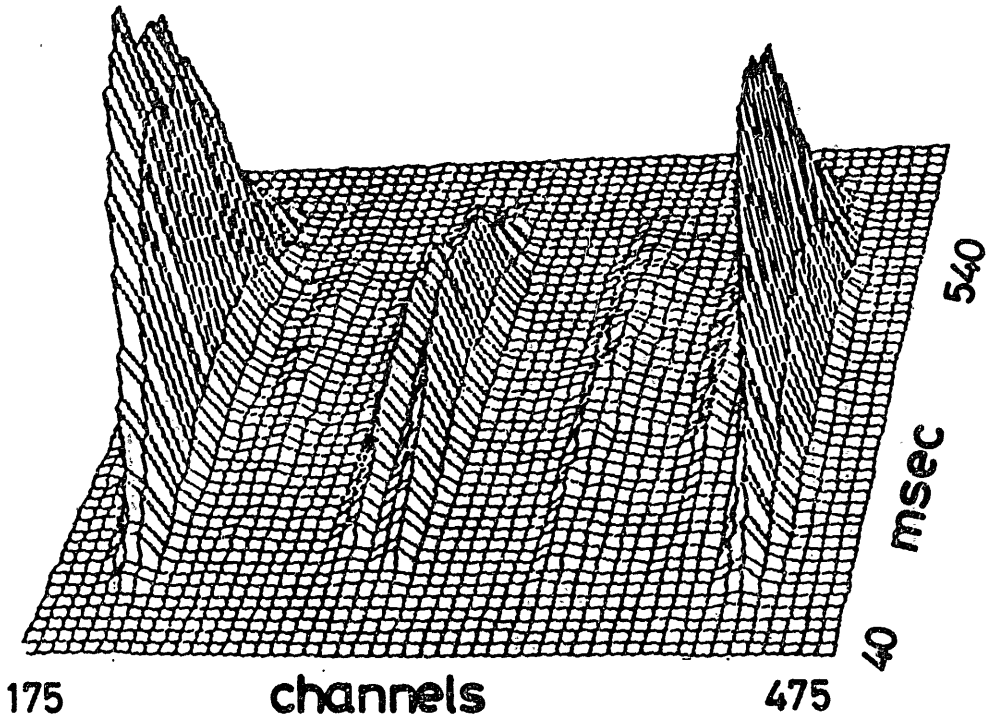

Fig.3. Time development of He-like argon spectrum

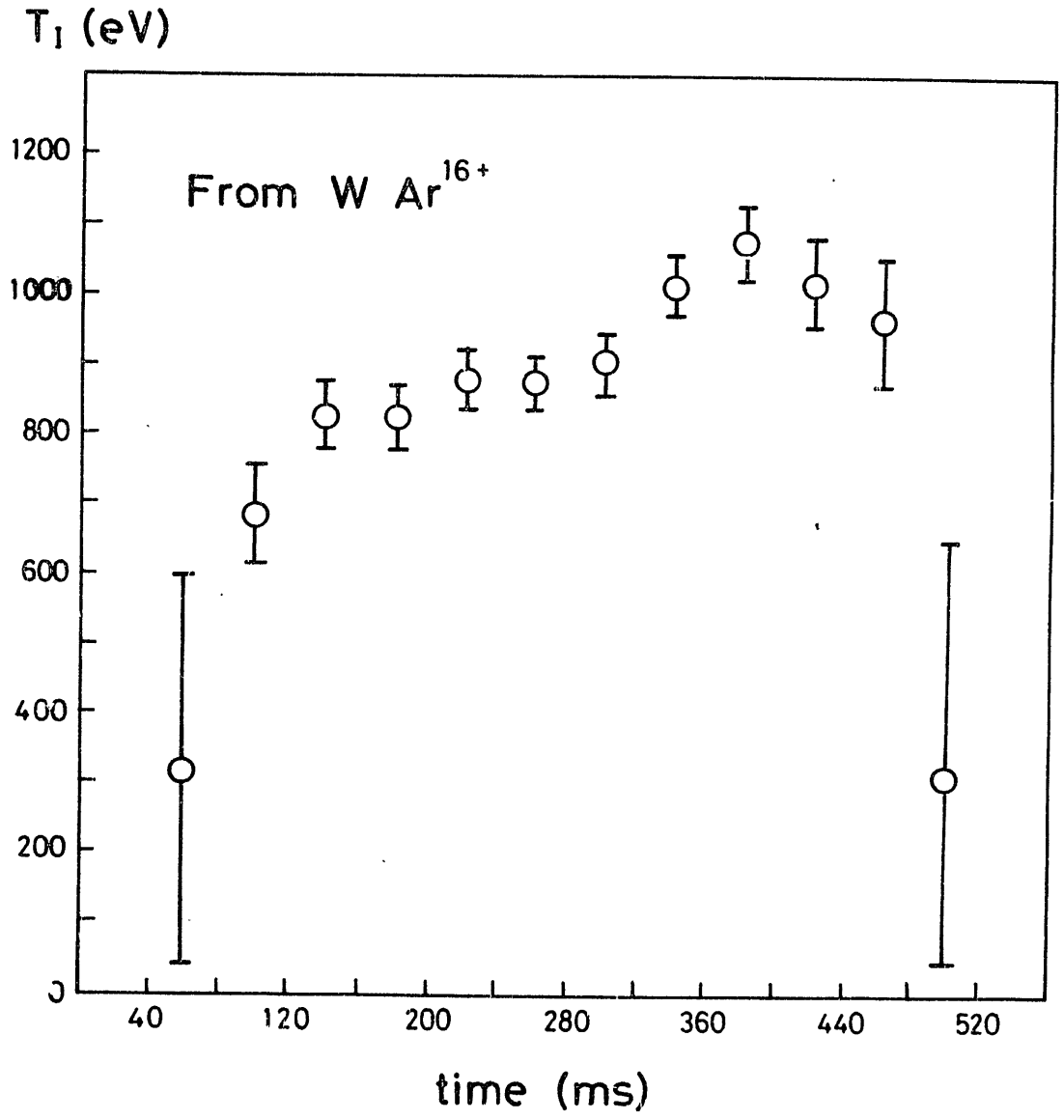

Fig.4. Ion temperature as a function of time

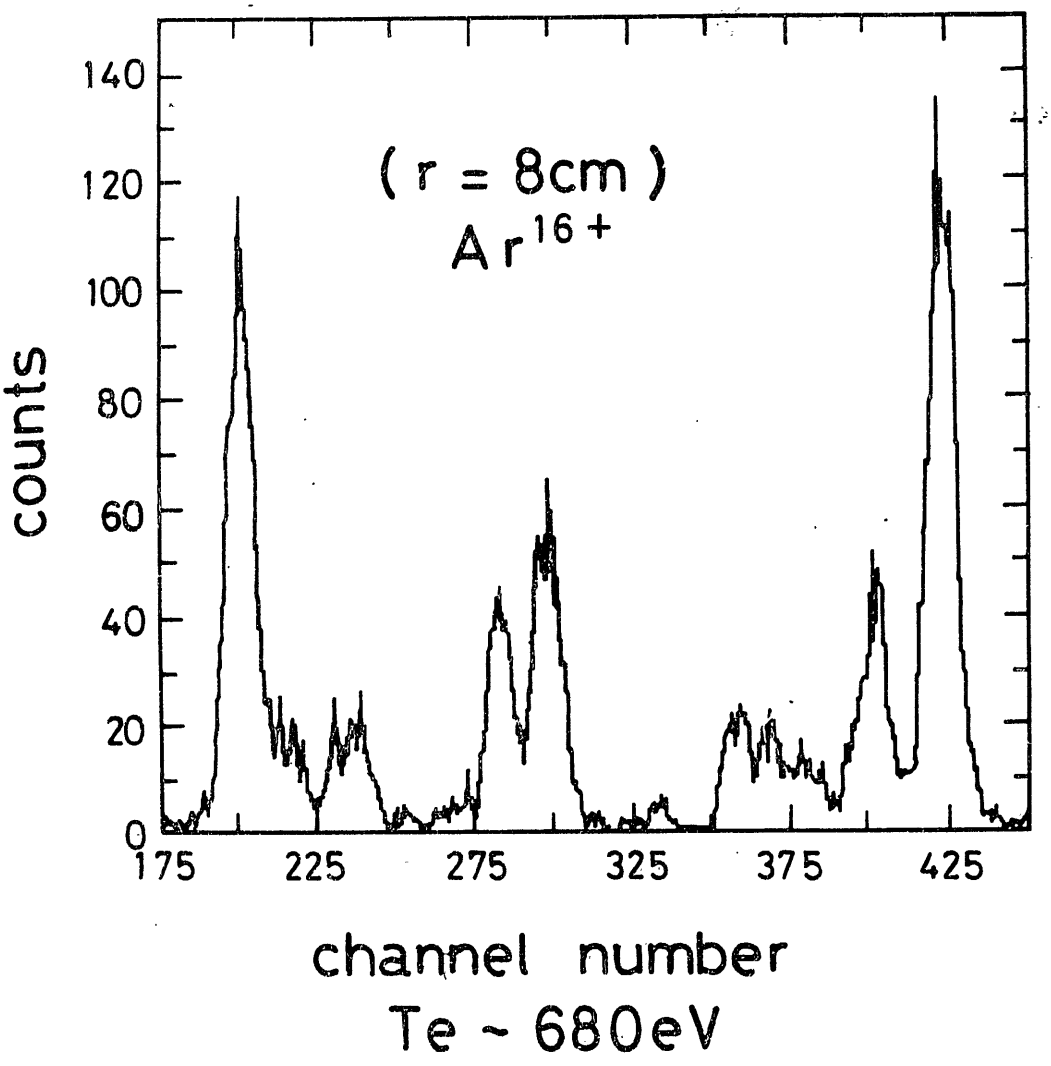

Fig.5. Spectrum of Ar16+ (r=8cm)

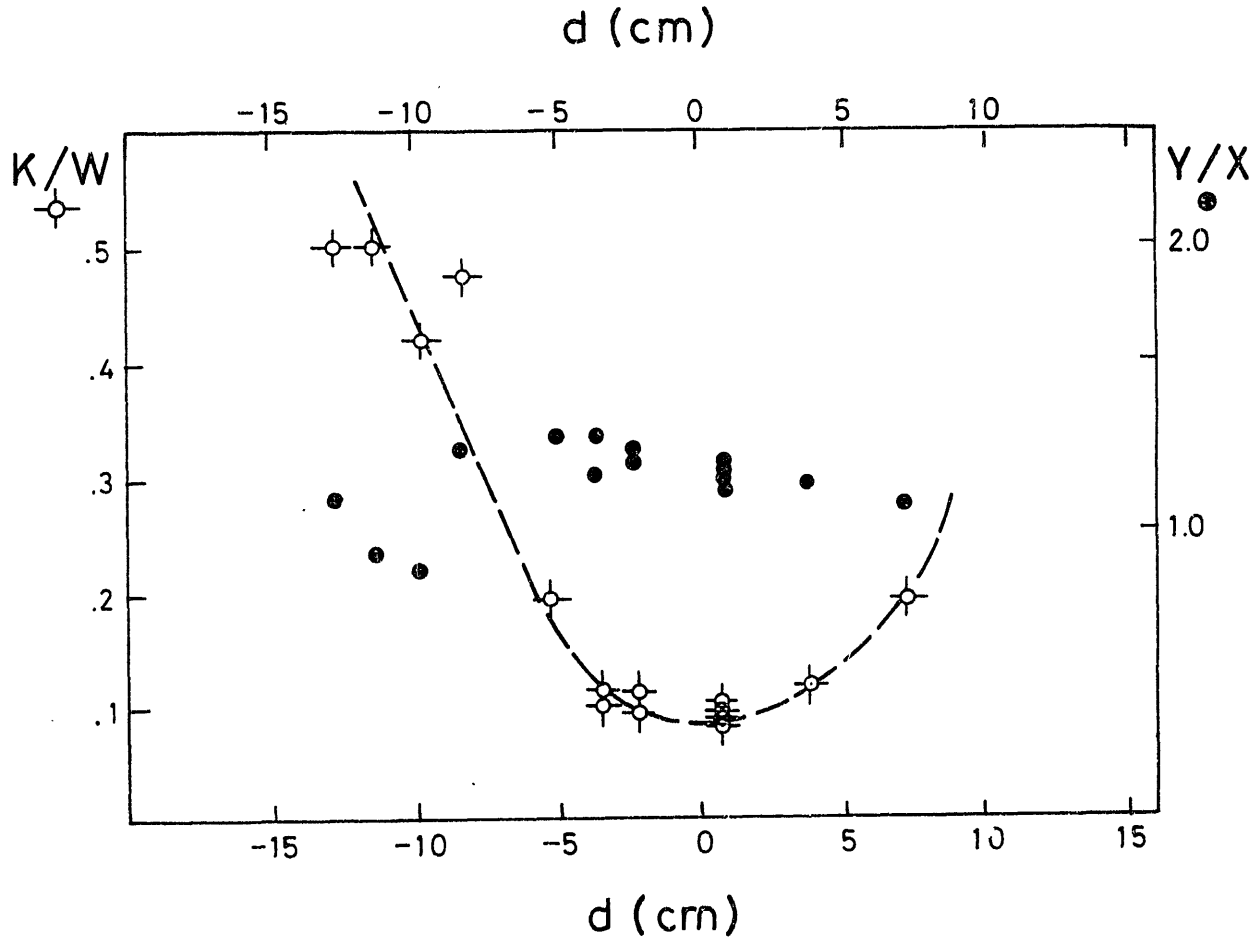

Fig.6. Li-like to He-like argon ratio as a function of radius

Atomic and Molecular Processes in Discharge Cleaning Plasmas

Nobuaki Noda

Institute of Plasma Physics, Nagoya University

Nagoya 464 Japan

Abstract

The discharge cleaning process is analyzed on the basis of zero-dimensional particle balance. An experimental result on the density dependence of the cleaning efficiency can be interpreted using this simple model of particle balance. The relation among the plasma parameters and the control parameters is also investigated. Cross sections of some molecular processes near threshold energy are found to important for those analyses.

1. Introduction

Discharge cleaning is one of the important techniques for reducing oxygen and carbon impurities which contaminate tokamak plasmas [1]. Low power continuous hydrogen discharges are used usuallyfor the purpose of effecient cleaning. Effectiveness of the electron cyclotron resonance (ECR) discharge has been clearly demonstrated on JIPP T-II[2], a toroidal device for tokamak/stellarator experiments in IPP, Nagoya University. At the moment, the principal object of the discharge cleaning study is to optimize this technique and to obtain a scaling law by which we are able to know the optimum design for future tokamaks. For this purpose, it is necessary to understand the basic processes of the discharge cleaning. It is convenient for the analysis to divide them into two parts; that is, i) the relation between the cleaning efficiency and the plasma parameters, and ii) the relation between the plasma parameters and the control parameters. The cleaning efficiency can be represented by the partial pressure P_{18} of H_2O because most of oxygen is removed from the torus as a form of water vapor by the pumping system. Then the first part of the analysis is to investigate P_{18} as a function of n_e and T_e, where n_e is the electron density and T_e the electron temperature of the plasma. The plasma parameters change depending on the hydrogen pressure P_2 and the input power P_{in} of the microwave, etc. Then the second part is to investigate the relation between n_e, T_e and P_2, P_{in}.

Discharge cleaning plasmas are not fully ionized and a typical value of n_e is 10^{10} - $10^{12}cm^{-3}$ and T_e is 3 - 10 eV, respectively.

2. Discharge Cleaning Process

In order to study the relation between P_{18} and n_e, T_e of the ECR plasma, we assume a simple zero-dimensional model of particle balance[3,4]. The reduction of oxygen consists of the following three processes: i) generation of an atomic hydrogen flux in the plasma, ii) production of water vapor by chemical reactions at the wall surface, iii) pump-out of the water vapor by the pumping system. In this model, we have taken account of H_2O molecules which are lost due to sticking to the wall and H_2O dissociation by electron impact. Both of these processes are competitive to the pump-out process (iii) of H_2O. Since the production rate of hydrogen atoms is written as $n_e n_2 k_2$ per unit volume, the total number of hydrogen atoms incident on whole of the wall surface per unit time is $F_2 = n_e n_2 k_2 V_p$, where n_2 is molecular hydrogen density, k_2 rate coefficient for production of one H atom by electron-impact dissociation of H_2 and V_p plasma volume. Taking account of the surface processes, such as dissolution and recombining release of H atoms on the surface, the Jülich group has shown that the water-release rate is proportional to the surface density n_{MO} of metal oxides and the flux density of atomic hydrogen[5]. Therefore, denoting the apparent cross section of water production on the wall surface as

s_{18}, we obtain the total number of H_2O molecules released from the wall per unit time as

$$F_{18} = F_2 n_{MO} s_{18} = n_{MO} s_{18} n_e n_2 k_2 V_p \quad . \qquad (1)$$

When the density of H_2O is n_{18}, the pump-out rate F_p of H_2O by the pumping system which has an effective pumping speed S_p is written as

$$F_p = S_p n_{18} \quad . \qquad (2)$$

Moreover, we take account of dissociation loss F_d as

$$F_d = n_e n_{18} k_{18} V_p \quad , \qquad (3)$$

and sticking loss F_{st} as

$$F_{st} = (1/4) n_{18} v_{18} A_w p_{st} \quad , \qquad (4)$$

where k_{18} is rate coefficient of electron impact dissociation of H_2O, v_{18} thermal velocity of H_2O molecules, p_{st} sticking probability and A_w area of the wall surface. In a steady state, a relation $F_{18} - F_p - F_d - F_{st} = 0$ holds. Substituting (1) - (4) into this relation, we obtain the following relation,

$$P_{18}/P_2 = n_{18}/n_2 = A \; / \; (\; 1 + B \; n_e^{-1}) \; , \qquad (5)$$

where $A = (k_2/k_{18}) s_{18} n_{MO}$ and $B = [\; (1/4) p_{st} v_{18} A_w + S_p \;] \; / \; k_{18} V_p$.

This relation indicates that, for sufficiently high electron densities, n_{18}/n_2 approaches $(k_2/k_{18}) s_{18} n_{MO}$ asymptotically and is saturated. This saturation should be seen in the densities

higher than B. This implies that one can reduce the cleaning time by raising n_e up to around B.

In order to estimate the value B, it is necessary to know k_{18} and p_{st}. Dissociation cross sections of H_2O have been measured by several authors and summarized by Olivero et al.[6] We have calculated k_{18} using the data in this literature and plotted against electron temperature in Fig. 1. In this figure, k_2 estimated from the data given in Ref. [7] are also plotted.

The sticking probability of stainless steel for H_2O is not known at 150 C. It is, however, reasonable to consider that p_{st} is larger than 0.1 after a long time cleaning. By this assumption, we can neglect S_p in calculating the value of B and we have obtained $B = 2.2 \times 10^{11}$ (cm^{-3}) for $p_{st} = 0.5$ and $T_e = 8$ eV. We have calculated P_{18}/P_2 for two values of p_{st}, 0.5 and 0.1, as plotted in Fig. 2. According to Eq. (5), a low value of p_{st} corresponds to a low value of B and this implies a saturation in P_{18}/P_2 occurs at a low n_e.

An experimental result in JIPP T-II[3,4] shows that the partial pressure ratio P_{18}/P_2 increases as the density increases and is saturated for the densities above 10^{11} cm^{-3}. This is shown in Fig. 2 compared to the calculated result. We can see in this figure that the calculated result for $p_{st} = 0.5$ is close to the experimental data. Thus we can interpret the relation between P_{18}/P_2 and n_e fairly well on the basis of the simple model for particle balance. Moreover, we can conclude that it is essential to raise the electron density so high that the

value of $n_e n_{18} k_{18} V_p$ (dissociation-loss rate) is as large as $p_{st}(n_{18}/4)v_{18}A_w$ (sticking-loss rate) in order to optimize discharge cleaning.

As is shown in Fig.1, the ratio k_2/k_{18} decreases as the electron temperature rises. Unfortunately no experimental data of P_{18} have been available as a function of T_e. Preliminary observation in JIPP T-IIU shows, however, that P_{18}/P_2 does not depend on T_e strongly, which is inconsistent to the calculated result in Fig. 1. On the other hand, there may be a large uncertainty for k_2/k_{18} in this low temperature region, too. More precise investigation is needed to understand the P_{18}- T_e relation both in the discharge cleaning experiments and in the modeling and elementary processes.

In the model above mentioned, the following processes are not taken into account,

a) $H_2^+ + H_2 \longrightarrow H_3^+ + H$,

$H_3^+ + e \longrightarrow 3H$ and

b) $H_2^+ + e \longrightarrow 2H$.

The process b) is negligible because the ionization degree of the plasma is less than 0.1. The process a) should be taken into account because the dissociative recombination of H_3^+ is considerably large. Taking into accountthis process, we obtain values of k_2/k_{18} several tens of percent higher than those in Fig. 1. However, the discussion described above is not affected greatly by the introduction of this process.

3. Particle and energy balance relating to the determination of the plasma parameters

In steady states, the electron temperature is determined by the following particle balance,

$$n_e n_2 k_2 = n_e / \tau_p \qquad (6)$$

where τ_p is the particle confinement time. The plasma confinement is determined by Bohm difusion, toroidal drift and E x B drift. In those three processes, the particle loss rate is proportional to T_e, that is, $\tau_p \sim 1/ T_e$. The ionization rate coefficient k_2 is dependent on T_e, too. Thus the equation (6) is rewritten as

$$k_2(T_e) = cT_e/n_2 \qquad (7)$$

where c is a constant determined by the dominant particle loss processes.

On the other hand, the electron density n_e is determined by energy balance. In discharge cleaning plasmas, the energy loss due to particle convection is negligible compared to the loss due to atomic and molecular processes because the plasmas are usually not fully ionized. Then the energy balance is written as

$$P_{in} = \sum_j w_j k_j n_e n_2 V_p \qquad (8)$$

where w_j is the energy loss through the j th atomic process and k_j the rate coefficient. The summation must be carried out over

all inelastic processes. If we denote the average energy loss of electrons during single electron-ion pair production as

$$\bar{w} = \left(\sum_j k_j w_j \right) / k_2 \qquad (9)$$

and substitute n_2 from eq. (6), we obtain

$$n_e = P_{in} \tau_p / \bar{w} V_p \ . \qquad (10)$$

Thus the T_e is determined by the filling pressure of hydrogen gas according to eq. (7) and the density by the input power according to eq. (10) . The important processes related to the particle and energy balance are the simple ionization of H_2 molecules $H_2 + e \longrightarrow H_2^+ + 2e$, and the dissociation $H_2 + e \longrightarrow 2H + e$. It is necessary to evaluate $\bar{w}$ as a function of T_e, and for this purpose the energy dependence of the cross sections of those processes , particularly around the threshold energies are important.

4. Summary

An experimental result shows that the cleaning efficiency rises as the density increases and is saturated for the densities above 10^{11} cm^{-3}. This can be interpreted by using a model based on zero-dimensional particle balance. The cross sections of the following molecular processes near the threshold energies are important to analyze the electron temperature dependence of the cleaning efficiency;

i) $H_2 + e \longrightarrow 2H + e$

ii) $H_3^+ + e \longrightarrow 3H$

iii) $H_2O + e \longrightarrow H + OH + e$.

The relation among plasma parameters and the control parameters are also investigated. The electron temperature is determined by the filling gas pressure according to the particle balance of the plasma. The density is determined by the input power according to the energy balance. In order to calculate this energy balance, it is necessary to know the average energy loss of electrons during single electron-ion pair production as a function of the electron temperature.

References

[1] H. F. Dylla, J. Nucl. Mater. 93 & 94 (1980) 61

[2] Y. Sakamoto, Y. Ishibe, S. Ishii, K. Okazaki, H. Oyama, K. Yano, N. Noda, K. Kawasumi, K. Kawahata and S. Tanahashi, J. Nucl. Mater. 111 & 112 (1982) 485

[3] N.Noda, S. Tanahashi, K. Kawahata, Y. Kawasumi, Y. Ishibe, S. Ishii, K. Okazaki and H. Oyama, Y. Sakamoto and K. Yano, J. Nucl. Mater. 111 & 112 (1982) 498

[4] N. Noda, S. Hirokura, Y. Taniguchi and S. Tanahashi J. Vac. Sci. and Technol. A 1 (1983)

[5] F. Waelbroeck, J. Winter, P. Wienhold, in: Proc. 5th Symp. on Plasma Chemistry, Edinburgh, 1981, Eds. B. Waldie et al., p. 351

[6] J. J. Olivero, R. W. Stagat and A. E. S. Green, J. Geophys. Res. 77 (1972) 4797

[7] E. M. Jones, CLM-R175, Culham lab. (1977)

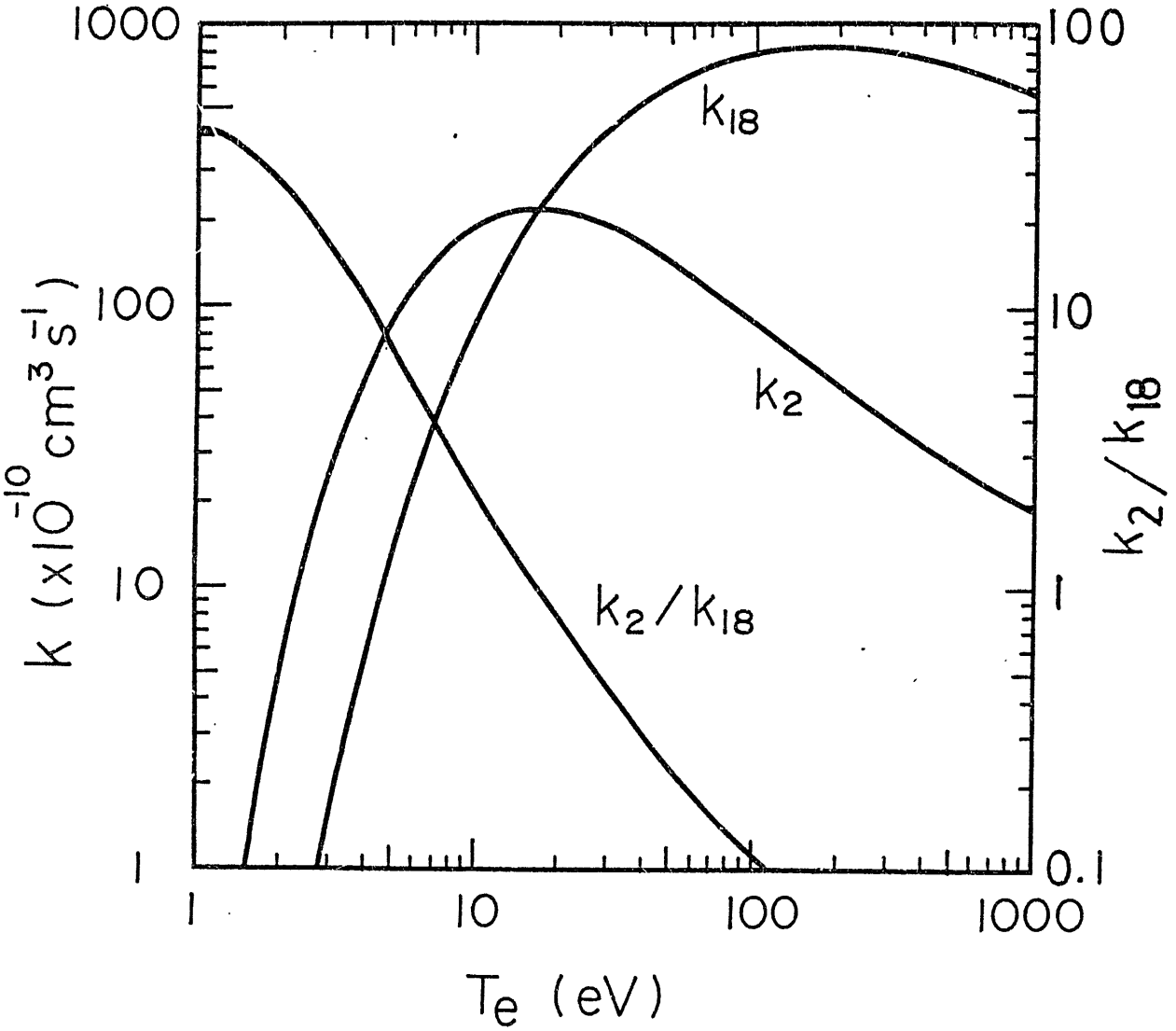

Fig. 1 Dissociation rate coefficients k_2 for H_2 and k_{18} for H_2O as a function of electron temperature [4)]

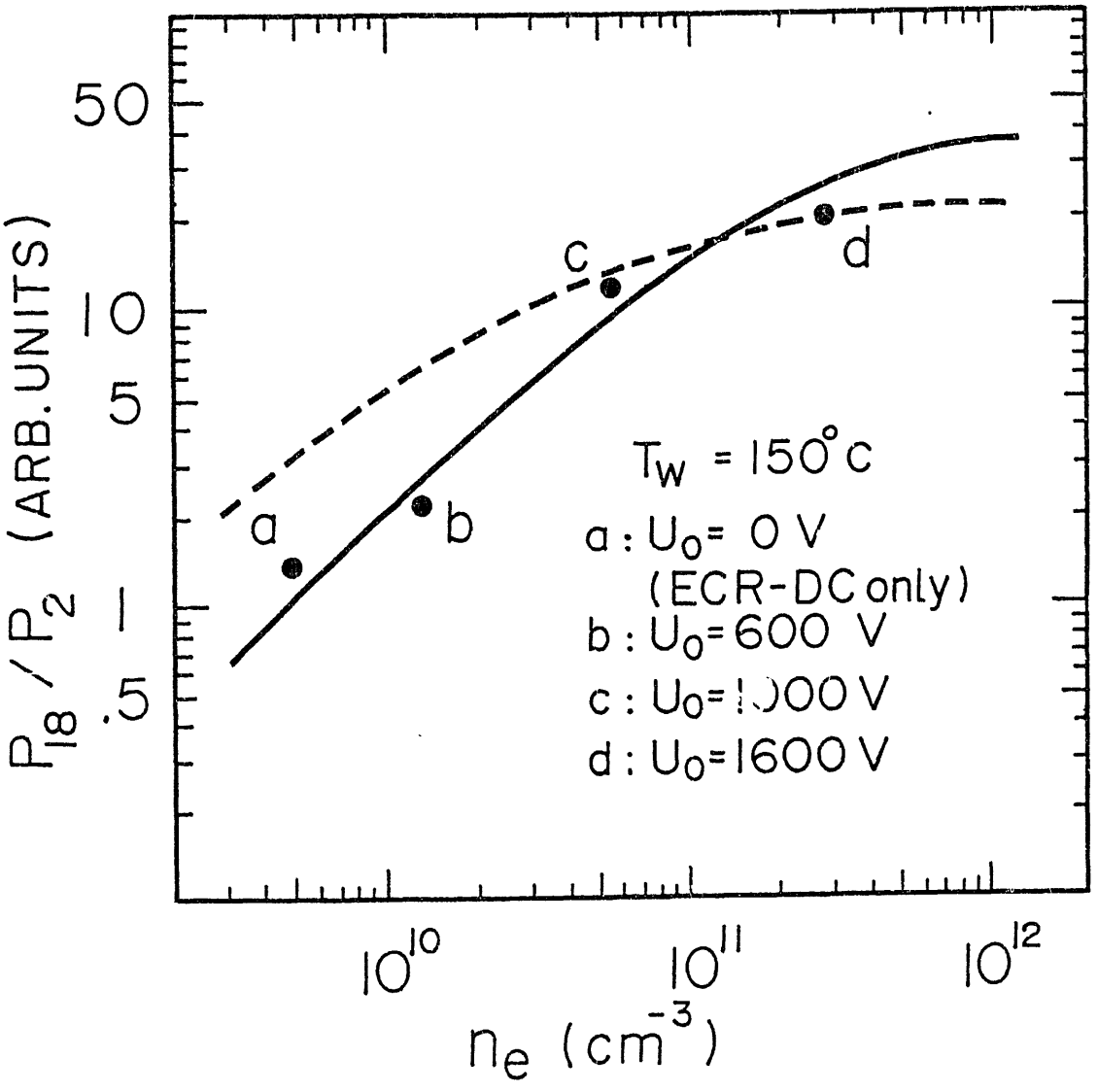

Fig. 2 Density dependence of P_{18}/P_2 [4]

closed circle : experimental

solid line : calculated as p_{st} = 0.5

dashed line : calculated as p_{st} = 0.1

A comment on atomic processes relevant to alpha particle diagnostics

M. Sasao and K.N. Sato

Instisute of Plasma Physics,
Nagoya University, Nagoya 464, Japan

Measurements of the alpha particle density and the velocity distribution in a magnetically confined DT-burning plasma are expected to give requisite information on fusion plasma physics. This is a brief note on atomic processes relevant to alpha particle diagnostics, especially on atomic data for a neutral beam probe technique [1] and on atomic data for the use of heavy ions.

In Fig. 1 is shown the concept of a neutral beam probe technique. A neutral atom injected neutralizes a fast alpha particle produced in the fusion through a two- electron

capture process and enables the alpha to escape from the magnetic field and to be detected. According to estimation by Princeton group [1] and by Nagoya group [2], a neutral He or Li beam of an intensity more than several mA, with a velocity higher than 0.6 times the initial alpha particle velocity, is desired in order to study the burning plasma physics.

Several atomic cross sections are necessary to obtain the alpha particle density and the velocity distribution from the measured neutral spectra.

I. σ_{20}, σ_{20}^* for He^{2+} in collisions with Li°, He° and He^*.

As for σ_{20} in $He^\circ + He^{2+}$, there are a lot of experimental data and they are summarized in IPPJ-DT-50. In most of these measurements, however, the metastable fraction in the produced neutral He was not measured.

σ_{20} for He^{2+} in collisions with Li° was not measured when the use of a neurtral beam was first proposed by Prof. Post and others in 1979 [1]. Three experimental results have been recently reported. Measurements by McCullough and others have covered the energy range of 30 keV - 800 keV[3], and measurements by Murray and others 50 keV - 160 keV [4]. Both data agree with each other in the overlapped energy region, as shown in Fig. 2. Cross sections in the range of 800 keV to 2 MeV were measured by the present authors and

others [5], who have paid special attention to determine the target vapour thickness precisely by measuring the Rutherford scattered particles from the Li oven, and obtained absolute values of cross sections . Their values around 800 keV agree with those of McCullough and others, which were obtained with the target thickness estimated from the oven temperature. These measured cross sections represent the average of σ_{20} and σ_{20}^{*} , the cross sections for double electron capture into the ground and metastable states, respectively.

Because there is expected to be large difference between the attenuation of He in the ground state and that of He in the metastable state in a hot plasma, a precise determination of the metastable fraction in the produced neutral He is desired, which is thought to be indispensable information of atomic physics for the neutral beam technique of the alpha particle diagnostics.

II. Ionization cross sections of $\overset{\circ}{Li}$, $\overset{\circ}{He}$, and/or He^{*} by electrons, D-, T-ions and impurity ions.

Among these cross sections, ionization in collisions with ions has the largest effect on the attenuation of the injected neutral beam in the velocity region considered here. While ionization cross sections for various neutral atoms by electron impact have been measured over a

wide energy region, there are not many data on the ionization by ion impact. But because the measured ion impact cross sections at relatively high energies usually do not deviate very much from the electron impact cross sections at the same velocities, a rough estimation of the attenuation is possible.

In Fig. 3 are shown the electron impact cross sections for Li. The experimental cross sections measured by Jalin and others [6] are about a factor of two smaller than the old measurement [7]. Transmission factors of a Li beams with the velocity of 0.6, 0.8 and 1.0 times the initial alpha particle velocity are calculated for "R-Tokamak" designed for D-T burning and are shown in the insert, indicating that the number of neutral atoms that reach the center of the plasma depend on ionization cross sections and the beam velocity as well as the ion densities.

Attenuation of the neutral beam can be estimated by beam monitoring system before and after the transit of the plasma, if the plasma density and the impurity densities are known.

III. He^- life times, collisional cross sections which are necessary to get neutralization efficiencies from He^- and Li^- with various methods, a metastable state fraction in a neutral He beam, atomic processes relevant to the ion source design, and so on.

A lot of atomic processes and cross sections have to be known in order to develop the neutral beam sources of the required quality. Some of them are related to negative ions because the negative ions have fairly high neutralization efficiencies, compared with those of the positive ions (typically 10^{-3} - 10^{-4})[1], in high energy region of interest.

Since the production of Li^- ions is more difficult and it is necessary to develop a new type of high energy accelerator for them, a He beam is desirable if the complicated problems related to the long life metastable state are solved. The metastable beam is undesirable because of its large attenuation and difficulty in measurement for its production cross sections through two-electron capture process, meanwhile the metastable fraction in a neutralized beam from negative ions in a gas cell or an electric field would be higher than 80 % according to extrapolation of the data below 400 keV [8] by Pedersen and others .

It has been suggested to use the auto-detachment process of He^- to get the pure ground state beam [2]. Two components with different life times have been found [9] in negative He ions, the shorter being 10 μsec, with the initial fraction of about 50%. Then, during the flight of 10 - 30 m from the exit of the accelerator, 10 - 30 % of the negative He ions will be decayed into the ground state. The fundamental investigations on practical application of

this idea are now under progesss at IPPJ.

The use of heavy ions as a diagnostic tool of alpha particles can be considered.

Considering that the Larmor radius of Ar^+ ion, for example in magnetic field of 5 T, is larger than the minor radius of a usual burning machine at the initial alpha particle velocity and that the proton impact ionization cross section of Ar^+ is small enough, the injection of high energy singly charged heavy ions can be considered as an alternative candidate of a probing beam. Injection of low-Z materials such as Be, B, or C should be also mentioned because the electron capture cross sections of an alpha particle from Be^{3+} , B^{4+}, or C^{5+} ion have maximum at 2-3 MeV. Although they will be naked within 100 μsec according to a rough estimation, one can expect a large signal of either photons or neutrals.

Recently electron impact ionization cross sections of highly ionized ions have been measured accurately at some laboratories [10]. Experimental data of ion-ion collisions are not well compiled. Estimations above mentioned have been done by using recent theoretical results by Lal and others [11] and by Olson [12] and the scaling law obtained by Nikolaev [13]. Electron capture cross sections of alpha particles from multiply charged ions are particlularly important in the energy range of hundreds of keV to a few MeV from the point of view of the fast alpha particl loss.

References

(1) D.E. Post, D.R. Mikkelson, R.A. Hulse, L.D. Stewart and J.C. Weisheit, J. Fusion Energy 1 (1981) 129 and PPPL-1592 (1979).
L.R. Grisham, D.E. Post, J.C. Weisheit, H.P. Eubank, D.R. Mikkelson and L.D. Stewart, PPPL-1661 (1980).

(2) M. Sasao, IPPJ-599 (1982) p.355.

(3) R.W. McCullough, T.V. Goffe, M.B. Shah, M. Lennon and H.B. Gilbody, J.Phys. B15 (1982) 111.

(4) G.A. Murray, F. Stone, M. Mayo and T.J. Morgan, Phys. Rev. A25 (1982) 1805.

(5) M. Sasao, K.N. Sato, A. Matsumoto, A. Nishizawa, S. Takagi, Y. Kanamori, Y. Haruyama and F. Fukuzawa, Abstract of XIII ICPEAC (Berlin,1983) p.569.

(6) R. Jalin, R. Hagemann and R. Botter, J. Chem. Phys. 59 (1973) 952.

(7) R.H. McFarland and J.D. Kinney, Phys. Rev. 137 (1965) A1058.

(8) E.H. Pedersen and P. Hvelplund, J. Phys. B6 (1973) 2600.
E.H. Pedersen, F.R. Simpson and P. Hvelplund, Phys. Rev. A11 (1975) 516.
E.H. Pedersen, Phys. Rev. A15 (1977) 53.

(9) L.M. Blau, R. Novick and D. Weinflash, Phys. Rev. Lett. 24 (1970) 1268.
F.R. Simpson, R. Browning and H.B. Gilbody, J. Phys. B4

(1971) 106.

E.H. Pedersen, F.R. Simpson and P Hvelplund, J. Phys. B7 (1974) L294.

(10) D.H. Crandall, R.A. Phaneuf and P.O. Taylor, Phys. Rev. A18 (1978) 1911.

A. Muller et al., J. Phys. B13 (1980) 1877.

D.C. Gregory, P.F. Ditter and D.H. Crandall, Phys. Rev. A27 (1983) 724.

R.A. Falk and G.H. Dunn, Phys. Rev. A27 (1983) 754.

R.A. Falk et al., Phys. Rev. A27 (1983) 762.

C. Achenbach, A. Muller and E. Salzborn, Phys. Rev. Lett. 50 (1983) 2070.

A. Matsumoto et al., Abstract of ICPEAC XIII (Berlin, 1983) p.198.

(11) M. Lal, M.K. Srivastava and A.N. Tripathi, Phys. Rev. A26 (1982) 305.

(12) R.E. Olson, Phys. Lett. 71A (1979) 341.

(13) V.S. Nikolaev, Sov, Phys. USPEKHI 8 (1965) 265.

(14) K.L. Bell, H.B.Gilbody, J.G. Hughes, A.E. Kingston and F.J. Smith, CLM-R216 (1982).

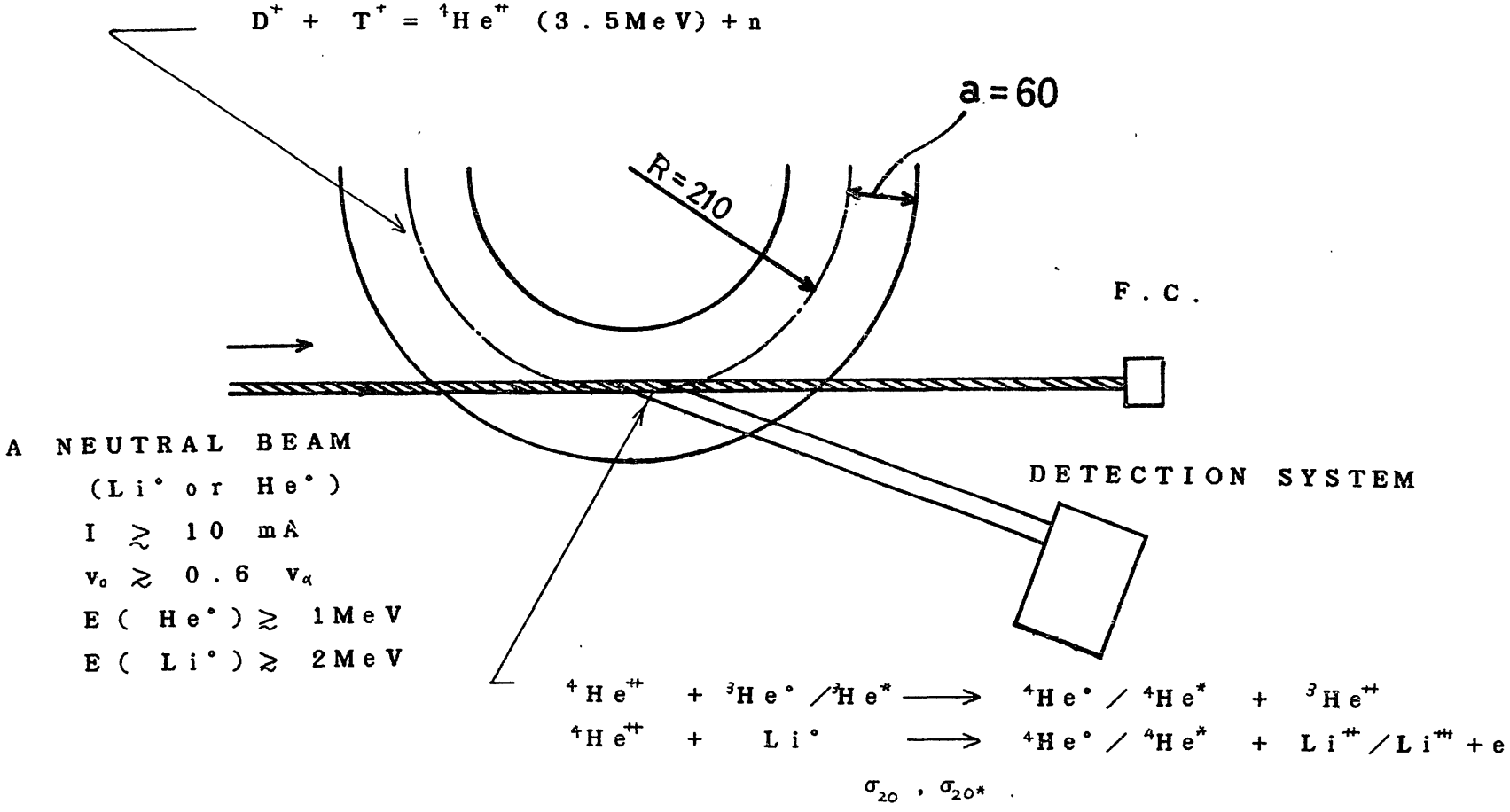

Fig. 1. The concept of a neutral beam probe tecnique.

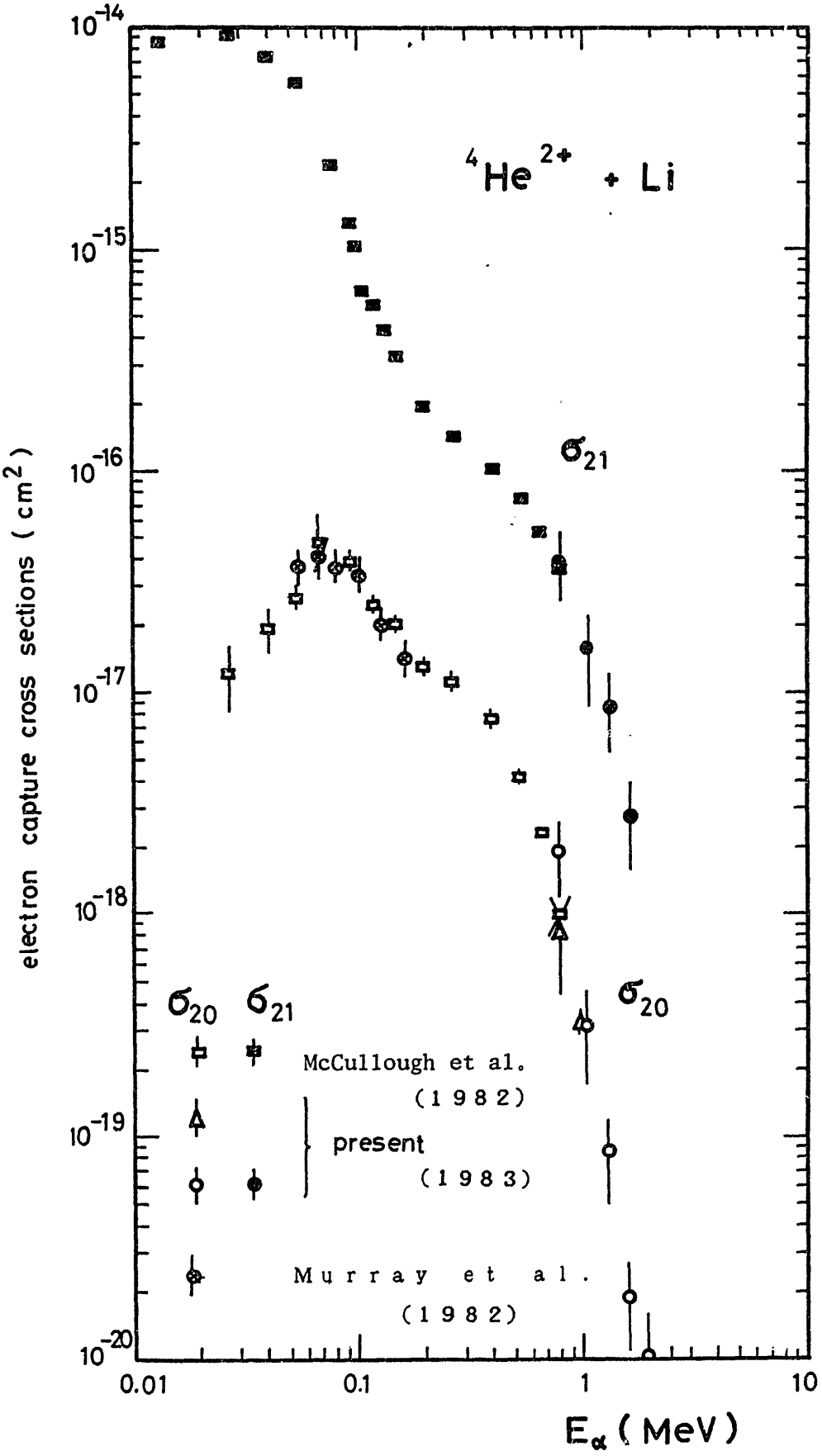

Fig. 2. Two-electron capture cross sections in He^{2+} + Li collisions.

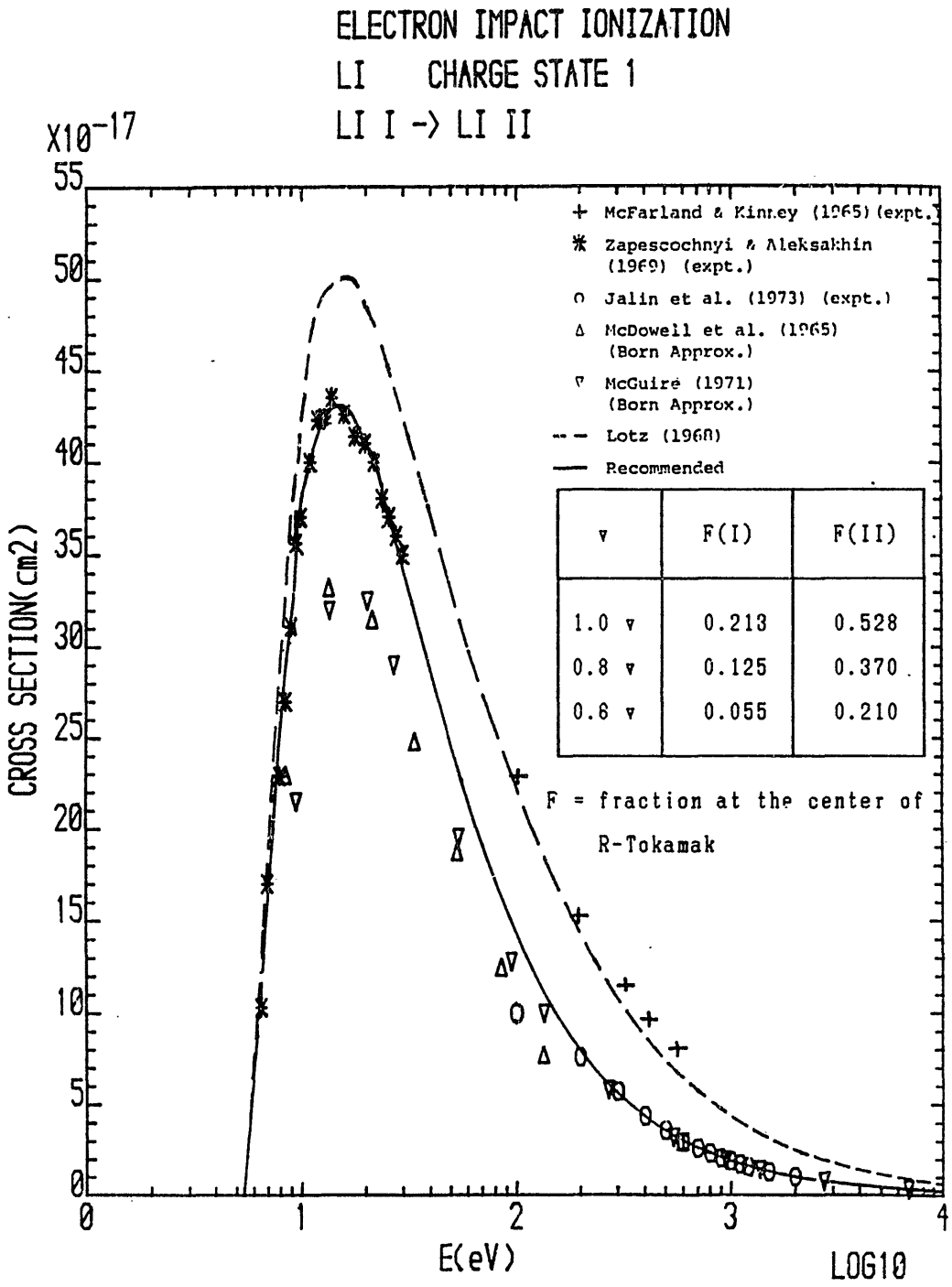

v	F(I)	F(II)
1.0 v	0.213	0.528
0.8 v	0.125	0.370
0.6 v	0.055	0.210

Fig. 3. Electron impact ionization cross sections for $Li^{14)}$. The calculated transmission factors of Li beams are tabulated in the insert for the R-Tokamak with 1% O^{8+} and 0.01% Fe^{26+} impurity ions using the cross sections measured by McFarland et al., (I), and by Jalin et al., (II).

Atomic Hydrogen Beam Probing with Spectroscopic Technique

S. GOTO, Y. ITOH and T. ISHIHARA
Plasma Physics Laboratory,
Faculty of Engineering,
Osaka University
Yamada-Oka, Suita, Osaka 565,Japan

Abstract

Possibilities of plasma diagnostics by means of spectroscopic analysis of injected atomic hydrogen beams and charge-transferred ions in plasmas are briefly discussed with relation to atomic cross sections requirements. Emphasis in this discussion is focused onto a magnetic field measurement and low-z impurity concentration measurements. A conventional diagnostic beam source of atomic hydrogen is also presented.

§I. Introduction

Beam probing methods are coming up as powerful diagnostics of characteristic behaviors of various plasmas. Plasma parameters which can be observed depend on the interactions one can expect between the beam and the plasma, and also on the detection methods one can employ. Here we shall discuss atomic hydrogen beam probing methods with spectroscopic technique, which have been developed in our laboratory. Along the beam path in the plasma two different photon emitters exist for the spectroscopic measurements. One is the beam atom itself and another the charge-transferred ion in the plasma. Each emitter may allow us to measure the following parameters.

Firstly, spectroscopic intensity observation of some atomic hydrogen Balmer lines could give us the ion density profile of hydrogen plasma along the beam penetration distance, if the beam attenuation is dominated by charge transfer process and if the electron temperature profile is known. This was already demonstrated in our previous presentation.[1] Most of the atomic cross sections relevant to this method are available in many publications.

Secondly, an emission line from the beam hydrogen can be used as magnetic field measurements through the Stark effect. The atomic hydrogens travelling through the magnetic field $\vec{B}$ with velocity $\vec{V}_b$ experience the induced electric field $\vec{V}_b \times \vec{B}$. Then, the spectral line shows a Stark broadening due to this electric field. Under a known

$\vec{V}_b$ this broadening measurement could provide an excellent method of the magnetic field determination,[2] which will be discussed in § 2.

Thirdly, as for observing the charge-transferred atoms from the plasma ions, we can easily imagine that the velocity distribution of the charge-transferred atoms reflects that of the plasma ions. Therefore, the Doppler profile measurement of an emission line of atoms leads to the ion temperature estimation. In a real experimental circumstance, however, the charge-transferred atoms coming from various positions along the beam path have to be taken into account. In such a case we need the charge transfer and electron impact ionization cross sections, which can also be found in literatures.

Finally, much progress of the impurity concentration determination by means of interaction between hydrogen and impurity ions has recently been made in tokamak confinement studies[3]. Some remarks on that are given in § 3. In § 4 a pulsed atomic hydrogen beam source developed ion our laboratory is briefly described with relation to impurity measurements .

§ 2. Magnetic Field Measurement

A hydrogen atom with the velocity $\vec{V}_b$ undergoes an electric field $\vec{E} = \vec{V}_b \times \vec{B}$ in the magnetic field B. Then a spectral line of the atom is split into many components by the Stark effect. For hydrogen Balmer series lines, the

unit separation $(\Delta\lambda)_0$ of each component can be expressed as $(\Delta\lambda)_0 = (\lambda_0)^2 |\vec{E}|/15620$, where λ_0 is the central unshifted wavelength in Å, $(\Delta\lambda)_0$ in Å and $|\vec{E}|$ in volts/cm. For the H_β line, $(\Delta\lambda)_0 = 0.0677 \sqrt{E_b}\, B_\perp$, where E_b is the beam energy in keV and $B_\perp$ the magnetic flux density in T perpendicular to $\vec{V}_b$. For $B_\perp$ = 1 T and E_b= 100 keV, $(\Delta\lambda)_0$ becomes 0.677 Å which could, in principle, be resolved by usual monochromator. When the line is broadened by other effects such as the Doppler effect and the slit widths of the monochromator, the observed line may take a broad profile with an effective width $\Delta\lambda$. Since it is considered that the width could be ruled by the most intense components, $\Delta\lambda$ is expected to be approximately $8(\Delta\lambda)_0 \simeq$ 5-6 Å for σ-components and $16(\Delta\lambda)_0 \simeq$ 8-9 Å for Π-components of the H_β line under B = 1 T and E_b = 100 keV. This broadening is fairly large, compared with those due to other effects.

Based on the consideration above the magnetic field measurement can be carried out through the profile measurement of a Balmer line. The possibility of this method has been experimentally demonstrated in our previous work[2]. A schematic diagram of the experimental setup is shown in Fig. 1. The hydrogen ion beam coming from the source is converted to the atomic beam in the drift tube at the end of which the magnetic field is applied. The hydrogen atoms emit photons through interaction with nitrogen molecules which fill along the beam path in order to neutralize the beam ions. The Balmer H_β line was

observed as shown in Fig. 1. Typical profiles obtained are presented in Fig. 2(a) for Π-components and in Fig. 2(b) for σ-components. The dashed line represents the calculated curve under the condition of $B_\perp = 1$ T and $E_b = 15$ keV. Because of low intensity of the line, the fairly wide slits were used so that each split component was not resolved but the observed profiles fit well to the calculated one.

In order to do such measurements, the required cross sections are those on the beam attenuation and on the spectral line intensity which are needed only during the course of designing the system.

§3. Impurity Measurement

The charge transfer process between the injected hydrogen atoms and impurity ions;

$$H + A^{+q} \longrightarrow H^+ + [A^{+(q-1)}]^* \longrightarrow H^+ + A^{+(q-1)} + h\nu$$

can serve as a method of particular impurity concentration measurement. Total cross sections for electron capture of the impurity A^{+q} are obtainable with a good accuracy and many experimental works of the measurement have been reported [3]. It is , however, remarked that the (n,ℓ) distribution of the excited state $[A^{+(q-1)}]^*$ in the electron capture process has to be evaluated properly. Some calculated values are given [4] but the experimental evidence is few. Information on the (n, ℓ) distribution is needed

urgently for this type of measurement.

The radiations from decay of $A^{+(q-1)}(n,\ell)^{*}$ to be observed in this process range mostly over the wavelength region of soft x-ray and vacuum ultra-violet. The absolute measurement, which is essential for the concentration determination, needs laborious works and skillful techniques. Instead of hydrogen atoms, other particles with the lower ionization potential could be used if one expects intense radiations in the visible and ultra-violet regions. Candidates could be the neutral lithium and the metastable helium. This has not been scarcely discussed up to now.

§4. A Pulsed Atomic Hydrogen Beam Source

In carrying out measurement of beam probing with spectroscopic technique, two key problems need to be overcome on the penetration length of the beam and on the brightness of the photon emitters. If the plasma conditions are given, the requirements for the beam energy and density can be derived from the relevant cross sections. As a consequence, we find that a high energy and high density beam is better for diagnostics, especially of a large bore or a high density plasma.

For this requirement we have developed and constructed a pulsed beam source shown in Fig. 3. A small z-pinch plasma gun is presented in the left-hand side of the figure. It has been found that an atomic hydrogen beam with $E_b \simeq$ 0.5 - 1 keV, density $\sim 10^{12}$ cm^{-3} and duration 2 - 3 μs can

be obtained at the distance $\sim$ 1 m from the gun by choosing appropriate operation conditions. This high density pulsed beam was applied to the ion density measurement already mentioned in §1. The generation of much higher energy beam is also planned to overcome the penetration problem. As illustrated in the figure, the beam atoms are converted to negative ions on the surface of W-plate with cesium thin layer. After acceleration of the negative ions up to several hundreds of keV by a Marx generator, a high energy neutral beam is obtained passing through the puffed gas. In this process we need information of conversion efficiency from the low energy neutral to the negative ion on the plate. Unfortunately, the efficiency is not known except that of H^+ to H^- process [5]...

§5. Summary

Up to now, most of atomic cross sections relevant to the beam-spectroscopic techniques have been evaluated with sufficient accuracies for the diagnostics. The urgent requirement is the (n,ℓ) distribution of the charge transfer process between the impurity ion and the probing beam atom. It is also expected that the beams such as metastable heliums and the related cross sections may provide easier way of impurity measurement, as discussed in §3. In addition, the conversion efficiency of the atomic hydrogen to the negative ion on a metal surface have to be known to get much higher energy beams.

References

1) Y. Ito et al., Jpn. J. App. Phys. 22, 981 (1983).

2) K. Tsukuda et al., Ko-On Gakkai-Shi (in Japanese) 9, 141 (1983).

3) R.J. Fonk et al., Phys. Rev. Lett. 49, 737 (1982).
A.N. Zinovev et al., JETP Lett. 32, 539 (1980).
V.V. Afrosimov et al., Sov. J. Plasma Phys. 5, 551 (1979).
R.C. Isler et al., Phys. Rev. A24, 2701 (1981).

4) R.E. Olson, Phys. Rev. A24, 1726 (1981).
A. Salop, J. Phys. B: Atom. Molec. Phys. 12, 919 (1979).

5) J. Los et al., Proc. 2nd Symp. On the Production and Neutralization of Negative Ions and Beams (Oct. 6-10, 1980), BNL-51304.

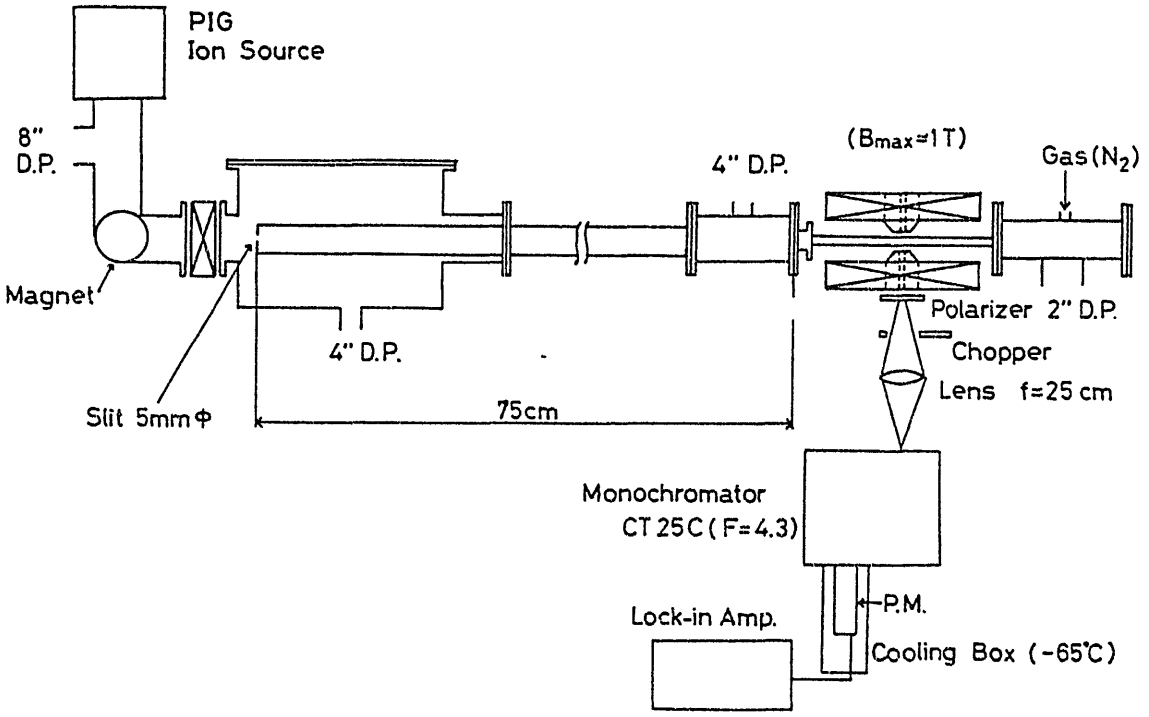

Fig.1. Experimental set-up for magnetic field measurement by beam probing with spectroscopic technique.

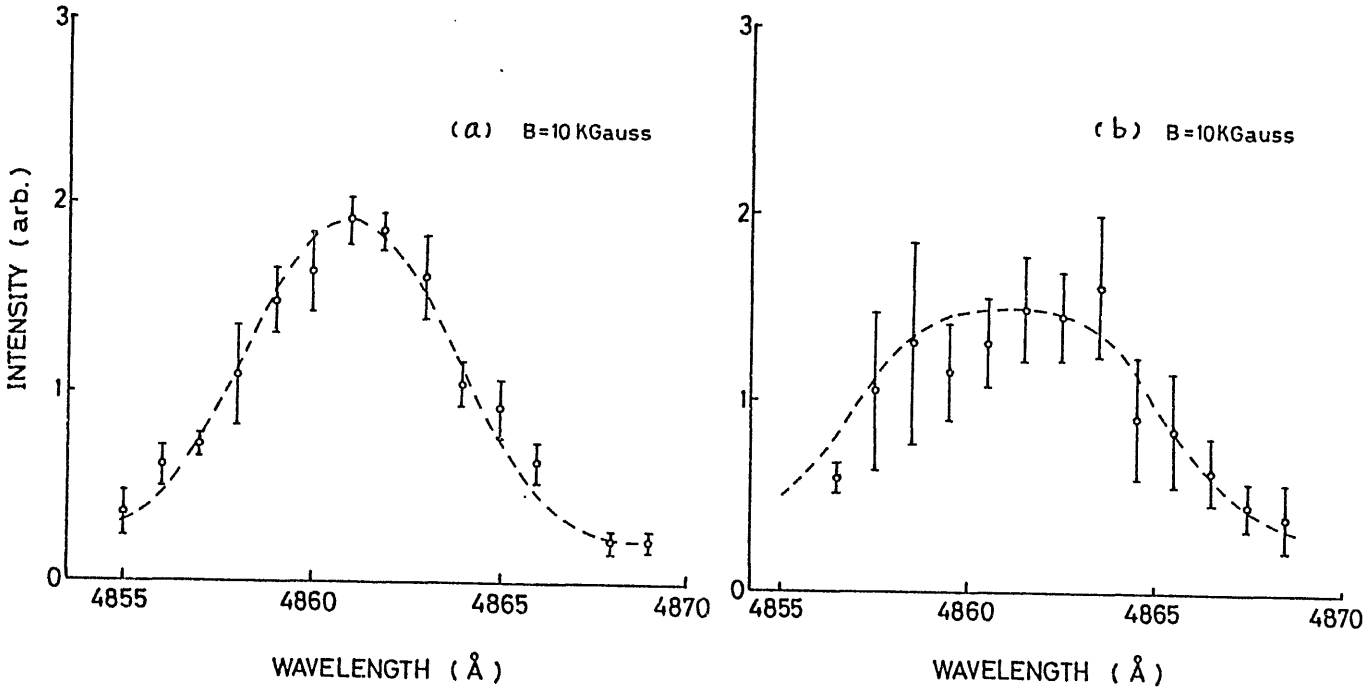

Fig.2. H_β-line profiles broadened due to $\vec{v}_b \times \vec{B}$ field.

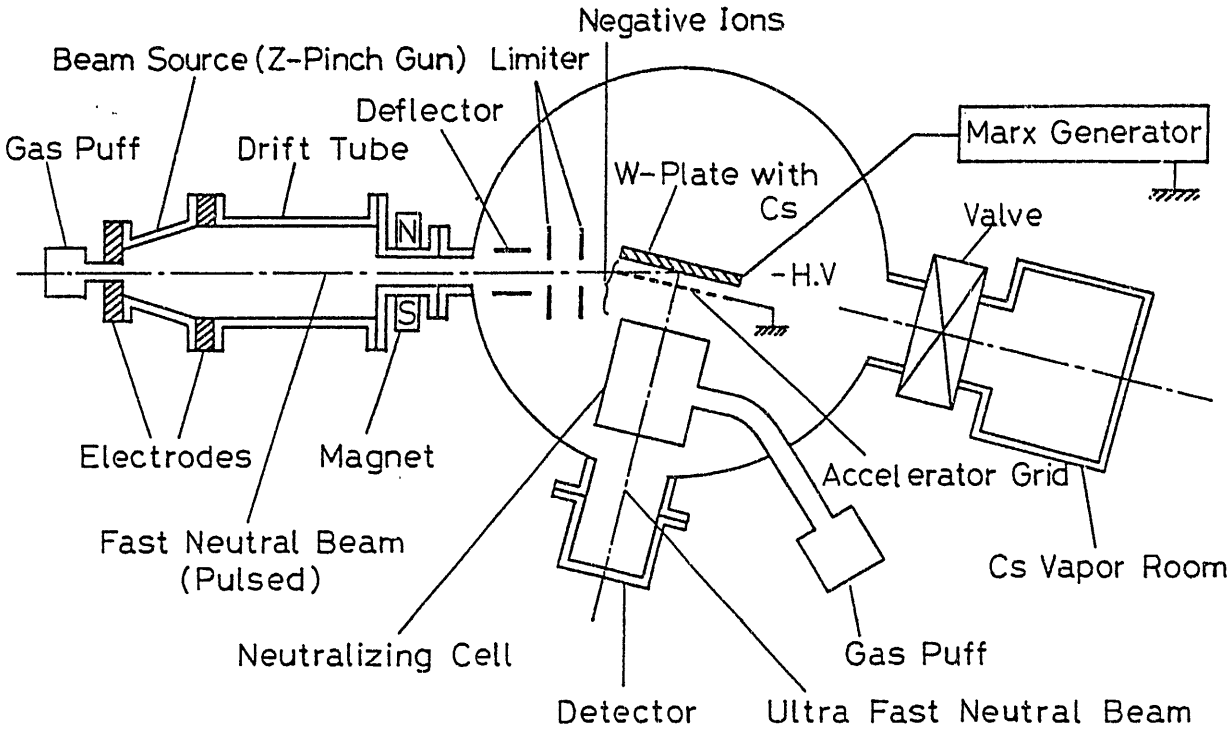

Fig.3. Schematic diagram of a pulsed atomic hydrogen beam source.

Energy Levels and Transition Probabilities of Low Z Ions for Electric Field Determination

Toshiatsu Oda and Tatehito Usui
Faculty of Science, Hiroshima University
Hiroshima 730, Japan
and
Ken Kawasaki
Physics Department, Faculty of Education
Okayama University, Okayama 700, Japan

Spectroscopic measurements are described of quasistatic electric fields in plasmas by laser fluorescence technique. Four level system is used, which is a modified one of the usual three level system of Baranger and Mozer. Laser induced fluorescence of the forbidden line (463.6 nm) by the Li I 274.1 nm line has been observed in lithium vapor to which static electric field is applied up to 11 kV/cm. A possible energy-level system of OVI is proposed.

1. Introduction

Electric field in plasmas is one of the important quantities for plasma diagnostics, which gives us, for example, knowledge of various instabilities in plasmas. Spectroscopic method of the electric field measurement using the Stark effect has been widely recognized to be useful because this method gives little disturbance to the plasma itself and, moreover, because time-and space-resolved measurements can be made by using the laser fluorescence technique.

Several investigations have been already made by using this technique.[1-3] Most of them were devoted to high-frequency Stark effect of atoms in plasmas; this effect was first theoretically investigated by Baranger and Mozer,[4] and was first experimentally demonstrated to be feasible by Kunze and Griem.[5]

Recently, we proposed an improved method over that of Baranger and Mozer for measuring quasistatic fields by using the laser fluorescence technique.[6,7] The energy levels of He I and Li I were used. In this paper, we describe the concept and the features of our method in brief and present a result of our preliminary experiment for Li I. In addition to He I and Li I, we discuss a possibility to use the energy levels of low Z ions, for example, carbon and oxgen which are common impurities in high temperature plasmas.

2. Concept of measurement

In our method, the four-energy level system is used instead of the three-level system considered in the plasma satellite line technique by Baranger and Mozer. One of the four-level systems of Li I is indicated, as an example, in Fig. 1. The dipole transition between the levels 2^2P and 4^2P is forbidden while all the other transitions are allowed except for the one between the levels 2^2S and 4^2D. The level 4^2P is mixed with the level 4^2D when a quasistatic electric field is applied. Then, the forbidden transition $4^2P \rightarrow 2^2P$ can take place. The intensity ratio S_F of the forbidden line to the allowed one ($4^2P \rightarrow 2^2S$) can be expressed by only a function of the field strength since the population density of the upper level is simply cancelled [7] in this ratio.

Our level system has another advantage: We can make signifi-

cant enhancements of both lines by using the laser fluorescence technique because the lower level 2^2S is the ground state.

3. Observation of the forbidden line from lithium vapor with applied electric field

The laser fluorescence technique has been applied to the level system shown in Fig. 1 by using thermal lithium vapor produced in a small oven. Experimental setup is shown in Fig. 2. A dye-laser excited by an N_2-laser and a second harmonic generator are used to generate a UV laser with tuned wavelength of the Li I allowed line (274.1 nm). The static electric field was applied to the lithium vapor up to 11 kV/cm. The fluorescences of both the forbidden and allowed lines were detected by a monochromator and photomultiplier system. Figure 3 shows a preliminary result of the forbidden line intensity versus the electric field strength plotted in log-log scale. The solid line represents the line intensity proportional to the square of the electric field strength. The observed forbidden line can be explained as the quadratic Stark effect.

4. Needs of data for the energy levels and the transition probabilities

Let us discuss needs for reliable data of the relevant energy levels and transition probabilities. For this purpose, analytic expression of the intensity ratio S_F will be more suitable. This expression has been already given by using the perturbation theory for weak electric field:[4)]

$$S_F = \hbar^2 \langle E^2 \rangle_{AV} R_{ij} / 6m^2 e^2 \omega_{ij}^2, \qquad (1)$$

where R_{ij} is the radial matrix element for the transition i → j, E is the electric field strength in plasmas, and ω_{ij} is the spacing between the levels i and j.

It should be noted that S_F is inversely proportional to ω_{ij}^2. Usually, the value of ω_{ij} is a small quantity as it is the difference between the closely existing levels. So, we need to know very accurate values of the relevant energy levels.

In eq.(1), the hydrogenic wavefunctions were used to calculate R_{ij}. The uncertainty for Li I is estimated to be 10 %, as Wiese has pointed out.[8] When we require more accurate field strength, more adequate wave functions should be used. This need is important if we use similar energy levels of low Z ions such as OVI. Fig. 4 shows an example of the energy level system of OVI (Li sequence), which is possible to be used for the electric field measurement.

References

1) C. F. Burrel and H. -J. Kunze: Phys. Rev. Lett. 29(1972)1445.

2) J. Hildebrandt and H. -J. Kunze: Phys. Rev. Lett. 45(1980)183.

3) U. Rebhan, N. J. Wiegart and H. -J. Kunze: Phys. Lett. 85A(1981) 228.

4) M. Baranger and B. Mozer: Phys. Rev. 123(1961)25.

5) H. -J. Kunze and H. R. Griem: Phys. Rev. Lett. 21(1968)1048.

6) T. Oda and K. Kawasaki: Jpn. J. Appl. Phys. 20(1981)L761.

7) K. Kawasaki, T. Usui and T. Oda: J. Phys. Soc. Jpn. 51(1982)3666.

8) W. L. Wiese, M. W. Smith and B. M. Glennon: Atomic Transition Probabilities Vol. 1 (NBS, 1966).

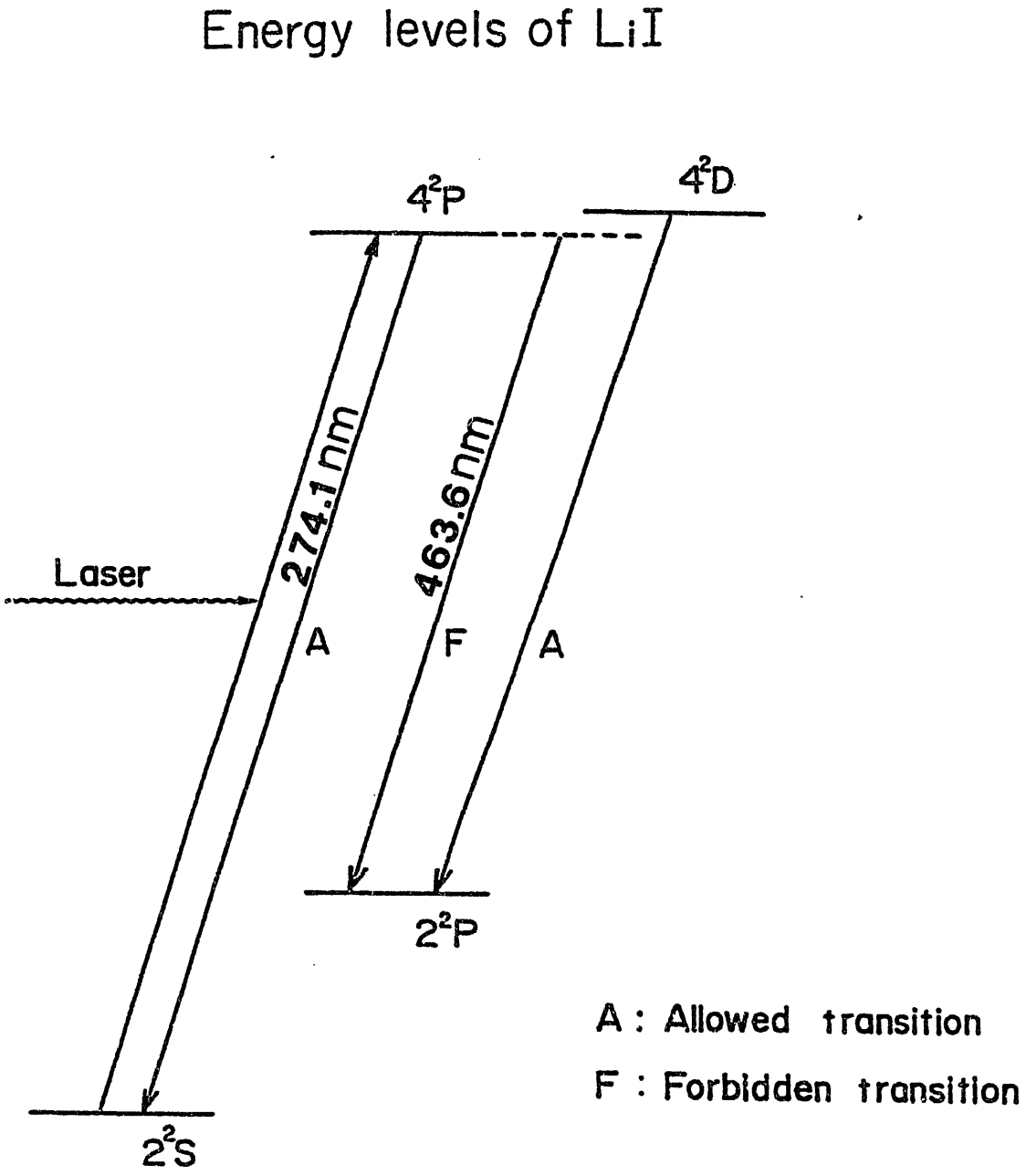

Fig. 1. The four level system of Li I. The population density of the common upper level i is enhanced by the resonance absorption from the lower level ℓ.

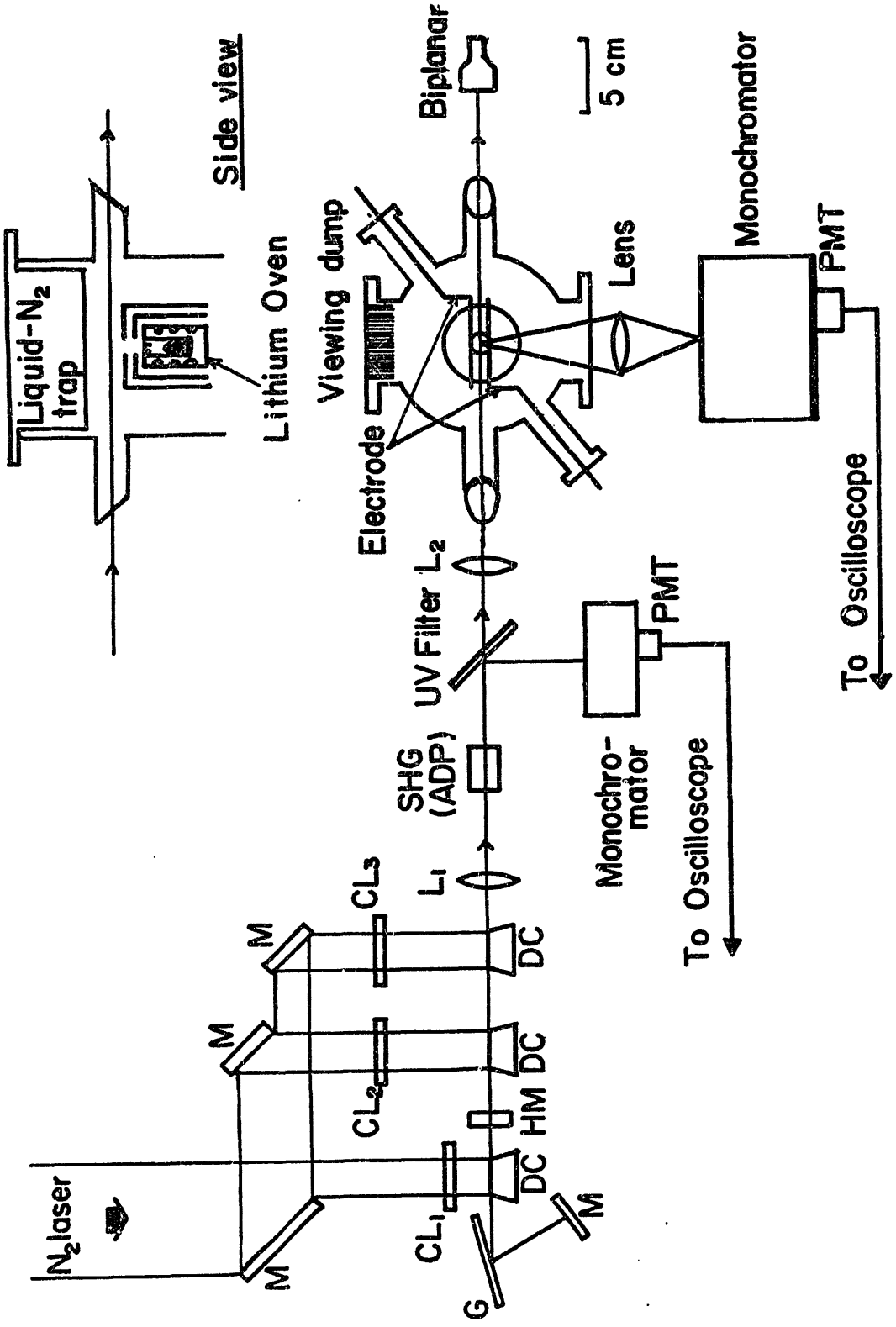

Fig. 2. Experimental setup

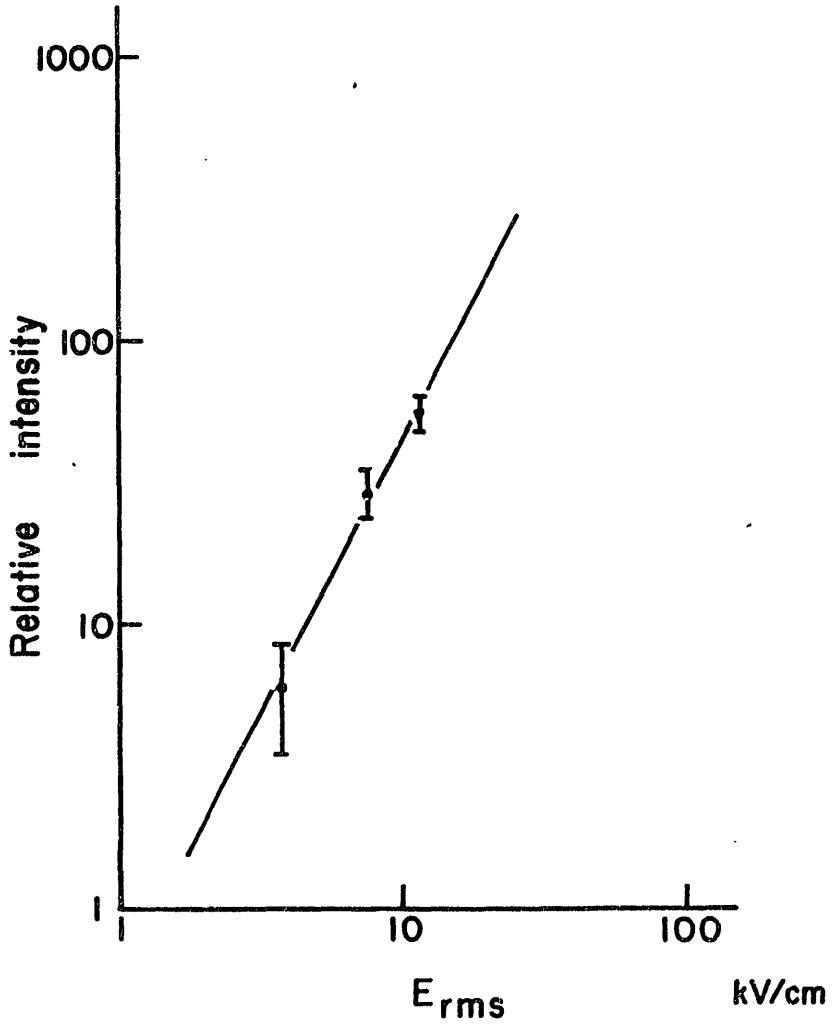

Fig. 3. The forbidden line intensity (Li I 463.6 nm) vs the electric field strength.

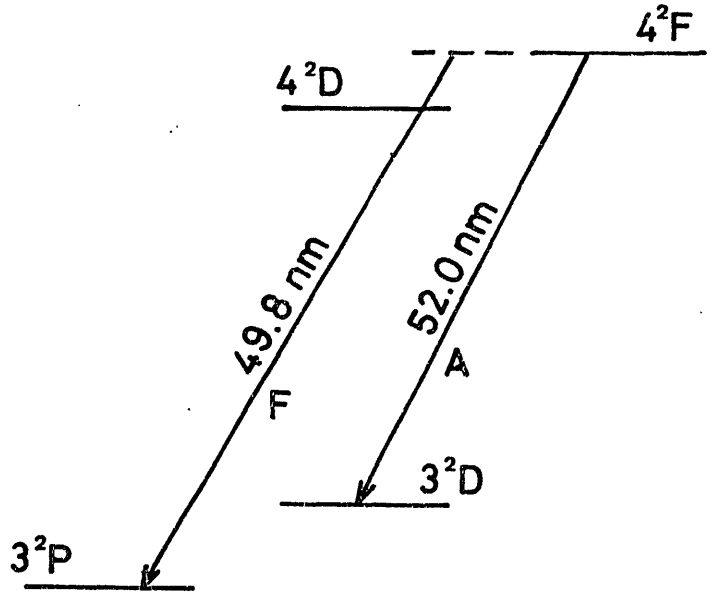

Fig. 4. The four level system of OVI.

Wavelength Measurement of X-Ray Lines from He-Like Ions

S.Morita and J.Fujita

Institute of Plasma Physics, Nagoya University 464

X-ray lines from highly stripped ions produced in high-temperature plasmas have been observed using a crystal spectrometer, and the wavelengths of He-like resonance series lines ($1snp\text{-}1s^2$ $n\geq 3$) for iron and He-like resonance lines ($1s2p\,^1P_1\text{-}1s^2\,^1S_0$) from titanium through zinc were determined for the first time.[1,2]

The high-temperature-plasma source is a coaxial discharge device called "vacuum spark", which is shown in Fig.1. The discharge is initiated by irradiation of the anode with a YAG laser light. When the capacitor bank with total capacity of 28μF is charged, the initial plasma produced by the laser irradiation closes the circuit from the capacitor bank. Electrons concentrate on the top of the anode and make the anode material evaporate . The main plasma formed from the anode element is produced in the space between the anode and the cathode.[3] Thus, we can easily get high-temperature plasmas of various elements by changing the solid materials of the anode electrode.

Figure 2 shows a time-integrated x-ray pin-hole photograph taken through a 100μm Be window, 5cm air and an Al filter (7μm thick), which transmits the x-rays of the wavelength below about 5Å. The "x-ray burst" region observed consists with the production region of M-shell-ionized ions.[4] The "hot spot " cor-

respond to the high-temperature plasma. The size of the "hot spot " was estimated to be less than 10μm in diameter from the blur of the appearance of the spots on the exposed photographs when four pin-holes of 100, 200, 400 and 1000μm in diameter were used. The parameters of this plasma can be determined from intensity ratios between He-like and Li-like satellite lines (electron temperature: about 2keV and electron density: about $10^{21}cm^{-3}$).[1)]

The Johann type crystal spectrometer[5)] is mounted to the vacuum spark through a Be window(100μm thick) so that the cylindrical axis of the crystal is parallel to the axis of the electrodes, as is shown in Fig.3. The radius of the Rowland circle of the spectrometer is 50cm and the crystal is Ge(220) with 2d spacing of 4.000Å. The distance between the crystal and x-ray source is fixed at 20.4cm regardless of the wavelengths of x-ray lines to be measured. The photographic film used is Kodak NS-5T x-ray film, which is set tangentially to the Rowland circle without bending. The spectrometer is evacuated to a pressure of about 10^{-2}torr.

All the x-ray lines associated with K-shell from the iron plasma have been measured, as shown in Fig.4. Fe Kα spectra(a) and (b) were obtained in 400 shots of discharge and the He-like resonance series lines (c) and (d) in 600 shots. The complex Kα spectra show that the iron ions in every charge state exist in the vacuum spark plasma. The He-like resonance series lines shown in (c) and (d) arise from the excited levels of 3p, 4p, 5p, 6p and 7p. The Li-like satellite lines are dominant even for the transitions of 3p-1s and 4p-1s.

The wavelengths of these spectral lines are determined using characteristic x-ray lines. Figure 5 is an example of the densitometer tracing of several characteristic lines used for the wavelength calibration.

The transition wavelengths obtained from the above spectra are listed in Table I with theoretical values by several authors.

The densitometer tracings of the Kα spectra from titanium through zinc are shown in Fig.6(a) and (b). The key letter w denotes the He-like resonance line. These spectra were obtained in about 400 shots while for titanium and vanadium in about 200 shots and chromium (SUS) in about 1000 shots. A spectrum of manganese (Z=25) is not recorded because its alloy suitable for the anode of the vacuum spark could not be obtained.

Measured wavelengths of the He-like resonance lines are listed in Table II. The uncertainties are also shown.

Figure 7 shows a comparison between the present experimental wavelengths and several theoretical wavelengths of the He-like resonance lines. The center line at zero or λ_s means Safronova's calculation.[11] The vertical lines show differences between Safronova's values and others. Our experimental values agree with Safronova's theoretical results. However, these theoretical values include some uncertainties in relativistic and QED parts of the calculated energy of the transition. Therefore, more accurate theoretical values are required.

References

1) S.Morita and J.Fujita: J.Phys.Soc.Jpn. 52(1983)1957.

2) S.Morita: J.Phys.Soc.Jpn. 52(1983)2673.

3) S.Morita and J.Fujita: Appl.Phys.Lett. 43(1983)443.

4) S.Morita, K.Kadota, T.Kagawa and J.Fujita: Phys.Lett. 94A(1983)147.

5) S.Morita, K.Kadota and J.Fujita: Jpn.J.Appl.Phys. 22(1983)1283.

6) R.Mewe and J.Schrijver: Astron.Astrophys. 65(1978)99.

7) A.M.Ermolaev, M.Jones and K.J.H.Phillips: Astrophys.Lett. 12(1972)53.

8) L.A.Vainshtein and U.I.Safronova: At.Data Nucl.Data Tables 21(1978)50.

9) M.Klapisch, J.L.Schwob, B.S.Fraenkel and J.Oreg: J.Opt.Soc.Am. 67(1977)148.

10) G.W.Erickson: J.Phys.Chem.Ref.Data 6(1977)831.

11) U.I.Safronova: Physica Scripta 23(1981)241.

12) A.M.Ermolaev: Phys.Rev. A8(1973)1651.

13) A.H.Gabriel: Mon.Not.R.Astron.Soc. 160(1972)99.

14) J.Hata and I.P.Grant: Mon.Not.R.Astron.Soc. 198(1982)1081.

Table I Wavelengths for resonance transitions of FeXXV and FeXXVI.

Ion	Transition		Experiment (Å)	Calculation (Å)				
			Present work	Mewe	Ermolaev	Vainshtein	Klapisch	Erickson
FeXXV	$1s2p-1s^2$	$^1P_1-^1S_0$	1.8504 ± 0.0004	1.873	1.84992	1.8499		
FeXXV	$1s3p-1s^2$	$^1P_1-^1S_0$	1.5738 ± 0.0006	1.580	1.57317	1.5728	1.5732	
FeXXV	$1s4p-1s^2$	$^1P_1-^1S_0$	1.4948 ± 0.0006	1.498	1.4946		1.4946	
FeXXV	$1s5p-1s^2$	$^1P_1-^1S_0$	1.4605 ± 0.0006	1.463	1.4607			
FeXXV	$1s6p-1s^2$	$^1P_1-^1S_0$	1.4433 ± 0.0006	1.445				
FeXXV	$1s7p-1s^2$	$^1P_1-^1S_0$		1.434				
FeXXV	$1s8p-1s^2$	$^1P_1-^1S_0$		1.427				
FeXXV	$1s9p-1s^2$	$^1P_1-^1S_0$		1.422				
FeXXV	$1s10p-1s^2$	$^1P_1-^1S_0$		1.419				
FeXXV	∞			1.405				
FeXXVI	2p-1s	$^2P_{1/2}-^2S_{1/2}$	1.7827 ± 0.0006			1.7827		1.7835
FeXXVI	2p-1s	$^2P_{3/2}-^2S_{1/2}$	1.7776 ± 0.0006			1.7774		1.7780
FeXXVI	3p-1s	$^2P_{1/2}-^2S_{1/2}$				1.5030	1.5034	1.5035
FeXXVI	3p-1s	$^2P_{3/2}-^2S_{1/2}$				1.5019	1.5023	1.5024

Mewe and Schrijver[6], Ermolaev, Jones and Phillips[7], Vainshtein and Safronova[8], Klapisch, Schwob, Fraenkel and Oreg[9], Erickson[10].

Table II Wavelengths of the He-like resonance lines w.

He-like resonance line w	Present experiment	Calculation by Safronova
Ti(22)	2.6104±0.0004Å	2.61045Å
V (23)	2.3820±0.0004	2.38201
Cr(24)	2.1822±0.0006	2.18209
Mn(25)	———	2.00614
Fe(26)	1.8504±0.0004	1.85046
Co(27)	1.7122±0.0006	1.71207
Ni(28)	1.5884±0.0004	1.58848
Cu(29)	1.4778±0.0004	1.47766
Zn(30)	1.3783±0.0005	1.37792

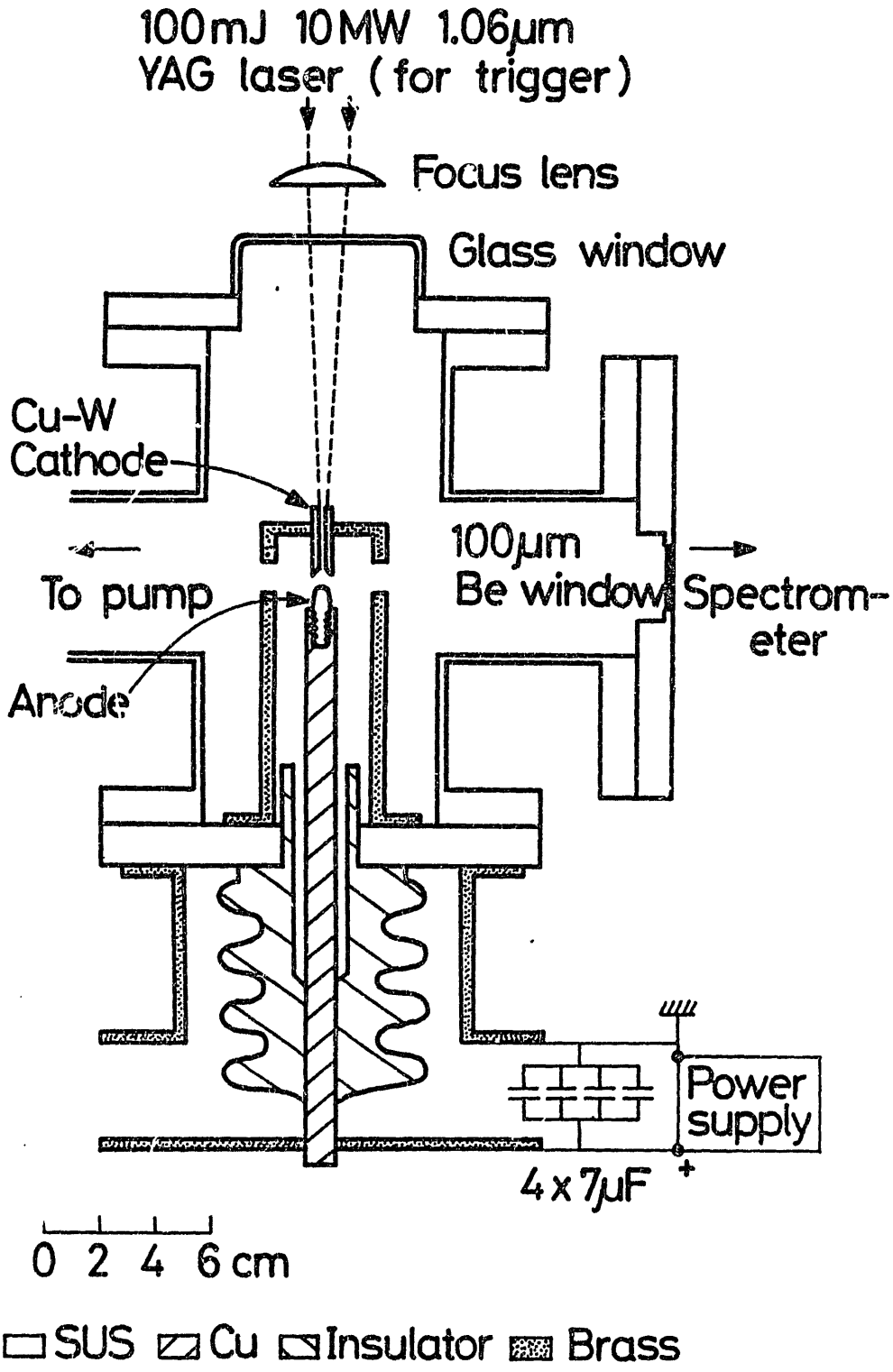

Fig.1. Cross-sectional view of the vacuum spark with cylindrical discharge chamber.

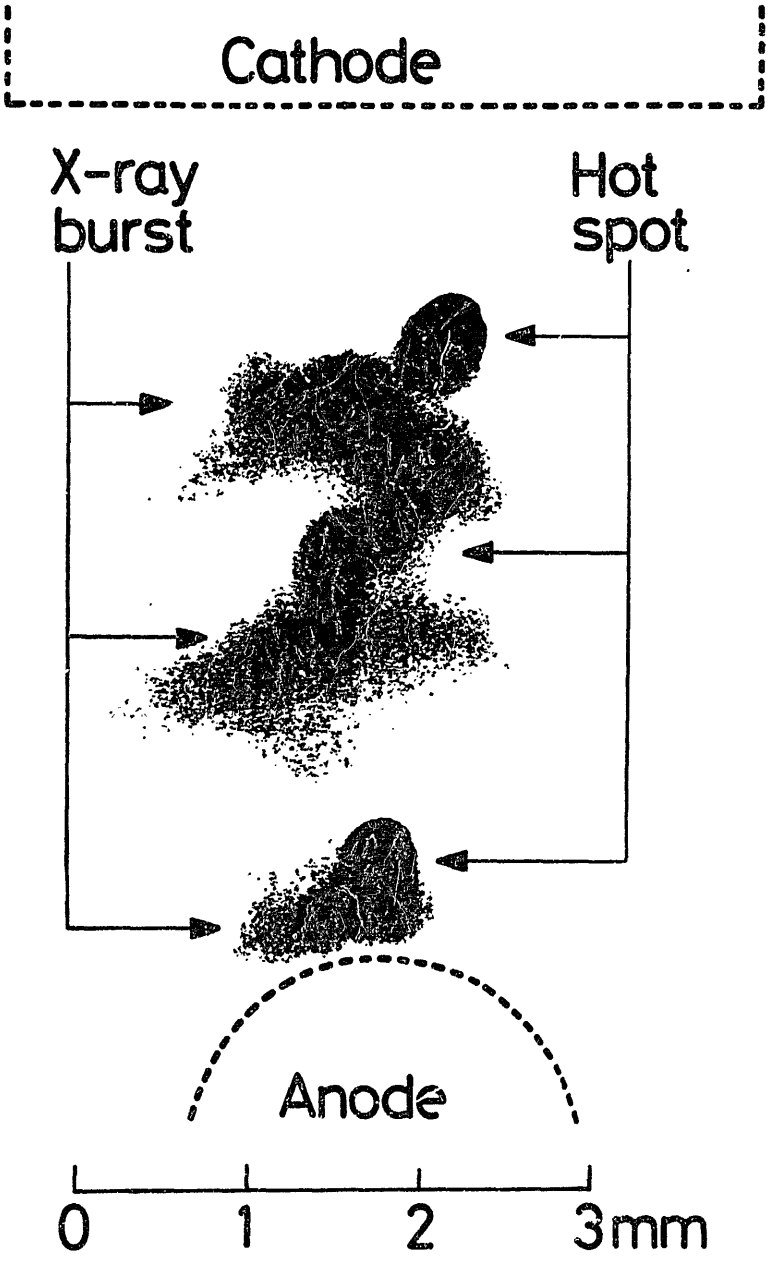

Fig.2. Time-integrated x-ray pin-hole photograph with Fe anode. The pin-hole camera responds to the wavelength region below 5Å. The "hot spots" reflect the size of the pin-hole of 400μm in diameter.

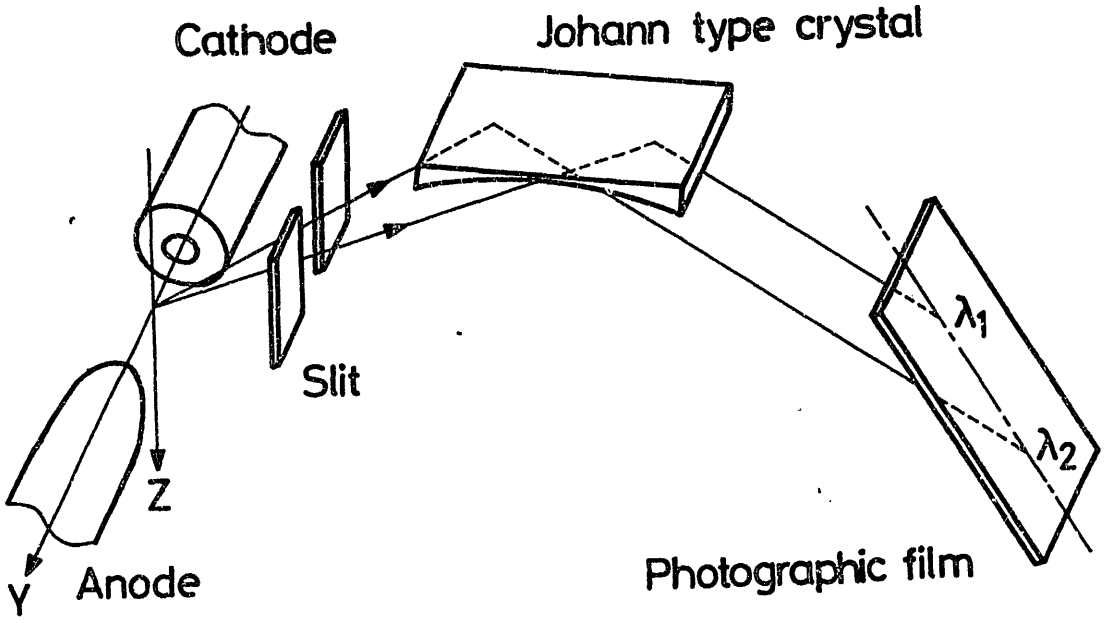

Fig.3. Arrangement of Johann type crystal spectrometer.

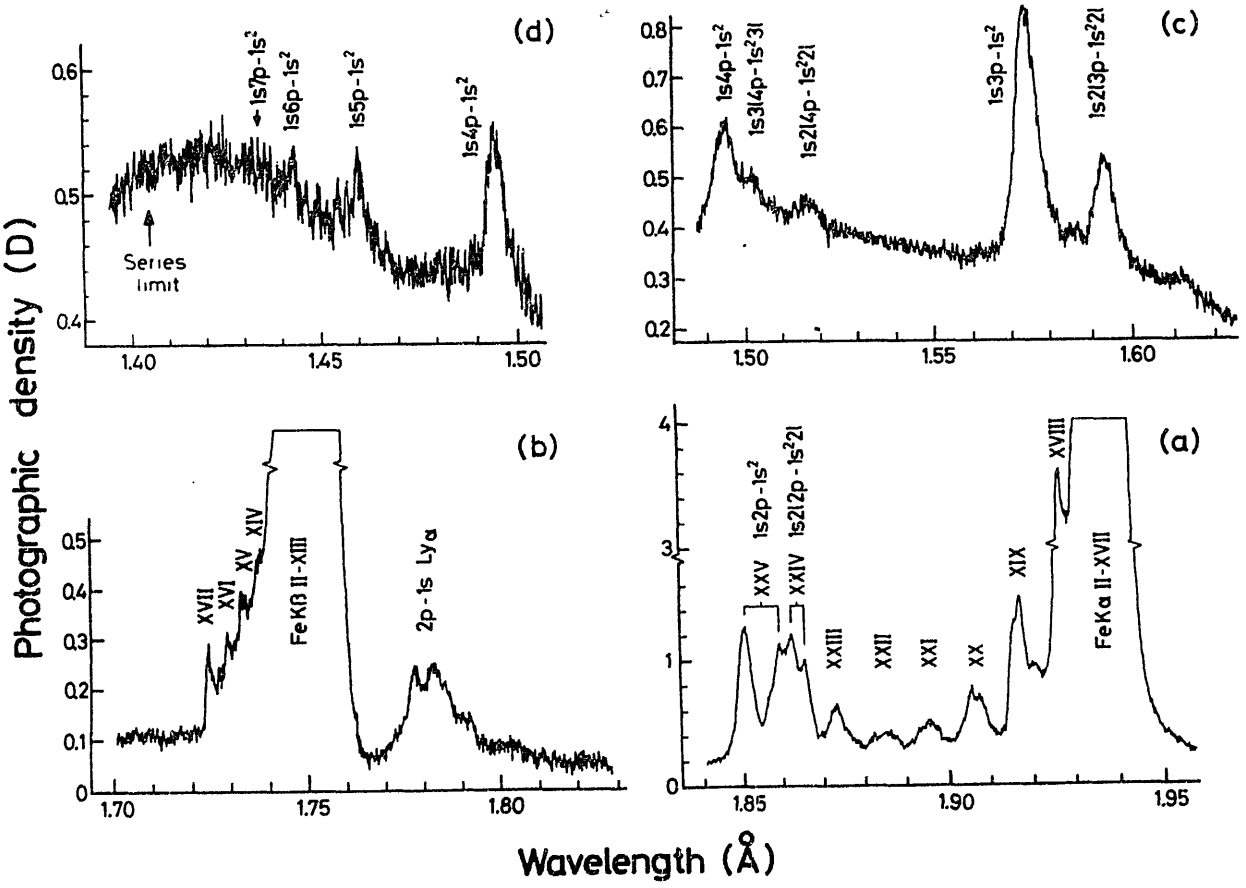

Fig.4. Densitometer tracings of K x-ray spectra emitted from vacuum spark iron plasmas.

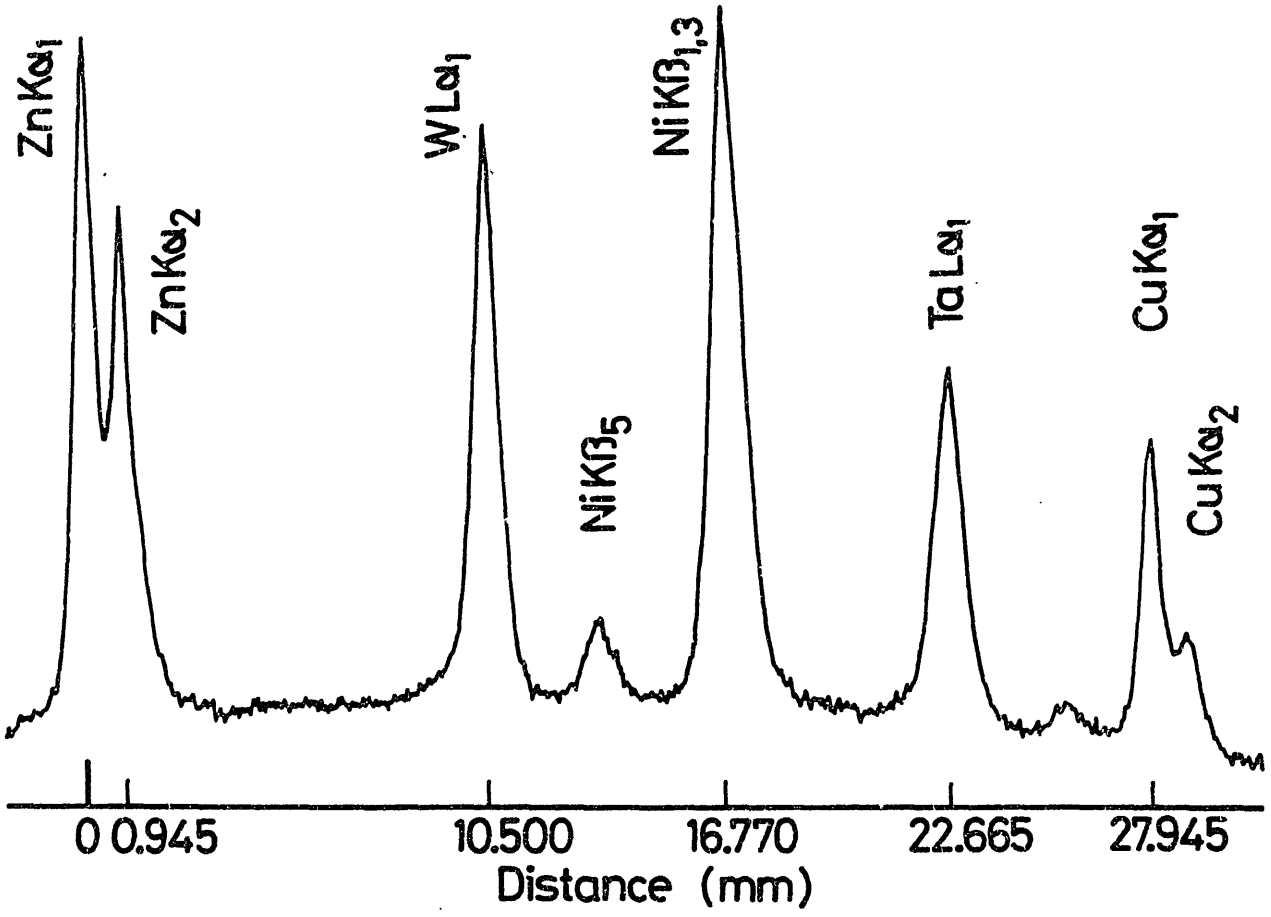

Fig.5. An example of the densitometer tracing of several characteristic x-rays used for the wavelength calibration.

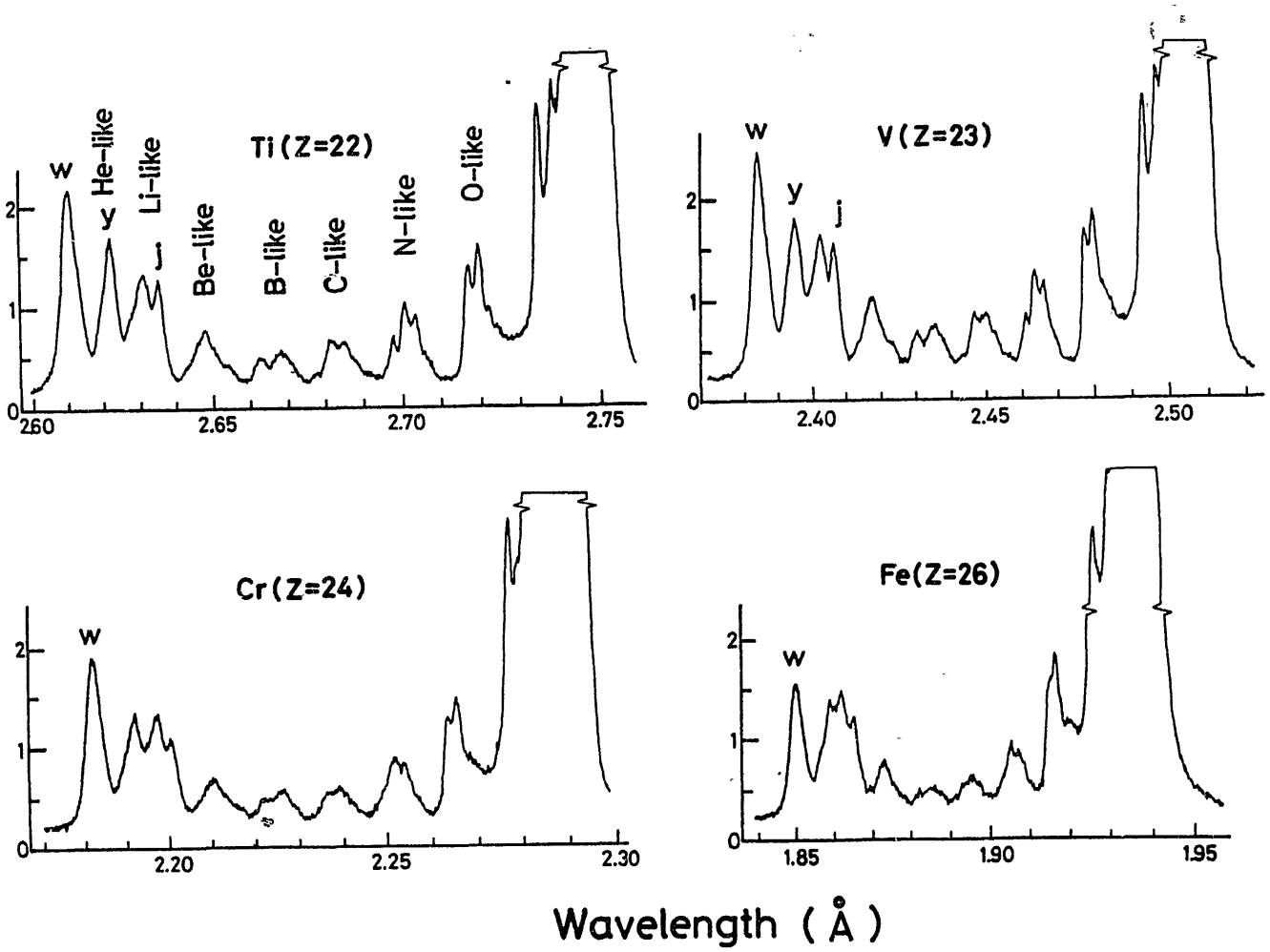

Fig.6(a). Kα spectra from the vacuum spark (titanium-iron); w denotes the He-like resonance line ($1s2p\,^1P_1$-$1s^2\,^1S_0$).

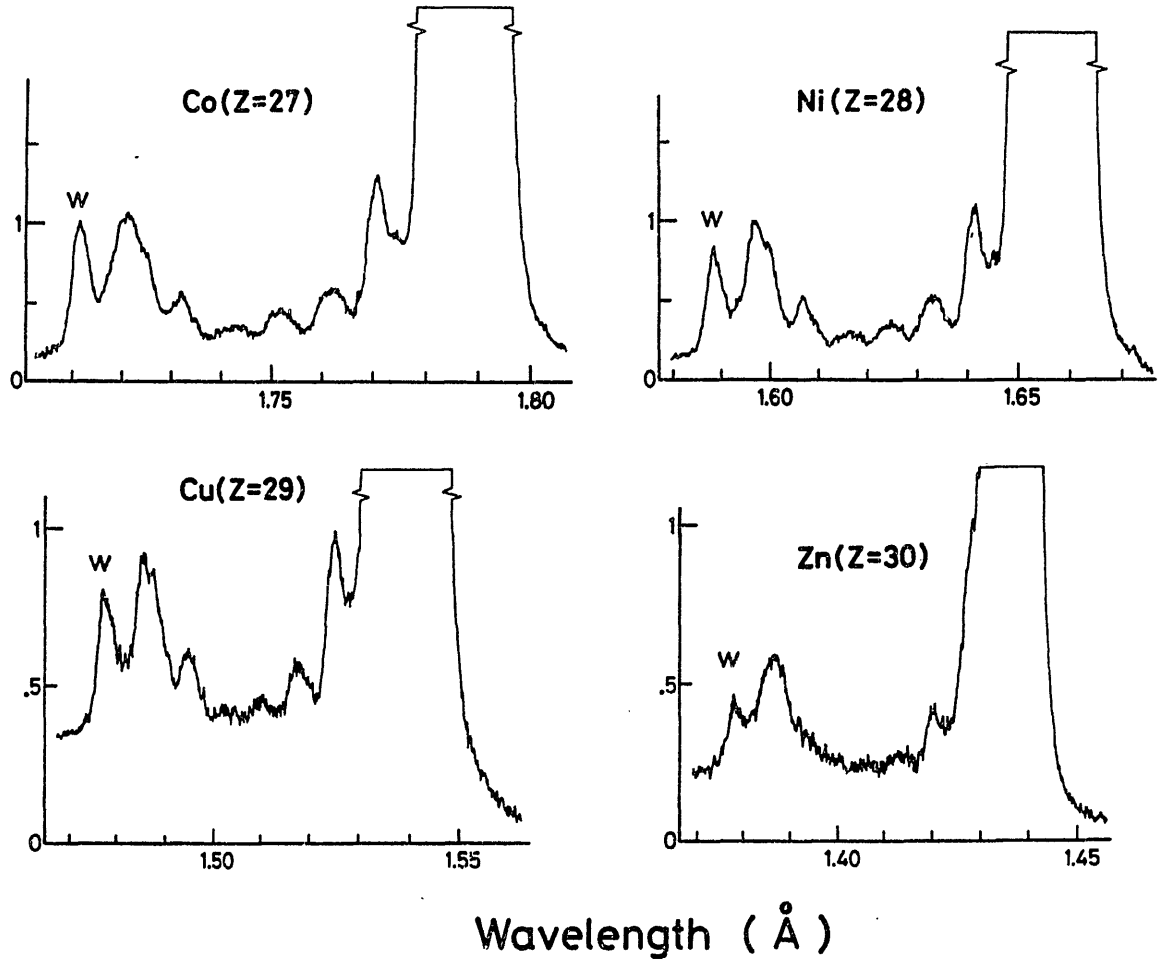

Fig.6(b). $K\alpha$ spectra from the vacuum spark (cobalt-zinc).

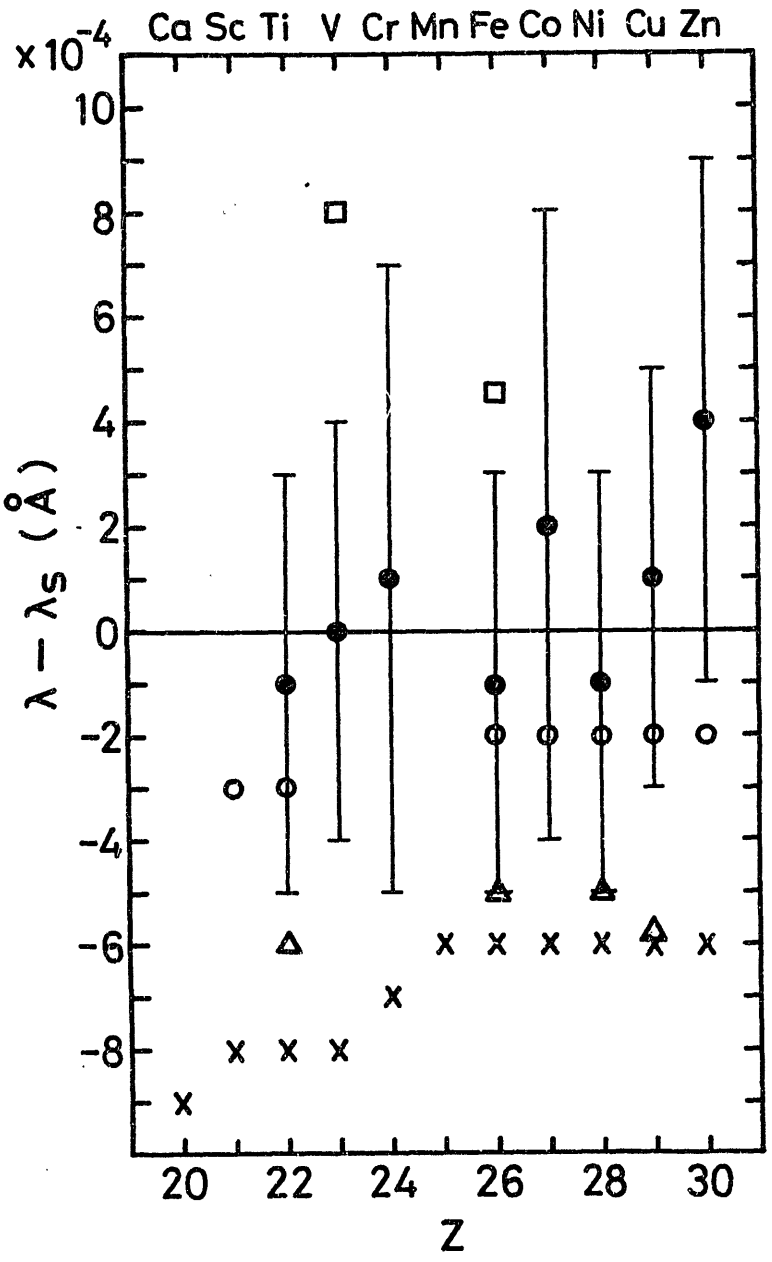

Fig.7. Comparison of the He-like resonance line between the present experimental values and several theoretical values; λ_s: Safronova[11], λ: Vainshtein and Safronova[8] (x), Ermolaev[12] (o), Gabriel[13] (Δ), Hata and Grant[14] (□) and the present experiment (●).

CHARGE EXCHANGE AND RELATED PROCESSES

H B Gilbody

Department of Pure and Applied Physics
The Queen's University of Belfast
Belfast BT7 1NN, Northern Ireland

I have been asked to discuss the current status of charge transfer in the context of the IAEA Coordinated Research Programme (CRP) on Atomic Collision Data for Diagnostics of Magnetic Fusion Plasmas. A meeting attended by experts active in both experimental and theoretical aspects of atomic collision physics was held in Vienna in June 1982. The proceedings of this meeting[1] contained a report by a Working Group on the status of charge transfer and related processes. A second meeting to be held in Nagoya after this symposium will be considering progress during the past year. In this short talk I shall try to summarise the main features of some of the data with which the CRP is concerned.

Over the past five years, the charge transfer process

$$X^{q+} + H \rightarrow X^{(q-1)+} + H^{+} \qquad (1)$$

has been the subject of considerable attention. Apart from H^+, He^+ and He^{2+}, there is particular interest in multiply charged plasma and wall-effect impurity ions, e.g. C, O, Fe, Ni, Ti. Experimental and theoretical data are now available for many species over a wide energy range (see recent reviews[2,3]).

Experiments, based mainly on the furnace target approach, have been mainly confined to the measurement of total cross sections $\sigma_{q,q-1}$ for electron capture into all final states of the product $X^{(q-1)+}$ ion. Data accurate to within about 20% are now quite extensive for velocities V > 1a.u. (corresponding to 25 keV amu-1) where cross sections are decreasing with velocity and, for a given velocity, increase with q. At these high velocities, cross sections $\sigma_{q,q-1}$ for different ions with the same initial charge q are not greatly different and can be described by simple relations of the form

$$\sigma_{q,q-1} = \sigma_o \, q^n \qquad (2)$$

The empirical scaling parameters σ_o and n depend on velocity. Values of n between 2 and 3 are typical. Corresponding values of $\sigma_{q,q-1}$ in molecular

hydrogen scale in a similar way, but even at high velocities, cross sections do not (as often assumed) approximate closely to twice the value of the cross section in atomic hydrogen. More general approaches[4,5] to scaling with a variety of targets, indicate that cross sections $\sigma_{q,q-1}$ may be generally predicted to within a factor of 2.

At velocities V < 1 a.u. experimental data on (1) are much less extensive, especially at energies below 1 keV amu^{-1}. At these low velocities, charge transfer in exothermic processes may occur very effectively through one or more pseudo-crossings of the adiabatic potential energy curves of the molecular system formed during the collision. Thus electron capture may occur selectively into one or a limited number of excited states. In general, no simple scaling laws apply and cross sections $\sigma_{q,q-1}$ for q > 4 generally exhibit only a weak dependence on velocity for a wide range of velocities below 1 a.u. Measurements of $\sigma_{q,q-1}$ carried out recently by Phaneuf[6,7,8] using a pulsed laser ion source in conjunction with a furnace target have provided cross sections below 1 keV amu^{-1} for multiply charged ions of C, O, Al and Fe in H. More measurements of this type with improved accuracy are urgently required.

At velocities V < 1 a.u. cross sections for electron capture into specified final states of the $X^{(q-1)+}$ product ion are of particular importance. A number of measurements in H_2, He and other targets have been carried out using both translational energy spectroscopy and photon emission spectroscopy (see for example[9,10]). Cross sections obtained for fully stripped ions demonstrate the selective nature of the capture process. For primary ions of the same charge, there is evidence that electron capture occurs primarily into states with the same quantum number.

In Belfast we have recently demonstrated[11] the feasibility of using translational energy spectroscopy with a furnace target to obtain, for the first time, cross sections for state selective capture in atomic hydrogen. Measurements have so far been carried out for N^{2+}, C^{2+} and C^{3+} in H at energies within the range 2-20 keV. The method requires only low primary beam fluxes and a final state energy resolution of up to 0.3 eV is possible at present. The technique also provides an unambiguous indication of the presence of any metastable species in the primary beam. Figure 1 shows a typical energy gain spectrum obtained[11] for 12 keV C^{3+} in H. Cross sections for capture into specific final states of C^{2+} derived from such spectra (accurate to within 10%) by reference to total cross sections σ_{tot} for capture into all final states are shown in figure 2. Recent theoretical predictions by Bienstock et al[12] based on full quantal calculations are shown. This is the first time that such predictions have

been tested by experiment and the measurements are currently being extended to other primary ion species.

In Grenoble[13], studies of state selective capture in H based on photon emission studies have commenced. An intense beam of fully stripped ions is passed through a tungsten tube furnace. The VUV emissions from the decay of excited collision products formed within the furnace are recorded. The method is limited to wavelengths which lie outside the background radiation of the furnace, but in principle, it can provide a higher energy resolution than methods based on translational energy spectroscopy. However, the overall accuracy of such measurements is limited mainly by the VUV calibration accuracy of about ±40%.

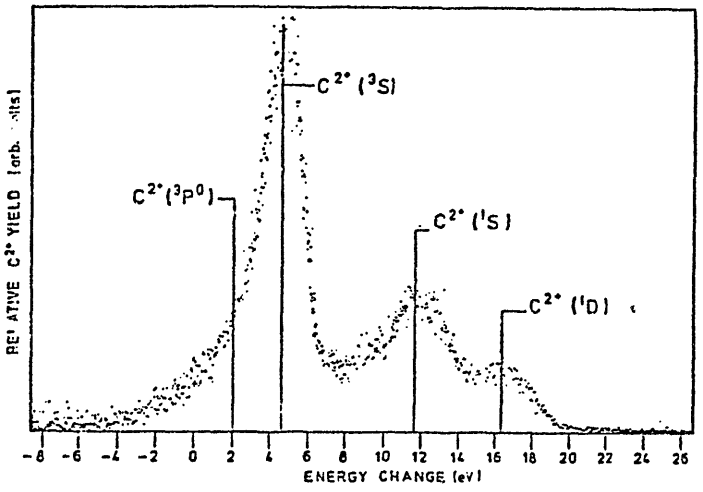

Fig 1 : Energy change spectrum for 12 keV C^{3+} in H

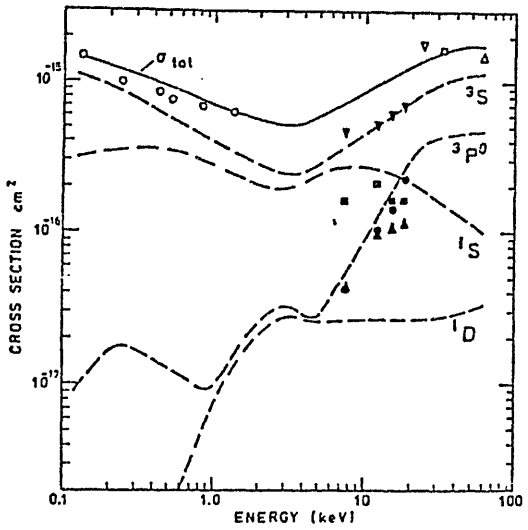

Fig 2 : Cross sections for capture into specified final states of C^{2+} in C^{3+}-H collisions. Experiment[11] Theory[12].

While the charge transfer process (1) is the main mechanism for electron removal from H atoms at velocities V < 1 a.u., at higher velocities the ionisation process

$$X^{q+} + H \rightarrow X^{q+} + H^{+} + e \qquad (3)$$

becomes dominant and there is a need to consider the total cross section for electron removal from H through the combined processes (1) and (3).

In Belfast we have used[14,15,16,17,18] a crossed beam coincidence counting technique incorporating time of flight spectroscopy to determine cross sections for the ionisation process (3) with high precision for 38-1500 keV H^+, 125-2200 keV He^{2+}, 214-2713 keV $Li^{(1-3)+}$, 190-2320 $C^{(2-6)+}$, $N^{(2-5)+}$ and $O^{(2-6)+}$. The technique may also be used (as an alternative to the furnace target approach) for the determination of cross sections for (1). A typical set of data obtained[18] for $Ar^{(3-9)+}$ in H is shown in figure 3.

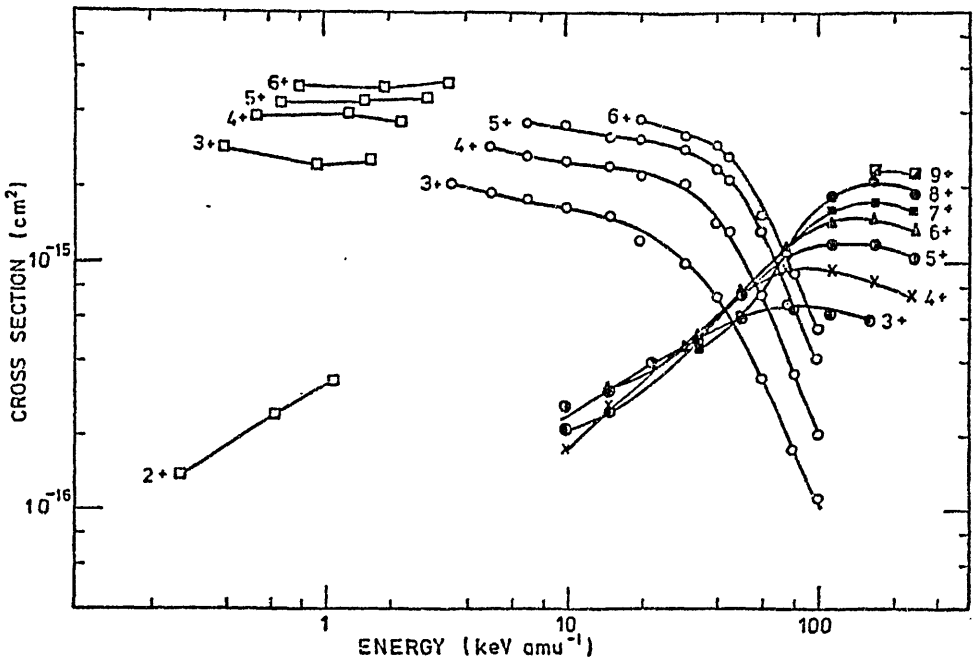

Fig 3 : Cross sections for charge transfer and ionisation in Ar^{q+}-H collisions.

□ Charge transfer - furnace target method[30]

○ Charge transfer - crossed beam coincidence method[18]

◪, ●, ■, ▲, ◍, ×, ⊕; Ionisation - crossed beam coincidence method[18].

As the charge transfer cross section decreases at high velocities, the rise in the corresponding ionisation cross section can be clearly seen. Thus total cross sections for electron removal from H for $q \geq 3$ are only weakly dependent on energy over a wide range.

At velocities where cross sections have decreased below the peak values, cross sections for (3) like those for (1) can be described by simple charge scaling relations of the type given in (2). A more general scaling relation has recently been developed by Gillespie[19] in which the ionisation cross section σ_i is given by

$$\sigma_i = q^2 f\left(q^{1/2} \frac{\alpha}{\beta}\right) \sigma_{Bethe}(\beta) \qquad (4)$$

where $f(q^{1/2} \frac{\alpha}{\beta})$ is a universal function with a simple analytic form, α is the fine structure constant, $\beta = V/c$ and $\sigma_{Bethe}(\beta)$ is the Bethe cross section for ionisation for H by fast protons. When $f(q^{1/2} \frac{\alpha}{\beta}) = e^{-\lambda (q^{1/2} \frac{\alpha}{\beta})}$ and $\lambda = 0.76$, the experimental data are correctly described[18] to within 15%. For the bare nuclei H^+, He^{2+}, Li^{3+} and C^{6+} the experimental data[17] show that the ionisation cross sections scale according to Z^2 (as predicted by the Born approximation) only at very high velocities. For each case the velocity at which the Born approximation becomes valid progressively increases with Z.

In an attempt to obtain a general scaling relation for the total cross section σ_e for electron removal from H, Olson et al[20] have used the classical-trajectory-Monte-Carlo (CTMC) method to calculate cross sections for ions with $1 \lesssim q \lesssim 50$ in the range 50-5000 keV amu^{-1}. An analytical fit to the theoretical cross sections provides a universal curve in which reduced cross sections σ_o/q are expressed in terms of the reduced energy E/q through the expression

$$\sigma_{e/q} = 4.6 \{(32\ q/E)\ [1-\exp(-E/32\ q)]\}\ 10^{-16}\ cm^2 \qquad (5)$$

where E is the energy in keV amu^{-1}. A similar expression has recently been obtained by Janev[21] also using a classical approach. Although there are departures from this universal curve at both low and high velocities, the experimental cross sections[18] are within a factor of 2 of the predicted values in the E/q range 20-150 keV amu^{-1}.

Extensive experimental data are now available for total electron capture cross sections in targets other than atomic hydrogen. Some data are also available for ionisation. Results for H_2, He and Li are of particular interest. Janev and Presnyakov[22] have compared experimental data with theoretical predictions and considered general scaling rules. For many electron targets transfer-ionisation processes of the type

$$X^{q+} + Y \rightarrow X^{m+} + Y^{n+} + (m + n - q)\ e \qquad (6)$$

involving capture of one or more electrons with the simultaneous multiple ionisation of the target have large cross sections even at low velocities (see for example[23]). A statistical interpretation of such processes at velocities $V < 1$ a.u. has been shown to be very successful[24].

An important method for the diagnostics of fast neutral hydrogen beams used for the supplementary heating of Tokamak devices relies on the observation of Balmer H_α emission following the neutralisation of hydrogen ions in H_2. The relevant cross sections for H_α emission by 1-100 keV, H, H^+, H_2^+ and H_3^+ have recently been determined[25] from studies of the 3s-2p, 3p-2s and 3d-2p decay modes following the collisional formation of excited H atoms. Measurements are currently being extended to H_2-H_2 collisions.

Cross sections for charge transfer

$$H^+ + A^{q+} \rightarrow H + X^{(q+1)+} \qquad (7)$$

and ionisation

$$H^+ + X^{q+} \rightarrow H^+ + X^{(q-1)+} + e \qquad (8)$$

involving collisions of protons with impurity ions are relevant to particle escape, enhanced energy loss and schemes for plasma diagnostics in fusion devices. A knowledge of the corresponding cross sections for He^{2+} impact is required for a proper understanding of alpha particle heating in the next generation of Tokamak devices. Experimental data on (7) and (8) are not very extensive and are limited to the singly charged ions (see review[26]) He^+, Li^+, C^+, N^+, Mg^+, Ti^+ and Fe^+. In Belfast[27], measurements with Tl^+ and Al^+ are also nearing completion. All these measurements, based on the method of intersecting beams, involve formidable problems and usually provide only the sum of cross sections (7) and (8). However, cross sections are absolute and do not rely on normalisation procedures. In the case of He^+ and Li^+, a coincidence technique has been used to obtain separate measurements of (7).

Provided that ground states are dominant in charge transfer, there is evidence[26] that cross sections for the reverse reaction

$$X^{q+} + H \rightarrow X^+ + H^+ \qquad (9)$$

can be used to provide reasonable estimates of the charge transfer cross section for $X^+ + H^+$ collisions. At the higher energies where measured cross sections for the sum of (7) and (8) are dominated by ionisation, the available data appear to fit to within a factor of two, a simple classical scaling relation[26].

Figure 4 shows recent experimental data for $H^+ - Tl^+$ collisions[27]. Cross sections for charge transfer calculated by Mapleton[28] at low

velocities are also shown. At high velocities where ionisation is dominant, the experimental values show the expected tendency to converge to the equivelocity cross sections for ionisation by electron impact[29].

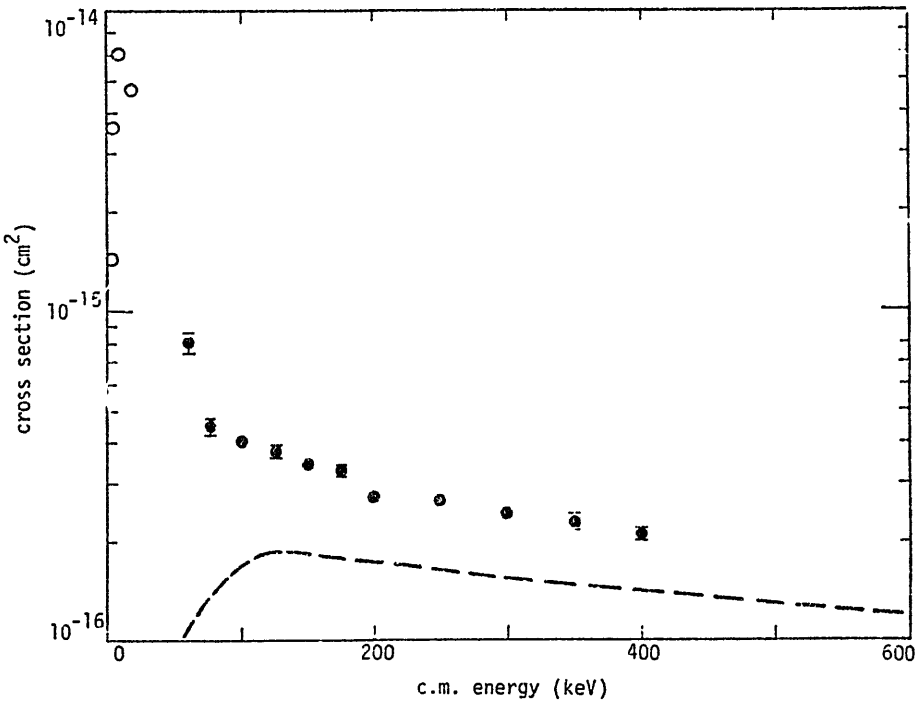

Fig 4 : Cross sections for H^+–Tl^+ collisions.

● Experiment[27] : Sum of cross sections for charge transfer and ionisation

o Theory[28] : Cross sections for charge transfer

----- Experiment[29] : Cross sections for ionisation by equivelocity electrons.

REFERENCES

1. IAEA Report INDC (NDS) - 136/GA (1982)
2. H B Gilbody : Physica Scripta 24 712 (1981)
3. R K Janev and B H Bransden : Advances in Atomic and Molecular Physics (Academic Press), Vol 19 (1983).
4. R K Janev and P Hvelplund: Comments on Atomic and Molecular Physics 11, 75 (1981)
5. A S Schlachter, J W Stearns, W G Graham, K H Berkner, R V Pyle and J A Tanis : Proc 13th Int Conf on Physics of Electronic and Atomic Collisions Berlin (1983), Abstracts p.525.
6. R A Phaneuf : IEEE TRans Nucl Sci NS-17, 1182 (1981).
7. R A Phaneuf, I Alvarez, F W Meyer and D H Crandall : Phys Rev A26, 1892 (1982).
8. R A Phaneuf : Phys Rev A - in course of publication (1983).
9. H Tawara, T Iwai, Y Kaneko, M Kimura, N Kobayashi, A Matsumoto, S Ohtani, K Okuno, S Takayi and S Tsurubuchi : Proc 13th Int Conf on Physics of Electronic and Atomic Collisions, Berlin (1983) Abstracts p.542.
10. Yu S Gordeev, D Dijkkamp, A G Drentje and F J de Heer. Proc 13th Int Conf on Physics of Electronic and Atomic Collisions, Berlin (1983)

Abstracts p.550.
11. R E McCullough, M Lennon, F G Wilkie and H B Gilbody : J Phys B 16 L173 (1983) and additional results to be published.
12. S Bienstock, T G Heil, C Böttcher and A Dalgarno : Phys Rev A25 2850 (1983).
13. S Bliman - private communication.
14. M B Shah and H B Gilbody ; J Phys B 14 2361 (1981).
15. M B Shah and H B Gilbody : J Phys B 14 2831 (1981).
16. M B Shah and H B Gilbody : J Phys B 15 413 (1982).
17. M B Shah and H B Gilbody : J Phys B 16 L449 (1983).
18. M B Shah and H B Gilbody : J Phys B - in course of publication (1983).
19. G H Gillespie : J Phys B 15 L729 (1982).
20. R E Olson, K H Berkner, W G Graham, R V Pyle, A S Schlachter and W Stearns : Phys Rev Letts 41, 163 (1981).
21. R K Janev : Phys Rev A - in course of publication (1983).
22. R K Janev and L P Presnyakov : Phys Rep 70 No 1 (1981).
23. W Groh, A Mueller, Ch Achenbach, A S Schlachter and E Salzborn : Phys Lett 85A 77 (1981).
24. A Mueller, W Groh and E Salzborn : Phys Rev Letts 51, 107 (1983).
25. I D Williams, J Geddes and H B Gilbody : J Phys B 15, 1377 (1982) and additional data to be published.
26. H B Gilbody : Proc 12th Int Conf on Physics of Electronic and Atomic Collisions, Gatlinburg. Invited Papers (S Datz Editor), N Holland (1982) p223.
27. M F Watts, G C Angel, K F Dunn and H B Gilbody : J Phys B - to be published.
28. R A Mapleton, M F Schneeberger and C A Steel, USAF Report (1975) AF-CRL:TR-75-0053.
29. T F Divine et al : Phys Rev A 13 (1976) 54-57.
30. D H Crandall, R A Phaneuf and F W Meyer : Phys Rev A22 379 (1980).

Summary of the Symposium on Atomic Collision Data for Diagnostics and Modelling of Fusion Plasma

Satio HAYAKAWA

Department of Astrophysics, Nagoya University
Nagoya 464, Japan

Abstract

Some methodological points of view concerning diagnostics and modelling are given by reference to papers presented at the Symposium. Balanced considerations are emphasized on the requirements to atomic data and on the design of experiments and calculations.

1. Introduction

At a similar symposium held here four years ago, I [1] gave an introductory talk which discussed the relevance of atomic processes to fusion plasma studies. In those days the contact between these two fields was rather weak; most plasma physicists wished as if electrons were left unbound to achieve fully ionized plasmas, while atomic physicists paied little attention to atomic processes which would play important roles in the behavior of plasmas. In the last four years these two fields have become closer, as proved by the present Symposium, and they will have to be merged to form a unified field of research for accomplishing fusion plasmas of human use.

The Symposium aimed at bringing together atomic physicists participating in the Coordinated Research Program of IAEA for atomic and molecular data, atomic physicists interested in fusion plasmas, and plasma physicists working in diagnostics and modelling of plasmas. A total of eighteen papers presented are concerned with the modelling and diagnostics of plasmas magnetically or inertially confined, novel methods of diagnostics, and the evaluation of cross section data. These papers and accompanied discussions served to mutual fertilization of different fields.

Since it may be unnecessary to repeat the abstracts of these papers, I shall give my methodological view on plasma diagnostics and modelling, and then discuss some recently developed methods of diagnostics relevant to atomic physics.

2. Diagnostics with Atomic Processes

Atomic processes have been more and more widely used for plasma diagnostics. This is because atomic processes are less ambiguous than plasma processes owing to a good understanding of atomic physics and the availability of reasonably accurate atomic data. Spectroscopic measurements have long been applied to diagnose not only laboratory plasmas along with electromagnetic measurements but also astronomical plasmas to which other methods are not readily applicable.

At present fairly accurate numerical data, either experimental or theoretical or both, are available for atoms, molecules and their ionized states. The accuracies generally achieved are on the order of 1 % or better for energy levels, by a factor of two or better for absolute cross sections, and of about 30 % or better for relative cross sections. These accuracies are good enough for designing diagnostic experiments and the first-order modelling. This implies that atomic data of as much as possible variety are useful even if they are based on semi-empirical guess. In other words, the data compilation should not be too strict to exclude inaccurate data but retain them with comments on their reliabilities.

I am emphasizing the above point, because only a limited number of data are directly available in comparison with a variety of data needed. It will not be possible to increase the number of directly measured or calculated data so as to satisfy users, plasma physicists, since data producers, atomic physicists, select processes to measure or calculate mainly from their interest and are reluctant to work for industrial

production. If users need more data for their own use, they may have to produce such data by themselves.

There is a good sign for this to be possible. Takako Kato showed us yesterday that a good number of electron collision cross sections are obtainable by plasma spectroscopy. Since stable, well-behaved plasmas are getting available, more data, particularly in highly ionized states, will be obtained from plasmas themselves. Although their accuracies will not be better than those achieved by beam crossing experiments, they may be good enough for plasma studies. I recall a historical example that the atomic data from plasma spectroscopy put a great step forward in physics. In early 1920's laboratory technology was not so advanced as to produce ions with a desired degree of ionization. Solar spectroscopy provided a unique opportunity to study the structure of such ions and gave the level structure of many electron systems. This provided one of the important bases of quantum mechanics which was invented shortly thereafter. Solar physics has gotten a pay back from quantum mechanics through the dielectronic recombination as mentioned by Dunn in the preceding paper.

Emphasizing a greater variety of data with some sacrifice of accuracy, I do not underestimate the importance of accuracy, but merely caution data producers who are sometimes reluctant to include inaccurate data in a compilation and data users who often conclude their papers with a request to more accurate atomic data. I shall make a comment on the latter, which was already raised in discussions yesterday.

The accuracy and reliability of plasma experiments depend on

several factors. The most difficult point may be poor reproducibility of plasmas produced by individual shots. Plasma properties measured in different shots should be normalized by monitoring suitable signals, for which appropriate atomic processes can be used. Even if the normalization is properly made, methods of measuring plasma parameters and the results depend on the configuration of the plasma contained in a complex apparatus and on the instrumentation of measurements. Errors associated therewith have to be compared with errors in atomic data, before requirements to their accuracies are set out. As the quality of experiment is dictated by the poorest of the above factors, one should analyze the whole experimental procedure to find out a good balance of accuracies. Although the balance of accuracies should be kept in mind, it is unfortunately sometimes forgotten, as found in some papers presented. Only after thorough investigation of interplaying factors, requirements to atomic data could be quantified.

3. Methodology of Modelling

A model is sometimes regarded as to simulate a physical reality, so that one attempts to construct a model as close as possible to a real object. Although this philosophy of modelling may be eventually adopted, it would not always apply to most cases of modelling.

The primary objective of modelling is to understand physics which would otherwise be embedded under complexity of a real world. The model for this purpose does not necessarily mimic the

real object but represents characteristic features of the object. Modelling with numerical simulation should be regarded as a numerical experiment in the sense that the experiment is designed to clarify the relationship among the fewest possible parameters. A model should therefore be devised so as to obtain the dependence on input parameters with sufficient clarity. Hence simplicity is emphasized at the expense of reality. In practice, however, most models are too complicated to understand physics taking place in plasmas.

The secondary objective of modelling is to interpret experiment. Hence diagnostics necessarily requires modelling. The model for this purpose should be more realistic than in the first case. In order to avoid complexity in the model, as this complicates interpretation, the experiment to be interpreted has to be designed on account of easy modelling. Some new methods of diagnostics reported at the Symposium meet this requirement. Hence the experimental system of a plasma has to be designed with careful account of plasma generation, diagnostics and modelling, so as to know what happens in the plasma with least ambiguity.

4. Progress in Diagnostics Methods

At the Symposium are reported several methods of diagnostics utilizing advanced technology and atomic properties. They provide useful means of studying not only fusion plasmas but also the atomic level structure.

X-ray spectroscopy has recently achieved the energy resolution of $\Delta E/E \lesssim 10^{-4}$ as reported by Morita and by Rice. The

resolution is approaching the capability of measuring the quantum electrodynamical level shift for heavy ions. The success depends primarily on the good position resolution for X-ray detection; a resolution of 40 μm is achieved with a proportional counter used for the Alcator-C experiment.

In this experiment reported by Rice, the spatial profile of electron temperature was obtained from the strengths of forbidden and satellite lines relative to resonance lines. If X-ray spetroscopy were appled to the JFT-2 and ISX-B experiments which showed different behaviours of the radial drift of ions according to the neutral beam injection parallel or antiparallel to the toroidal current, as reported by Kasai, one would have been able to obtain an unambiguous interpretation of this interesting phenomenon. For example, they measured only one line of 93.9 Å ($\Delta n = 0$, allowed) of FeXVIII, whereas Sato showed that a set of 16 Å ($\Delta n = 1$, allowed), 93.9Å and 974.8Å ($\Delta n = 0$, forbidden) lines should be measured for obtaining the spatial distributions of electron temperature, electron density and ion density.

Metastable states have been employed for probing the electron density through the competition between radiative transitions and collisional deexcitations. The applicability of this method is further developed by the laser induced fluorescence at IPP. Fujimoto reported a more advanced method of the laser induced fluorescence spectroscopy observing the disalignment of a sublevel with particular magnetic quantum number by linearly polarized light. Such a method has been applied to molecular physics and solid state physics, and is for the first time demonstrated by Fujimoto in plasma physics.

The laser induced fluorescence is incorporated with beam probe diagnostics, as reported by Kadota. The beam probe method is proved to be powerful, since it gives not only the densities and temperatures of electrons and ions, but also the magnetic field strength and electric potential by measuring ions of different charge states. Rapid progress in the study of charge transfer reactions as reviewed by Gilbody will make the beam probe method more fruitful.

5. Atomic Processes in High Density Plasmas

Atomic processes in high density plasmas require special considerations, since the effect of field particles strongly perturbs that of nuclear Coulomb field, as already remarked earlier.[1] Physics of high density plasmas has been almost monopolized by astrophysics and geophysics, taking particular account of electron degeneracy, but now becomes a subject of laboratory plasma physics as well through inertial confinement fusion. Atomic processes in hot dense plasmas reviewed by Kagawa et al.[2], and a bibliographic compilation thereupon by Kato et al.[3] provide useful references in this field, although many important works developed in connection with astrophysics are missing.

Phenomena in a high density plasma produced by implosion are not easily measurable, because the plasma is confined in a small volume for an extremely short time interval. A spatial resolution of about 100 μm is achieved for the X-ray image with use of a random mask and a pin-hole camera, while a time resolution of

$\sim$ 100 ns is attained by an X-ray streak camera as reported by Y. Kato. Further technical developments shall be made by reference to techniques available in astronomy and high energy physics.

Theoretical analyses of atomic and hydrodynamic processes occurring during implosion are developed by Nishihara with full use of knowledge of degenerate stars. However, little attention has yet been paid to interactions with waves, though waves play important roles in dense plasmas, as noted earlier[1] for electrostatic waves. It has recently been realized in connection with the accretion onto neutron stars that the contribution of waves is significant to the slowing down of ions.

6. Concluding Remarks

Concluding the Symposium, I reemphasize that various factors dictating the behaviour of a plasma have to be taken into account with good balance. Without well balanced considerations atomic processes would not be properly incorporated with fusion plasma studies.

The balance is also indispensable in planning experiments. In the past much effort was made for plasma production in comparison with diagnostics. The trend is going to be reversed. For example, the Ignitor program is planned to allocate more budget for diagnostics than for plasma production. This does not necessarily mean to buy fancy measurement instruments, but to allocate more man power for diagnostics than for plasma production. This allows one to design a plasma facility taking full account of diagnostics incorporated with a plasma to be

produced.

In designing a plasma facility, atomic processes have to be taken into account for diagnostics and modelling. This will be accomplished by the active cooperation of atomic physicists in design and the deeper considerations of plasma scientists into atomic processes. The Symposium has been successful in promoting this trend.

References

1) S. Hayakawa, IPPJ-AM-13 (1979) p.1.

2) T. Kagawa, T. Kato, T. Watanabe and S. Karashima, IPPJ-AM-31 (1983)

3) T. Kato, J. Hama, T. Kagawa, S. Karashima, N. Miyanaga, H. Tawara, N. Yamaguchi, K. Yamamoto and K. Yonei, IPPJ-AM-29 (1983)

PROGRAM

Symposium on Atomic Collision Data for Diagnostics and Modelling of Fusion Plasmas

August 29 - 30, 1983
Institute of Plasma Physics
Nagoya University, Nagoya

August 29 (Monday)

9:00 Registration

Chairman: T. Oda (Hiroshima Univ.)

9:30 Opening talk — H. Momota (IPP, Nagoya)

9:45 Atomic processes in diagnostics of Tokamak plasmas — S. Kasai (JAERI)

10:30 Impurity Transport in Tokamaks — T. Amano (IPP, Nagoya)

- coffee break -

11:45 Numerical analysis for scrape-off plasmas in FER divertor chamber — M. Sugihara (JAERI)

- lunch -

Chairman: H. Suzuki (Sophia Univ.)

13:45 Emission properties of highly ionized iron spectra for spectroscopic plasma diagnostics — K. Sato (IPP, Nagoya)

14:30 Evaluation of excitation cross section by plasma spectroscopy — T. Kato (IPP, Nagoya)

- coffee break -

15:45 Diagnostics and simulation in G-XII implosion experiments — Y. Kato (Osaka Univ.)

16:30 Atomic processes for modelling of inertial confinement fusion plasma — K. Nishihara (Osaka Univ.)

August 30 (Tuesday)

Chairman: Y. Kaneko (Tokyo Metropolitan Univ.)

9:30 Atomic collision data for beam probe diagnostics of magnetically confined high temperature plasmas
K. Kadota (IPP, Nagoya)

10:15 The effect of excitation anisotropy in the laser-induced fluorescence spectroscopy of plasmas
T. Fujimoto (Kyoto Univ.)

- coffee break -

11:30 Spectroscopy in Heliotron K. Kondo (Kyoto Univ.)

High resolution X-ray spectra of H- and He-like Argon from the Alcator C Tokamak
J. Terry, J. Rice (MIT)

- lunch -

Chairman: J. Fujita (IPP, Nagoya)

13:45 Topics related to plasma diagnostics

Atomic and molecular processes in discharge cleaning plasmas N. Noda (IPP, Nagoya)

A comment on atomic processes relevant to alpha-particles diagnostics
K.N. Sato, M. Sasao (IPP, Nagoya)

Atomic hydrogen beam probing with spectroscopic technique.
S. Goto (Osaka Univ.)

Energy levels and transition probabilities of low Z ions for electric field determination
T. Oda (Hiroshima Univ.)

Wavelength measurement of X-ray lines from He-like ions
S. Morita (IPP, Nagoya)

14:45 Charge exchange and related processes
H.B. Gilbody (Univ. Belfast)

Evaluation of electron-ion collision data in CRP
G. Dunn (JILA, Colorado)

- coffee break -

16:15 Summary talk S. Hayakawa (Nagoya Univ.)

List of Participants

Symposium on Atomic Collision Data for Diagnostics and Modelling of Fusion Plasmas

August 29 - 30, 1983
Nagoya Univ. Nagoya

V.A. Abramov	I.V. Kurchatov Inst. Atomic Energy, Moscow, U.S.S.R.
T. Amano	IPP, Nagoya Univ., Nagoya
V.A. Belyaev	I.V. Kurchatov Inst. Atomic Energy, Moscow, U.S.S.R.
S.L. Bliman	Centre d'Etudes Nucleaires de Grenoble, Ave. des Martyrs 53, B.P. No. 85, Centre de Tri, F-38041 GRENOBLE CEDEX, France
G.H. Dunn	Joint Inst. for Lab. Astrophysics, University Colorado, Boulder, COLORADO 80309, U.S.A.
T. Fujimoto	Eng. Phys. Dept., Kyoto Univ., Kyoto
J. Fujita	IPP, Nagoya Univ., Nagoya
H.B. Gilbody	Dept. of Pure & Applied Physics, The Queen's University, Belfast BT7 INN, Northern Ireland, U.K.
S. Goto	Eng. Dept., Osaka Univ., Osaka
T. Hara	IPCR, Saitama
S. Hayakawa	Phys. Dept., Nagoya Univ., Nagoya
S. Himeno	IPP, Nagoya Univ., Nagoya
P. Hvelplund	Physical Institute, University of Aarhus, DK-8000 AARHUS, Denmark
K. Iguchi	IPP, Nagoya Univ., Nagoya
Y. Itikawa	Inst. Space & Astronautical Sci., Tokyo
T. Iwai	Dept. Lib. Art, Kansai Medical Univ., Hirakata
K. Kadota	IPP, Nagoya Univ., Nagoya
T. Kagawa	Phys. Dept., Nara Women's Univ., Nara
H. Kakihana	IPP, Nagoya Univ., Nagoya
Y. Kaneko	Phys. Dept., Tokyo Metropolitan Univ., Tokyo

S. Kano	Laser Sci. Center, Univ. Electro-Communication, Tokyo
S. Kasai	JAERI, Tokai
T. Kato	IPP, Nagoya Univ. Nagoya
Y. Kato	Inst. Laser Eng., Osaka Univ., Osaka
K. Katsonis	Atomic Data Section, IAEA, Vienna, Austria
I. Katsumata	Research Inst. Atomic Energy, Osaka City Univ., Osaka
T. Kawamura	IPP, Nagoya Univ., Nagoya
Y. Kawasume	IPP, Nagoya Univ., Nagoya
N. Kobayashi	Phys. Dept., Tokyo Metropolitan Univ., Tokyo
K. Kondo	Plasma Phys. Lab., Kyoto Univ., Kyoto
A. Lorenz	Atomic Data Section, IAEA, Vienna, Austria
A. Matsumoto	IPP, Nagoya Univ., Nagoya
M. Matsuzawa	Eng. Phy., Univ. Electro-Communication, Tokyo
M. Mimura	Research Inst. Atomic Energy, Osaka City Univ., Osaka
S. Miyake	Weld. Res. Inst., Osaka Univ., Osaka
H. Momota	IPP, Nagoya Univ., Nagoya
K. Mori	Japan Information Center of Science & Technology, Tokyo
S. Morita	IPP, Nagoya Univ., Nagoya
Y. Nakai	JAERI, Tokai
S. Nakazaki	Appl. Phys. Dept., Miyazaki Univ., Miyazaki
K. Nishihara	Inst. Laser Eng., Osaka Univ., Osaka
N. Noda	IPP, Nagoya Univ., Nagoya
Y. Obata	JAERI, Tokai
T. Oda	Phys. Dept., Hiroshima Univ., Hiroshima
S. Ohtani	IPP, Nagoya Univ., Nagoya
K. Okuno	Phys. Dept., Tokyo Metropolitan Univ., Tokyo
M. Otsuka	IPP, Nagoya Univ., Nagoya
J. Rice	MIT, Cambridge
E. Salzborn	Inst. fuer Kernphysik, Strahlenzentrum der Justus-Liebig-Univ., Leihgesterner Weg 217, D-6300 GIESSEN, Federal Republic of Germany
K. Sasao	IPP, Nagoya Univ., Nagoya

K. Sato	IPP, Nagoya Univ., Nagoya
K.N. Sato	IPP, Nagoya Univ., Nagoya
M. Sugihara	JAERI, Tokai
H. Suzuki	Phys. Dept., Sophia Univ., Tokyo
S. Takagi	IPP, Nagoya Univ., Nagoya
K. Takayanagi	Inst. Space & Astronautical Sci., Tokyo
H. Tawara	IPP, Nagoya Univ., Nagoya
J. Terry	MIT, Cambridge
F. Tsuboi	IPP, Nagoya Univ., Nagoya
K. Tsuchida	IPP, Nagoya Univ., Nagoya
T. Usui	Phys. Dept., Hiroshima Univ., Hiroshima
K. Wakiya	Phys. Dept., Sophia Univ., Tokyo
T. Watanabe	IPCR, Saitama
H. Winter	Inst. fuer Allgemeine Physik, Technische Universitaet Wien, Karlsplatz 13, A-1041 WIEN, Austria
T. Yamaguchi	IPP, Nagoya Univ., Nagoya

LIST OF IPPJ-AM REPORTS

IPPJ-AM-1* "Cross Sections for Charge Transfer of Hydrogen Beams in Gases and Vapors in the Energy Range 10 eV–10 keV"
H. Tawara (1977) [Published in Atomic Data and Nuclear Data Tables 22, 491 (1978)]

IPPJ-AM-2* "Ionization and Excitation of Ions by Electron Impact –Review of Empirical Formulae–"
T. Kato (1977)

IPPJ-AM-3 "Grotrian Diagrams of Highly Ionized Iron FeVIII-FeXXVI"
K. Mori, M. Otsuka and T. Kato (1977) [Published in Atomic Data and Nuclear Data Tables 23, 196 (1979)]

IPPJ-AM-4 "Atomic Processes in Hot Plasmas and X-Ray Emission"
T. Kato (1978)

IPPJ-AM-5* "Charge Transfer between a Proton and a Heavy Metal Atom"
S.Hiraide, Y. Kigoshi and M. Matsuzawa (1978)

IPPJ-AM-6* "Free-Free Transition in a Plasma –Review of Cross Sections and Spectra–"
T. Kato and H. Narumi (1978)

IPPJ-AM-7* "Bibliography on Electron Collisions with Atomic Positive Ions: 1940 Through 1977"
K. Takayanagi and T. Iwai (1978)

IPPJ-AM-8 "Semi-Empirical Cross Sections and Rate Coefficients for Excitation and Ionization by Electron Collision and Photoionization of Helium"
T. Fujimoto (1978)

IPPJ-AM-9 "Charge Changing Cross Sections for Heavy-Particle Collisions in the Energy Range from 0.1 eV to 10 MeV I. Incidence of He, Li, Be, B and Their Ions"
Kazuhiko Okuno (1978)

IPPJ-AM-10 "Charge Changing Cross Sections for Heavy-Particle Collisions in the Energy Range from 0.1 eV to 10 MeV II. Incidence of C, N, O and Their Ions"
Kazuhiko Okuno (1978)

IPPJ-AM-11 "Charge Changing Cross Sections for Heavy-Particle Collisions in the Energy Range from 0.1 eV to 10 Mev III. Incidence of F, Ne, Na and Their Ions"
Kazuhiko Okuno (1978)

IPPJ-AM-12* "Electron Impact Excitation of Positive Ions Calculated in the Coulomb-Born Approximation –A Data List and Comparative Survey–"
S. Nakazaki and T. Hashino (1979)

IPPJ-AM-13 "Atomic Processes in Fusion Plasmas – Proceedings of the Nagoya Seminar on Atomic Processes in Fusion Plasmas Sept. 5-7, 1979"
Ed. by Y. Itikawa and T. Kato (1979)

IPPJ-AM-14 "Energy Dependence of Sputtering Yields of Monatomic Solids"
N. Matsunami, Y. Yamamura, Y. Itikawa, N. Itoh, Y. Kazumata, S. Miyagawa, K. Morita and R. Shimizu (1980)

IPPJ-AM-15 "Cross Sections for Charge Transfer Collisions Involving Hydrogen Atoms"
Y. Kaneko, T. Arikawa, Y. Itikawa, T. Iwai, T. Kato, M. Matsuzawa, Y. Nakai, K. Okuno, H. Ryufuku, H. Tawara and T. Watanabe (1980)

IPPJ-AM-16 "Two-Centre Coulomb Phaseshifts and Radial Functions"
H. Nakamura and H. Takagi (1980)

IPPJ-AM-17 "Empirical Formulas for Ionization Cross Section of Atomic Ions for Electron Collisions –Critical Review with Compilation of Experimental Data–"
Y. Itikawa and T. Kato (1981)

IPPJ-AM-18 "Data on the Backscattering Coefficients of Light Ions from Solids"
T. Tabata, R. Ito, Y. Itikawa, N. Itoh and K. Morita (1981)

IPPJ-AM-19 "Recommended Values of Transport Cross Sections for Elastic Collision and Total Collision Cross Section for Electrons in Atomic and Molecular Gases"
M. Hayashi (1981)

IPPJ-AM-20 "Electron Capture and Loss Cross Sections for Collisions between Heavy Ions and Hydrogen Molecules"
Y. Kaneko, Y. Itikawa, T. Iwai, T. Kato, Y. Nakai, K. Okuno and H. Tawara (1981)

IPPJ-AM-21 "Surface Data for Fusion Devices – Proceedings of the U.S–Japan Workshop on Surface Data Review Dec. 14-18, 1981"
Ed. by N. Itoh and E.W. Thomas (1982)

IPPJ-AM-22 "Desorption and Related Phenomena Relevant to Fusion Devices"
Ed. by A. Koma (1982)

IPPJ-AM-23 "Dielectronic Recombination of Hydrogenic Ions"
T. Fujimoto, T. Kato and Y. Nakamura (1982)

IPPJ-AM-24 "Bibliography on Electron Collisions with Atomic Positive Ions: 1978 Through 1982 (Supplement to IPPJ-AM-7)"
Y. Itikawa (1982)

IPPJ-AM-25 "Bibliography on Ionization and Charge Transfer Processes in Ion-Ion Collision"
H. Tawara (1983)

IPPJ-AM-26 "Angular Dependence of Sputtering Yields of Monatomic Solids"
Y. Yamamura, Y. Itikawa and N. Itoh (1983)

IPPJ-AM-27 "Recommended Data on Excitation of Carbon and Oxygen Ions by Electron Collisions"
Y. Itikawa, S. Hara, T. Kato, S. Nakazaki, M.S. Pindzola and D.H. Crandall (1983)

IPPJ-AM-28 "Electron Capture and Loss Cross Sections for Collisions Between Heavy Ions and Hydrogen Molecules (Up-dated version of IPPJ-AM-20)
H. Tawara, T. Kato and Y. Nakai (1983)

IPPJ-AM-29 "Bibliography on Atomic Processes in Hot Dense Plasmas"
T. Kato, J. Hama, T. Kagawa, S. Karashima, N. Miyanaga, H. Tawara, N. Yamaguchi, K. Yamamoto and K. Yonei (1983)

IPPJ-AM-30 "Cross Sections for Charge Transfers of Highly Ionized Ions in Hydrogen Atoms (Up-dated version of IPPJ-AM-15)"
H. Tawara, T. Kato and Y. Nakai (1983)

IPPJ-AM-31 "Atomic Processes in Hot Dense Plasmas"
T. Kagawa, T. Kato, T. Watanabe and S. Karashima (1983)

IPPJ-AM-32 "Energy Dependence of the Yields of Ion-Induced Sputtering of Monatomic Solids"
N. Matsunami, Y. Yamamura, Y. Itikawa, N. Itoh, Y. Kazumata, S. Miyagawa, K. Morita, R. Shimizu and H. Tawara (1983)

IPPJ-AM-33 "Proceedings on Symposium on Atomic Collision Data for Diagnostics and Modelling of Fusion Plasmas, Aug. 29 – 30, 1983"
Ed. by H. Tawara (1983)

Available upon request to Research Information Center, Institute of Plasma Physics, Nagoya University, Nagoya 464, Japan, except for the reports noted with*.